ENZYMATIC PROTEIN LABELING AND POLYMERIC MATERIALS FOR CANCER-THERAPY AND ANTI-FOULING APPLICATIONS

A THESIS

SUBMITTED TO THE FACULTY OF THE

UNIVERSITY OF MINNESOTA

BY

KEUN-YOUNG PARK

IN PARTIAL FULFILLMENT OF THE REQUIREMENTS

FOR THE DEGREE OF

DOCTOR OF PHILOSOPHY

ADVISOR: DR. MARK D. DISTEFANO

AUGUST 2021

Acknowledgements

Although I may be listed as the sole author of this thesis, all the work described in this compilation was indeed impossible without the many great people who provided me with unfathomable support. Obtaining an advanced degree is truly a proud accomplishment for an individual. However, after enjoying that transient feeling of pride, I hope to utilize this degree as a reminder to stay humble and to strive to share with others all the blessings that I have received.

With that, I would first like to thank my Lord Jesus Christ for walking with me through this arduous but astonishing journey. I hope that the steps I take in the future align with God's plan and that I pursue a meaningful life, one that makes him proud.

I cannot thank enough my advisor, Dr. Mark Distefano, who helped me set foot into the field of chemical biology, which was a completely unknown realm of chemistry to me before the start of my doctoral degree. Without his support, and most importantly, his immense patience, I could not have survived the many obstacles throughout this journey. Mark was not only a great research advisor but a respectable mentor in various aspects of life, who I looked up to for guidance throughout my PhD journey.

2015 was the year I started my PhD, but most importantly, it was the year I started my own family. My wife Min and daughter Dannah became my new inspiration, motivation, and priority, who I am thrilled to continue this ongoing journey of life.

During my degree, my loving parents and I had become most physically distanced yet most emotionally connected. Raising a child while pursuing a PhD, just like my parents did, led me to realize their immeasurable depth of love for their children. I have forever received, and now I hope to return.

My in-laws provided so much love and support as if I were their biological son. I am grateful for having such great new family members added to my life.

Dr. David Odde took me into his lab as an affiliate, and he provided me complete freedom to operate with all resources in the Odde lab, which allowed me to explore science beyond chemistry. I appreciated having worked with such a caring, passionate scientist.

Working as the Mass Spectrometry Lab TA with Joe and Sean was a valuable and

memorable experience. I am grateful to have worked with such supportive and wholesome people.

Last and not least, I would like to thank my comrades who fought with me every day on the battlefield, especially the members of the Distefano group, my colleagues in neighboring labs, and my Korean friends at the U and from church. Those small everyday interactions made the journey sustainable.

Table of Contents

List of Tables

List of Figures

Chapter 1. A not-so-ancient grease history: click chemistry and protein lipid modifications

Reproduced with permission from Kiall F. Suazo, Keun-Young Park, and Mark Distefano. A Not-So-Ancient Grease History: Click Chemistry and Protein Lipid Modifications

This chapter comprises of sections from a manuscript published in the journal Chemical Reviews. The review article embodied a complete story on the details of various lipid modifying enzymes and how click chemistry was exploited in research with those enzymes, both in studying the biological significance of protein lipid modification and for performing biotechnological applications in a site-specific fashion. This chapter focuses on the latter part of the review paper. Starting with an introduction to different types of click chemistry reactions that have been utilized in biological environments, a description of the use of protein-lipid modifying enzymes for specific applications is presented. Concluding remarks and future directions are presented in the final section.

1.1 Introduction

Protein lipid modification involves the attachment of hydrophobic groups to proteins via ester, thioester, amide or thioether linkages; this process occurs in eukaryotes but not prokaryotes.[1,2] The most common purpose of such modifications is to cause the association of the resulting proteins to various membranes where they can interact with other proteins involved in signal transduction pathways. Proteins containing such modifications are involved in a diverse range of cellular functions including cell division, subcellular organization, secretion and differentiation.[3–7] Due to their critical role in such processes, these lipid-modified proteins are often mutated in various diseases or targets for therapeutic intervention.[8–11] In addition, the consensus sequences that mark proteins for lipidation are often simple and can be incorporated into other proteins to render them membrane-bound or provide a new site for selective modification. That feature has been exploited for a myriad of applications ranging from protein immobilization to the

creation of protein-drug conjugates for therapeutic applications.[12,13] Click chemistry has played a key role in both illuminating features of protein lipid modification as well as exploiting it for the aforementioned alternative applications.[14–18]

In this review, the specific click chemical reactions that have been employed to study protein lipid modification and their use for specific labeling applications are first described. That is followed by a description of the use of protein-lipid modifying enzymes for specific labeling applications including protein immobilization, fluorescent labeling, assembly of nanostructures and the construction of protein drug conjugates. Concluding remarks and future directions are presented in the final section.

1.2. Click chemistry

A term coined by Sharpless and coworkers, click chemistry is defined as reactions that are modular, wide in scope, give very high yields, generate only inoffensive byproducts, require simple reaction conditions, and use benign solvents such as water.[19] Click chemistry closely overlaps with bio-orthogonal chemistry, which is defined as reactions that do not interfere with biological processes that proceed rapidly and selectively under physiological conditions.[20] Tools developed for click chemistry enable bio-orthogonal reactions and developments in chemical biology stimulate the conception of novel click chemistry. Before the birth of these two concepts, chemistry and biology were somewhat disconnected as many advances in chemistry were inapplicable to living systems. The development of click chemistry revolutionized chemical biology, especially when performed in tandem with enzymatic labeling due to the synergetic effects generated by the unique advantages that the two components each provide. To be used in cellular environments, the participating click chemistry functionalities require a few additional characteristics. The molecular reaction components must possess cell penetrating capabilities and click-induced modifications must introduce minimal perturbation, which often necessitates the reaction components to be hydrophobic, neutrally charged, and small in size. Fortunately, many types of click reactions meet these criteria. Therefore, the bio-orthogonality of click chemistry has

allowed selective labeling and therefore real-time investigation of enzymatic processes of interest both *in vitro* and *in vivo*, providing insights into many biological questions and biomedical challenges including cancer, Alzheimer's disease, and coronavirus, among others. The site-specificity and rapid rates of both click chemistry and enzymatic labeling have also been purposed to tackle those biomedical challenges by efficiently functionalizing therapeutic molecules of interest. The combination of the two principles has created a powerful and multifunctional "Swiss Army knife-like" tool. In this section, click reactions that are most commonly used specifically in tandem with lipid modifying enzymes are described (Fig. 1.1). For a broader scope of click chemistry or applications to other specific fields, readers are directed to other reviews including those included in the current thematic issue.[21–25]

One type of click reactions involve azides which are a versatile functionality due to their small size, stability and inertness. Azides are known to be truly bio-orthogonal as they are essentially absent in biological systems.[22] The first bio-orthogonal click reaction reported was a Staudinger ligation between an azide and a functionalized triphenylphosphine (Fig. 1.1A). Bertozzi and coworkers exploited a modified version of the classic Staudinger reaction where they appended an ester to the phosphine component to prevent the hydrolysis of the aza-ylide intermediate, and instead via intramolecular trapping pushed the reaction towards a stable amide-linked product.[26] This classic reaction has been and is still widely used for many applications both in cellular environments and in live animals due to its selectivity and biocompatibility.[27] However, slow reaction kinetics ($k \sim 10^{-3}$ $M^{-1}s^{-1}$) and the oxidation-prone phosphine reagents have driven investigations into alternative click chemistries,[28] which has led to the emergence of the copper-catalyzed azide-alkyne cycloaddition (CuAAC, Fig. 1.1B), the most widely used click chemistry to date. CuAAC takes advantage of a Cu(I) catalyst which lowers the activation barrier for the formation of the triazole ring, resulting in significantly enhanced kinetics ($k \sim$ 10-100 $M^{-1}s^{-1}$).[29–32] Cu(I) is typically prepared *in situ* from Cu(II) salts by reducing agents, and is stabilized by various ligands that allows the reaction to proceed in aqueous conditions.[33–35] The use of copper however is a double-edged sword, as its cytotoxicity is a significant liability. Cu(I) is involved in protein oxidation via reactive oxygen species (ROS) that also causes DNA strand breaks,[32] which restricts the application of

CuAAC with proteins or living cells. Efforts have been made to overcome the toxicity issue by utilizing novel ligands[36,37] or improved azide structures[38–40] which allow reduced copper concentrations while maintaining reaction efficiency, or reducing the generation of reactive oxygen species (ROS).[34,41] Strain-promoted azide-alkyne cycloaddition (SPAAC, Fig. 1.1C) is an alternative to CuAAC which exploits activated alkynes incorporating ring strain to eliminate the requirement for metal catalysts.[42] The non-toxic nature of copper-free click chemistry has allowed SPAAC to be employed in various *in vivo* applications.[25] The use of SPAAC has significantly grown in the field of protein conjugation, often used in tandem with enzymatic labeling to maximize its selectivity and site-specificity. The growth is expected to continue as many pharmaceutical companies have established platforms for synthesizing site-specific antibody drug conjugates (ADC) based on site-specific installation of an azide and use of strained-alkyne payloads.[43] In terms of accelerating the rate of SPAAC, progress has been made through various strategies including adding electron-withdrawing fluorines adjacent to the alkyne,[44] adding a ketone to distort the alkyne into a more reactive geometry,[45] adding a nitrogen in the ring for increased hydrophilicity,[46] or forming a fused ring system for additional ring strain.[47] However, the rate of SPAAC ($k \sim 0.1\text{-}1\ M^{-1}s^{-1}$) still falls far behind CuAAC, and there are concerns that the large size and hydrophobicity of the ring-fused strained alkynes are prone to modulate the properties of target molecules or introduce off-target binding.[48,49]

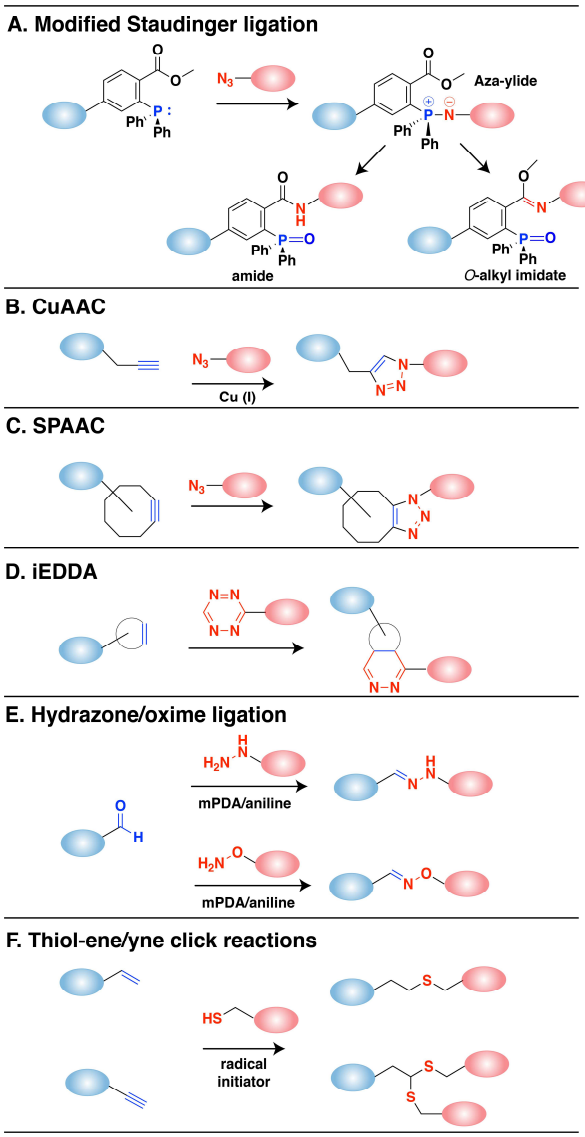

Figure 1.1 Reaction scheme of biorthogonal click reactions for modifying proteins of interest. (A) Modified Staudinger ligation between an azide and phosphine reagent. An aza-ylide intermediate is formed followed by a transfer to the ester forming an amide bond. The O-alkyl imidate product can occur especially with aryl azides. (B) The copper-catalyzed azide-alkyne cycloaddition reaction (CuAAC) is a 1,3-dipolar cycloaddition between alkynes and azides that results in a 1,2,3-triazole product. (C) Strain-promoted azide-alkyne cycloaddition (SPAAC) reaction that employs strained octynes. (D) Inverse-electron demand Diels-Alder (iEDDA) reaction between strained alkenes (trans-cyclooctene or norbornene) with tetrazine. (E) Reaction between aldehyde and hydrazines or aminooxy compounds to form hydrazone or oxime bonds, respectively. These reactions can be catalyzed by aniline and related reagents (mPDA). (F) Radical reactions between thiols and alkenes or alkynes initiated by UV light.

Strained alkenes such as trans-cyclooctenes (TCO) or norbornenes undergo inverse electron demand Diels-Alder (iEDDA, Fig. 1.1D) reactions with tetrazines, which is the fastest click reaction identified to date ($k > 10^3$ $M^{-1}s^{-1}$). Although tetrazine ligation exploits ring strain to achieve accelerated rates under copper free conditions, it has been shown to be orthogonal to SPAAC which therefore allows the use of both reactions simultaneously for selective labeling of multiple targets.[50,51] The fast rate even at low concentrations makes it especially useful in radiolabeling studies where the short half-life of isotopes requires rapid labeling,[52] or tracking and imaging of fast dynamic biological processes in living cells.[23] In imaging studies, tetrazine-conjugated fluorophores have been used as turn-on probes due to the dual functionality of the tetrazine as both a bio-orthogonal moiety and a fluorescence quencher.[25] Similar to SPAAC, the biggest drawback in tetrazine ligation is the hydrophobicity and large size of the ring-containing alkenes. However, smaller dienophiles such as cyclopropenes or azetines have been shown to retain reactivity and aqueous stability which introduces minimal perturbation at the target site comparable to products of the CuAAC reaction.[53–55]

Aldehydes and ketones undergo transamination reactions with amine nucleophiles that exhibit the α-effect, namely, increased nucleophilicity from the presence of lone pair electrons on the atom adjacent to the amine.[24] to form oximes or hydrazones. Although endogenous intracellular aldehydes and ketones do exist, oxime and hydrazone ligation (Fig. 1.1E) are considered bio-orthogonal as the α-effect nucleophile counterpart is rare and the reaction can be useful in other biological environments where aldehydes and ketones are absent. Oxime and hydrazone ligation products are among the smallest possible products in size among other click reaction products which therefore results in minimal structural perturbation. Rapid rate ($k \sim 1\text{-}10^3$ $M^{-1}s^{-1}$) at physiological conditions has been achieved by careful structural design of the substrates[56] and use of various catalysts.[57–60] While an oxime linkage is more stable than a hydrazone,[61] both ligation products are susceptible to hydrolysis, and especially for hydrazones that have a low equilibrium constant (K_{eq}) which at low concentration reactions causes incomplete product conversion and dissociation of the products.[59] However, the instability of oximes and hydrazones has actually provided them with a unique reversible capability which has been exploited for various

applications.[62–64] For studies that require stable products, modified ligation reactions have been developed that utilize the reaction of aldehydes with alternative nucleophiles that yield stable C-C bonds instead of the labile C=N bonds.[65–67] Due to their unique advantages, the use of oxime and hydrazone ligation has been well established for site-specific protein labeling and *in vitro* cell surface labelling especially in combination with enzymatic labelling methods which allows controlled installment of an aldehyde.[68,69] However, *in vivo* applications employing aldehyde and ketones are considerably more limited.

Thiol-ene (and thiol-yne) reactions (Fig. 1.1F) are click reactions that occur between thiols and alkenes or alkynes. Thiol-ene click chemistry has been heavily utilized for the functionalization of polymeric materials or nanoparticles.[70,71] While the use of thiol-ene chemistry in biochemical applications has held challenges in retaining its bio-orthogonality and site-specificity due to cellular thiols and other nucleophilic and electrophilic groups prone to side reactions,[72–74] it has been shown that exploiting photochemistry, in which the reaction proceeds via a single electron radical chemistry, provides enhanced selectivity.[75] Additionally, using light as the external stimulus allows applications in studies that require spatiotemporal control. These properties of thiol-ene click chemistry have prompted its use for protein modification such as surface immobilization, extracellular matrix (ECM) generation, and protein patterning in hydrogels.[76,77]

1.3 Proteins of interest site-specifically functionalized via lipid modifying enzymes and click chemistry for biotechnological applications

Previous sections described the use of click chemistry for biological studies of proteins modified via lipidating enzymes. In the following sections, we focus on prior art that has exploited those enzymes for the modification of proteins of interests (POI) with various functionalities together with click chemistry. Protein modification via enzymatic methods provide unique advantages. The site-specificity allows homogenous product formation with controlled stoichiometry, as opposed to conventional chemical methods such as cysteine-maleimide or lysine-*N*-hydroxylsuccinimide ester chemistry in which conjugation of a specific site or number of amino acid residues is difficult to

achieve. Precise control over the site of modification tends to cause minimal perturbation of native protein activity. For instance, modification via *S*-prenylation occurs at the C-terminus and *N*-myristoylation at the N-terminus, which are often distanced from the active sites of target proteins. Enzymatic labeling is bio-orthogonal as it occurs only on proteins that contain the specific consensus sequence, Ca_1a_2X for *S*-prenylation and MGXXXS/T/C for *N*-myristoylation. This allows selective labeling of the POI in mixtures such as crude lysates, which eliminates purification steps which is important in biotechnology where downstream processing of protein products is responsible for over half of the total production cost.[78] Finally, enzymatic reactions enable fast modifications with high yields under mild conditions, in contrast to other site-specific methods such as unnatural amino acid incorporation which is often limited by low protein yields and technical difficulties.[79]

While a number of different lipid modifying enzymes exist, as noted above, the products of palmitoylation yield a hydrolysis-prone thioester linkage that is potentially susceptible to loss of the conjugated payload in various biological environments. Similarly, the ester linkages from cholesterylation and GPI-modification have related instability features, that has prompted the development of biotechnological applications that utilize lipid modifying enzymes to be focused on *S*-prenylation and *N*-myristoylation. In future research, it will be interesting to see advances that allow the expansion of the range of exploitable lipid modifying enzymes. For instance, it may be become possible to utilize palmitoylation in situations that require reversible attachment and detachment of a payload, or by enhancing the linker stability through formation of an amide bond instead of the thioester through an intramolecular *S*-to-*N* shift.[80]

1.3.1 C-terminal protein functionalization through S-prenylation

Protein *S*-prenylation allows site-specific protein modification of almost any protein by simple appending of a short Ca_1a_2X recognition motif onto the C-terminus of the POI. The use of *S*-prenylation for biotechnological applications has mostly evolved around FTase for a number of reasons. The synthesis of analogues of farnesyl diphosphate is much easier than that of

geranylgeranyl diphosphate due to their simpler structure. FTase is known for its promiscuity that enables it to accept a wide variety of substrates including ones that incorporate a bulky aryl group or even a biotin functionality.[81,82] The plasticity of FTase can be even further improved by engineering the active site via mutagenesis.[82,83] While GGTase-1 accepts various analogues as well, it still exhibits more limited lipid substrate specificity compared to FTase.[84] In the case of RabGGTase , an additional REP component is required for the reaction to proceed which adds additional complexity to the overall process. In this section, the development and assessment of various isoprenoid analogues (Fig. 1.2 and 1.3) and their combination with click chemistry for a variety of applications are described (Fig. 1.4).

A large number of FPP analogues which contain biorthogonal moieties for click chemistry that can be recognized as substrates by FTase have been developed by Distefano and coworkers. In their initial report, a geranylazide diphosphate (C10-Az-OPP, Fig. 1.3) was synthesized from geraniol.[85] The product was a mixture of isomers in an approximately 1:1 ratio which was inseparable due to the facile sigmatropic interconversion of the allylic azide substrates and/or products. Nonetheless, C10-Az-OPP was confirmed as a substrate for FTase when evaluated with a peptide substrate *N*-dansyl-GCVIA (Dn-GCVIA). Although the incorporation of the analogue was slower than with FPP, the reaction was complete within a practical time frame (2 h at 30 ºC). The azide-functionalized peptide was then reacted with a triphenylphosphine-based reagent that contains an electrophilic ester moiety. Interestingly, while the Staudinger reaction showed high product conversion, mass spectrometry analysis of the product indicated the presence of an *O*-alkyl imidate-linkage instead of the conventional amide-linkage (Fig. 1.1). Based on reports suggesting that alkyl azides yield the former while aryl azides yield the latter,[86] it was assumed that the β-branched allyl azide substructure of GPP exhibits a reactivity more similar to that of aryl azides.

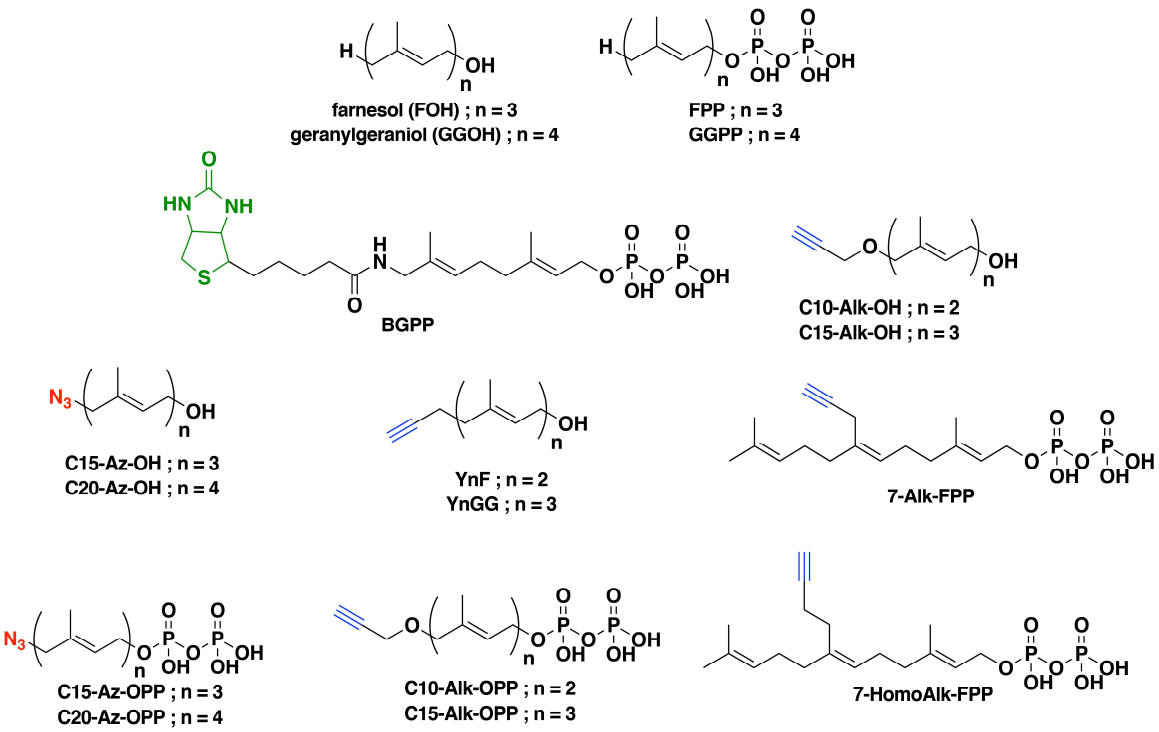

Figure 1.2 Bio-orthogonal isoprenoid analogues for probing protein prenylation. Native substrates farnesol (FOH) and geranylgeraniol (GGOH) or their diphosphate forms FPP and GGPP modified with azide or alkyne functionalities suitable for CCML. A biotinylated isoprenoid can also be used to directly label Rab substrates but not of those for FTase and GGTase-I.

In a subsequent report, Rose et al. reported on C15-Az-OPP (Fig. 1.3).[87] The new analogue showed similar properties to C10-Az-OPP, in that it was obtained as an isomeric mixture, showed similar reaction rates against Dn-GCVIA, and the product of Staudinger ligation again yielded an *O*-alkyl imidate-linked product instead of the amide-product as confirmed via mass spectrometry analysis.

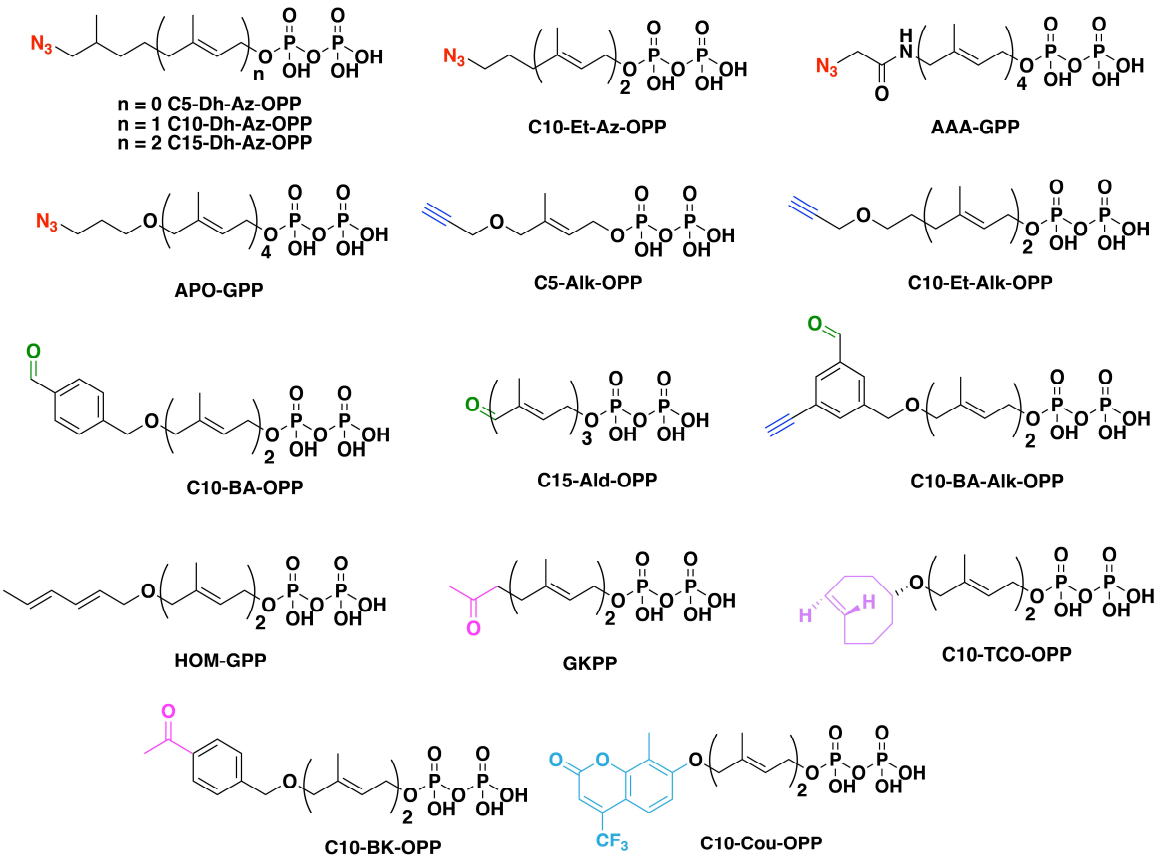

Figure 1.3 Additional isoprenoid analogues used in enzymatic C-terminal modification of proteins. Isoprenoids are modified with an azide, alkyne, aldehyde, alkene, ketone and fluorophore functionalities for selective bioconjugation.

In a more intensive study on the product formed from Staudinger ligation, Xu et al. prepared a new azide analogue 6,7-dihydrogeranylazide, which lacks the alkene present at C-6 (C10-Dh-Az-OPP, Fig. 1.3).[88] *S*-prenylation of Dn-GCVIA with that analogue indicated that the absence of the third isoprene unit brings about structural perturbation when bound to the FTase active site leading to a rate of reaction that was much slower than FPP. Nonetheless, C10-Dh-Az-OPP showed similar rates to the previous C10-Az-OPP analogue which was sufficient to be completely converted to product with longer reaction times. Interestingly, mass spectrometric analysis of the reaction product between the prenylated peptide and a phosphine-based reagent indicated the formation of only alkoxyimidate products instead of the predicted amide despite the non-allylic nature of the azide. To gain a better understanding, model reactions with simpler

compounds were run between the dihydroprenylazide substrate precursor (the unphosphorylated alcohol) and three model phosphine reagents. While ESI-MS analysis indicated the formation of both imidate and amide products, LCMS and NMR analysis both revealed that in fact the amide is the dominant product where in some cases the imidate form was completely undetectable. The results suggested that product analysis using mass spectrometry could give contradicting results due to potential variations in ionization efficiencies of the products. Nonetheless, the report showed evidence of alkoxyimidate products from Staudinger ligation that can form when particular reagent types were used. These observations were significant since they highlighted the potential problem of product mixtures that can sometimes occur with the Staudinger ligation.

Duckworth et al. constructed a model protein by fusing a CVIA sequence to the C-terminus of GFP, which was then selectively immobilized onto agarose beads by installation of an azide moiety via enzymatic *S*-prenylation followed by capture via CuAAC (Fig. 1.4A).[89] Based on the study above, the new azide analogue (C15-Dh-Az-OPP) was composed of three isoprenoid units but lacked the alkene present in the terminal isoprene unit. Investigation of the rate of *S*-prenylation with Dn-GCVIA showed that 10,11-dihydrofarnesylazide diphosphate (C15-Dh-Az-OPP, Fig. 1.3) at saturating concentrations (10 μM) was only 2.7-fold slower than with FPP, while the previously reported C10-Dh-Az-OPP showed a significantly reduced catalytic efficiency, which indicated that the presence of a third isoprene unit and the absence of an alkene in that unit makes the azide-containing analogue a much better substrate for FTase. After enzymatic labeling with C15-Dh-Az-OPP of GFP-CVIA, CuAAC with alkyne-functionalized agarose beads was carried out for 15 h at 25 ºC. Analysis of the fluorescence intensity of the beads indicated a 96% immobilization efficiency. Interestingly, 8% of GFP-CVIA was shown to be immobilized under the same click conditions even in the absence of the clickable azide, which was presumably due to nonspecific interactions caused by Cu(I)-induced activation of the alkyne-agarose.[90] Selective capture could be obtained from protein mixtures containing as little as 1% GFP-N_3 on account of the highly efficient click reaction.

Poulter and coworkers prepared GFP- and GST-(glutathione S-transferase) immobilized glass surfaces exploiting Staudinger ligation or CuAAC (Fig. 1.4B) using similar chemistry.[91] Target proteins were enzymatically labeled with an azide- or alkyne-containing farnesyl diphosphate

analogue (C10-Et-Az-OPP or C10-Et-Alk-OPP, Fig. 1.3) followed by click reaction with phosphine- or azide-derivatized glass slides that resulted in regio- and chemoselective protein immobilization. Although nonspecific binding of proteins lacking the clickable moiety was also observed, proteins covalently immobilized via click chemistry were found to be more robust; click-immobilized proteins were found remaining attached to the slides after treatment with an acidic saline solution for 2 h at 80 ºC, which was sufficiently harsh to strip antibodies bound to their respective antigenic proteins, and remained bound to slides after 4 days in buffer while nonspecifically bound proteins had fully dissociated.

In a follow-up report, Poulter and coworkers described eleven additional farnesyl diphosphate analogues each bearing azide or alkyne functionality, where five were shown to be substrates for yFTase (the yeast enzyme).[92] Comparison of the steady-state kinetic parameters of the analogues with Dn-GCVIA indicated that the presence of a bulky or branched *w*-isoprenoid unit, charged amino groups, or rigid chains may hinder their compatibility with the active site of yFTase. Azide-farnesylated Dn-GCVIA products showed two closely eluting species with identical mass determined via LC-MS, which indicated isomeric products resulting from either incorporation of both regio-isomers of the azide analogue or incorporation of a single isomer which subsequently undergoes rearrangement.

By exploiting CuAAC with a model protein GFP-CVIA site-specifically labeled with an alkyne-functionality, Duckworth et al. performed surface-immobilization and fluorophore labeling of proteins (Fig. 1.4A and 1.4C).[93] A continuous fluorescence-based enzyme assay was employed to evaluate the C10-Alk-OPP as a substrate for yeast FTase (yFTase). Although farnesylation of Dn-GCVIA with the isoprenoid analogue was approximately 12-fold slower than the natural substrate FPP, GFP-CVIA was fully converted to the alkyne-product within a timeframe (3 h at 30 ºC) suitable for downstream applications. The alkyne-labeled GFP was then immobilized onto azide-functionalized agarose beads under CuAAC conditions. Interestingly, while immobilization of GFP-alkyne on azide-agarose and GFP-azide on alkyne-agarose both showed highly efficient immobilization in 1 h (93% for both), conjugation to the alkyne-resin was shown to result in a higher degree of nonspecific binding. These results indicated that even for the same CuAAC reaction,

immobilization characteristics could vary upon the choice of functionality carried by each clickable reagent. For instance, in proteomic studies, using an azide-resin to prevent false-capturing of undesired proteins would be especially important.[90] Fluorophore labeling of GFP-alkyne was achieved with Texas Red bearing an azide, demonstrating the wide applicability of the reported site-specific labeling method. Förster resonance energy transfer (FRET) calculations gave a Förster distance of 40 Å, which was consistent with the R-distance of 37 Å predicted by a model of the GFP-Texas Red conjugate.

Distefano and coworkers synthesized protein-DNA conjugates which self-assembled into tetrahedral nanostructures (Fig. 1.4D).[94] The model protein GFP-CVIA was farnesylated with azide functionality, which was exploited to conjugate with an alkyne-containing oligonucleotide 33 bases in length. The GFP-DNA was initially shown to form a complex with a Texas Red carrying a complementary 33-mer DNA strand evidenced by FRET. The hybridization of complementary DNA strands was further utilized in constructing a tetrahedral structured GFP-DNA nanoassembly by mixing four types of GFP-DNA conjugates and briefly annealing the mixture at 54 ºC. The number of GFP molecules per tetrahedron, observed by single molecule spectroscopy, could be controlled by changing the composition of the oligonucleopeptide building blocks. Overall, the advantage of having a compact recognition tag for site-specific protein conjugation was demonstrated through its application towards GFP-DNA nanostructure assembly that requires precisely spaced and oriented proteins.

Waldmann and coworkers studied the effects of the isoprenoid analogue structure on *S*-prenylation and click chemistry.[95] Four isoprenoid analogues were synthesized, each containing a diene (HOM-GPP, Fig. 1.3), either an amide-linked (AAA-GPP, Fig. 1.3) or aliphatic azide (APO-GPP, Fig. 1.3), or biotin (BGPP, Fig. 1.2). Affinity assays indicated all four analogues bind to the active site of FTase despite differences in length compared to the native FPP. However, while the azide and diene analogues showed product formation with Dn-GCVLS and the TKCVIM-tagged model proteins cyan fluorescent protein (CFP), RFP and small GTPase Ypt7, the biotin analogue did not show conversion. Reaction with GGTase-I failed to process the biotin analogue as well, which indicated that the complexity of analogue design involves factors beyond simply length. The

azide-functionalized proteins obtained via FTase were shown to maintain solubility and functionality post-labeling and underwent Staudinger ligation with a model phosphine. The azide analogue containing the amide-linkage was shown to react much faster than the aliphatic analogue due to its stronger electrophilicity. Functionalization of the diene-labeled protein via Diels-Alder cycloaddition was shown, which required a higher excess of dienophile and low pH conditions.

Wollack et al. studied methods to improve the solubility of proteins functionalized via farnesylation.[96] Following the farnesylation with a truncated alkyne-prenyl analogue (C5-Alk-OPP, Fig. 1.3) composed of a single isoprenoid unit, the last three amino acids of the "Ca_1a_2X" box were enzymatically removed, which resulted in site-specifically alkyne-labeled peptides or proteins with a net gain of only a single cysteine and nine additional non-hydrogen atoms. Although kinetic assays with OrG-RTRCVIA-OH (OrG: Orange Green) showed that the C5-alkyne analogue, C5-Alk-OPP, was a poor substrate for yFTase compared with FPP, near-complete (>85%) labeling was achieved upon extended incubation. Carboxypeptidase Y (PY) could be utilized to cleave off the -a_1a_2X residues without yielding undesired proteolytic degradation of the peptide. The minimalistic labeling methodology was applied for immobilization of alkyne-mCherry on azide-functionalized agarose, in which the absence of the "VIA" sequence did not affect immobilization efficiency, demonstrating the innocuousness of the method on protein stability and click reactivity. Comparison of C5-Alk-OPP and the dihydro analogue C5-Dh-Az-OPP for Hcp1 labeling demonstrated that minimizing the hydrophobicity of the lipid substrate could lead to enhanced product-solubility.

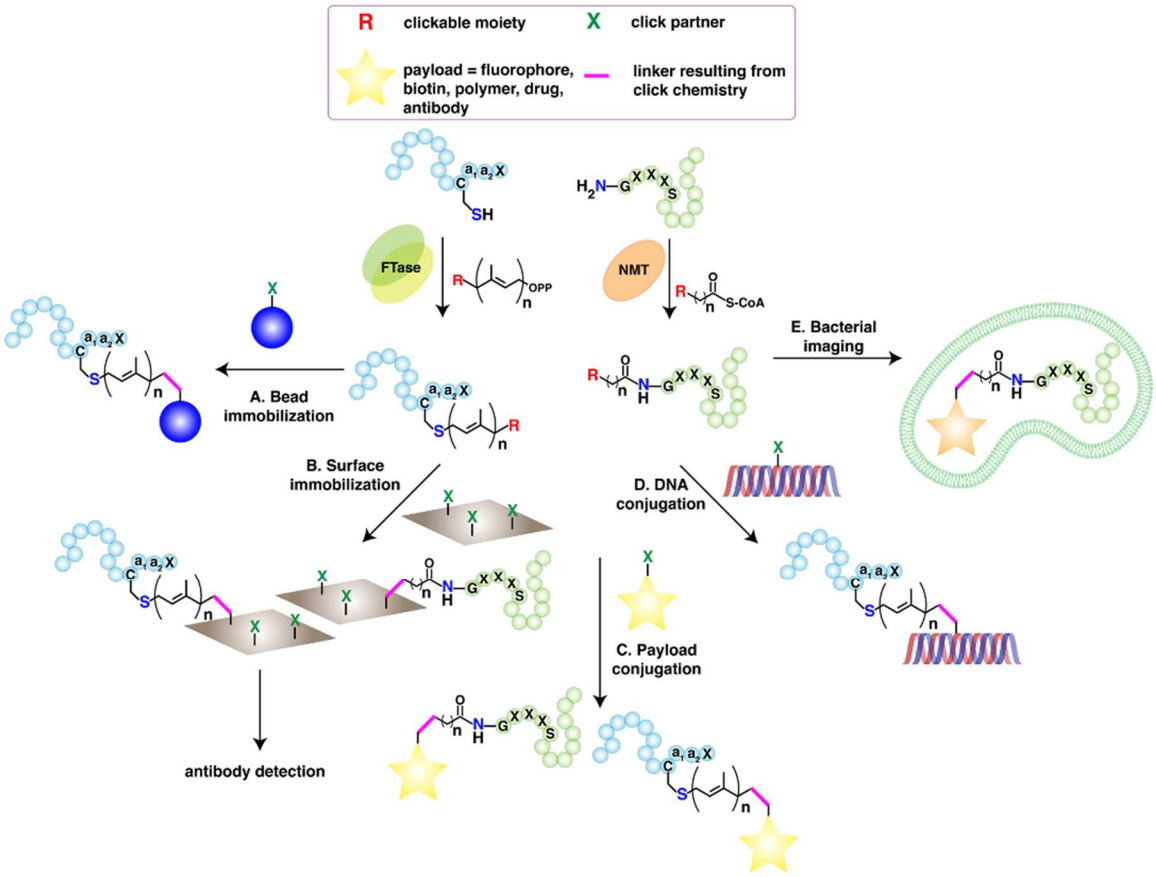

Figure 1.4 Applications of site-specific enzymatic protein labeling through C-terminal cysteine prenylation with FTase and N-terminal acylation with NMTs. (A) Immobilization of proteins enzymatically prenylated with clickable isoprenoids on beads functionalized with clickable moieties. (B) Immobilization of tagged proteins on glass or gold surfaces coated with clickable functionalities. (C) Direct protein modification of lipidated proteins with various payloads such as fluorophores, affinity handles, polymers, drugs, or antibodies. (D) Generation of DNA-protein crosslinks through reaction between functionalized DNA and proteins prenylated with clickable isoprenoid analogues. A nucleotide base is modified with a biorthogonal moiety prior to DNA synthesis. (E) Incubation of myristoyl probes in bacteria enables visualization of N-myristoylation of heterologously expressed proteins. Bio-orthogonal fluorophores are reacted with the tagged proteins inside live bacteria.

The range of exploitable click chemistries that could be employed via FTase-catalyzed labeling was expanded by Rashidian et al. who developed an aldehyde-containing analogue of FPP (C15-Ald-OPP, Fig. 1.3).[97] The catalytic efficiency of the aldehyde analogue was shown to be comparable to previously developed azide or alkyne analogues. Dn-GCVIA was successfully

farnesylated with the analogue by FTase which could subsequently undergo fluorophore addition. While the C15-Ald-OPP-labeled Dn-GCVIA rapidly formed an oxime-ligated product with aminooxy-AlexaFluor-488 in the presence of aniline, reactions with Texas-red hydrazine were shown to be unsuccessful, suggesting that low μM reaction conditions are not suitable for hydrazone formation due to its lower equilibrium constant. Farnesylation of GFP-CVIA with the aldehyde analogue manifested complete product formation within 2 h at 30 ºC in the presence of FTase. Oxime ligation-induced surface labeling of aldehyde-functionalized GFP with aminooxy-agarose beads in the presence of 100 mM aniline was achieved with ~30% efficiency, while labeling with aminooxy AlexaFluor-488 and 100 mM aniline showed 60% efficiency. Overall, oxime ligation was shown an efficient bio-orthogonal functionality for labeling chemistry, which could be a potential alternative to CuAAC where copper-free conditions are necessary such as in cellular environments.

Tate and coworkers utilized site-specific labeling with GGPP analogues using RabGGTase and REP-1 in tandem with click chemistry to functionalize a series of target proteins.[98] C20-Az-OPP (Fig. 1.2) was synthesized, which despite the interconversion between 14-azido and cis/trans 16-azido regio-isomers, was successfully transferred to a range of recombinant Rab proteins containing both single (Rab18) and dual (Rab6, GST-tagged Rab11, Rab27a, Rab38, Rab1a) *S*-prenylation motifs. Comparison of CuAAC, phosphine-mediated ligation, and strain-promoted cycloaddition, using the requisite biotin derivatives showed that CuAAC is the most efficient and selective click reaction. That method was then used to detect geranylgeranylated proteins in cells which is described above in Section 7.1.1.

Proteins farnesylated with the natural substrate FPP were shown to undergo oriented immobilization via thiol-ene click reactions.[99] H-, N-, and K-Ras were farnesylated with FPP using FTase, followed by immobilization on thiol-poly(amidoamine) (PAMAM) functionalized SiO_x/Si slides (Fig. 1.4B) by exposure to UV light through a photomask. Immunodetection of surface-bound Ras with an anti-Ras-Cy3 antibody revealed fluorescent micropatterns indicating successful immobilization. Interestingly, the labeling efficiency of farnesylated K-Ras was ~20 fold higher than the others, which could be attributed to the interaction between the C-terminal polylysine domain of K-Ras and the carboxylic acid groups present on the glass-bound PAMAM. Based on that

observation, mCherry and Rab6A each containing 4 or 6 lysines at their C-termini were generated, respectively. Farnesylated products from both proteins underwent efficient immobilization even directly from crude lysate. The method was extendable to a co-expression system, in which the engineered mCherry was farnesylated with endogenous FPP by FTase in *E. coli*. The resulting modified proteins in crude lysate could be immobilized using a longer thiol linker and with extended UV exposure time. Utilizing proteins prenylated with the natural substrate FPP for biotechnological applications was an interesting approach, obviating the development and assessment of analogues that contain a click-reactive functionality. Similar work was reported recently where Distefano and coworkers exploited the site-specifically labeled lipid groups for binding of multivalent protein scaffolds to cells via hydrophobic interaction.[100] While the work was unique in that it utilized protein *S*-prenylation for protein-conjugation without the involvement of covalent interactions, it should be noted that the work could be expanded to incorporate click chemistry for a stronger and more selective binding-interaction between multiple target substrates.

Taton and coworkers synthesized protein-oligodeoxynucleotide (protein-ODN) conjugates by combining farnesylation and copper-free click chemistry.[101] Conjugation of ODN was carried out by farnesylation with either C10-Az-OPP or C15-Az-OPP of GFP or mCherry, followed by SPAAC with a DIBO-modified ODN. SPAAC proceeded over a range of pH values (3.5-12.3) and temperature (room temperature and 4 °C), and the product yield was comparable to CuAAC, demonstrating its wide applicability, simplicity, and high efficiency. ODN-conjugated proteins were utilized for supramolecular assembly via hybridization of the complementary DNA sequences. To this end, GFP and mCherry were each conjugated with complementary DBCO-ODNs and dimerized either at room temperature or 55 °C. Interestingly, while CuAAC-generated conjugates formed heterodimers under both annealing conditions, SPAAC-generated conjugates only dimerized at elevated temperatures presumably due to the more hydrophobic strained-alkyne moiety. Surface immobilization of protein-ODN conjugates on ODN-functionalized agarose beads was shown, which demonstrated the usefulness of SPAAC as an alternative to CuAAC in functionalizing proteins at low concentrations.

Rashidian et al. utilized oxime and hydrazone formation to reversibly immobilize or label

proteins in crude cell lysate.[62] In addition to the previously reported C15-Ald-OPP alternative substrate containing an alkyl aldehyde,[97] a geranylaldehyde analogue containing an aryl aldehyde (C10-BA-OPP) was developed. Although the catalytic efficiency of the aryl analogue was 4-fold lower than the alkyl-substituted compound, higher synthetic yields gave it the advantage of being much easier to produce. Reactions of aldehyde-functionalized Dn-GCVIA and GFP-CVIA with Texas red hydrazide or AlexaFlour-488 aminooxy indicated that while the reaction rate is much faster for hydrazone formation, oxime ligation shows higher conversion due to higher association constants. Fluorophore labeling of GFP could be achieved using either hydrazone or oxime formation, in which the products displayed FRET. Reversible immobilization was achieved by utilizing the two click reactions sequentially. GFP-aldehyde was initially captured on hydrazide-functionalized agarose beads (Fig. 1.4A), followed by release with high concentrations of hydroxylamine, where aniline was employed as a catalyst in both reactions. The method was highly reversible with a 95% immobilization efficiency and 80% release efficiency, and could be applied to selective functionalization of proteins from crude lysate without purification. As an example, a therapeutically relevant glucose-dependent insulinotropic polypeptide (GIP-CVIM) was PEGylated from crude extract using this chemistry.

While the high chemoselectivity and reversibility of imine-based reactions make them a useful click reaction, they suffer from slow reaction kinetics especially for ketones and therefore often require catalysts. Rashidian et al. screened various catalysts for oxime and hydrazone formation and found that m-phenylenediamine (mPDA) is up to 15 times more efficient than aniline.[60] At identical concentrations, mPDA was about 2-fold more efficient than aniline, but its higher water solubility allowed reactions to proceed at much higher concentrations which resulted in much greater acceleration since the rate of reaction is first order in catalyst. At pH 7, oxime ligation between an aldehyde-functionalized GFP and a dansylated aminoooxy reagent was completed in 90 s with 750 mM mPDA while 100 mM aniline only showed minimal product conversion (<7%). It was noted that both catalysts were less effective for protein aldehydes than simple model aldehydes, suggesting that the species conjugated to the aldehyde can modulate its reactivity. Protein labeling via reversible immobilization using mPDA resulted in faster and higher

yields compared to aniline. It was found that Schiff base formation starts to compete with oxime ligation at high mPDA/aminooxy ratios, and therefore ratios below 250:1 were recommended. Fluorophore labeling of a therapeutically relevant protein ciliary neurotrophic factor (CNTF) via oxime ligation with aminooxy AlexaFluor-488 was achieved using 80 mM mPDA. The mPDA catalyst was shown to be effective for labeling ketone-containing proteins as well. PEGylation of an aldehyde-containing DHFR with 500 mM mPDA manifested a 2.5-fold increase in rate while 100 mM aniline had negligible enhancement. A number of other groups have reported other efficient aniline-based catalysts for this reaction as well.[24]

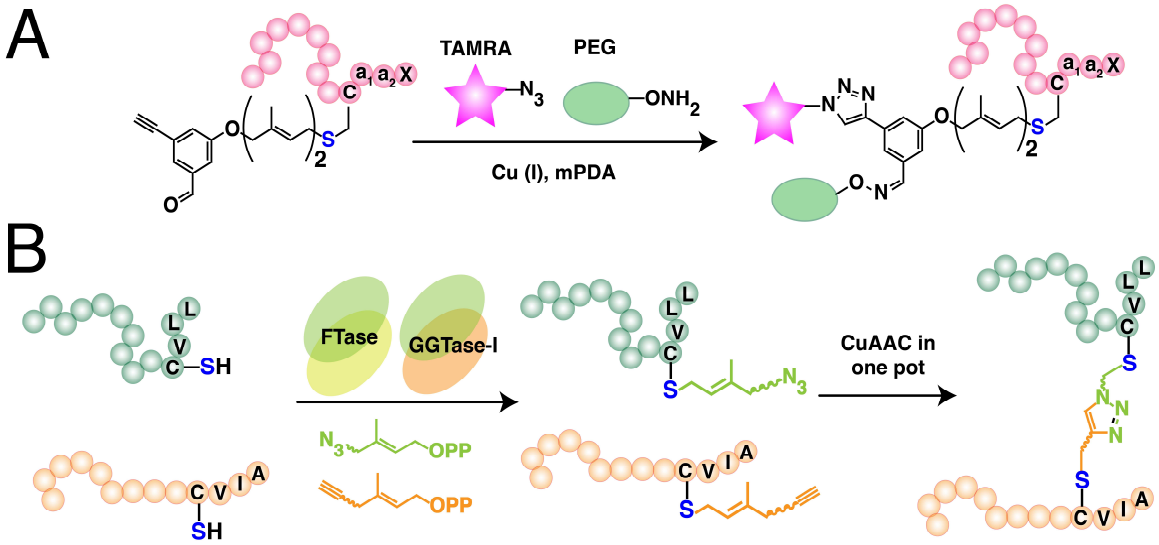

Figure 1.5 Simultaneous protein labeling through prenylation. (A) Simultaneous labeling of a protein using a tri-orthogonal isoprenoid analogue containing both alkyne and aldehyde for CuAAC and oxime ligation, respectively. (Ref. 542) (B) One-pot dual labeling using orthogonal isoprenoid analogues for tail-to-tail protein bioconjugation. FTase and GGTase-I have substrate preferences for the length of isoprenoid used. (Ref. 385)

The orthogonality between CuAAC and oxime ligation to achieve simultaneous dual protein labeling was exploited by Rashidian et al.[102] A tri-orthogonal molecule incorporating an aldehyde and alkyne functionality on an allylic diphosphate (C10-BA-Alk-OPP) was synthesized and confirmed as an alternative substrate for FTase by farnesylation of Dn-GCVIA and GFP-CVIA. Simultaneous oxime ligation and CuAAC with aminooxy-PEG and azido-TAMRA (Fig. 1.5A) was

shown with GFP and CNTF that had been labeled with the tri-orthogonal analogue. Under the conditions employed, oxime ligation was found to be more efficient than CuAAC, but nonetheless both reactions reached near completion within 12 h. The method was applied towards constructing chemically self-assembled nanoring structures (CSANs) by mixing a dual-functionalized GFP labeled with aminooxy-TAMRA and azido-bis-MTX with dimeric DHFR proteins functionalized with anti-CD3 antibodies. The resulting protein nanostructure was shown to undergo selective membrane binding and energy-dependent endocytosis when treated with $CD3^+$ T-leukemia cells, where the GFP and TAMRA components could be detected by both fluorescence and FRET measurements. In a subsequent methods article, Mahmoodi et al. provided a detailed description of the procedures for protein immobilization and release exploiting the reversible imine-base reaction and simultaneous protein labeling utilizing CuAAC and oxime click chemistry.[103] In comparing *m*-PDA versus *p*-PDA in oxime and hydrazone ligation, the authors noted that at higher catalyst concentrations, *m*-PDA favors Schiff base formation over the desired product, while *p*-PDA does not exhibit such limitations and therefore allows faster reactions. However, *p*-PDA was shown to be prone to oxidation in air, especially in the presence of copper catalysts, which suggested that *m*-PDA would be more suitable for reactions that require prolonged incubations or simultaneous click conditions.

Maynard and coworkers utilized oxime and CuAAC click chemistry for chemoselective protein immobilization on gold surfaces (Fig. 1.4B).[104] For covalent immobilization, two sets of proteins and gold surfaces were functionalized with two different types of complementary click components. Horse heart myoglobin (HHMb) was modified at its N-terminus with an aldehyde via a PLP reaction with pyridoxal 5'-phosphate, and mCherry-CVIA was farnesylated with C15-Alk-OPP. Complementary gold surfaces were functionalized with an aminooxy-alkanethiol or azide-alkanethiol by microcontact printing with a PDMS stamp. Immobilized proteins were visualized via fluorescence microscopy which demonstrated the potential of the method in applications that target uniformly oriented proteins.

Poulter and coworkers constructed uniformly oriented antibody arrays on site-specifically immobilized antibody-binding proteins (Fig. 1.4C).[105] Truncated recombinant forms of antibody-

binding proteins A, G, and L were constructed to include five antibody-binding domains from wild-type *S. aureus* protein, an N-terminal His_6-tag, and a C-terminal CVIA motif. The chimeric proteins were farnesylated with C10-Et-Alk-OPP and immobilized onto azide-functionalized glass slides. The high selectivity and binding affinities of the immobilized antigens were shown through a series of assays involving various concentrations and mixtures of protein A, G, and L. The surface-bound antigens were utilized to fabricate an array of antibodies by a "sandwich" procedure, where glass-bottomed slides (with silicone isolators) were coated with recombinant antibody-binding protein L followed by incubation with monoclonal antibodies directed to either GFP or GST. A mixture of GFP and GST was added to the wells and the captured proteins were visualized using fluorescent antibodies, which indicated selective antibody-dependent protein detection without cross-reactivity. The antigen-bound slides could be reused by treatment with acidic buffer to strip away the antibody layer while leaving the covalently immobilized antigens attached for use in another round of protein-detection. In a follow-up paper, they showed that their "sandwich-type" antibody arrays that exhibit regioselectively immobilized antigens show superior properties compared to randomly oriented antigens immobilized on commercially epoxy-modified slides.[106] As described in their previous work, a sandwich structure for detecting GFP was constructed by immobilizing an alkyne-functionalized recombinant protein L onto azide-glass slides, followed by incubation with a mouse anti-GFP IgG antibody. Captured GFP was detected with D7Light 680-labeled mouse anti-GFP IgG with high sensitivity and low cross-reactivity against the components of the sandwich array. For comparison, a sandwich structure with random orientation was constructed by immobilizing protein L on commercial epoxy-modified slides in a non-specific fashion. Regioselectively immobilized slides showed superior fluorescent outputs demonstrating the advantages that result from site-specific immobilization. Slides showed unaltered detection sensitivities after up to 6 cycles of regeneration. Poulter and coworkers subsequently expanded the scope of their immobilization methodology from glass to gold surfaces.[107] Thiol or dithiocarbamate (DTC) self-assembled monolayers (SAMs) were prepared on gold slides for subsequent azide surface-functionalization. Alkyne functionalized GFP or GST, prepared by *S*-prenylation with an isoprenoid analogue was immobilized onto the gold surface via CuAAC and visualized with complementary fluorescent antibodies. A concentration

dependent increase in immobilization was observed only under click conditions, indicating a low degree of nonspecific binding. While the immobilized proteins could be released with β-mercaptoethanol (BME) from both types of gold surfaces, proteins on DTC SAMs were shown to be much more resistant to displacement, indicating a more robust sulfur-gold linkage in the case of DTC over thiols.

Trans-cyclooctene (TCO) functionality was site-specifically incorporated by protein farnesylation for subsequent functionalization via tetrazine ligation.[108] Successful labeling of an Oregon Green-CVIA peptide and GFP-CVIA showed that the developed TCO geranyl diphosphate analogue (C10-TCO-OPP) was a substrate for yFTase. The relatively compact volume of cyclooctene and hydrophobic characteristics of the analogue were thought to be the key factors of substrate-compatibility of the analogue in the FTase active site. The TCO-labeled peptide and protein both rapidly reacted with dipyridyl-tetrazine known to exhibit cell-penetrating properties, which combined with the copper-free click features of this chemistry has important implications for experiments that require protein lipid modification in live cells.

Dozier et al. examined the kinetic behavior of mutated FTases to study how the enzyme's active site could be expanded to improve the catalytic efficiencies for bulkier FPP analogues.[83] Docking experiments suggested that positions W102*β*, Y154*β*, and Y205*β* were important for controlling the volume of substrates that could be accommodated. Thus, those positions were altered to alanine via site directed mutagenesis which yielded mutants W102A*β*, Y154A*β*, and Y205A*β*. When tested using a Dn-GCVLS substrate, some FTase mutants were found to exhibit substantial improvements. For example, mutant W102A*β* showed a 43-fold higher catalytic efficiency for processing a benzaldehyde-containing analogue over FPP, and mutant Y205A*β* showed improved activities for a cyclooctene analogue and a dramatic 300-fold increased catalytic efficiency for a coumarin-containing analogue (C10-Cou-OPP). Some mutations however gave only minimal improvements such as the mutant Y154A*β* which displayed improved binding affinities (lower K_m) for the benzaldehyde analogue which, however, was offset by a decreased k_{cat}. Overall, it was shown that mutagenesis of FTase could be exploited to expand the variety of susceptible FPP analogues, that could potentially broaden the types of click chemistry applications

associated with protein *S*-prenylation.

In a related work, Zhang et al. employed simultaneous enzymatic labeling of two different target proteins each selectively with different functionalities by exploiting the distinct specificities of rat GGTase-I (rGGTase-I) and rat FTase (rFTase).[109] Based on a previous report which showed that rGGTase-1 has a larger binding pocket compared to that of rFTase, various isoprenoid analogues that contain a clickable functionality were evaluated as substrates for the two enzymes in search for candidates that exhibit enzyme specificity. When tested with GFP-CVIA, C10-Alk-OPP was shown to be a substrate for rFTase and an aryl ketone containing C10 isoprenoid (C10-BK-OPP) for rGGTase-I, and no cross-reactivity between the enzymes and substrates was observed. rFTase was shown to be able to prenylate CVIA substrates with C10-Alk-OPP but not related CVLL substrates while C10-BK-OPP and azide-containing C20-Az-OPP could be transferred to CVLL substrates only with rGGTase-I. Exploiting the substrate selectivity and noncomplementary Ca_1a_2X sequences, an all-in-one reaction was shown to successfully label GFP-CVLL and RFP-CVIA simultaneously with C10-BK-OPP and C10-Alk-OPP, respectively, in the presence of both rFTase and rGGTase-I (Fig. 1.5B). Utilizing the methodology further, a one pot site-specific dimerization of proteins was carried out by selectively labeling GFP-CVLL with C15-Az-OPP and GFP-CVIA with C10-Alk-OPP, followed by addition of CuAAC reagents which produced GFP-GFP homodimers in high yield. A similar reaction was carried out to synthesize GFP-RFP heterodimers demonstrating the generality of the developed method to form site-specific tail-to-tail protein dimers.

DNA-protein cross-links (DPCs) are important DNA lesions that interfere with DNA processing which leads to various mutations and cytotoxicity. However, studies on DPCs have been limited due to difficulties in obtaining structurally defined site-specific DPCs. Tretyakova and coworkers investigated the effect of DPCs on DNA replication by exploiting *S*-prenylation and click chemistry for the preparation of site-specific DNA-protein or -peptide crosslinks (Fig. 1.4D).[110] SDS-PAGE and tandem mass spectrometry confirmed the successful site-specific crosslinking between prenylation-induced GFP-C15-Dh-Az-N_3 and an alkyne-labeled 23-mer oligodeoxynucleotide via CuAAC. DNA-peptide crosslinks were generated using synthetic azide-containing 10- or 23-mer peptides, which were both produced in high yields. The DPCs were subjected to primer extension

with translesion synthesis (TLS) polymerases hpol k, n and t either through a standing start or running start assay with an 18-mer template. In both assays, TLS polymerases showed successful extension of the primer for control templates, while complete obstruction for all three types of TLS polymerases was observed for both GFP and 23-mer conjugated DPCs. For the DPC containing the 10-mer, polymerases were shown to bypass the lesion and extend the primer with different efficiencies. Overall, these assays demonstrated how different peptide/protein sizes have an effect on primer extension near the site of DNA adduction and suggest that large DPCs would require a proteolytic mechanism for them to be processable by TLS polymerases.

Combination of *S*-prenylation and click chemistry was utilized for the synthesis of homogenous protein-drug conjugates. Kim and coworkers site-specifically linked a toxic monomethyl auristatin F (MMAF) warhead to repebodies, which are protein scaffolds with a high affinity for epidermal growth factor receptor (EGFR).[111] Repebodies were engineered with a C-terminal CVIM, which was exploited for *S*-prenylation with a geranyl ketone diphosphate (GKPP). Subsequent oxime ligation with a β-glucuronide-linked and aminooxylated MMAF without the employment of a catalyst under acidic conditions produced a homogenous repebody-MMAF conjugate (RDC). The site-specific RDCs showed high serum stability in human plasma due to the hydrolysis-resistant oxime linkage which is advantageous in targeted drug delivery. Towards EGFR-positive cell lines, RDCs showed higher efficacy compared to cell-impermeable MMAF, where the RDC with the highest binding affinity showed the highest cytotoxicity. RDCs had negligible effect on EGFR-negative MCF7 cells, indicating receptor-specific cytotoxicity. Mouse studies revealed that RDCs exhibit antitumor activities, although complete tumor suppression could not be achieved presumably due to the short half-life of RDCs in blood due to the small size of the protein.

Shin and coworkers developed an LC-MS/MS based method to assess the linker stability of ADCs (antibody-drug conjugate).[112] The ADC used in their study was a HER2-targeting antibody that was site-specifically conjugated with an MMAF via methods similar to those reported by Kim and coworkers, using site-specific GKPP labeling with FTase followed by payload-conjugation via oxime chemistry.[111] Evaluation of the pharmacokinetic profile of the ADC was accomplished by quantifying the drug component of the ADC remaining in plasma. For this, the plasma MMAF

concentrations were determined from integration of LC-MS/MS analysis previously standardized using a range of concentrations (19 - 960 ng/ml) fit to a quadratic equation. That method was used to assess the linker stability of ADCs in rat plasma, where 85 % of MMAF was found to remain bound to the ADC after incubation in rat plasma for 7 days at 37 °C. *In vivo* rat studies showed a similar half-life for the ADC to that of trastuzumab, demonstrating the stability of the oxime linkage.

Distefano and coworkers functionalized Designed Ankyrin Repeat Proteins (DARPins), a type of a small protein scaffold, with a fluorophore using *S*-prenylation and click chemistry.[113] The DARPin used in the study was engineered to bind to epithelial cell adhesion molecules (EpCAM) which is a well-known marker overexpressed in certain cancer cells, and to contain a C-terminal CVIA motif to be recognized by the FTase. Site-specific labeling with C10-Az-OPP followed by SPAAC with a TAMRA-DBCO yielded functionalized DARPins with high yields (>85%). The EpCAM-binding affinities of the fluorophore functionalized DARPins were assessed by flow cytometry. A high degree of binding activity was observed in EpCAM-overexpressing MCF-7 cells which was absent in EpCAM-negative U87 cells, and the high binding affinity to MCF-7 could be turned off when cell surface EpCAMs were blocked with incubation with an excess of unlabeled DARPins. Overall, site-specific labeling of a fluorophore to DARPins allowed high retention of the protein function and did not introduce non-specific interactions.

1.3.2 N-terminal protein functionalization through N-myristoylation

N-myristoylation of various myristic acid analogues allows the site-specific N-terminal modification of various POIs. The acid analogue requires conversion to a myristoyl-CoA thioester by an endogenous *E. coli* enzyme acyl-CoA synthetase in order to be recognized as a substrate by the enzyme N-myristoyl transferase (NMT). Therefore, protein conjugation via NMT-mediated labeling and click chemistry has mostly been performed at the cellular level, either in (live) cells or crude lysates prior to POI purification. Examples of such applications are imaging of specific protein functions in (live) bacteria in which the small tag allows minimal adverse effect on the native protein function,[114,115] or surface immobilization of POIs from crude lysate in which purification of the excess

myristic acid analogues is unnecessary as opposed to conjugation of a molecular payload.[116,117] While most of the prior work has been focused on click reactions that involve an azide, it would be interesting to see future development of new myristic acid analogues that could expand the range of utilizable click chemistries.

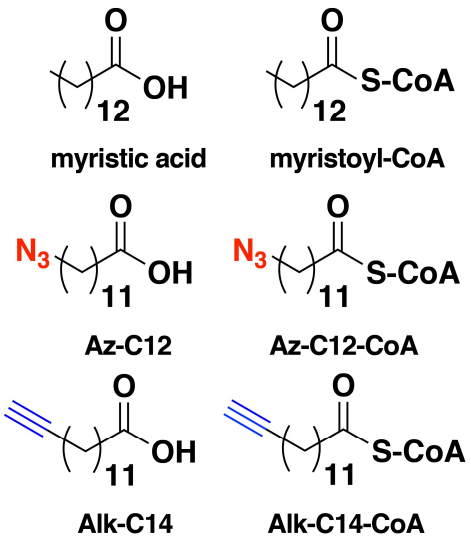

Figure 1.6 Clickable analogues of myristic acid and myristate-S-CoA for metabolic and in vitro labeling of myristoylated proteins. These probes are more selective for labeling N-myristoylated proteins.

Tate and coworkers were the first to report site-specific labeling exploiting a combination of *N*-myristoylation and click chemistry.[118] Az-C12-CoA (Fig. 1.6) was incubated with *C. albicans* NMT (CaNMT) and a model peptide that possesses the canonical GXXXS N-terminal *N*-myristoylation target motif. Incubation of equimolar substrates with a catalytic quantity of CaNMT (0.25%) led to a complete enzymatic reaction with rates comparable to that of the native substrate myristoyl-CoA. *P. falciparum* ADP ribosylation factor 1 (PfARF1), a natural substrate of NMT, was functionalized with an azide exploiting *N*-myristoylation which was subsequently captured by a phosphine-labeled biotin via Staudinger ligation with high efficiency (>99%). The method was utilized for a one-pot biotin labeling by feeding an azide-containing myristic acid to an engineered *E. coli* co-expressing CaNMT and PfARF1, followed by addition of biotin-phosphine to the resulting

lysate. Pull-down with avidin-beads indicated successful *in cellulo* functionalization of PfARF1 with >99% efficiency, which indicated successful uptake of the azido-myristic acid into the cells followed by transformation to the active CoA analogue via endogenous *E. coli* enzyme acyl-CoA synthetase. In a subsequent report, Tate and coworkers expanded the scope of click reactions utilizing a new alkyne-analogue.[119] The azide- or alkyne-containing myristoyl-CoA analogues Az-C11-CoA (Fig. 1.7) and Alk-C14-CoA (Fig. 1.6), which were designed so that the chain length and flexibility closely adhere to the native substrate, were both successfully transferred to a model peptide that contains the N-terminal region of PfARF1.

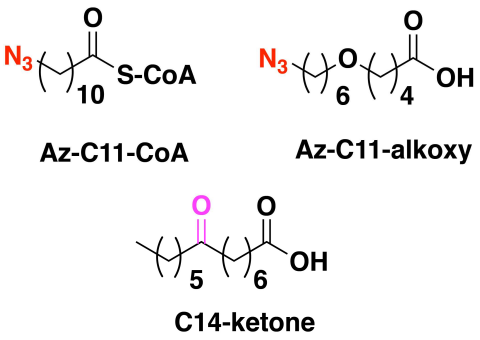

Figure 1.7 Additional myristoyl analogues used in enzymatic N-terminal modification of proteins. These analogues are functionalized with azides or ketones and vary in length compared to Az-C12 and Alk-C14.

While both reactions were rapid and comparable to the native substrate, the alkyne analogue was found to be two-fold faster. Both analogues were subjected to a one-pot labeling experiment in an *E. coli* co-expression system similar to the one described in their previous report, where the functionalized PfARF1 was subsequently reacted with biotin-capturing reagents containing either an alkyne, azide, or triarylphosphine. While capturing via both CuAAC and Staudinger ligation were shown to be successful, CuAAC was found to be more efficient similar to prior reports.[23] Within CuAAC approaches, conjugating alkyne-payloads to the azide-labeled protein was shown more effective than the converse,[90] presumably due to the benefits of having a large excess of activated alkyne when used as the capturing reagent. The labeling methods mentioned above were described in detail in a subsequent protocol paper, in which a multifunctional

alkyne-reagent carrying a biotin and TAMRA was labelled to an azide-containing PfARF1 by CuAAC.[120]

Tirrell and coworkers exploited the bio-orthogonality of NMT-catalyzed protein labeling and click chemistry for fluorophore labeling and immobilization of a target protein from crude cell lysate.[121] Two types of GFPs were engineered with different NMT recognition sequences, yARF-GFP which contained a motif from yeast ADP-ribosylation factor, and Fyn-GFP which featured a motif from the Src family tyrosine-protein kinase Fyn. Co-expression of each GFP with human NMT in *E. coli* with Az-C12, followed by lysis of the cells and CuAAC with the resulting lysate with an alkyne-TAMRA yielded selectively and site-specifically conjugated GFP-TAMRA. Incubation of the azide-labeled GFP-containing cell lysate on strained cyclooctyne-coated glass slides resulted in successful surface immobilization of GFP. While strained alkynes could undergo various side reactions, including processes involving free thiols present in GFP, SPAAC was found to be faster than those non-specific reactions, allowing control over the orientation of immobilized proteins by site-specific conjugation through the N-terminus.

NMT-mediated protein labeling was applied to calmodulin (CaM), a biologically relevant Ca^{2+}-binding protein.[116] The solvent-accessible N-terminus of CaM was engineered to display an NMT recognition sequence, derived from either human calcineurin B (CaN) or yeast ADP ribosylation factor. In addition, two types of linkers were employed to connect the NMT recognition sequence to the protein which led to a total of five engineered CaM constructs. All five were successfully labeled with an azide moiety when co-expressed in *E. coli* with human NMT1 in the presence of Az-C12 and were shown to maintain Ca^{2+}-binding and CaN-activating abilities comparable to that of wild type (WT) CaM. As the NMT-motif derived from CaN showed superior activity, it was selected for one-pot fluorophore labeling by subjecting the cell lysate containing the azide-labeled construct to CuAAC with alkyne-TAMRA. A single fluorescent band was observed by SDS-PAGE analysis which indicated selective labeling of the target protein as a result of the bio-orthogonality of NMT-mediated labeling and CuAAC. Various CaM-immobilized resins were prepared and tested for their capability to bind to and purify CaN. CaM-resins prepared via SPAAC with chemoenzymatically generated azide-CaM and azadibenzocyclooctyne-functionalized resins

(ADIBO-resins) showed CaN yields 10-fold higher than resins prepared by immobilizing WT CaM on NHS-ester or cyanide activated resins, demonstrating the advantage of protein immobilization in a site-specific fashion.

Tirrell and coworkers also utilized the NMT labeling system to visualize proteins in bacteria.[114] The target proteins were chemotaxis proteins Tar and CheA, and cell division proteins FtsZ and FtsA, which were each co-expressed in an *E. coli* system with NMT and methionyl aminopeptidase. The addition of Az-C12 or Az-C11-alkoxy simultaneously during the induction stage of protein expression, followed by the addition of a bicyclononyne-containing BODIPY reagent to the subsequently produced lysate led to complete modification of all four target proteins. *In situ* imaging of fixed and permeabilized cells was conducted on cells expressing each of the target proteins equipped with C-terminal myc tag fusions for immunofluorescence confirmation using an anti-myc AF647-conjugated antibody. Polar localization of Tar and CheA and septal localization for FtsZ and FtsA could be visualized in both BODIPY and AlexaFluor-647 channels; the former allowed imaging of the myristoylated proteins while the latter was used to detect myc. This demonstrated the utility of NMT-catalyzed fluorophore labeling for imaging bacterial proteins in cells, which could even be applied to live cells. The details of the sample preparation and labeling protocols for live cell imaging of bacterial proteins were further described in a follow-up methods paper.[115]

In a related work, Zhang and coworkers assessed whether the labeling of myristic acid analogues instead of the natural substrate alters protein function using a model protein ADP-ribosylation factor (Arf1).[122] Arf1 was myristoylated with five myristic acid analogues resulting in modified proteins that showed membrane-associating and GTP-hydrolyzing activities similar to endogenous Arf1 while non-myristoylated Arf1 lacked either properties. Additionally, an Arf1 labeled with Az-C14-ketone (Fig. 1.7) could be conjugated with a fluorescent hydrazine reagent. Importantly, in these studies, the authors described a methodology that could be used to determine the suitability of lipid-modification methods to monitor protein function in cells.

Calmodulin (CaM) conjugated Sepharose resin was prepared by a combination of *N*-myristoylation and click chemistry, which led to improved purification efficiencies of CaM-binding

proteins.[117] Azide-functionalized CaM was prepared by *N*-myristoylation with Az-C12, which was subsequently immobilized onto DBCO- or alkyne-functionalized Sepharose resin via SPAAC or CuAAC. DBCO-resin was shown to immobilize larger amounts of CaM compared to simple alkyne-resin and was shown to outperform commercial resin in purifying a CaM-binding protein calcineurin (CaN). CaM-resin was prepared directly from azide-CaM present in clarified lysate, which showed higher CaN purification efficiencies compared to resin prepared from purified azide-CaM. CaM-resin was tested for purification of calcium/calmodulin dependent kinase II alpha (CaMKII) which has traditionally been isolated using IMAC purification. Exploiting the CaM-resin yielded a product with higher purity and less degradation compared to purification using Ni-NTA resin. In their following methods paper, Kinzer-Ursem and coworkers described the details of CuAAC-mediated functionalization of CAM myristoylated with Az-C12.[123] In addition to fluorophore labelling with an alkyne-functionalized AlexaFluor-647, protein-immobilization on gold nanoparticles (AuNP) was shown where it was noted that cyclooctyne-functionalized AuNP resulted in aggregation leading to inferior conjugation with SPAAC compared to CuAAC.

Tirrell and coworkers expanded their work from 2016 by imaging bacterial proteins in live cells with nanometer resolution.[124] To exploit direct stochastic optical reconstruction microscopy (dSTORM), two cell-permeable photo-switchable rhodamine spirolactam dyes were developed. These dyes exhibited photon budgets comparable to conventional STORM dyes in the absence of additives such as oxygen-scavenging buffers or reducing agents that are usually required for facilitating the photo-switching of conventional dyes. Following the co-expression of target proteins with NMT in *E. coli* in the presence of Az-C12, bicyclononyne-functionalized dyes were added, which yielded live cells containing the fluorophore-labeled proteins that were then subjected to imaging without fixation or permeabilization. Chemotaxis proteins Tar and CheA and cell division proteins FtsZ and FtsA were observed with a mean localization precision in the nanometer range. While modification of the N-terminus presumably caused minimal perturbation of protein function, indicated by the successful imaging of live cells, the effect of the peptide tag and fluorophore were shown to vary for each protein of interest.

Table 1.1 Summary of click chemistry conditions and yields that involve site-specific protein labeling via lipid modifying enzymes

Entry	Application	Analogue & Click Conditions	Yield	Ref
Farnesyl transferase (* indicates geranylgeranyl transferase type 1 or Rab geranylgeranyl transferase)				
Staudinger ligation				
1	Surface immobilization	C10-Et-Az-OPP 1-20 μM GFP- or GST-Azide diphenylphosphine slides 50:1 DMF/water 1.5 h	NA	91
2	Proof-of-concept	C10-Az-OPP 0.9 mM Dn-GCVIA-N_3 45 mM phosphine reagent 48 h	NA	85
3	Proof-of-concept	C15-Az-OPP 0.9 mM Dn-GCVIA-N_3 45 mM phosphine reagent 48 h	NA	87
4	Proof-of-concept	AAA-GPP, APO-GPP 0.5 nmol GPP-N_3 2.5 nmol phosphine 25 mM HEPES pH 7.2, 40 mM NaCl, 2 mM $MgCl_2$ 8 h rt	Completion in 1.5 h Completion in 4 h	95
CuAAC				
5	Surface immobilization	C15-Dh-Az-OPP 0.1 mM GFP-N_3, Alkyne-beads 1 mM $CuSO_4$, 1 mM TCEP, 0.1 mM TBTA 43 mM NaH_2PO_4	96% immobilization (>80%	89

		1 h 25 ºC	covalent)	
6	Surface immobilization	C10-Et-Az-OPP, C10-Et-Alk-OPP 1-20 μM GFP- or GST-alkyne N_3-slides 1:3 glycerol/water 1.7 mM $CuSO_4$/TBTA/TCEP 2-7 h 4 ºC	NA	91
7	Surface immobilization	C10-Alk-OPP, C15-Dh-Az-OPP 50 μM GFP-alkyne and -N_3 Corresponding agarose (-N_3 or -alkyne) 1 mM $CuSO_4$, 1 mM TCEP, 0.1 mM TBTA overnight 25ºC	93%	93
		25 μM GFP-alkyne Texas red-N_3 1 mM $CuSO_4$, 1 mM TCEP, 0.1 mM TBTA 1 h 25 ºC	81%	
8	Fluorophore labeling GFP-DNA nanostructure assembly	C15-Dh-Az-OPP 20 μM GFP-N_3 22 μM DNA-alkyne 50 mM NaH_2PO_4, pH 7.3 1 mM $CuSO_4$, 1 mM TCEP, 0.1 mM TBTA 1 h rt	72%	94
9	Surface immobilization	C5-Alk-OPP 80 μM mCherry-alkyne Agarose-N_3 50 mM NaH_2PO_4 pH 7.3 1 mM $CuSO_4$, 1 mM TCEP, 0.1 mM TBTA 4 h rt	NA (presence or absence of VIA does not affect click efficiency)	96
10	GFP-ODN oligoconjugation	C10-Dh-Az-OPP, C15-Dh-Az-OPP 14 μM Protein-N_3 17 μM DNA-alkyne	>90% (GFP)	101

		1 mM $CuSO_4$, 1 mM TCEP, 0.2 mM TBTA 24 h rt	>81% (mCherry)	
11	Surface immobilization	C15-Alk-OPP 0.1 mM mCherry-alkyne N_3-gold 1 mM $CuSO_4$, 1 mM TCEP, 0.1 M TBTA 43 mM NaH_2PO_4 pH 7.3 2 h	NA	104
12	Antibody immobilization	C10-Et-Alk-OPP 100 µM antibody-alkyne Glass-N_3	NA	105
13	Sandwich antibody arrays	0.7 mM $CuSO_4$, 0.7 mM TCEP, 0.35 mM TBTA PBS pH 7.4 2 or 4 h rt		106
14	Antibody arrays	C10-Et-Alk-OPP 5 or 80 µM Protein-alkyne Gold-N_3 0.5 mM $CuSO_4$, 0.5 mM TCEP, 50 µM TBTA PBS pH 7.4 4 h rt	NA	107
15	Protein/peptide-DNA conjugation	C15-Dh-Az-OPP 10 µM DNA-alkyne 60 µM GFP-N_3 1 mM $CuSO_4$, 1 mM TCEP, 0.1 mM TBTA 50 mM PB pH 7.5 1.5 - 2 h rt	70-80%	110
16*	Protein dimerization (FTase & GGTase-1)	C10-Alk-OPP, C20-Az-OPP 50 µM GFP-N_3 50 µM RFP(or GFP)-alkyne 1 mM $CuSO_4$, 1 mM TCEP, 0.1 mM TBTA	23% (simultaneous prenylation) 29%	109

			(separate prenylation)	
17*	Biotin labeling (GGTase-1 Rab GGTase)	C20-Az-OPP 1 μM REP-1-N_3 50 μM Biotin-alkyne 1 mM $CuSO_4$, 10 mM sodium ascorbate, 0.1 mM TBTA 40 min 37 ºC	NA	98
CuAAC & oxime ligation				
18	Simultaneous fluorophore labeling and PEGylation	C10-BA-Alk-OPP GFP-aldehyde/alkyne PEG_{3k}-aminooxy TAMRA-N_3 1 : 3.85 : 15 ratio 40 mM mPDA 1 mM $CuSO_4$, 1 mM TCEP, 0.1 mM TBTA 15 h	>95% for both	102
Oxime ligation				
19	Surface immobilization	C15-Ald-OPP 20 μM GFP-aldehyde Alkyne-agarose 100 mM aniline 0.1 M PB pH 7.0 15 min rt	30%	97
	Fluorophore labeling	25 μM GFP-aldehyde 125 μM AF488 100 mM analine 0.1 M PB pH 7.0 30 min rt	60%	
20	Fluorophore labeling & PEGylation from crude	C10-BA-OPP 54 μM GFP-aldehyde Hydrazide-agarose 100 mM aniline		62

	lysate (model reaction conditions)	0.1 M PB pH 7.0 45 min rt	95% (Hydrazone)	
		200 mM Hydroxylamine 100 mM aniline 0.2 M PB pH 7.0 3 h rt	80% (Oxime)	
21	Assessment of mPDA as catalyst (model rxn conditions)	C10-BA-OPP 10 μM GFP-aldehyde 50 μM Dn-aminooxy 750 mM mPDA 100 mM PB pH 7.0 90 s rt	Completion	62
22	Antibody-drug conjugation	GKPP 12 μM repebody-aldehyde 120 μM beta-glucuronide MMAF 200 mM Na-acetate buffer pH 4.5 10% DMSO 24 h 30 ºC	97.4%	111
SPAAC				
23	GFP-ODN conjugation	C10-Dh-Az-OPP, C15-Dh-Az-OPP 14 μM GFP-N_3 4.6 μM ODN-DIBO H_2O or 0.1 M NaCl PB pH 3.5-12.3 Overnight, rt or 4 ºC	95% (GFP) k_{rt}=6 $M^{-1}s^{-1}$ $k_{4\ ºC}$=0.8 $M^{-1}s^{-1}$ 27% (mCherry)	101
24	Fluorophore labeling	C10-Az-OPP DARPin-N_3 TAMRA-DBCO	Near completion	113

		1 : 5 molar ratio PBS (400 mM NaCl) 3 h rt		
Tetrazine ligation				
25	Proof of concept	C10-TCO-OPP 33 µM GFP-TCO 530 µM benzylamino-tetrazine 4 h rt + overnight 4 ºC	NA	[108]
		20 µM OrG-TCO 50 µM dipyridyl-tetrazine 15 min	Completion	
Thiol-ene				
26	Surface immobilization	FPP 0.1-100 µM Farnesylated protein Thiol-functionalized slides 2.5 mM DTE, 20% glycerol UV 365 nm 10 min 6 Jcm^{-2} (H, -N-, and K-Ras & Rab6A) or 20 min 12 J cm^{-2} (mCherry)	NA	[99]
Diels-alder cycloaddition				
27	Proof of concept	HOM-GPP 50 µM CFP-alkene 40 eq 6-maleimidohexanoic acid 50 mM Na_2HPO_4 pH 6, 40 mM NaCl, 2 mM $MgCl_2$ 15 h rt	30%	[95]
N-Myristoyl transferase				
Staudinger ligation				

28	Biotin labeling	Az-C11-CoA 3 nmol PfARF1-N_3 200 µM Biotin-phosphine 2 h 37 ºC	>99%	[119]t
CuAAC		Az-C12 (for entries 29-32)		
29	Biotin and fluorophore labeling	100 µg PfARF1-N_3 50 µM Alkyne-biotin/TAMRA 0.5 mM $CuSO_4$, 0.5 mM TCEP, 50 µM TBTA 1 h rt	NA	[120]
30	Fluorophore labeling	GFP-N_3 (in cell lysate) 5.2 µM TAMRA-alkyne 3.5 mM $CuSO_4$ (Modified Invitrogen™ Click-iT Kit instructions) 50 Tris-HCl pH 8.0 1% SDS 25 min rt	NA	[121]
31	Fluorophore labeling	CaM-N_3 (in cell lysate) 5.2 µM TAMRA-alkyne 3.5 mM $CuSO_4$ (Modified Invitrogen™ Click-iT Kit instructions) 20 min rt	NA	[116]
32	Surface immobilization	1, 2 or 5 mg ml^{-1} CAM-N_3 Alkyne-resin 2 mM $CuSO_4$, 10 mM THPTA, 10 mM sodium ascorbate	NA	[117]
SPAAC		Az-C12 (for entries 33-38), Az-C11-alkoxy (for entry 38)		
33	Surface immobilization	GFP-N_3 (in 0.25-1 mg ml^{-1} cell lysate) Glass-DIBO or -ADIBO 40 min	90% specificity	[121]
34	Surface immobilization	0.5 mg ml^{-1} CaM-N_3 (estimation in 3.5 mg ml^{-1} cell lysate) ADIBO-resin	NA	[116]

		Overnight 4 ºC		
35	Surface immobilization	1, 2 or 5 mg ml^{-1} CAM-N_3 DBCO-resin 20 mM HEPES pH 7.5 Overnight 4 ºC	NA	117
36	Fluorophore labeling and live-cell imaging	Cells expressing recombinant protein-N_3 20 µM BODIPY-BCN PBS 0.5-1 h, rt or 37 ºC		115
37	Fluorophore labeling and live-cell imaging	Cells expressing recombinant protein-N_3 200 nM Rhodamine-BCN PBS 1 h 37 ºC	NA	124
38	Fluorophore labeling and live-cell imaging	Protein-N_3 (in 0.4 mg ml^{-1} cell lysate) 2 µM BODIPY-BCN PBS 0.5 h, rt or 37 ºC	NA	114
Hydrazone ligation				
39	Fluorophore labeling	C14-ketone Arf1-ketone 1 mM Fluorescein-hydrazide PBS 16 h 4 ºC	NA	122

1.4 Conclusion

Click chemistry has played a critical role in illuminating the process of protein lipidation, as well as in discerning their roles in controlling protein function, localization, and protein-protein interactions. The ability to use metabolic labeling to incorporate lipid analogues containing

functionality that can be subsequently modified for various analyses has proved to be a versatile strategy. Click reactions with affinity handles have allowed proteins to be pulled down and identified by proteomic methods. Incorporation of quantitative mass spectrometric methods into such workflows have made it possible to study the regulation of protein lipid modification and the impact of specific inhibitors. Click reactions with fluorophores have enabled the localization of lipidated proteins to be studied and their levels quantified. Overall, much information has been gained concerning the biology of protein *S*-prenylation using this approach. However, as mentioned, most of the currently available tools are only applicable to fixed cells and therefore efforts into applying click chemistry in molecular imaging inside live cells or tissues needs to be pursued moving forward.

In a similar way, the use of click chemistry in conjunction with protein lipidation has proved to be a powerful approach for site selective protein modification. Site-specific enzymatic incorporation, either *in vitro* or *in cellulo*, of lipid substrates bearing appropriate functional groups has enabled a diverse range of modifications to be performed on either the N-termini (via *N*-myristoylation) or C-termini (via *S*-prenylation) of target proteins. Applications include immobilization, fluorescent labeling and drug conjugation; this approach has also proved useful for the construction of more complex architectures including protein nanostructures and protein-DNA conjugates. On the other hand, enzymatic *S*- and *N*-acylation has been applied in only developing platforms for screening of fatty acylation inhibitors. There are no reports so far in using such types of lipid modification for bioconjugation strategies, which can be attributed to their lack of sequence specificity (*e. g.* unclear recognition motifs) and the susceptibility of *S*-acylated substrates to hydrolysis.

Throughout the above studies, click chemistry has played a central role. A summary of the features of different click chemistries that have been used for studying and exploiting protein lipid modification is shown Fig. 1.8. This graphic emphasizes that individual click reactions have different attributes that make them more or less suitable for different applications and illustrate that there is no one single reaction that is best for all applications. For example, while the alkene and tetrazine reactants are somewhat large, making it difficult to incorporate them into substrates without attenuating their enzymatic reactivity, the inverse electron demand Diels Alder (iEDDA) reaction is

the fastest click reaction discovered to date. The superior kinetics of iEDDA that does not require toxic catalysts allows click reactions to be applicable for live cell studies, which could even be expanded to *in vivo* environments. Among click reactions that involve azides and alkynes, the copper-catalyzed version (CuAAC) is not compatible with live-cell experiments due to toxicity issues while the strain-promoted (SPAAC) reaction is considerably slower and the presence of a large hydrophobic moiety appended to a protein can create solubility/stability problems. Nonetheless, both reactions remain to be a powerful tool especially for *in vitro* studies due to the robustness of the reaction, and since the small size of azide and alkyne groups that can be readily introduced into the protein substrates without abrogating their reactivity. Oxime and hydrazone forming reactions are particularly attractive due to the structural innocuity of small aldehyde and ketone groups but that is partially offset by slower reaction rates, incomplete orthogonality (due to the presence of some aldehydes and ketones in cells) and hydrolytic instability; at the same time, oxime and hydrazone products manifest the highly useful feature that their formation is reversible that has been utilized for one-pot labelling and purification of protein-conjugates. Alternative ligation reactions with aldehydes that forms a stable C-C bond instead of an imine have been reported as well,[67,125] which could be exploited to expand the scope of click reactions involving aldehydes.

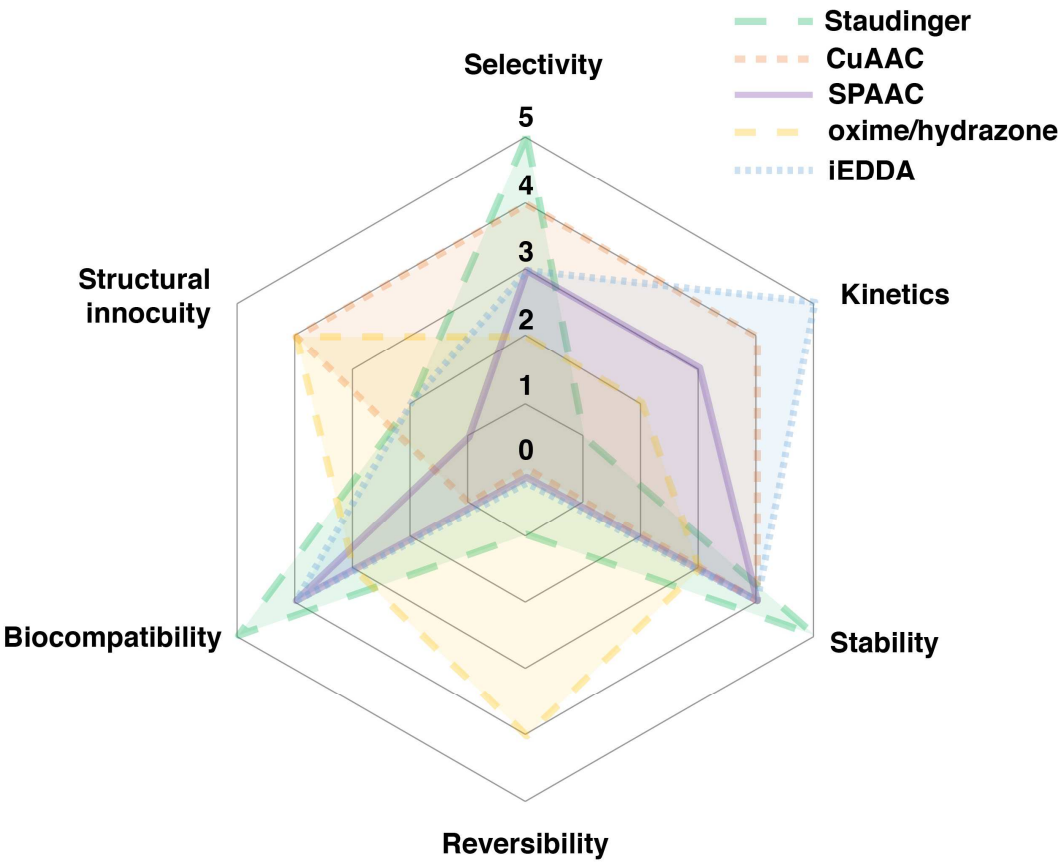

Figure 1.8 Considerations in the applicability of click chemistry in protein or cellular environments. Individual reactions were given a rating from 5 (highest) to 0 (lowest) for each category based on how much they satisfy each of the following criteria. Kinetics: High rate constant; Selectivity: Selective reaction between click functionalities without side reactions with biologically endogenous functionalities; Stability: High stability of the resulting linkage; Structural Innocuity: Minimal adverse effect of the coupling partners and/or resulting linkage on cellular or protein activity; Biocompatibility: Applicability of the reaction conditions for live cell or in vivo experiments; Reversibility: Reversibility of the click chemistry product.

For studies of protein lipid modification to advance further, both the understanding of enzyme-substrate interaction and click chemistry will need to evolve. Developing enzymes that are more tolerant towards a wider variety of analogue substrates would broaden the scope of applicable click reactions, that is currently heavily focused on alkyne and azide functionalities due to their small size. In terms of potential improvements in click chemistry, new functionalities will need to be developed that allow minimalist additions to enzyme substrates that have limited impact on enzyme

recognition, while exhibiting increased click reactivity to allow the detection of modified proteins present at very low concentrations in cells. The further development of click chemistries that permit experiments with live cells and that have minimal effects on the structure, function, stability and solubility of proteins will significantly broaden the types of questions that can be addressed using *in cellulo* metabolic labeling and *in vitro* modification. For instance, click reactions with rates comparable to iEDDA that do not require bulky ring systems would be particularly useful. Click reactions that proceed at equimolar concentrations compared to the target protein, even in the absence of catalysts, would open up *in vivo* applications where localized high concentrations are difficult to achieve. Applying two-photon chemistry to thiol-ene click chemistry could be utilized for experiments that require spatiotemporal control in *in cellulo* or *in vivo* applications due to the low toxicity and tissue penetrating capabilities of that method. While these future directions are raised here in the context of protein lipidation, they are obviously all germane to many other types of protein modifications.

Chapter 2. Targeted drug delivery and imaging with site-specific DARPin-polymer constructs

Therapeutic proteins exhibit highly specific functions, few side effects, and low immune responses, which are often difficult to achieve with small-molecule drugs. Despite its distinctive advantages, the innate structural instability of proteins remains to be one of their main drawbacks, which has led to studies that involve the conjugation of synthetic polymers to enhance the half-life of the polypeptide-based drugs in the bloodstream. Key factors to consider in the conjugation step are site-specificity, yield, and ease of purification, as they directly affect protein activity, product homogeneity, and scaleability. The most commonly used polymer-conjugation method, direct chemical modification with presynthesized polymers, lacks site-specificity that often leads to reduced protein activity. In addition, the steric effects related to the size of the polymer often causes low conjugation yields which in turn leads to difficulties in purification. Therefore, new strategies are in demand.

In this work, protein prenylation and in situ controlled radical polymerization are exploited to overcome the limitations in conventional protein-polymer conjugation techniques. A tumor-targeting antibody mimetic DAPRin (Designed Ankyrin Repeat Protein) is site-specifically functionalized with an ATRP (Atom Transfer Radical Polymerization) initiator moiety via protein prenylation. In situ polymerization is then employed from the DARPin-macroinitiator with a variety of customized monomers to yield DARPin-polymer constructs capable of tumor-targeted imaging and drug delivery. We demonstrate that utilization of the described methods results in DARPin-polymer constructs with high therapeutic efficacies due to the highly retained protein activity, enhanced pharmacokinetics, and high drug-to-antibody ratios (DAR).

2.1 Introduction

Protein-based therapeutics continue to dominate the drug market. As of 2019, 7 out of 10 top-selling drugs were therapeutic proteins.[126] This wide use of protein-drugs comes from its unique advantages that are often difficult to achieve with small molecule therapeutics. To name a few,

proteins exhibit highly specific functions, few side effects, and low immune response, which render them ideal for therapeutic applications. Antibodies are particulary important protein therapeutics due to their capability to perform targeted imaging and drug delivery based on the high affinity their of epitopes against specific antigens.[127] However, like many proteins, antibodies cab suffer from short half-life in the circulation which can impair their broader applicability. Conjugation of hydrophilic polymers such as polyethylene glycol (PEG) to extend the circulation time of proteins has been a widely used strategy to combat this limitation. Many FDA-approved PEGylated protein products have been released in the market, with many more under development.[128]

It is important to maximize the protein activity and yield for the product derivatization method to be widely applicable to therapeutically relevant proteins. The polymerization method is one aspect that can be optimized for higher drug efficacies. The grafting-from conjugation method which involves synthesis of the polymer directly from the protein-macroinitiator has been gaining attention over the conventional grafting-to method which requires the conjugation of a presynthesized polymer to the target protein. The key first step for this method is the installation of a polymerization initiator moiety into the target protein to render it a macroinitiator. This in situ polymerization method exhibits several advantages over the grafting-to method. The first of these is easier purification, as the method only requires separation of large macromolecular products from small monomers, while the grafting-to products require a more vigorous separation between macromolecules both large in size.[129] The yield tends to be higher as well compared to grafting-to methods due to the lower steric hindrance between the initiator molecule and protein compared to protein-macromolecule interactions.[130] This advantage becomes even more apparent when conjugating branched polymers as they are especially difficult to give high conjugation yields using grafting-to methods due to the bulky side chains.[131] Since earlier reports based on model proteins,[132–134] the use of grafting-from techniques has steadily expanded into the realm of therapeutically relevant proteins.[135,136]

Another important aspect to consider in protein-polymer conjugation is the site of modification. Conventional protein labeling methods have involved maleimide or activated-ester

functionalized molecules that react with the thiol or amine moieties present in the protein of interest. However, proteins that undergo direct chemical modification methods have often shown to suffer from reduced bioactivity due to the lack of control over the site of modification that leads to heterogeneous product mixtures. Uncontrolled labeling of the protein may also obstruct the binding/active site leading to deactivated protein products. Therefore, new methods that enable site-specific conjugation has been necessitated.[129,137] One solution is to exploit the promiscuity of various enzymes to site-specifically conjugate various probes that are analogous to the native substrate of the enzyme. Enzymatic protein labeling allows precise control of the site of modification and the number of modification sites under mild reaction conditions, in contrast to chemical conjugation which lacks site-specificity and can require more vigorous conditions. While unnatural amino acid (UAA) incorporation allows site-specific installment of specific functionality of interest, that method can be difficult to optimize and often leads to low protein production yields.[138] The unique advantages of enzymatic labeling has led to increased application in biotechnology, often in conjunction with click chemistry for site-specific introduction of fluorophores, drugs, or polymers.[13,139]

Protein prenylation is an important post-translational modification involving the attachment of a C15 or C20 isoprenoid to target proteins that contain a C-terminal CaaX recognition motif catalyzed by prenyltransferases.[11] The modification occurs site-specifically at the cysteine residue of the CaaX box through formation of a covalent C-S bond. The promiscuity of the protein farnesyltransferase (PFTase) has been exploited in prior studies to site-specifically install various chemical moieties that include azides, alkynes, cyclooctenes, or aldehydes or ketones, followed by subsequent click-chemistry with fluorophores, polymers, or toxins to prepare functional protein-conjugates.[13,139] Such application of farnesylation towards biotechnological applications exhibit unique advantages. The modification occurs stoichiometrically and site-specifically with high yield which produces homogenous protein products. The labeling occurs at the C-terminal cysteine which is usually distanced from the active site, hence leading to highly retained post-modification protein activity. The method is highly versatile, as PFTase can selectively recognize virtually any type of protein by simply attaching a the CaaX-box sequence to the protein of interest. As the

recognition motif is only four amino acids long, minimal perturbation is introduced to the target protein structure.

In this study, protein prenylation was utilized to create site-specific protein-polymer conjugates for tumor-targeted imaging and drug delivery (Fig. 2.1). While there have been prior studies that utilized enzymatic labeling for site-specific polymer conjugations, they are limited to sortase-[136,140] or intein-mediated labeling.[141] Therefore, we sought to expand the scope of enzymes by utilizing yeast PFTase (yPFTase). In this work, the protein of interest was a Designed Ankyrin Repeat Proteins (DARPins), a protein scaffold genetically engineered and selected to bind to specific tumor-associated antigens. DARPins have been shown to be a promising alternative to immunoglobin G (IgG) antibodies due to its many important advantages. DARPins exhibit high rigidity and stability against proteases, they are easy to produce in bacteria in high yields, they can be easily engineered, and they are small size in (20 kDa) that facilitates tumor penetration. In contrast, IgGs require a more complex mammalian expression system and often suffer from poor tumor penetration due to their large size (150 kDa).[142] The DARPin construct chosen for this study was one that targets epithelial cell adhesion molecules (EpCAM), which is a useful cancer target due to its overexpression in solid tumors and its ability to internalize that can be exploited to facilitate intracellular delivery of cytotoxic payloads.[143] Previous reports have demonstrated the use of EpCAM-targeting DARPins for tumor-targeted delivery of a toxin or an imaging agent.[144–146] Grafting-to PEGylation of DARPins was shown to improve the therapeutic efficacy in mouse studies by increasing the serum half-life.[144] Here, we aimed to improve the therapeutic efficacy of DARPins with a site-selectively conjugated and payload-functionalized polymer prepared by in situ copolymerization and copper-free click chemistry. Conjugation of a hydrophilic polymer was found to enhance the pharmacokinetic properties of DARPins, and taking advantage of the hydrophilic polymer as a “trailer” attached to the DARPin “vehicle” allowed loading of multiple hydrophobic payloads without diminishing the stability of the protein. While the focus of this effort was tumor-targeted imaging and drug delivery, the modular characteristics of this approach should allow a variety of other modifications to be implemented in a seamless manner.

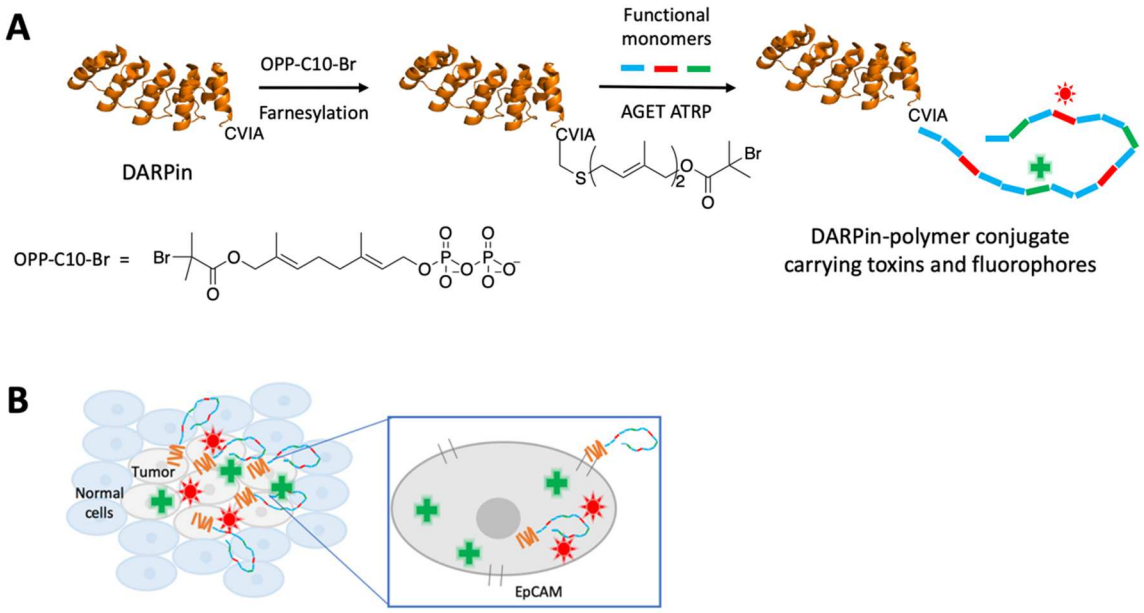

Figure 2.1 DARPin-polymer conjugates prepared by site-specific enzymatic labeling and in situ polymerization for tumor targeted imaging and drug delivery. (A) ATRP from the site-specific DARPin-Br macroinitiator with functional monomers of interest yields DARPin-polymer conjugates carrying toxins, fluorphores, and so on. (B) The DARPin-vehicle allows targeted delivery of the payloads to the tumor, and the overexpressed EpCAM on the tumor surface prompts receptor-mediated endocytosis of the payload, which allows tumor targeted imaging or toxicity.

2.2 Experimental

Synthesis of OPP-C10-iBr and OPP-C10-Acr (side product)

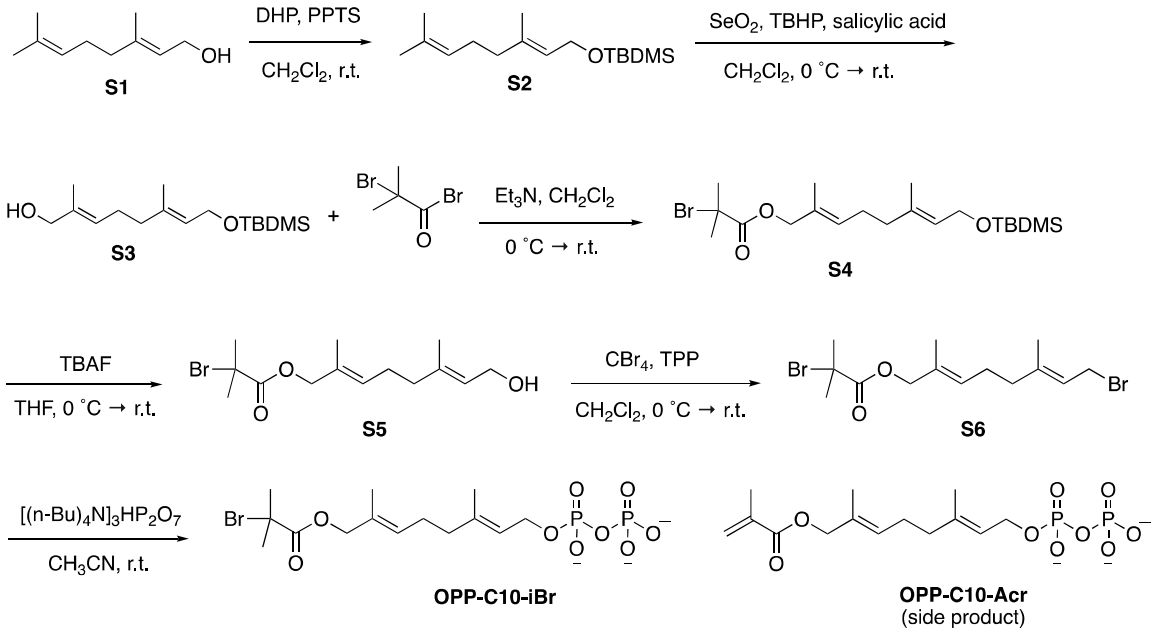

(2E,6E)-2,6-dimethyl-8-((tetrahydro-2H-pyran-2-yl)oxy)octa-2,6-dien-1-yl 2-bromo-2-methylpropanoate (S4)

Compounds **S2** and **S3** were prepared as previously described (*Mapping the Isoprenoid Binding Pocket of PDEd by a Semisynthetic, Photoactivatable N-Ras Lipoprotein*). **S3** (2 g, 7.86 mmol) and TEA was added to 50 mL dry CH_2Cl_2 and cooled to 0 °C in ice bath. 2-bromoisobutyryl bromide (2.42 g, 11.8 mmol) was added dropwise to the reaction mixture which was stirred at 0 °C for 1 h followed by overnight stirring at rt. After washing three times each with HCl (0.5 M) and H_2O, the organic phase was collected and dried over Na_2SO_4. Solvent was removed *in vacuo* and the product was purified by silica gel flash column chromatography (9:1 Hex:EtOAc, v/v) to afford **S4** (2.79 g, 93%) as a yellow oil.

^{1}H NMR (300 MHz, $CDCl_3$) δ ppm 0.06 (s, 6H), 0.89 (s, 9H), 1.81 (s, 3H), 1.61 (s, 3H), 1.66 (s, 3H), 1.92 (s, 6H), 2.01-2.20 (m, 4H), 4.18 (d, J = 6.6 Hz, 2H), 4.53 (s, 2H), 5.30 (m, 1H), 5.48 (m, 1H)

^{13}C NMR (75 MHz, $CDCl_3$) 4.3, 14.5, 17.0, 26.6, 26.7, 31.4, 39.5, 56.5, 72.1, 125.5, 130.2, 130.4, 146.8, 172.0

HRMS (m/z): $[M + H]^+$ calcd for $[C_{15}H_{27}O_3]^+$ 433.1695, found 433.1692.

(2E,6E)-8-hydroxy-2,6-dimethylocta-2,6-dien-1-yl 2-bromo-2-methylpropanoate (S5)

To a solution of **S4** (1 g, 2.31 mmol) in dry THF (15 mL) was added TBAF (1.21 g, 4.61 mmol) at 0 °C and stirred for 15 min followed by stirring at rt for 2.5 h. After quenching the reaction by adding CH_3OH (15 mL), and the reaction mixture was concentrated *in vacuo* and purified by silica gel flash chromatography (7:3 Hex:EtOAc, v/v) to afford 570 mg (0.5 g, 68 %) of **S5** as a clear oil.

^{1}H NMR (300 MHz, $CDCl_3$) δ ppm 0.06 (s, 6H), 0.89 (s, 9H), 1.42 (s, 6H), 1.94 (s, 6H), 2.10-2.20 (m, 4H), 4.14 (d, *J* = 6.6 Hz, 2H), 4.53 (t, *J* = 6.6 Hz, 2H), 5.39-5.41 (m, 2H)

^{13}C NMR (75 MHz, $CDCl_3$) 14.4, 14.5, 16.8, 18.9, 26.5, 31.4, 39.4, 59.7, 70.9, 72.1, 124.7, 126.1, 130.4, 139.1, 172.1

HRMS (m/z): $[M + H]^+$ calcd for $[C_{15}H_{27}O_3]^+$ 433.1695, found 433.1692.

(2E,6E)-8-bromo-2,6-dimethylocta-2,6-dien-1-yl 2-bromo-2-methylpropanoate (S6)

PPh_3 (polymer-supported beads, 1.31 g, 3.92 mmol) was added to a solution of **S5** (0.5 g, 1.57 mmol) in dry CH_2Cl_2 (15 mL), and the reaction solution was stirred for 30 min at rt to let the beads swell. After slowly adding CBr_4 (0.779 g, 2.35 mmol), the reaction mixture was stirred at rt overnight. Once full conversion top product was confirmed via TLC analysis, the reaction mixture was filtered to separate the beads and concentrated *in vacuo*. After removing the CBr_4 using a Waters Sep-Pak reversed-phase C_{18} cartridge, the crude product was used for the next step without further purification.

(2E,6E)-8-((2-bromo-2-methylpropanoyl)oxy)-3,7-dimethylocta-2,6-dien-1-yl diphosphate (OPP-C10-iBr) and (2E,6E)-8-(methacryloyloxy)-3,7-dimethylocta-2,6-dien-1-yl diphosphate (OPP-C10-Acr)

S6 (0.393 g, 0.923 mmol) and $[(n\text{Bu})_4\text{N}]]_3HP_2O_7$ (1.39 g, 1.38 mmol) was added to dry CH_3CN (5 mL) and was left to stir overnight at rt. The reaction mixture was concentrated *in vacuo*, and the product was converted to the ammonium salt form using an ion exchange column (Dowex 50W-

W8 ion exchange resin). Briefly, a column packed with the resin was washed with three column volumes of H_2O/conc. NH_4OH (2:1, v/v), followed by equilibration with solvent A (49:1 25 mM NH_4HCO_3:iPrOH, v/v). The crude product was loaded onto the column in 1 mL solvent A and eluted with additional solvent A, lyophilized, and purified by RP-HPLC with a semipreparative column using a gradient of 25 mM NH_4OCO_3 (A) and CH_3CN (B). OPP-C10-Acr started to elute from 12% B, followed by elution of OPP-C10-Br. Fractions containing OPP-C10-Br were collected and lyophilized to yield white powder. OPP-C10-Acr was shown to form as side product, which was collected separately but not used in this work.

For OPP-C10-Br,

^{1}H NMR (500 MHz, D_2O) δ ppm 1.54 (s, 3H), 1.58 (s, 3H), 1.78 (s, 6H), 1.97 (t, *J* = 7.5 Hz, 2H), 2.06 (q, *J* = 7.4 Hz, 2H), 4.32 (t, *J* = 6.5 Hz, 2H), 4.42 (s, 2H), 5.32 (t, *J* = 7.0 Hz, 1H), 5.40 (t, *J* = 7.2 Hz, 1H)

^{31}P NMR (203 MHz, D_2O) -6.52 (d, *J* = 26.4, 1P), -10.4 (d, *J* = 26.4, 1P)

HRMS (m/z): $[M - H]^-$ calcd for $[C_{14}H_{24}Br_1O_9P_2]^-$ 477.0085, found 476.9947.

For OPP-C10-Acr,

^{1}H NMR (300 MHz, D_2O) δ ppm 1.41 (s, 3H), 1.45 (s, 3H), 1.74 (s, 3H), 1.91-2.05 (m, 4H), 4.27 (t, *J* = 6.8 Hz, 2H), 4.39 (s, 2H), 5.27 (t, *J* = 6.8 Hz, 1H), 5.35 (t, *J* = 6.8 Hz, 1H), 5.52 (s, 1H), 5.93 (s, 1H)

^{31}P NMR (121 MHz, D_2O) -9.72 (d, *J* = 22.6, 1P), -5.81 (d, *J* = 22.6, 1P)

HRMS (m/z): $[M - H]^-$ calcd for $[C_{14}H_{23}O_9P_2]^-$ 397.0823, found 397.0397.

Synthesis of sacrificial initiator resin

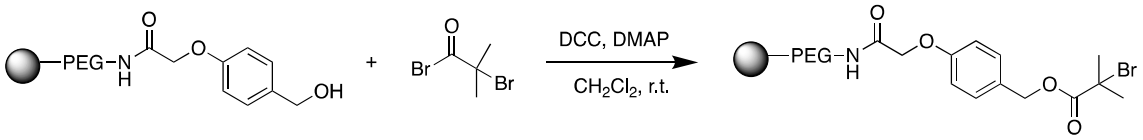

The synthesis method was adopted from Maynard (*citation*). Briefly, to 1500 mg of NovaSyn TGA resin (90 μm, loading capacity 0.2 - 0.3 mmol/g) in 40 mL dry CH_2Cl_2, was added 2-bromo-2-methylpropionic acid (1303 mg, 7.80 mmol), DCC (2414 mg, 11.7 mmol), and DMAP (238 mg, 1.95

mmol). After an overnight reaction at rt, the resin was washed with CH_2Cl_2, water, then THF, followed by drying under vacuum for 3 days. The conjugation of the initiator moiety was confirmed by NMR spectroscopy (150 mg/mL in solvent).

^{1}H NMR (400 MHz, $CDCl_3$) δ ppm 1.75-2.16 (6H), 2.90-5.00 (100H), 4.40-4.60 (2H), 5.02-5.34 (2H), 6.76-7.50 (4H)

Synthesis of azide-methacrylate (Az-MA)

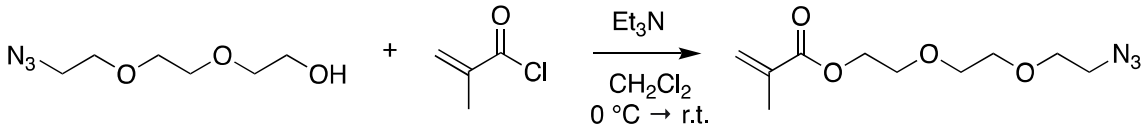

A mixture of 2-[2-(2-azidoethoxy)ethoxy]ethanol (701 mg, 4 mmol) and TEA (294 µL, 4 mmol) in 25 mL dry CH_2Cl_2 was cooled down to 0 °C. Methacryloyl chloride (492 µL, 4.4 mmol) was added dropwise to the reaction mixture which was left to stir overnight at rt. The solvent was removed in vacuo and the crude product was purified by silica gel flash column chromatography (3:1 Hex:EtOAc, v/v) to afford **Az-MA** (325 mg, 33%) as a colorless oil.

^{1}H NMR (400 MHz, $CDCl_3$) δ ppm 1.93-1.98 (m, 3H), 3.39 (t, J = 4.8 Hz, 2H), 3.64-3.72 (m, 6H), 3.76 (t, J = 4.0, 2H), 4.31 (t, J = 4.0 Hz, 2H), 5.58 (m, 1H), 6.13 (m, 1H)

HRMS (m/z): $[M + Na]^+$ calcd for $[C_{10}H_{17}N_3O_4Na_1]^+$ 266.1111, found 266.1122.

Synthesis of azide-methacrylamide (Az-MAm)

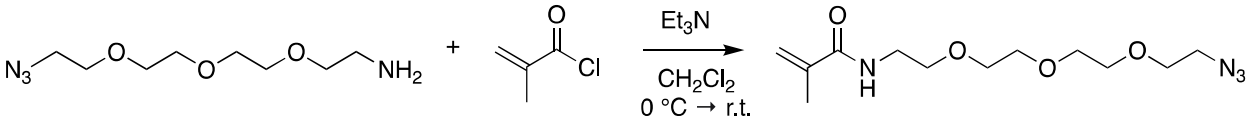

A mixture of 11-azido-3,6,9-trioxaundecan-1-amine (220 mg, 1.0 mmol) and TEA (74.1 µL, 1.0 mmol) in 5 mL dry CH_2Cl_2 was cooled down to 0 °C. Methacryloyl chloride (135 µL, 1.2 mmol) was added dropwise to the reaction mixture which was left to stir overnight at rt. The solvent was removed in vacuo and the crude product was purified by silica gel flash column chromatography (1:19 CH_3OH:CH_2Cl_2, v/v) to afford **Az-MAm** (265 mg, 92%) as a colorless oil.

^{1}H NMR (400 MHz, $CDCl_3$) δ ppm 1.95-1.98 (m, 3H), 3.39 (t, *J* = 4.8 Hz, 2H), 3.48-3.55 (m, 2H), 3.57-3.71 (m, 12H), 5.58 (m, 1H), 5.70 (m, 1H)

HRMS (m/z): $[M + Na]^+$ calcd for $[C_{12}H_{22}N_4O_4Na_1]^+$ 309.1533, found 309.1535.

Synthesis of rhodamine-methacrylate (Rhod-MA)

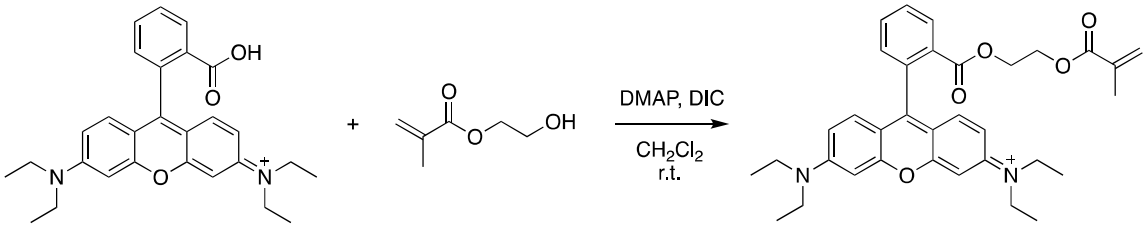

A mixture of rhodamine B (1 g, 2.09 mmol), 2-hydroxyethyl methacrylate (279 µL, 2.30 mmol), and DMAP (25.5 mg, 0.209 mmol) in 30 mL dry CH_2Cl_2 was cooled down to 0 °C. The reaction was then initiated by adding DIC (234 µL, 2.30 mmol) dropwise, which was stirred overnight at rt under Ar (g). The solvent was removed in vacuo and the crude product was purified by silica gel flash column chromatography (gradient from 0:100 to 100:0 iPrOH:EtOAc, v/v) to afford **Rhod-MA** (825 mg, 71%) as a sticky solid.

^{1}H NMR (400 MHz, $CDCl_3$) δ ppm 1.33 (t, *J* = 8.0 Hz, 12H), 3.65 (q, *J* = 8.0 Hz, 8H), 4.15-4.21 (m, 2H), 4.27-4.33 (m, 2H), 5.55 (s, 1H), 6.02 (s, 1H), 6.81 (d, *J* = 4.0 Hz, 2H), 6.93 (dd, *J* = 8.0, 4.0 Hz, 2H), 7.07 (d, *J* = 12 Hz, 2H), 7.32 (d, *J* = 8.0 Hz, 1H), 7.74 (td, *J* = 8, 1.6 Hz, 1H), 7.84 (td, *J* = 8, 1.6 Hz, 1H), 8.29 (d, *J* = 8 Hz, 1H)

HRMS (m/z): $[M]^+$ calcd for $[C_{34}H_{39}N_2O_5]^+$ 555.2853, found 555.2856.

Synthesis of doxorubicin-PEG4-DBCO (Dox-DBCO)

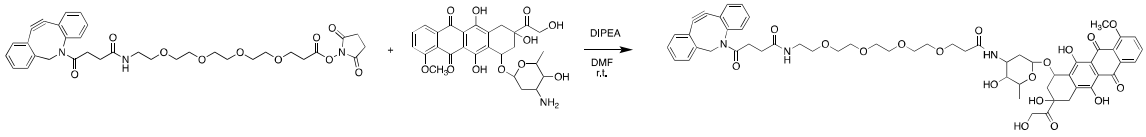

To a mixture of doxorubicin hydrochloride (5.52 mg, 10.2 µmol) and DBCO-PEG4-NHS ester (6 mg, 9.2 µmol) in 6 mL dry DMF was added DIPEA (2.98 mg, 23.1 µmol). After stirring at rt for 20 h, the solvent was removed in vacuo. TLC and LCMS analysis indicated (near) complete conversion to the product. Therefore, the crude product was used without further purification. Yield was 43%,

which was determined by measuring the absorption at 485 nm in 1:99 DMSO:water (ε = 11,500 $L \cdot mol^{-1} \cdot cm^{-1}$ at 25 °C).

HRMS (m/z): $[M + Na]^+$ calcd for $[C_{57}H_{63}N_3O_{18}Na_1]^+$ 1100.3999, found 1100.3999.

Expression and purification of the CVIA-proteins

Plasmids encoding the POI with an N-terminal His-tag and C-terminal CVIA tag were co-transformed into BL21 (DE3) cells. The *E. coli* cells were plated on LB-Agar plates containing 50 µg/mL kanamycin and grown overnight at 37 °C. A single colony was selected to inoculate 50 mL of LB media containing 50 µg/mL kanamycin, which was grown overnight at 37 °C with shaking at 250 rpm. 10 mL of the culture media was added to 1 L of LB media containing 50 µg/mL kanamycin. Once the cell culture was grown at 37 °C 250 rpm to an OD600 of 0.6 - 1.0, protein expression was induced by adding 0.5 mM IPTG. The cells were grown for another 4 h at 37 °C 250 rpm and harvested by centrifugation at 5,400 g for 10 min. The cell pellet was resuspended in 50 mL of buffer A (20 mM Na_2HPO_4/NaH_2PO_4, 500 mM NaCl, 50 mM Imidazole, 10 % Glycerol) containing 1 mL of inhibitor cocktail (Sigma Aldrich P8340) and lysed by pulse sonication (10 sec on, 10 sec off) at 50 W for 10 minutes total. Centrifugation of the lysis extract was performed at 13,000 g for 30 min, and the soluble fraction was collected and purified by immobilized metal ion affinity chromatography (IMAC) using Ni-NTA Agarose (Qiagen).

Enzymatic incorporation of OPP-C10-iBr or C10-azide

Enzymatic reaction mixtures (15 mL) contained Tris·HCl (50 mM, pH 7.5), $MgCl_2$ (10 mM), KCl (20 mM), $ZnCl_2$ (100 µM), DTT (5.0 mM), **D1**-CVIA (**D4**-CVIA, GFP-CVIA) (5 µM), OPP-C10-iBr or C10-azide (30 µM), and yPFTase (600 nM). The reaction mixture excluding the isoprenoid analogue and yPFTase was incubated on ice for 0.5 h, followed by addition of the two reagents and incubation for 6 h at 30 °C. The product mixture was then buffer exchanged (x3) into PBS and concentrated to 100 µL using an Amicon Centriprep centrifugation device (10,000 MW cut-off, 15 mL). The product was characterized by LCMS and SDS-PAGE analysis. The subsequent protein

concentration was calculated by BCA assay for the DARPin conjugates and UV absorbance at 488 nm (ε=55,000 $M^{-1} \cdot cm^{-1}$) for the GFP conjugate.

In situ ATRP from the site-specific protein-macroinitiator

$OEGMA_{500}$ monomer (273 µmol) and sacrificial initiator resin (10.5 mg, 2.65 mol) was added to 100 µL of the protein-macroinitiator solution (75 nmol). Az-MA (8.18 - 24.5 µmol) or Rhod-MA (8.18 - 24.5 µmol) was also added to this solution depending on the intended application. To this solution was added 400 µL of a catalyst solution composed of $CuBr_2$ (2.65 µmol) and TPMA (26.5 µmol) in PBS. Polymerization was initiated by adding 50 µL of ascorbic acid (265 nmol) in PBS. All solutions were separately purged with argon for 30 min after formulation. After 6 h of polymerization at rt, the reaction was quenched by exposure to air. The product solution was purified from sacrificial initiator resin using a 0.22 µm centrifugal filter and subjected to anion exchange chromatography (AExC) with a HiTrap Q HP column to remove unreacted monomers from the products. A linear gradient of 2.5% per min from Buffer A (20 mM HEPES, pH 8.0) to Buffer B (20 mM HEPES, 1 M NaCl, pH 8.0) was applied. The fractions containing the D1-polymer conjugates were collected and concentrated using an Amicon Centriprep centrifugation device (10,000 MW cut-off) and subjected to purification and analysis by size exclusion chromatography (SEC) with a Superdex 200 10/300 column (GE Healthcare) with PBS. For samples that require the functionalization with a DBCO reagent, click reaction was employed to the AExC-purified product followed by SEC purification. The FPLC used for chromatography purifications was a Knauer AZURA BioLC device. The collected SEC fractions were concentrated using an Amicon Centriprep centrifugation device (10,000 MW cut-off), which was subjected to 12 or 15% SDS-PAGE for purity analysis and BCA assay for concentration analysis.

Characterization of the grafted polymer

For the characterization of the polymer-component without the protein, size exclusion chromatography analysis was carried out after trypsin digestion of the protein-component following a protocol adapted from Thermo Scientific. Briefly, the protein-polymer conjugate in 50 mM Tris·HCl

(pH 8.0) was incubated with 8 M urea and 5 mM DTT at 37 °C for 1 hour. After adding 15 mM iodoacetamide, the mixture was incubated in the dark at rt for 30 min, followed by dilution with 50 mM Tris·HCl to produce a urea concentration below 2 M, after which 5 µg/µL trypsin and 1 mM $CaCl_2$ were added and incubated overnight. The mixture was concentrated using an Amicon Centriprep centrifugation device (10,000 MW cut-off), purified with a PD-10 column equilibrated with milli-Q water, lyophilized, solubilized in THF, and subjected to a THF-solvent system Wyatt device SEC with a Phenogel 5 µm 10E3A column.

Functionalization of the protein-polymer conjugates via copper-free click chemistry

For protein-polymer species containing clickable azide-functionality in the polymer, payload-conjugation was performed with the AEx-purified mixture by adding a 3-5 fold molar excess of the DBCO-reagent. The reaction was allowed to proceed overnight at 4 °C and was subjected to SEC purification as described above.

Quantification of the incorporated clickable- or dye-monomers

For individual characterization of the protein and fluorophore concentrations of **D1**-POEGMA-TAMRA, absorbance measurements were taken at two different wavelengths. The protein concentration was measured using a standard BCA assay protocol (Thermo Scientific). However, absorbance was measured at 640 nm instead of 565 nm to avoid spectral overlap with TAMRA. The fluorophore concentration was measured similarly using a standard curve that was obtained using rhodamine B solutions of varying concentrations. The absorbance was measured at 475 nm to maximize the range of measurable concentrations. All measurements were performed in a 96-well plate. The volume of solution was 210 µL for BCA assays (200 µL BCA solution and 10 µL protein solution) and 100 µL for fluorophore concentration measurements.

Serum stability of D1-POEGMA

The stability of the ester linkages in **D1**-POEGMA-TAMRA was investigated by serum stability experiments. Mouse plasma (lithium heparin plasma, BioIVT) was filtered through a 0.22 µm

syringe filter. **D1**-POEGMA-TARMA in PBS were then added to the mouse plasma to obtain a final concentration of 1 μM in 50% (v/v) mouse serum and divided into 80 μL aliquots. After 0, 6, 24, and 48 h incubation in a 37 °C water bath, each aliquot was flash-frozen in liquid nitrogen and stored at -20 °C. For SDS-PAGE analysis of the serum-incubated **D1**-POEGMA-TARMA, 12 μL of Ni-NTA resin (Qiagen) in PBS was added to each aliquot after thawing to capture the His_8-tagged **D1**. After incubation for 1 h in the dark at rt, the supernatant was removed by centrifugation and the resin was washed with PBS (x2). For the release of the captured protein, 20 μL of Laemmli buffer containing 1 M imidazole was added to each aliquot and incubated at rt for 10 min and then 95 °C for 10 min. The resulting samples were was then loaded into individual wells of a 15% SDS-PAGE gel and subjected to electrophoresis. In-gel fluorescence analysis was performed using a Typhoon FLA 9500 biomolecular imager.

Preparation of D1-TAMRA

To a solution of **D1**-azide in PBS, 5-fold molar excess of the TAMRA-DBCO was added. The reaction proceeded overnight at 4 °C and was subjected to a series of buffer exchanges using an Amicon Centriprep centrifugation device (10,000 MW cut-off). Product was characterized by SDS-PAGE.

Flow cytometry

The binding affinity of the DARPin-polymer conjugates was characterized by flow cytometry. Briefly, cells (MCF7, HT29, or U87) were grown to ~70% confluency, washed twice with PBS, detached with trypsin, and divided into aliquots of $1x10^5$ cells in PBSA (PBS containing 1 mg/mL BSA). After pelleting via centrifugation and removal of the PBSA, cells were treated with 100 μL of 100 nM DARPin at 4 °C for 45 min, followed by washing with PBSA (x3), and incubation with 25 μL of Alexa Fluor 488-conjugated Anti-6x-His Tag Monoclonal Antibody (Invitrogen, MA121315A488, 1:500) in PBSA for 45 min at 4 or 37 °C. Cells were quantified using a BD Fortessa X-30 H0081 flow cytometer, and data analysis was performed with FlowJo software (v10).

Confocal microscopy

Cell binding and internalization of DARPin-polymer conjugates were characterized by confocal microscopy. Briefly, $1x10^4$ cells (MCF7, HT29, or U87) were transferred to a glass-bottom dish (35 mm) and incubated overnight at 37 °C 5% CO_2 to allow for adhesion. After decanting the DMEM media, cells were washed with DPBS (x3) and incubated with 200 µL of 100 nM DARPin for 1 h at 4 °C. The cells were then washed with DPBS (x3) and subjected to a secondary incubation with 200 µL of Alexa Fluor 488-conjugated Anti-6x-His Tag Monoclonal Antibody (Invitrogen, MA121315A488, 1:500) in PBS for 45 min at 4 or 37 °C. After washing with DPBS (x3), cells were stained with 500 µL of 0.5 µg/mL Hoechst dye for 10 min at rt, washed with DPBS (x3), and fixed with 500 µL of 4% paraformaldehyde for 15 min at rt. After washing with DPBS (x3), cells were imaged with a Nikon A1Rsi Confocal microscope with SIM Super Resolution. Data analysis was performed with Image J software.

In vitro toxicity of DARPin-POEGMA-MMAE constructs

An XTT-assay was utilized to assess the toxicity of D1-POEGMA-MMAE against three cell lines, HT29, MCF7, and U87. Briefly, 2,000 cells in 50 µL DMEM media were aliquoted into each well of a 96-well plate and incubated for 24 h in the 37 °C 5% CO_2 incubator. After decanting the media, 50 µL of media containing serial dilutions of **D1**-POEGMA-MMAE was added and incubated for 96 h. The media was decanted once again followed by addition of 50 µL XTT reagent. Absorbance was measured at 480 nm and 650 nm (reference wavelength) after 1, 2, and 3 h incubation. Data was analyzed in Excel and plotted using the software Prism.

2.3 Results and Discussion

yPFTase-mediated site-specific installation of the initiator moiety

Ac2 and E3_5 DARPin constructs[146] that contain an N-terminal His_8-tag and a C-terminal CVIA-tag were expressed in *E. coli* and purified using an IMAC column. Both the EpCAM-binding Ac2-CVIA construct (**D1**-CVIA) and the negative control E3_5 construct (**D4**-CVIA) were obtained with high yield (>10 mg/L of liquid culture). The OPP-C10-Br isoprenoid analog that contains the ATRP-initiator moiety was prepared from geraniol through a six-step synthesis. A side product to

OPP-C10-Br was also produced via elimination of the bromide which is denoted as OPP-C10-Acr. The two products were separable by HPLC. This work only focused on utilizing OPP-C10-Br for in situ polymerization from DARPins, and it was later found that the yield of OPP-C10-Br could be improved by utilizing a THP protecting group instead of the TBDMS, as the elimination of the bromide occurs during the TBDMS deprotecting step. However, it should be noted that OPP-C10-Acr is a potentially valuable isoprenoid analog that has potential for related applications. For instance, one could envision a grafting-through preparation of protein-polymer conjugates with acrylate-labeled proteins that behave as a macromonomer, and hence becomes incorporated into the polymer chain via copolymerization with other synthetic monomers.

Farnesylation of **D1**- and GFP-CVIA with OPP-C10-Br was assessed by LCMS. Analysis of the **D1** and GFP reaction solution by LCMS showed high product conversion to the **D1**-Br and GFP-Br (>90% for both), indicated by the near-complete shift of the starting material peak (28159 and 19359 Da, respectively) to the product peak (28461 and 19660 Da, respectively) which exhibits a higher retention time. Deconvolution of the product peak revealed a mass increase consistent with the addition of a single isoprenoid derived from OPP-C10-Br, indicating site-specific and stoichiometric labeling of the C-terminal cysteine residue (Fig. S2.1). While a peak at a retention time that corresponds to the unmodified CVIA-protein was observed, the intensity was much lower than the product peak and was insufficient for deconvolution, which overall indicated that the amount of starting material was quite small (<10% of product) and that farnesylation with OPP-C10-Br was highly efficient. Control experiments lacking the yPFTase or OPP-C10-Br in the reaction mixture did not show any prenylated protein, indicating that the product conversion was indeed formed an enzymatic reaction (data not shown).

Exploiting the stability of DARPins, farnesylation conditions were adjusted to higher protein concentrations to maximize the material obtainable per reaction batch. While previous studies had set the target protein concentration to 2.4 μM, **D1**-CVIA could be farnesylated at concentrations up to 10 μM. The OPP-C10-Br and yPFTase concentrations were changed accordingly to 40 μM and 600 nM, respectively. Although some protein precipitation was observed,

the highly concentrated protein solutions required a lesser number of post-prenylation buffer exchanges, making this the preferred method.

In situ ATRP and click chemistry for functionalized D1-POEGMA conjugates

Grafting-from polymerization was performed in PBS based on an AGET-ATRP protocol adopted from Maynard and coworkers.[135] Briefly, the DARPin-macroinitiator was subjected to polymerization with sacrificial initiator resin which was included to facilitate the reaction by increasing the effective initiator concentration.[132] The resulting DARPin-POEGMA conjugates were found to be stable and soluble after the polymerization reactions consistent with the mild reaction conditions employed for AGET ATRP. The resin was easily removed post-reaction by simple filtration. In these reactions, copolymerization with various monomers was performed where the monomer type and composition were varied based on the desired product characteristics. The main component of the monomer mixture was oligoethylene glycol methacrylate ($OEGMA_{500}$, POEGMA once polymerized), a commercial PEG-branched monomer that has been shown to enhance the pharmacokinetics of the protein-polymer conjugates.[136,140] For DARPin-POEGMA conjugates purposed for fluorescence imaging studies, a TAMRA-fluorophore was incorporated into the polymer using two different methods. The first employed direct incorporation by copolymerization with a rhodamine-methacrylate monomer. The other method required a two-step procedure where the polymer was first functionalized with azides through copolymerization with an azide-methacrylate monomer, followed by labeling with a TAMRA via copper-free click chemistry with a TAMRA-DBCO reagent. While the former method was simpler, it required custom-developed monomers for alternative applications due to the lack of methacrylate-functionalized payloads available in the market. In contrast, installing an azide within the polymer, capitalized on the various DBCO-containing reagents that are commercially available including fluorophore, toxins, and ligands for metal-mediated PET imaging. [52] Work with the fluorescent polymers for cellular imaging is presented below with additional examples using toxins and metal chelators in subsequent sections.

DARPin-POEMGA products were purified and analyzed using a combination of anion exchange chromatography (AExC) and size exclusion chromatography (SEC). Peaks that shifted to a shorter retention time in SEC and bands that appear in the higher molecular weight region in SDS-PAGE both indicated successful polymerization (Fig. 2.2B and 2.2C). As reported in prior studies, macromolecular species unrelated to the DARPin were observed in addition to the DARPin-POEMGA product, which were suspected to be a result of uncontrolled polymerization from monomers in the reaction solution or polymers cleaved from the sacrificial resin.[135] The formation of these impurities could not be prevented even after adding excess ligand to stabilize the copper catalyst. Nonetheless, the quantity of these macromolecules was relatively low compared with the protein-polymer product and could be efficiently separated from the product by AExC purification.

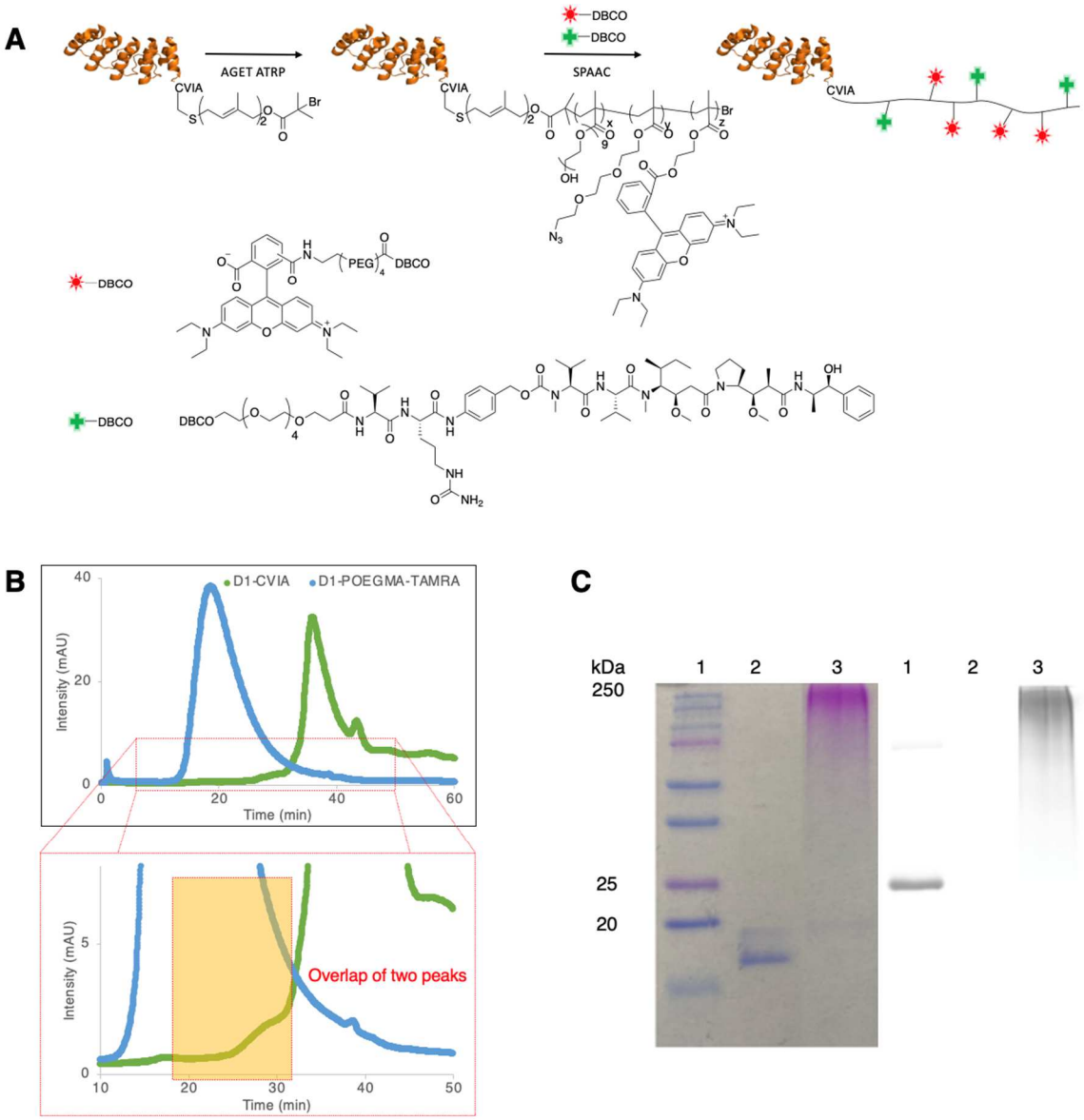

Figure 2.2 In situ ATRP from **D1**-Br. (A) Schematic of the AGET ATRP reaction from **D1**-Br that yields site-specific **D1**-POEGMA (x : y : z = 70 : 0-3 : 0-3). (B) SEC trace of **D1**-CVIA and **D1**-POEGMA. The zoom-in region shows the overlap between the **D1**-monomer and **D1**-polymer which is presumed to be causing incomplete separation of the two macromolecular species. (C) SDS-PAGE of **D1**-CVIA and **D1**-POEGMA (lane 1, protein ladder; lane 2, **D1**-CVIA; lane 3, **D1**-POEGMA). The left shows a Coomassie stained gel, and the right shows a fluorescence-scanned image of the identical gel before Coomassie staining.

Despite the subjection to a series of anion exchange and size exclusion column chromatographies, some residual **D1**-monomer species was found to be present in the **D1**-POEMGA solution, indicated by the band near the 20 kDa region observed in SDS-PAGE analysis (Fig. 2.2C). This was found to be due to the distinctive SEC elution pattern of **D1**-monomers (Fig. 2.2B, Fig. S2.2). Instead of eluting as a sharp peak in the SEC analysis, **D1**-CVIA eluted over a broad range of retention volume that overlaps with **D1**-POEGMA, causing insufficient separation of the two species (Fig. 2.2B, Fig. S2.2). Use of reducing agents in the buffer did not narrow the **D1**-CVIA peak in the SEC, indicating that the broad peak is not due to the protein dimerization of **D1** but rather a characteristic of the protein itself, perhaps due to some interaction with the column material. SDS-PAGE of **D1**-POEGMA performed without reduction or heating prior to loading did not intensify the **D1**-monomer band, demonstrating that the cleavage of the protein-polymer linkage is unlikely a contributing factor to the issue with **D1**-monomer impurities (data not shown). Nonetheless, as both the farnesylation and ATRP initiation efficiency was high, the purity of the DARPin-POEGMA over DARPin-monomers was shown to be over 80%.

To assess the physical properties of the POEGMA component, SEC analysis was performed on **D1**-POEGMA after trypsin digestion of the **D1**. The results revealed a highly converted product with low dispersity (Mn = 35.1 kDa, D = 1.27), which was especially noteworthy as the reaction time was much shorter compared with then previous reports.[135] We hypothesized that this high ATRP efficiency results from having the initiation-site located at the easily assessable C-terminus of **D1**-Br, suggesting the advantages of exploiting protein prenylation for in situ polymer conjugation reactions.

D1-POEGMA polymer, copolymerized with the azide- or rhodamine-monomer (**D1**-POEGMA-Azide or **D1**-POEGMA-Rhodamine) were subjected to an spectrophotometric analysis to quantify the number of incorporated functionalized monomers per one **D1**-POEGMA.[147] First, the protein concentration was quantified by performing a BCA assay evaluated at 640 nm (Fig. 2.3). The azide (following the conjugation of TAMRA-DBCO) or rhodamine concentration was quantified by measuring the absorbance at 475 nm (Fig. 2.3). The two wavelengths were selected to minimize spectral overlap. Dividing the fluorophore concentration by the protein concentration yielded the

ratio of functionalized monomers per **D1** in the **D1**-polymer conjugate. This ratio could be easily tuned by altering the monomer concentrations in the polymerization reaction solution, and a correlation was observed between the composition of the monomer mixture and the polymer product. This was presumably due to the similar reactivity ratios between the monomers as they all contain the same unhindered alkene.

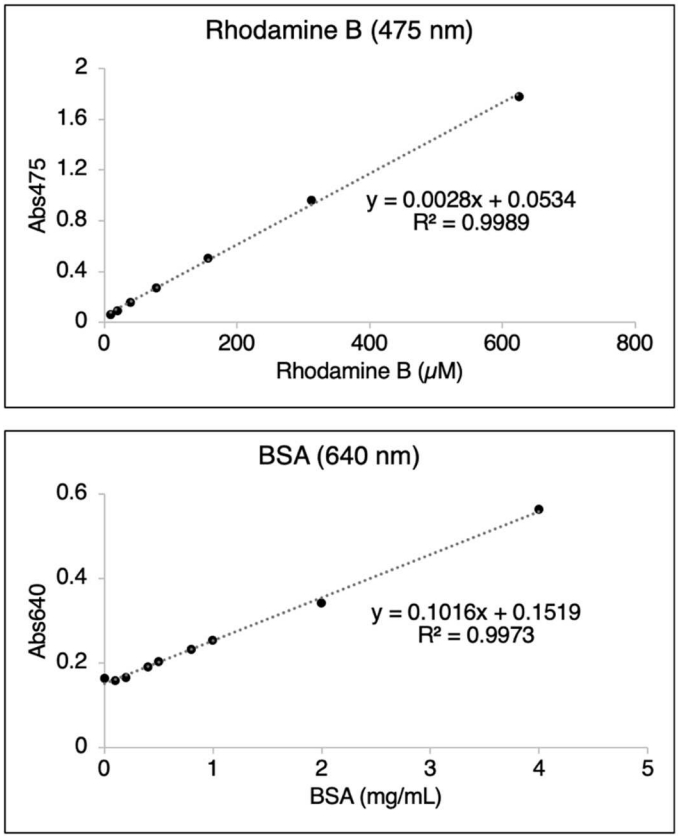

Figure 2.3 Working curves for the calculation of **D1** and TAMRA concentrations, and hence the **D1** to TAMRA ratio in **D1**-POEGMA-TAMRA. (A) Absorbance at 475 nm for various rhodamine B solutions with varying concentrations. (B) Absorbance at 640 nm for various BSA solutions after incubation in BCA solutions.

Having the protein-vehicle carry multiple payloads is an important feature in the ADC field as it allows maximization of the therapeutic effect. For instance, antibodies carrying multiple fluorophores allows enhanced signals in tumor imaging studies[147,148] and multiple toxins allow increased tumor-specific toxicity.[149–152] However, attaining this high cargo : protein ratio is currently

a difficult challenge with ADCs since the hydrophobicity of the payload often causes protein instability or aggregation.[153,154] Therefore, it was noteworthy that a high number of functionalized monomers per **D1** could be achieved without negatively affecting the stability of **D1**. While 3 fluorophores per **D1** was achieved, we are currently in the process of increasing the loading of the payload even further. In later sections, we show that **D1**-POEGMA can be functionalized with up to 3 MMAE toxins which is well known for its effectiveness against tumors but manifest limitations due to its hydrophobicity.[155] We hypothesize that the high loading capacity obtained here was enabled by conjugating the payloads to the POEGMA instead of directly to the DARPin. The hydrophilicity of the polymer may mask the hydrophobicity of the payloads, and the distance introduced between the payload and DARPin may reduce the interaction of the two, both serving to minimize protein destabilization. We also anticipated that the high loading of cargo could result in enhanced therapeutic efficacy, which is discussed in later sections of this paper.

Serum stability

Previous studies have shown that ester bonds can be susceptible to carboxylesterase-mediated hydrolysis under physiological conditions, which could lead to undesired loss of the payload and hence non-target toxicity for ADCs carrying an ester-linkage.[156] This effect was shown to be much more apparent in mouse serum or mouse animals due to the higher carboxylesterase activity that is present in mice compared to human.[156] Prior research from Distefano and coworkers conducted with a payload conjugated **D1** has also shown that the ester-linkage bridging the two molecules is susceptible to hydrolysis in mouse serum, and that could be a source of non-specific toxicity in EpCAM-negative cell lines.[157] As the protein-polymer conjugates reported here contained multiple esters, between the protein and polymer and between the polymer backbone and side branches, the serum stability of **D1**-POEGMA-TAMRA was assessed. We hypothesized that the steric hindrance of the branched-POEGMA may protect the ester-linkages from enzymatic hydrolysis. Indeed, even after 48 h in mouse serum, the ester-linkage connecting **D1** to POEGMA was found to be stable. The **D1**-monomer band in SDS-PAGE remained unchanged throughout the 48 h incubation, indicating that POEGMA remained linked to **D1** (Fig. 2.4). The ester bonds linking

the TAMRA fluorophores to the backbone of POEGMA was also found to be stable in mouse serum evidenced by the consistent fluorescence signals of the **D1**-POEGMA-TAMRA band in SDS-PAGE across all time points. The stability of the ester-bonds in the polymer side branches suggested that other payloads including toxins would remain stably bound to **D1**-POEGMA as well, and that the toxin loaded **D1**-POEGMA conjugates would be capable of targeted drug delivery without exhibiting non-specific toxicity due to the loss of the toxin.

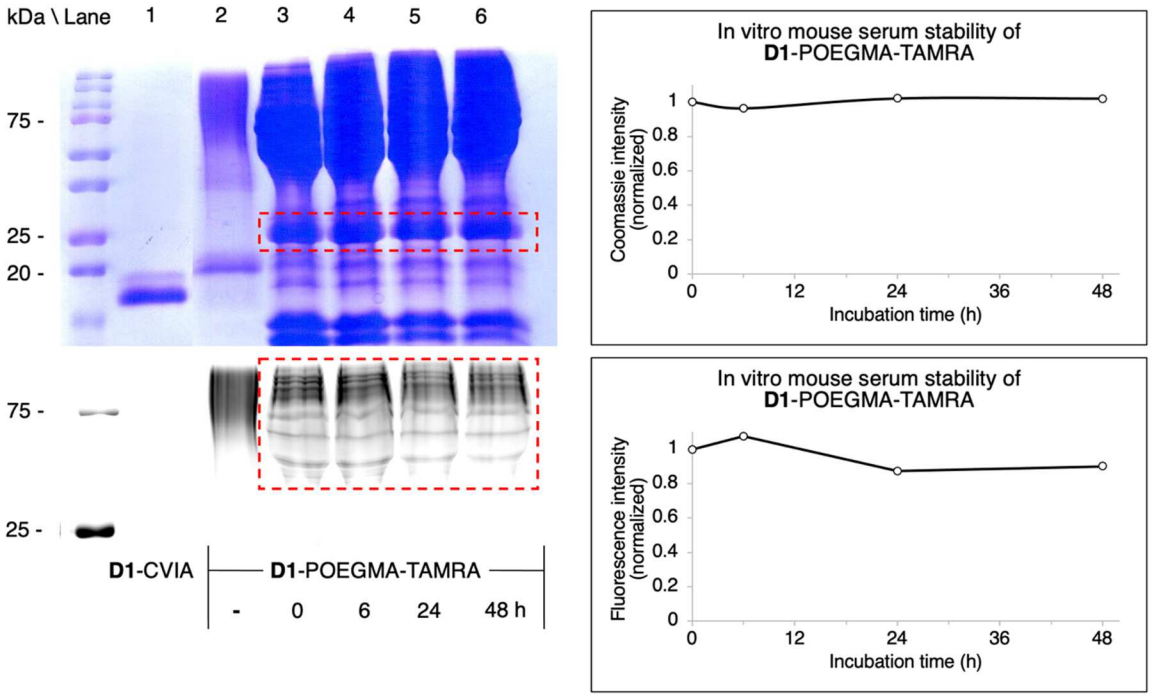

Figure 2.4 Stability of **D1**-POEGMA-TAMRA in mouse serum. Incubation of the DARPin-polymer conjugate up to 48 h did not result in increased intensity of the band near 20 kDa which corresponds to the DARPin-monomer, indicating that the ester-linkage connecting the two macromolecules remain intact. TAMRA-signals remained constant as well which indicated that the esters connecting the fluorophore to POEGMA remained uncleaved.

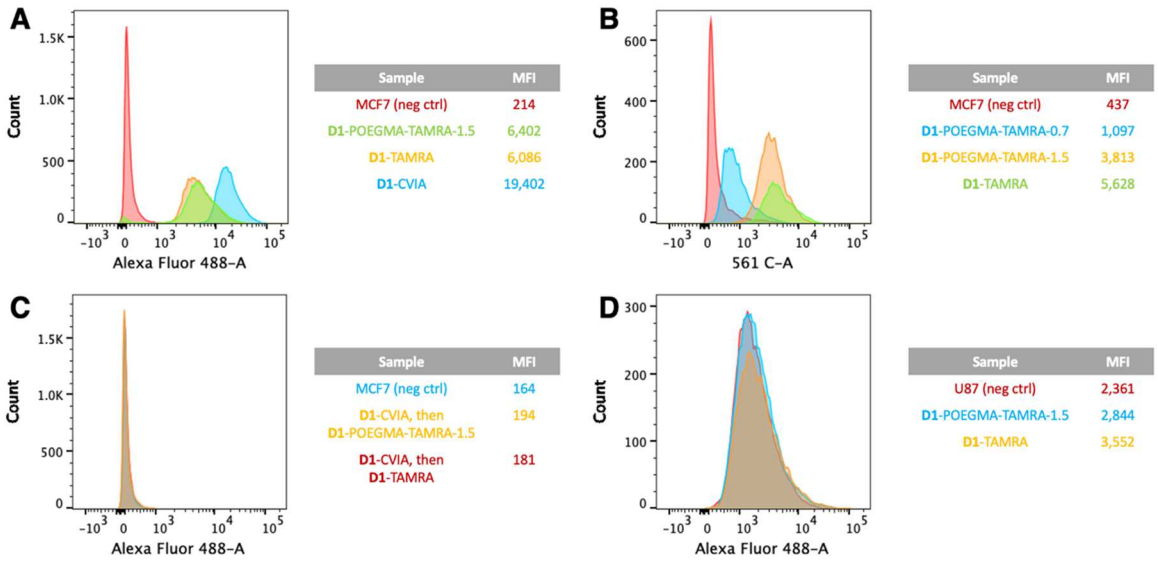

Figure 2.5 Flow cytometry analysis of EpCAM-selective cell surface binding of **D1**-POEGMA-TAMRA. A) MCF7 cells monitored by AlexaFluor-488 channels after treatment with **D1**- conjugates. **D1**-POEGMA-TAMRA shows exhibit similar binding to MCF7 cells compared with the non-polymer conjugated **D1**-TAMRA. B) MCF7 cells monitored by TAMRA channels after treatment with **D1**-conjugates. Increasing fluorophore-loading in **D1**-POEGMA-TAMRA results in higher MFI. C) Competition studies with MCF7 cells. Blocking cell surface EpCAMs with **D1**-CVIA before incubating the cells with **D1**-conjugates nullifies their cell binding activity. D) U87 cells monitored by AlexaFluor-488 channels following treatment with **D1**-conjugates. Due to the low expression of EpCAM in U87 cells, cell-binding activity of **D1**-conjugates are not observed. MFI: Mean fluorescence intensity.

High retention of cell binding affinity of D1-POEGMA

Macromolecule-conjugated antibodies often manifest diminished affinity towards their epitopes. One of the main factors that contribute towards this reduced activity is the polymer-induced steric hindrance that interferes with the antibody-antigen interaction.[144,158,159] This detrimental effect becomes even more exacerbated when the conjugation occurs non-specifically near or directly on the variable region of the antibody that is crucial for antigen-recognition.[160,161] As the DARPin-polymer conjugates described contain branched polymers that have been reported

to minimize activity loss of the modified protein,[162] their ability to bind to cells expressing cell surface cancer markers was investigated. For this, flow cytometry assessment of **D1**-POEGMA-TAMRA was performed (Fig. 2.5). The EpCAM-specific binding affinity of **D1**-POEGMA-TAMRA was explored with MCF7 cells serving as an EpCAM positive cell line[163,164] and U87 as a negative control (low EpCAM expression).[164] Cell-binding was analyzed using two fluorescence channels. One channel detected the fluorescence emitted from TAMRA that is conjugated to POEGMA, and the other detected AlexaFluor-488 signals emitted from anti-His-AlexaFluor-488 antibodies bound to the His_8-tag of **D1** through a secondary antibody staining protocol. The former was monitored to evaluate whether multiple fluorophores can enhance EpCAM detection through signal amplification, and the latter was utilized to assess the binding affinity of site-specifically modified **D1**.

D1-POEGMA-TAMRA was found to bind effectively to EpCAM-expressing MCF7 cells. Two different D1-POEGMA-TAMRA conjugates were assessed, one that carries 0.7 TAMRA per **D1** and one that carries 1.5. For convenience, the number of payloads will be further denoted by adding the number at the end of the name of the conjugate. Cells analyzed by flow cytometry in the presence of **D1**-POEGMA-TAMRA-1.5 gave a mean AlexaFluor-488 fluorescence of 6,402 compared to the cells alone that yielded a mean fluorescence of 214 (Fig. 2.5A). Its binding activity could be completely nullified by preincubating the MCF7 cells with **D1**-CVIA lacking the TAMRA fluorophore (Fig. 2.5C). In that case, a mean AlexaFluor-488 fluorescence of 194 was observed. Binding to EpCAM-negative U87 cells was not observed; the mean fluorescence of U87 cells was 2,844 in the presence of **D1**-POEGMA-TAMRA and 2,361 it its absence, respectively (Fig. 2.5D). These results suggests that the binding affinity of **D1**-POEGMA-TAMRA was indeed specific for EpCAM. Both TAMRA and AlexaFluor-488 fluorescent signals were observed together via flow cytometry analysis with MCF7 cells treated with **D1**-POEGMA-TAMRA, indicating that the labeling of cells with TAMRA is caused by the **D1**-targeting moiety. Most importantly, the EpCAM-specific binding affinity of **D1** was well preserved despite being conjugated to a macromolecule. **D1**-TAMRA prepared by farnesylation of a single azide followed by copper-free click reaction with a TAMRA-DBCO, which is denoted as **D1**-TAMRA, exhibited similar AlexaFluor-488 signal intensities with **D1**-POEGMA-TAMRA when incubated with MCF7 (MFI = 6,086 for **D1**-TAMRA vs. 6,402 **D1**-

POEGMA-TAMRA-1.5). The similar binding affinities regardless of the presence of POEGMA suggests that there is no significant loss of binding activity upon polymerization and that steric hindrance is a complicating factor. We hypothesize that this is a result of the site of polymer-conjugation being located at the C-terminus of **D1**. There, the covalent modification should have minimal effect on three internal repeat units of **D1** that comprises the antigen binding domain since they are remote from the C-terminal capping repeat motif whose purpose is to shield the core to enhance protein stability and increase overall molecular mass. The branched rod-shaped morphology of POEGMA is expected to point away from the protein rather than encapsulating it as a linear PEG would do, which may also have a positive effect in maintaining the binding activity of **D1**. We do note that despite the site-specific nature of the farnesylation-induced protein modification, there is some loss in activity of the **D1**-conjugates compared to **D1**-CVIA (MFI = 6,402 for **D1**-POEGMA-TAMRA-1.5 vs. 19,402 for **D1**-CVIA), which we assume is an inevitable cost for proteins undergoing covalent modifications.

The advantage of incorporating payloads through the backbone of the hydrophilic polymer of **D1**-POEGMA could be readily observed by flow cytometry. **D1**-POEGMA-TAMRA carrying a higher number of dyes displayed higher TAMRA fluorescence signals (MFI = 1,097 for **D1**-POEGMA-TAMRA-0.7 vs. 3,813 for **D1**-POEGMA-TAMRA-1.5) (Fig. 2.5.B). We hypothesize that even higher fluorescence signals would be obtainable by increasing the number of fluorophores even further. In such case, while there may be some loss in activity due to the covalent protein-modification, the overall efficacy of DARPins can be compensated by the unique advantage of carrying payloads.

Tumor cell targeted imaging

The EpCAM-specific binding activity of the DARPin-polymer conjugates was also evaluated via confocal imaging. Briefly, the **D1**-POEGMA-TAMRA and **D4**-POEGMA-TAMRA were each incubated with MCF7 and U87 cells, followed by washing and incubation with anti-His_6-AlexaFluor-488 antibodies. The binding experiments were conducted at both 4 and 37 °C (Fig. 2.6). Fluorescent signals were only observed for the **D1**-POEGMA-TAMRA treated EpCAM-positive

MCF7 cells. The absence of signals in U87 cells indicated that the conjugated POEGMA does not induce non-specific binding (data not shown); furthermore, the imaging results indicate that **D1**-POEGMA-TAMRA retained its specificity towards EpCAM after conjugation with a polymer. Those results are consistent with the flow cytometry data noted above. **D1**-POEGMA-TAMRA was observed to be bound to the surface of MCF7 cells when incubated at 4 °C and internalized when the temperature was raised to 37 °C. Cell entry at elevated temperatures is consistent with receptor-mediated endocytosis of **D1** by EpCAM. The TAMRA (linked to the POEMGA) and AlexaFluor-488 (bound to **D1**) signals on the cell surface were found to colocalize, indicating that the delivery of the fluorescent payload is facilitated by the **D1** protein, and that the ester-linkages within on the protein-polymer conjugate are stable under physiological conditions.

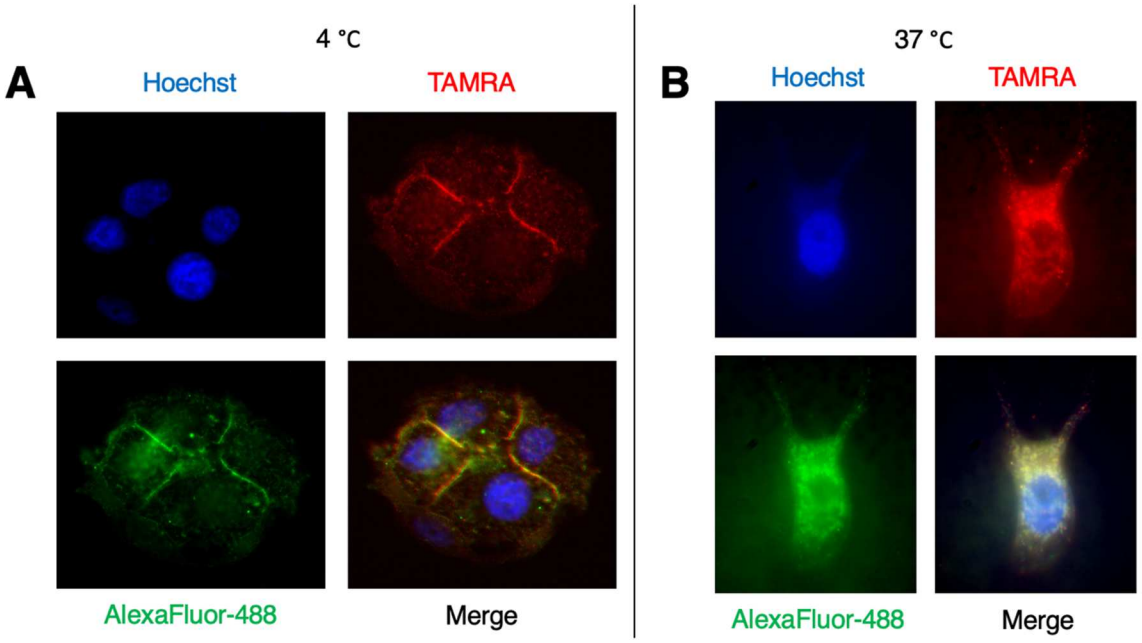

Figure 2.6 Confocal imaging of the EpCAM-specific binding of **D1**-POEGMA-TAMRA on MCF7 cells. (A) At 4 °C, D1-POEGMA-TAMRA bind to the cell surface, and (B) at elevated temperatures of 37 °C they undergo receptor-mediated endocytosis. Colocalization of the TAMRA and AlexaFluor-488 signals indicate that the fluorescent payload is delivered to cells by the **D1**-binding activity to EpCAM.

Tumor cell targeted drug delivery

To target tumor cells, **D1**-POEGMA was functionalized with multiple cytotoxic drug molecules utilizing the same synthetic strategy that was employed for fluorophore-conjugation. The toxin chosen was a commercially available DBCO-labeled monomethyl auristatin E (MMAE) derivative that incorporates a valine-citrulline-*p*-aminocarbamate (vc-PABC) linker that allows intracellular release of the payload in its unmodified form.[165] For convenience, the toxin will be further denoted as MMAE-DBCO. The number of MMAEs per **D1** could not be directly quantified due to technical limitations. However, a prior study had demonstrated that MMAE-DBCO is efficiently conjugated to azide-labeled proteins even at low concentrations.[157] Therefore, we assumed that the amount of MMAE per **D1** would be most likely the same as the number of TAMRA per **D1**. It was worth noting that low concentrations (2 eq to the azide) were adapted not by choice, but due to the extremely low water-solubility of MMAE-DBCO, which caused precipitation of the reagent when conditions identical to TAMRA-DBCO labeling (5 eq) were used. This demonstrated the high hydrophobicity of MMAE and indicated how it becomes a major challenge in achieving high DAR.[166] Despite labeling of multiple MMAEs, **D1**-POEGMA-MMAE was impressively stable in solution without precipitation, demonstrating the advantage of linking multiple hydrophobic payloads through the hydrophilic polymer.

Targeted toxicity of **D1**-POEGMA-MMAEs (carrying 1 or 3 MMAEs per **D1**) were evaluated via cell-based studies using an XTT assay that detects the presence of live cells (Fig. 2.7). Three cell lines were evaluated. HT29 cells were added here to serve as a cell line that exhibits higher EpCAM-expression levels compared with MCF7 cells. U87 cells were employed as an EpCAM-negative control. As expected, the level of toxicity showed a correlation with EpCAM-expression levels. **D1**-POEGMA-MMAE-3 exhibited the highest toxicity for HT29 cells (IC_{50} = 6.16) and the lowest for U87 cells (IC_{50} = 116). Higher toxicity (lower IC_{50}) was also observed with increasing number of MMAEs per **D1**-POEGMA (in HT29 cells, IC_{50} = 6.16 vs. 28.2 for **D1**-POEGMA-MMAE-3 and **D1**-POEGMA-MMAE-1, respectively), demonstrating the advantage of increasing the DAR for ADCs and related molecules. **D1**-POEGMA-MMAE-1 was shown to exhibit low IC_{50} values in the nanomolar range for both EpCAM-positive cell lines, demonstrating its therapeutic efficacy.

However, its toxicity was less effective than that of MMAE-DBCO itself or the **D1**-MMAE (non-polymer conjugate) from previous studies.[157] This may result from the effect of the conjugated POEGMA, which in addition to reducing the EpCAM-binding affinity, causes impaired internalization of **D1**.[167] However, what was important was how increasing the DAR from one to three in **D1**-POEGMA-MMAE was able to reduce the IC_{50} to single digit nanomolar concentrations, resulting in potency that is comparable to the non-polymer conjugated **D1**-MMAE. Thus, similar to other polymer-conjugated ADCs, we expect that the conjugated POEGMA would add another advantage in animal systems, elongated circulation, which would more than compensate for the loss of binding affinity and result in an overall positive effect.[144,167]

The EpCAM selectivity of **D1**-POEGMA-MMAE was demonstrated, indicated by the difference in IC_{50} values between HT29 and U87 (6.16 vs. 116 for **D1**-POEGMA-MMAE-3).The IC_{50} of U87 was below of that of MMAE-DBCO (31.0), indicating that the **D1** conjugation plays a key role in preventing non-selective internalization of the toxins. However, it was notable how **D1**-POEGMA-MMAE was still exhibited some level of toxicity even for the negative control U87 cells. Interestingly, the IC_{50} values did not change upon the number of MMAE per **D1** (IC_{50} = 114 and 116 for **D1**-POEGMA-1 and **D1**-POEGMA-3, respectively) as opposed to how it correlated with the level of toxicity in EpCAM-positive cells. This suggests that the source of toxicity in U87 cells could be due to something other than the **D1**-mediated delivery of MMAE. At this point, we presume that free-unconjugated MMAE that has been hydrolytically cleaved from POEGMA is what is causing off-target toxicity, leading to elevated potency in U87 cells. While it was confirmed that the ester bonds located in the side branches of POEMGA were stable, we hypothesize that once the MMAE-DBCO, which itself contains a lengthy $(PEG)_4$-vc-PAB linker, is conjugated to the azide moieties on POEGMA, the length of that side-branch may extend enough to expose the vc-PAB linker to enzymes present in the environment. Although the vc-PAB linker was originally developed to selectively release payloads only inside tumor cells due to the effect of cathepsin B enzymes that are upregulated in tumor cells,[168] several recent studies have reported that the linker can be cleaved by other biological entities including carboxylesterase 1C[169] or other types of cysteine cathepsins.[170] Studies have also indicated that some types of cancer cells that include U87 cells

secrete proteolytic enzymes such as cathepsins in the surrounding media, resulting in extracellular proteolytic activity against ADCs that contain vc-PAB linkages.[171] In an actual tumor environment in a living organism, extracellular release of the payload could be a beneficial bystander effect which would contribute towards combating not only antigen-positive but also antigen-negative cancer cells in a heterogeneous tumor population.[171] Despite loss of payload during plasma circulation, in vivo tolerance would be high as the release would occur only at the vicinity of tumors.[172] The wide use of the FDA approved ADCs that utilize the MMAE-vc-PAB warhead[173] also indicates that the overall efficacy using the cleavable linker prevails over its negative effects. Therefore, we believe the limited in vitro selectivity results we show are an artifact from selecting an inappropriate negative control U87 together with the enzymatic degradability of the vc-PAB linker. In the near future, we aim to perform alternative studies that could properly demonstrate the EpCAM-selective toxicity of **D1**-POEGMA-MMAE. Some options would be trying other EpCAM-negative cell lines such as HEK293T or RL cells that may not secrete proteolytic enzymes and was confirmed a suitable EpCAM negative cell line in prior studies,[144] adding **D4**-POEGMA-MMAE as the negative control DARPin, or using a **D1**-POEGMA-MMAE in which the MMAE-linker does not contain the vc-PAB moiety.

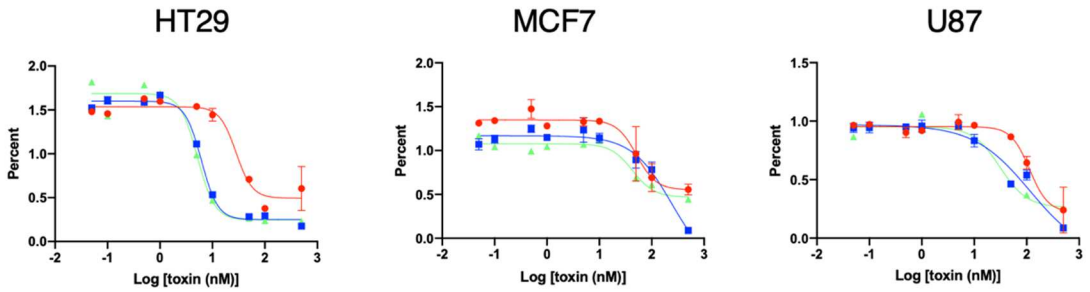

Cell \ IC_{50}	D1-POEGMA-MMAE-1	D1-POEGMA-MMAE-3	DBCO-MMAE
HT29	28.2	6.16	5.16
MCF7	51.2	240	43.0
U87	114	116	31.0

Figure 2.7 EpCAM-targeted cytotoxicity of **D1**-POEGMA-MMAE. The cytotoxicity against EpCAM-positive HT29 and MCF7, and EpCAM negative U87 were determined by XTT assays. Three toxins were compared, **D1**-POEGMA carrying 1 (green) or 3 (red) MMAEs, and DBCO-MMAE (blue).

Toxin	**D1**-POEGMA-MMAE-3	DBCO-MMAE
$IC_{50,U87}$ / $IC_{50,HT29}$	18.8	6.00

Table 2.1 Selectivity ratios of cytotoxicity. The IC_{50} of the toxins in U87 were divided by the IC_{50} in HT29 cells to demonstrate the capability of **D1** to selectively deliver toxins to EpCAM positive tumor cells.

Radiolabeled D1-POEGMA for in vivo imaging

To use the above strategy for in vivo imaging applications via positron emission tomography (PET) imaging, some modification to the above design were made. For PET imaging, the focus was to decrease the molecular weight to shorten the circulation time in the system. While this may seem counterintuitive since targeted cancer therapies with antibodies often favor using elongated polymers for enhanced pharmacokinetics, procedures for PET imaging are typically different. Due to the high sensitivity of the PET reagents, it was preferable that the imaging reagent-conjugates clear from the bloodstream quickly to decrease background and improve contrast. Therefore, we aimed to reduce the molecular weight of POEMGA by replacing the $OEGMA_{500}$ monomer with $OEGMA_{200}$. It was deemed that simply changing the length of the side branch would be easier than readjusting the polymerization conditions such as the monomer concentration or reaction time to achieve polymers with lower molecular mass.

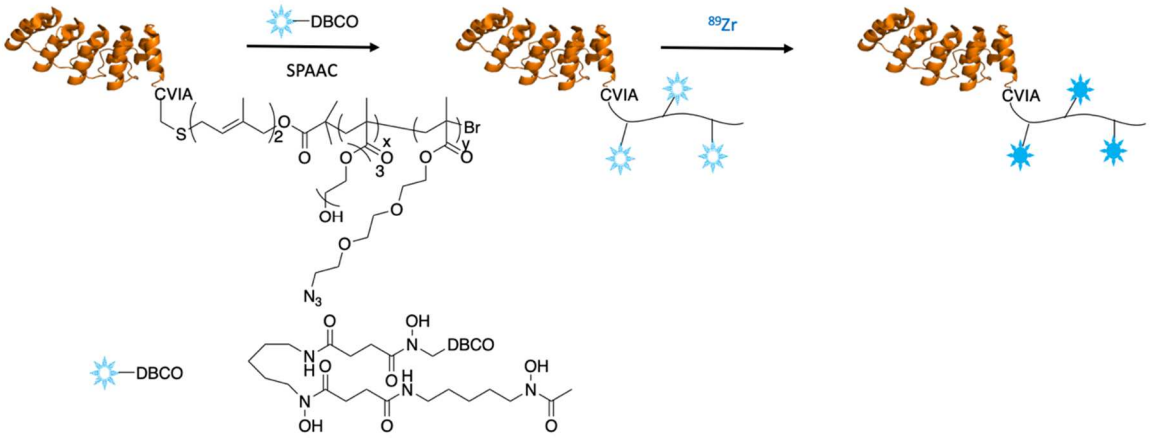

Figure 2.8 Preparation of **D1**-POEGMA-DFO for in vivo tumor PET imaging. AGET-ATRP from **D1**-Br with $OEGMA_{200}$ and Az-MA followed by SPAAC with DFO-DBCO yields **D1**-POEGMA-DFO (x : y = 100 : 0-9). Subsequent incubation with ^{89}Zr renders the radionuclide to bind to the DFO-chelator, hence allowing the DARPin-polymer conjugate to be used for PET imaging.

Polymerization with $OEGMA_{200}$ was shown to be successful as indicated by SEC analysis (Fig. S2.3). Trypsin digestion of **D1** and subsequent analysis of the liberated polymer showed a molecular weight (Mn = 12.8 kDa, D = 1.28) that was 35% of the polymer produced with $OEGMA_{500}$ (Mn = 35.1 kDa, D = 1.27). As the percent-reduction of molecular weight indicated that the degree of polymerization (DP) between POEGMA from $OEGMA_{500}$ and $OEGMA_{200}$ were nearly identical, it was assumed that the number of incorporated Az-MA per **D1** should be similar as well. Interestingly, that was not the case, and it was shown that the number of azides incorporated in POEGMA is reduced to nearly half. In other words, the comonomer mixture with $OEGMA_{500}$ that yielded 4 azides per **D1** was only resulting in 2 azides per **D1** when $OEGMA_{200}$ was used instead. Nonetheless, the number of incorporated azides in POEGMA showed a correlation with the concentration of the starting mixture, and therefore the desired azide to **D1** ratio could be achieved by increasing the Az-MA concentration in the comonomer mixture.

Following the characterization of **D1**-POEGMA-Azide synthesized with $OEGMA_{200}$, the azides were further conjugated with DFO-chelators by SPAAC with DFO-DBCO. DFO was chosen as it is a well-known chelator of ^{89}Zr that is widely used for radiolabeling antibodies for PET

imaging[174]. The labeled samples are currently being characterized by flow cytometry to confirm that **D1** maintained its binding activity post-functionalization. Afterward, the radiolabeled **D1**-POEGMA will be administered to mice bearing an EpCAM-positive tumor for subsequent tumor analysis.

2.4 Conclusion

Site-specific DARPin-polymer conjugates were synthesized via enzymatic labeling and in situ polymerization methods. The resulting polymers could be easily customized with various functionalities by adjusting the composition of the copolymerization reaction solution. Two applications with these protein-polymer conjugates were pursued in this study including tumor selective imaging and toxicity. By having the hydrophilic polymer that is conjugated to the protein carry the fluorophore and toxins rather than directly conjugating the payloads to the protein itself, increased loading capacity of the payload could be achieved. For instance, three molecules of MMAE toxins known for its hydrophobicity could be loaded onto a single **D1**. Currently we are in the process of aiming for an even higher number. Having multiple fluorophores per **D1** increased the tumor detecting abilities of DARPins, and increased toxin loading per **D1** enhanced its tumor specific in vitro toxicity to levels similar to the non-polymer conjugated **D1**-MMAE. This was an especially noteworthy performance as conjugating polymers to antibodies are known to adversely affect the toxicity in cell-based studies as the added polymer frequently impedes the ability of the protein to bind to cell surface receptors and undergo endocytosis. Tumor targeted PET imaging of a tumor embedded in a mouse model is currently in progress using radiolabeled **D1**-POEGMA. We expect the hydrophilic POEGMA that allows conjugation of multiple hydrophobic DFO ^{89}Zr-chelators would enable efficient PET imaging of the tumor. In the future, it will be interesting to assess the ability of DARPin-polymer-toxin conjugates to target and kill solid tumors in an animal model, since what makes polymer conjugation particularly useful is the elongated circulation time in the system due to the increased molecular weight that leads to a prolonged effect and hence potentially higher therapeutic efficacy.

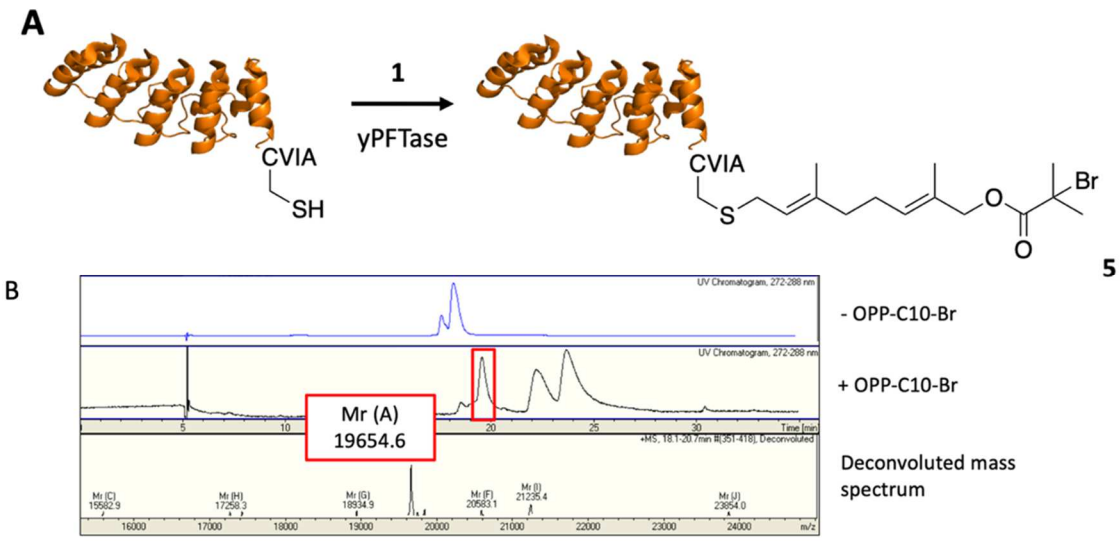

Figure S2.1 Farnesylation of OPP-C10-Br with **D1**-CVIA. (A) Scheme of the prenylation reaction of **D1**-CVIA with OPP-C10-Br (**1**) to yield the site-specific **D1**-macroinitiator (**5**). (B) In situ AGET ATRP from **5** that yields DARPin-POEGMA-Rhodamine conjugates.

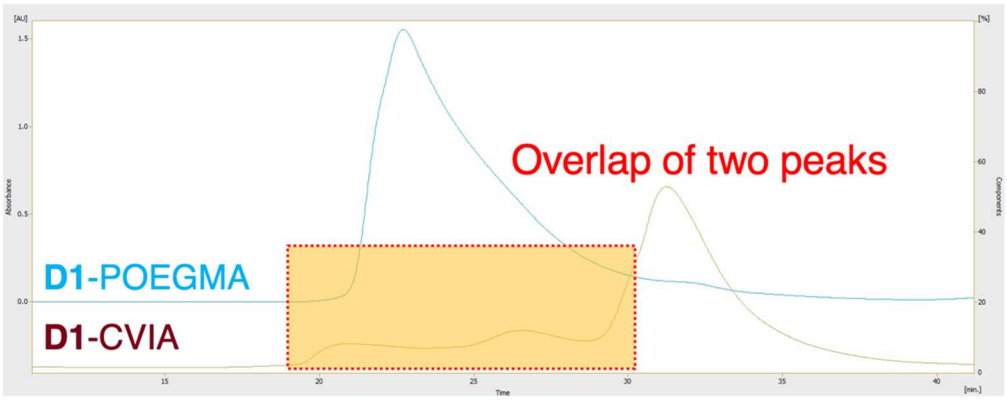

Figure S2.2 SEC trace of **D1**-CVIA compared to **D1**-POEGMA. While the SEC trace in Figure 2.2B was obtained using a Superdex 200 column, the trace in Figure S2.2 was obtained using a Superdex 75 column. Both columns use similar resins (dextran and agarose) but differ in the separation range (10-600 kDa for Superdex 200, 3-70 kDa for Superdex 75). The SEC trace collected with Superdex 75 more clearly demonstrated the widely ranged retention volume of **D1**-CVIA that results in incomplete separation from **D1**-POEGMA.

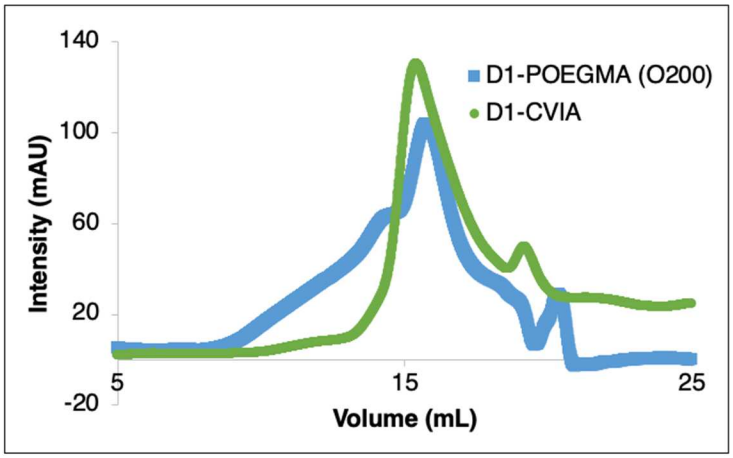

Figure S2.3 SEC trace of **D1**-CVIA overlapped with **D1**-POEGMA prepared with OEGMA. Shift in retention volume after polymerization indicates successful grafting-from polymerization with $OEGMA_{200}$.

Chapter 3. Site-specifically immobilized enzymes for antifouling applications

3.1 Introduction

Biofilm formation results from surface-attached microorganisms that aggregate within its self-produced extracellular polysaccharides.[175] For humans, this phenomenon is disadvantageous in many ways. Bacterial infections are the most common type of acute and chronic infection that increases patient mortality and morbidity. Surfaces of medical devices have been shown to induce formation of biofilms, being a challenge for patients.[176,177] From a naval industry standpoint, biofilms are problematic as they often lead to biofouling that causes microbiologically influenced corrosion (MIC) or biocorrosion of metal surfaces, which leads to significant costs in cleaning of the surface and reapplying of protectants.[178] Biofilm covered surfaces also facilitate the adhesion of larger organisms such as algae and mussels, which causes an even more significant cost due to increased fuel consumption from higher frictional drag. The cost that results from combating biofilms in the United States marine industry alone has been reported to be 55 billion USD per year.[179–181]

Methods to prevent biofilm formation in the marine industry have been developed based on a variety of different approaches. The most traditional and common strategy is the use of biocides. However, on top of tolerance, due to the bacterial resistance[182] that occurs when organisms exist in a biofilm, the overall resistance of bacteria toward biocides and antimicrobial agents has been reported to have increased up to 1000 times, diminishing the effectiveness of this method.[183] The toxic effects of biocides on the marine environment also remain an issue. While organic biocides and copper oxides have been introduced as a replacement for the more toxic tributyltin, there has not yet been enough evaluation of how these substances impact the environment.[184] Therefore, alternative methods to biocides have been gaining attention. One example is the use of small molecule inhibitors that inhibit the gene expression of key virulence factors.[185] While the field is developing rapidly, the mechanism of action of these molecules are still not fully understood, which has hindered their application especially in the medical device area. Anti-adhesion coating is another growing field, which aims to prevent surface attachment of the

microbes without necessarily eradicating them. The coating often exhibits hydrophilic or ionic properties that lead to the formation of a hydration layer, which in turn prevents the adsorption of biomolecules to the surface. As that method does not involve potency against microbes, it does not produce dead microorganisms which may attach to the surface and become a site for biofilm growth. Hydrophilic polymer coatings that use PEG (Poly(ethylene glycol) are a good example of anti-adhesive coatings. Polymer brushes with PEG side chains have been demonstrated to be effective in reducing bacterial adhesion on surfaces in lab settings.[186] Other alternatives to PEG have been demonstrated as well which include zwitterionic or amphiphilic polymers.[187] However, the long term stability of these polymeric coatings has been an issue, especially for marine antifouling applications which require prolonged stability and antibacterial effectiveness for durations of years.

Application of quorum quenching (QQ) enzyme has recently arisen as a method that achieves antibacterial effects through an alternative mechanism, interference of bacterial cell communication. Quorum sensing (QS) is a communication mechanism that bacteria exploit by secreting chemicals known as autoinducers to the environment, purposed to regulate collective behavior. Once the accumulated autoinducers reach a certain threshold, a “quorum” is reached, which triggers signaling that prompts gene expression and various physiological activities.[188] QQ enzymes such as lactonases prevent biofilm formation by degrading these AHL autoinducers, thus disrupting QS.

The use of QQ enzymes holds many advantages over the traditional biofilm prevention methods. It is environmentally friendly as the antibacterial effect is localized to the ship hull, and the enzymes released to the environment do not lead to toxic effects, since unlike tributyltin or copper, these proteins naturally degrade and do not bioaccumulate. The environmental impact is even further mitigated since these enzymes can be used in small catalytic quantities. Strategies using QQ enzymes can be more effective, especially against gram-negative bacteria that utilize small molecules such as N-acyl homoserine lactones (AHLs) as the autoinducer, since they are more resistant to antibiotics from having thick impermeable cell walls. Since QQ enzymes prevent biofilm formation by disrupting communication of bacteria rather than by directly affecting their survival, the chances of developing resistance against QQ methodologies are low. Finally, the

strategy does not have to consider delivery mechanisms into the cell as the antibacterial effect does not require endocytosis of any of the involved substances.

The effectiveness of surface immobilized QQ enzymes for antifouling purposes has been demonstrated in several cases. Seah and coworkers demonstrated antifouling activities of AHL-degrading SsoPox enzymes immobilized in alumina fibers via electrostatic interactions.[189] Since then, various studies have been reported where QQ enzymes were immobilized onto various substrates such as membranes,[190] capsules,[191] mesoporous silica,[192] and steel coupons.[180] However, most studies have implemented a non-covalent immobilization strategy and have monitored only short periods of effectiveness. These bring into question whether the strategies could be implemented into field applications that require potency for a minimum of 6 months. Ones that did exploit covalent interactions required the use of crosslinking reagents such as glutaraldehyde, and the non-specific conjugations that resulted from it were shown to result in substantial loss of enzyme activity post-immobilization.[193]

Among various QQ enzymes, *Sso*Pox, a hyperthermostable phosphotriesterase-like lactonase (PLL) isolated from the archaeon *Sulfolobus solfataricus*, is a particularly promising enzyme due to its wide applicability and robustness.[194] The *Sso*Pox-W263I variant was developed based on *Sso*Pox, in which the W236I mutation was found to enhance both AHL and organophosphorous-degrading activities while maintaining high thermal stability (T_m = 88 °C), high catalytic activity at a wide range of temperatures (-18 to 70 °C), high tolerance to a wide range of organic solvents, and high promiscuity which allows high activity against a variety of lactones.[195] Promising biofouling and biocorrosion inhibition activities were reported in preliminary studies of *Sso*Pox-W236I where the enzyme was applied to steel surfaces in the form of a silica gel-immobilized coating.[180] However, non-specific covalent immobilization using glutaraldehyde was shown to result in only 15% retention of the enzyme activity.[195] Non-covalently immobilized enzymes coatings resulted in significantly diminished antibacterial activities due to the low durability of the coating method, where enzyme leakage and deterioration of the silica coating was not able to remain effective even for a short term 8-week study.[180]

In this study, *Sso*pox-W236I was site-specifically modified with various chemical

functionalities for immobilization or visualization purposes. Site-specific labeling was achieved by exploiting protein farnesylation, in which the promiscuity of the farnesyltransferase (PFTase) allows the enzyme to modify most proteins that contain a C-terminal CaaX sequence with analogs of its natural substrate farnesyl diphosphate (FPP).[13] Previous studies by Distefano and coworkers showed various biotechnological applications using the FTase enzyme,[85,93,102] often in combination with click chemistry.[139] Compared to non-selective chemical modification methods, site-specific enzymatic labeling allows highly retained activity of the protein-product, since the method allows control over the site of modification. Labeling only occurs at the C-terminal cysteine residue of the CaaX motif, which is often distant from the active site. Reactions occur under mild conditions in aqueous buffer which is beneficial for proteins in general. Exploiting this methodology, incorporation of three types of functionalities were focused on here: diazirine, isobutyryl bromide, and azide. The labeled enzymes were subsequently subjected to light-induced covalent immobilization, protein-polymer conjugation for immobilization, fluorophore conjugation for visualization, and quantification, respectively. Preliminary lab-based studies are shown, which are expected to soon develop into a long term (>6 months) field study at locations including the Duluth Superior Harbor.

3.2 Experimental

Synthesis of OPP-C10-diazirine (C10-DA)

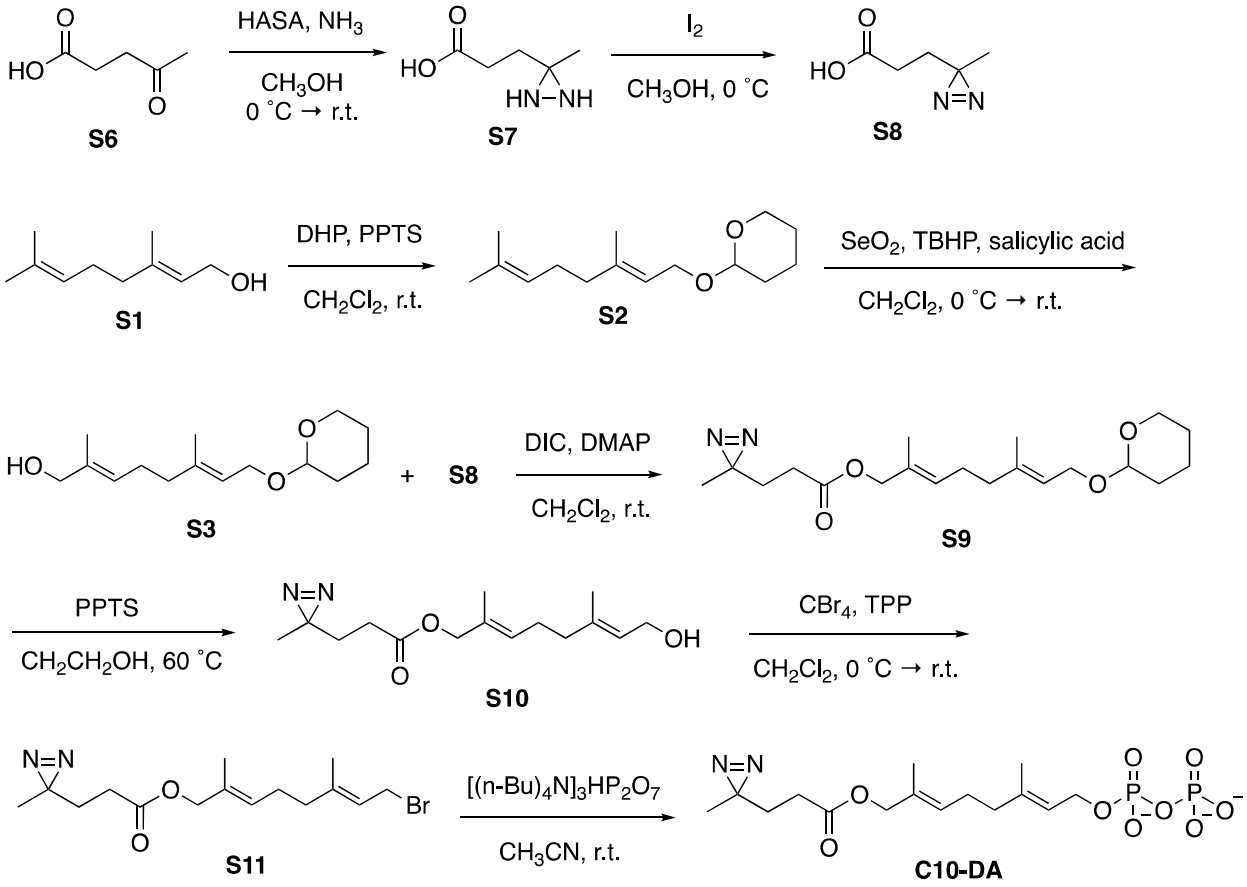

3-(3-methyldiaziridin-3-yl)propanoic acid (S7)

Levulinic acid **S6** (2 g, 17.2 mmol, 1 eq) was dissolved in 7 N NH_3 in CH_3OH (17.2 mL, 120.7 mmol, 7 eq). The resulting solution was stirred under N_2 in an ice-bath for 3 h. A solution of hydrolxylamine-O-sulfonic acid (2.30 g, 20.64 mmol, 1.2 eq) in CH_3OH (12 mL) was added dropwise at a rate of 1 s^{-1}. The reaction mixture was stirred for 20 h and allowed to warm to rt. N_2 was bubbled through the solution for 1 h to remove NH_3 gas. Vacuum filtration and concentration resulted in a yellow oil that was used in the next step without purification.[196]

3-(3-methyl-3H-diazirin-3-yl)propanoic acid (S8)

Diaziridine **S7** was dissolved in CH_3OH (15 mL) and stirred on ice for 5 min in a tin foil-covered flask. Triethylamine (4.6 mL, 33.5 mmol) was added and allowed to stir for 5 min. Slowly, chips of I_2 were added until the solution remained a brown-red color for longer than 5 min after the last

addition. The reaction solution was diluted with EtOAc and washed with 1 M HCl and aqueous 10% sodium thiosulfate until the organic layer was colorless. The aqueous layer was further extracted with EtOAc (2 × 20 mL). The organic layers were combined, dried over $MgSO_4$, and concentrated to afford diazirine acid **S8** as a brown residue (1.07 g, 50%). Spectral data obtained were in good agreement with those reported in the literature.[196]

(2E,6E)-2,6-dimethyl-8-((tetrahydro-2H-pyran-2-yl)oxy)octa-2,6-dien-1-yl 3-(3-methyl-3H-diazirin-3-yl)propanoate (S9)

S3 was prepared as previously described[62]. To a solution of protected alcohol S6 (0.575 g, 4.49 mmol, 1 eq) and DMAP (55.0 mg, 0.45 mmol, 0.1 eq) in CH_2Cl_2 (6 mL) was added a solution of the diazirine acid **S3** (1.260 g, 4.94 mmol, 1.1 eq) in CH2Cl2 (6 mL). DIC (0.679 g, 5.39 mmol, 1.2 eq) was added, and the resulting solution was stirred at rt for 16 h. The reaction mixture was filtered and concentrated. Purification by flash chromatography (4:1 Hex:EtOAc, v/v) afforded 848 mg (53%) of diazirine **S9** as a clear oil. Spectral data obtained were in good agreement with those reported in the literature.[196]

(2E,6E)-8-hydroxy-2,6-dimethylocta-2,6-dien-1-yl 3-(3-methyl-3H-diazirin-3-yl)propanoate (S10)

To a solution of **S9** (800 mg, 2.2 mmol, 1 eq) in CH_2CH_2OH (12 mL) was added PPTS (55.2 mg, 0.22 mmol, 0.1 eq). The reaction flask stirred at 60 °C for 2 h. The reaction mixture was concentrated in vacuo and purified by flash chromatography (7:3 Hex:EtOAc, v/v) to afford 570 mg (93 %) of diazirine alcohol **S10** as a clear oil. Spectral data obtained were in good agreement with those reported in the literature.[196]

(2E,6E)-8-bromo-2,6-dimethylocta-2,6-dien-1-yl 3-(3-methyl-3H-diazirin-3-yl)propanoate (S11)

Diazirine alcohol **S10** (100 mg, 0.357 mmol, 1 eq) was converted to the corresponding bromide in the presence of resin-bound PPh_3 (374 mg, 1.43 mmol, 4 eq) and CBr_4 (474 mg, 1.43 mmol, 4 eq) dissolved in CH_2Cl_2 (8 mL). The resulting solution was allowed to stir for 2 h at rt. After the reaction was complete, excess CBr_4 and resin-bound PPh_3 were removed from the mixture by filtration.

Removal of the solvent afforded 105 mg (60%) of diazirine bromide **S11** as a clear oil. Spectral data obtained were in good agreement with those reported in the literature.[196]

(2E,6E)-3,7-dimethyl-8-((3-(3-methyl-3H-diazirin-3-yl)propanoyl)oxy)octa-2,6-dien-1-yl diphosphate (C10-DA)

The crude bromide **S11** (122 mg, 0.357 mmol) was dissolved in dry acetonitrile and a solution of $(n\text{-}Bu_4N)_3HP_2O_7$ (644 mg, 0.714 mmol) in dry acetonitrile was added into the reaction mixture at rt. After initiating the reaction, an ion-exchange column (Dowex 50WX8, 50-100 mesh, Sigma Aldrich, 217492) was prepared and washed with 3 bed volumes of 3:1 H_2O:(conc.) NH_4OH (v/v) and equilibrated with 4 bed volumes of 25 mM 49:1 NH_4HCO_3:i-PrOH (v/v), i.e., solvent C. After stirring for 4 h, the crude product was loaded on the ion-exchange column and eluted with solvent C. Fractions containing the product were combined and concentrated by lyophilization. After adding 3 mL 0.1 M NH_4HCO_3, the product was extracted with 1:1 CH_3CN:iPrOH (x2) and purified by cellulose column chromatography using a cellulose-packed column (2.0 x 14 cm^2) equilibrated with 9:1 THF: 0.1 M NH_4HCO_3 (v/v). Step-elution was performed with THF:0.1 M NH_4HCO_3 (200 mL of 9:1, 200 mL of 8:2, and 100 mL of 7:3, v/v) at a flow rate of 5.0-6.0 mL/min. Fractions containing the phyrophosphates were determined by ESI-MS, combined, and concentrated by lyophilization. Yield was determined as 13 mg (17%) by ^{31}P NMR spectroscopy using an internal standard (Na_2HPO_4).

^1H NMR (400 MHz, D_2O): δ ppm 5.45 (d, J = 5.9 Hz, 1H), 5.36 (s, 1H), 4.43 (s, 2H), 4.36 (t, J = 6.0 Hz, 2H), 2.22 (t, J = 7.0 Hz, 2H), 2.15-2.08 (m, 2H), 2.06-1.99 (m, 2H), 1.66-1.50 (m, 8H), 0.93 (s, 4H)

^{31}P NMR (162 MHz, D_2O): δ ppm -6.54 (d, J = 21.8 Hz), -10.31 (d, J = 21.8 Hz).

HRMS (m/z): $[M - H]^-$ calcd for $[C_{15}H_{25}N_2O_9P_2]^-$ 439.1041, found 439.1062.

Mutagenesis, expression, and purification of *Sso*Pox-CVIA

Strain E. coli BL21 (DE3) were transformed with plasmids pGro7/GroEL and pET22b *Sso*Pox-W263I for chaperone and *Sso*Pox-W263I expression, respectively. The linker sequence for KCVIA, GSGTKCVIA, or GGKKKKKKTKCVIA was added to the C-terminal end of the *Sso*Pox-W261I

template for 3 different types of *Sso*Pox-constructs. A first preculture of 100 mL was made from adding a glycerol stock in LB medium containing 100 µg/mL ampicillin and 34 µg/mL chloramphenicol, which was grown at 37 °C with shaking at 180-200 rpm until the OD_{600} reaches 0.6. This preculture was used to inoculate the second preculture in the same medium and grown in the same conditions until the OD_{600} reaches 0.6, which was again used to inoculate the ZYP-5052 medium containing 1000 µg/mL ampicillin and 34 µg/mL chloramphenicol and incubated at 37 °C with shaking at 180-200 rpm. Once the OD600 reached 0.6, protein production was induced by adding 100 µM $CoCl_2$ and 0.2% (w/v) L-arabinose, and the temperature was reduced to 18 °C with shaking at 220 rpm. After 16 h, cells were harvested by centrifugation at 4,400 g for 20 min. The cell pellet was resuspended in lysis buffer (50 mM HEPES, 150 mM NaCl, 200 µM $CoCl_2$, 250 µg/mL DNAse 1, 0.1 mM phenylmethylsulfonylfluoride (PMSF), 20 mM $MgSO_4$, pH 8.0) and lysed by sonification (3x30 sec cycles at 45% amplitude, QSonica sonicator Q700). The lysis extract was centrifuged 14,000 g for 30 min, and the soluble fraction was collected and heated at 80 °C for 20 min, followed by another round of centrifugation. *Sso*Pox-CVIA was precipitated and concentrated by incubation in 75% ammonium sulfate overnight at 4 °C. Followed by resuspension in HEPES buffer (50 mM HEPES, 150 mM NaCl, pH 8.0), the protein solution was filtered through a 0.22 µm syringe filter, followed by buffer exchange to remove ammonium sulfate and concentration with an Amicon Centriprep centrifugation device (30,000 MW cut-off). The proteins were finally purified by SEC with a HiLoad 16/600 Superdex 75 pg column (GE Healthcare) with HEPES buffer. The purity of the collected fractions after concentration using an Amicon Centriprep centrifugation device (30,000 MW cut-off) was analyzed by 12.5% SDS-PAGE, and the concentration was measured using a NanoDrop 2000 spectrophotometer (Thermo Scientific).

Paraoxonase activity measurements of *Sso*Pox-CVIA

The phosphotriesterase activity was measured following a method that was described previously.[195] Briefly, 5 µL of enzyme solution and 185 µL of activity buffer (50 mM HEPES, 150 mM NaCl, 0.2 mM $CoCl_2$, pH 8.0) was added to a 96-well plate. The enzyme reaction was initiated by adding 10 µL of 20 mM ethyl paraoxon, which was followed by measuring the production of p-nitrophenolate

via absorption at 405 nm for 40 min.

Enzymatic incorporation of the diazirine into GFP-CVIA or *Sso*Pox-CVIA

Enzymatic reaction mixtures (15 mL) contained Tris·HCl (50 mM, pH 7.5), $MgCl_2$ (10 mM), KCl (20 mM), $ZnCl_2$ (100 μM), DTT (5.0 mM), GFP-CVIA or *Sso*Pox-CVIA (5 μM), C10-DA (40 μM), and PFTase (800 nM). The reaction mixture excluding the isoprenoid analogue and PFTase was incubated on ice for 0.5 h, followed by addition of the two reagents and incubation for 6 h at 30 °C. The product mixture was then buffer exchanged (x3) to x1 PBS and concentrated to 100 μL using an Amicon Centriprep centrifugation device (10,000 MW cut-off). The product was characterized by LCMS (xx) and SDS-PAGE analysis. The subsequent protein concentration was calculated by BCA assay for the *Sso*Pox-product and UV absorbance at 488 nm (ε=55,000 $M^{-1}\cdot cm^{-1}$) for the GFP-product.

Enzymatic incorporation of an azide into *Sso*Pox-CVIA

Enzymatic reaction mixtures (4 mL) contained Tris·HCl (50 mM, pH 7.5), $MgCl_2$ (10 mM), KCl (20 mM), $ZnCl_2$ (100 μM), DTT (5.0 mM), *Sso*Pox-CVIA (20 μM), C10-Az (100 μM), and PFTase (7 μM). The reaction mixture excluding the isoprenoid analogue and PFTase was incubated on ice for 0.5 h, followed by addition of the two reagents and incubation for 6 h at 30 °C. The product mixture was then buffer exchanged (x3) to x1 PBS and concentrated to 100 μL using an Amicon Centriprep centrifugation device (10,000 MW cut-off). The product was characterized by LCMS and SDS-PAGE analysis. The subsequent protein concentration was calculated by BCA assay.

Enzymatic incorporation of an alkyne into *Sso*Pox-CVIA

Enzymatic reaction mixtures (15 mL) contained Tris·HCl (50 mM, pH 7.5), $MgCl_2$ (10 mM), KCl (20 mM), $ZnCl_2$ (100 μM), DTT (5.0 mM), *Sso*Pox-CVIA (2.5 μM), C15-Alk (40 μM), and PFTase (800 nM). The reaction mixture excluding the isoprenoid analogue and PFTase was incubated on ice for 0.5 h, followed by addition of the two reagents and incubation for 6 h at 30 °C. The product mixture was then buffer exchanged (x3) to x1 PBS and concentrated to 100 μL using an Amicon Centriprep

centrifugation device (10,000 MW cut-off). The product was characterized by LCMS and SDS-PAGE analysis. The subsequent protein concentration was calculated by BCA assay.

Enzymatic incorporation of an ATRP-initiator into *Sso*Pox-CVIA

Enzymatic reaction mixtures (6 mL) contained Tris·HCl (50 mM, pH 7.5), $MgCl_2$ (10 mM), KCl (20 mM), $ZnCl_2$ (100 μM), DTT (5.0 mM), *Sso*Pox-CVIA (20 μM), OPP-C10-iBr (100 μM), and PFTase (3 μM). The reaction mixture excluding the isoprenoid analogue and PFTase was incubated on ice for 0.5 h, followed by addition of the two reagents and incubation for 6 h at 30 °C. The product mixture was then buffer exchanged (x3) to x1 PBS and concentrated to 100 μL using an Amicon Centriprep centrifugation device (10,000 MW cut-off). The product was characterized by LCMS and SDS-PAGE analysis. The subsequent protein concentration was calculated by BCA assay.

Covalent incorporation of GFP-DA or *Sso*Pox-DA into paint

For covalent incorporation of the protein into paint, diazirine labeled proteins were added to paint for a final concentration of 1.2-3.4 μM. 500 μL of the protein-paint mixture was aliquoted on a 12-well plate (Corning, CLS3513) and dried overnight under a stream of air. Photocrosslinking was conducted upon UV irradiation at 365 nm and 100 $\mu J \cdot cm^{-2}$ for 10 min (Analytik Jena, CL-1000L). Minimal photobleaching was observed for the GFP-DA. For control studies, non-labeled proteins that lack the diazirine were subjected to the same procedure.

Surface immobilization of GFP-DA or *Sso*Pox-DA on paint

500 μL of paint was aliquoted on a 12-well plate (Corning, CLS3513) and dried overnight under a stream of air. To the layer of paint on the bottom of the wells, 10-30 μL of 60-100 μM diazirine labeled protein solution was aliquoted and dried overnight under a stream of air. Photocrosslinking was conducted upon UV irradiation at 365 nm and 100 $\mu J \cdot cm^{-2}$ for 10 min (Analytik Jena, CL-1000L). Minimal photobleaching was observed for the GFP-DA. For control studies, non-labeled proteins that lack the diazirine were subjected to the same procedure.

Quantification of the retained GFP-DA in or on paint

The 12-well plate containing paint-immobilized GFP-DA was immersed a 1 L beaker containing water and stirred in the dark. The beaker was exchanged with fresh water every 2 days. The amount of immobilized protein retained in or on paint was analyzed by taking out the plates periodically and quantifying the fluorescence intensities with a Typhoon FLA 9500 biomolecular imager.

In situ ATRP from the site-specific *Sso*Pox-macroinitiator

$OEGMA_{500}$ monomer (273 μmol) and sacrificial initiator resin (10.5 mg, 2.65 mol) was added to 100 μL of the *Sso*Pox-macroinitiator solution (120 nmol). To this solution was added 400 μL of the catalyst solution composed of $CuBr_2$ (2.65 μmol) and TPMA (26.5 μmol) in PBS. Polymerization was initiated by adding 50 μL of ascorbic acid (265 nmol) in PBS. All solutions were separately purged with argon for 30 min after formulation. After 6 h of polymerization at rt, the reaction was quenched by exposure to air. The product solution was purified from sacrificial initiator resin using a 0.22 μm centrifugal filter and subjected to anion exchange chromatography (AExC) with a HiTrap Q HP column to remove unreacted monomers from the products. A linear gradient of 2.5% per min from Buffer A (20 mM HEPES, pH 8.0) to Buffer B (20 mM HEPES, 1 M NaCl, pH 8.0) was applied. The fractions containing the *Sso*Pox-polymer conjugates were collected and concentrated using an Amicon Centriprep centrifugation device (10,000 MW cut-off) and subjected to purification and analysis by size exclusion chromatography (SEC) with a Superdex 200 10/300 column (GE Healthcare) with PBS. For samples that require the functionalization with a DBCO reagent, click reaction was employed to the AExC-purified product followed by SEC purification. The FPLC used for chromatography purifications was a Knauer AZURA BioLC device. The collected SEC fractions were concentrated using an Amicon Centriprep centrifugation device (10,000 MW cut-off), which was subjected to 12% SDS-PAGE for purity analysis and BCA assay for concentration analysis.

3.3 Results and Discussion

Screening of the *Sso*Pox-CVIA constructs for site-specific modification via protein farnesylation

*Sso*Pox proteins were engineered by mutagenesis with a C-terminal CVIA sequence for recognition by the PFTase enzyme. Three different SsoPox-CVIA constructs were prepared with differing spacer sequences, *Sso*Pox-KCVIA, *Sso*Pox-GSGTKCVIA, and *Sso*Pox-GGKKKKKKTKCVIA. The first was the minimal linker sequence, the second linker was designed to be flexible, and the third was adopted from the C-terminal sequence of the K-Ras protein which is a native substrate for the PFTase.[197] Prenylation reactions containing the three constructs were tested with the isoprenoid analogs OPP-C10-iBr, OPP-C10-Acr, C10-Az[85], C10-DA, and C15-Alk,[198] and the products were characterized by LC-MS. As the HPLC retention volume of *Sso*Pox enzymes overlapped with yPFTase, analysis was focused on the deconvoluted mass. While none of the analogs were shown to react with the first and third constructs, the second construct *Sso*Pox-GSGTKCVIA (will be denoted as *Sso*Pox-CVIA from hereon for simplicity) was shown to undergo enzymatic labeling with most of the isoprenoid analogs. However, efficiencies varied between analogs and therefore farnesylation conditions were adjusted accordingly. For OPP-C10-iBr, 10 μM analog with 200 nM PFTase was able to result in near full conversion of 2.5 μM *Sso*Pox to the farnesylated product, similar to conditions utilized in previous studies.[102] However, in the cases of C10-Az and C15-Alk, the isoprenoid analog and PFTase concentrations had to be elevated to 40 μM and 800 nM, respectively, to achieve the same degree of labeling. OPP-C10-Acr did not show any modified protein products despite optimization of the labeling conditions and was therefore excluded from further studies. As for the C10-DA, reaction with **D1**-CVIA and GFP-CVIA showed fully converted products with 10 μM isoprenoid analog and 200 nM PFTase, indicating efficient recognition and turnover of the analog by the PFTase. However, to guarantee full conversion of the *Sso*Pox-CVIA to the DA-labeled product, the conditions were adjusted to higher concentrations, 40 μM and 800 nM isoprenoid analog and PFTase, respectively.

Following enzymatic labeling, the modified *Sso*Pox enzymes exhibited a tendency to adhere to the centrifugal filters employed during the buffer exchange procedures. Hydrophilic enzymes including *Sso*Pox contain a large number of salt bridges uniformly localized on the protein surface. These salt bridges are involved in complex interactions including dimerization of the two subunit termini that results in the overall increase in stability of the protein.[199] Therefore, we

presume that covalent modification of *Sso*Pox at the C-terminus, despite its site-specific characteristics, may be causing interference of the ionic interaction between the two termini which in turn was leading to protein aggregation and precipitation.[200,201] However, it is important to note that most of the precipitated proteins could be re-solubilized back into solution by simple vortexing. Nonetheless, to maximize yield, farnesylation conditions were optimized to minimize protein loss during purification steps. A significant effort was made to increase the protein concentration in the reaction solution to minimize the number of post-farnesylation buffer exchange steps. Interestingly, *Sso*Pox-CVIA was shown to be stable even at 20 μM farnesylation conditions, indicating its extremely high stability. To accommodate the increase in the protein substrate concentration, the analog concentration was also increased to 40-100 μM and the PFTase to 4-7 μM. While high concentrations for both the analog and enzyme were chosen to ensure that the reaction proceeds with high efficiency, this may have been excessive, as according to steady state kinetics, analog concentrations above K_m would not bring any benefit. Further optimization will probably be necessary for each individual reaction

Bioorthogonal fluorophore labeling of prenylated *Sso*Pox

Based on the demand for a method to quantify surface applied *Sso*Pox to easily visualize and quantify the degree of application and to track the remaining enzymes over time, this question was investigated first. One way to realize this is to modify the enzyme with fluorophores that would allow both qualification and quantification via optical measurements. Therefore, bioorthogonal fluorophore labeling was conducted on *Sso*Pox-CVIA prenylated with either an azide or alkyne probe. While CuAAC of TAMRA-azide to *Sso*Pox-Alkyne did appear to be successful to some extent as evidenced by the fluorescing protein solution after purification of the product, the recovered yield was too low for it to be applicable for actual use. This low yield was presumably due to the instability of *Sso*Pox-Alkyne compared to other site-specific *Sso*Pox products, which was indicated by the distinctly low recovery yields after farnesylation. The CuAAC reaction conditions are presumed to have an effect as well since they require a copper catalyst that may contribute towards protein oxidation and aggregation.[32] The azide labeled *Sso*Pox was shown to successfully

undergo SPAAC with TAMRA-DBCO with high efficiency (>90%) as indicated by SDS-PAGE, also with a reasonable recovery yield (~15%) (Fig. 3.1). The activity of the modified *Sso*Pox enzyme was measured to see whether the site-specific fluorophore conjugation introduces a detrimental effect to the enzyme's antifouling efficacy. However, in the process of doing so, it was found that enzyme activity varies widely upon post-purification storage conditions. Therefore, activity comparisons before and after fluorophore labeling were postponed, and optimized storage conditions are currently under investigation.

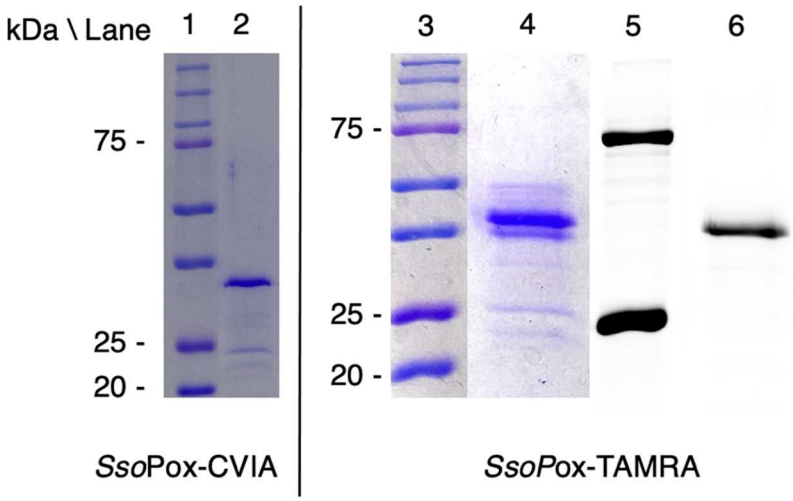

Figure 3.1 SDS-PAGE of TAMRA-labeled *Sso*Pox. The fluorophore was site specifically labeled through farnesylation of an azide followed by copper-free click reaction with TAMRA-DBCO. The upshifted in band that fluoresces indicates successful fluorophore labeling with high yield (lane 1, 3 and 5, protein ladder; lane 2, *Sso*Pox-CVIA; lane 4 and 6, *Sso*Pox-TAMRA). Lanes 1-4 shows Coomassie stained gels, and lanes 5 and 6 shows a fluorescence-scanned image of the identical gel before Coomassie staining.

Bioorthogonal polymer conjugation of prenylated *Sso*Pox

Prior studies from the Elias group have focused on incorporating *Sso*Pox enzymes into silica gels to achieve an antifouling layer on metal coupons.[180] Exploiting the high stability of *Sso*Pox enzymes under various conditions including high heat and in organic solvents,[193] the study was later expanded to enzyme immobilization in paint (*manuscript in preparation*). Despite the

harsh organic components of paint, *Sso*Pox enzymes were found to be active, successfully exhibiting antifouling properties. However, mere physical entrapment of the enzyme within paint was found insufficient to retain the protein in paint for long durations. *Sso*Pox enzymes eventually diffused out from the paint and therefore the coatings became ineffective over time.

To increase the degree of physisorption and therefore achieve higher retention of *Sso*Pox in paint, site-specific polymer conjugation via protein prenylation was investigated. Two conjugation methods were explored, grafting-to and grafting-from. Grafting-to conjugation involves the labeling of a pre-synthesized polymer to the protein via complementary reactive handles on each component. This method allows easier characterization of the polymer, while it may lead to complications in post-conjugation purification, or even low conjugation yields due to steric hindrance. The grafting-from method employs the initial installment of an initiator moiety which transforms the protein into a macroinitiator, followed by polymerization directly from the protein-initiator to yield protein-polymer conjugates. The method experiences minimal steric hindrance as it only requires incorporation of a much smaller initiator-molecule rather than a macromolecule, which often leads to high conjugation efficiencies. As the purification of protein-polymer conjugates most often exploit separation by size, the grafting-from method manifests easier purification, as the macromolecular products are more easily distinguishable from a mixture with small monomers than large macromolecules.

Exploiting the site-specifically labeled azide, grafting-to PEGylation with PEG_{10k}-DBCO was conducted by SPAAC. We were expecting a highly efficient reaction, as we had already shown that SPAAC-induced fluorophore labeling with TAMRA-DBCO leads to complete product conversion. However, PEGylation was shown to only yield ~70% product conversion (data not shown). Increasing the concentrations of the reagents did not lead to improvement. We hypothesize that this limitation is due to the effect of steric hindrance when conjugating two macromolecules.

Grafting-from polymer conjugation was investigated for several reasons. First, this method was pursued to overcome the limited conjugation yields that were observed in the grafting-to trials. The second reason was for purification purposes. Although thorough purification was not required for this particular study since the protein-products would be blended with paint, we deemed that

achieving easier purification would be useful for future applications that may require high-purity polymer-conjugated products. A third reason was to conjugate a custom “sticky” polymer using monomers that contain moieties reactive to paint, which would allow covalent anchoring of the *Sso*Pox-polymer conjugates to the substrate. With these goals under consideration, in situ polymerization from OPP-C10-Br labeled *Sso*Pox-CVIA was studied. ATRP conditions were adopted from prior studies that were conducted with DARPins and GFPs. The monomer employed was $OEGMA_{500}$ as it was shown to successfully polymerize in prior studies, and since the pendant hydroxyl groups of the side chains were expected to undergo covalent interactions with the molecules that compose paint. SEC analysis of the crude product post-polymerization confirmed synthesis of *Sso*Pox-POEGMA conjugates (Fig. 3.2). However, the initiation efficiency and therefore product-conversion was extremely low, along with the negligibly low recovery yield after purification. Therefore, investigation of the grafting-from method for polymer-conjugation to *Sso*Pox was suspended. While it was difficult to pinpoint a specific reason for the unsuccessful outcome with the *Sso*Pox enzymes, it was presumed to be at least partially associated with the tendency of the modified *Sso*Pox enzymes to aggregate.

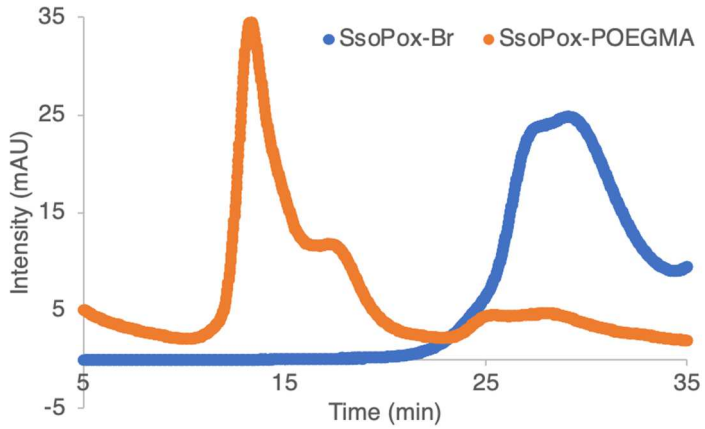

Figure 3.2 Polymer-conjugation to *Sso*Pox enzymes. Comparison of the SEC traces of grafting-from conjugated *Sso*Pox-POEGMA and *Sso*Pox-CVIA. Shift in retention time after in situ polymerization indicate successful conjugation of a polymer.

Covalent surface immobilization of *Sso*Pox on paint

Once irradiated upon light, diazirines form a reactive carbene that can covalently bond to nearby molecules. The small size of diazirines allows them to be incorporated into probes that can be recognized by enzymes, such as how C10-DA can be used with PFTase for site-specific labeling of specific target proteins.[196] These diazirine based probes have been widely used in the field of chemical biology for various purposes such as investigation of ligand-receptor interactions, identification of inhibitor binding sites, and identification of protein-protein interfaces.[202] Here, we envisioned expanding the applicability of site-specifically incorporated diazirines for protein-immobilization purposes. While there had been studies that focused on surface-immobilization,[203,204] we sought to achieve covalent incorporation of proteins into the substrate as well by exploiting the stability of *Sso*Pox in various organic media.

GFP was first utilized as the model protein since its immobilization efficiency could be easily measured by its fluorescence. Preliminary surface immobilization studies of GFP-DA on polyacrylamide gels were unsuccessful. We suspected this to be due to the high-water content of hydrogels, which may be causing the photoactivated-diazirine to react with water molecules rather than the desired substrate. Therefore, paint was chosen as the alternative substrate. To generate an even surface, 500 µL of paint was aliquoted to the wells of 16-well plates and dried overnight. Using excess amounts of paint led to concave surfaces due to the capillary action of the paint with the walls of wells. 34 µM GFP-DA and the negative control GFP-CVIA were each spotted onto separate paint-coated wells followed by photoirradiation. The concentration of the protein solution was chosen based on microprinting conditions utilized in prior studies[205] as it was shown to result in successfully physisorbed fibronectin on PDMS. While there was a concern that the photocrosslinking conditions may cause photobleaching, GFPs were found to maintain a similar level of fluorescence even after photoirradiation, which would therefore allow quantitative analysis of the degree of immobilization via fluorescence measurements (Fig. 3.3A). Prior to optical analysis, each well was washed with PBS four times to remove unbound-GFP.

Analysis of the wells using a fluorescence scanner indicated successful immobilization of the GFP-DA, unlike GFP-CVIA, which did not show any presence of surface-retained protein.

However, the degree of immobilization was low, and instead of an evenly distributed layer of protein, GFPs were found to be immobilized only along the circumference of the contact area of the protein-solution to paint (Fig. 3.3B). This phenomenon called Marangoni effect or coffee-ring effect was observed was due to the higher evaporation rate at the contact lines which causes a strong capillary flow that leads to accumulation of the particles in solution along those lines.[206] To obtain a more homogenous layer of immobilized protein, the printing step was modified by adjusting the GFP solution to a higher concentration and adding an overnight evaporation step after aliquoting the protein solution to each well to further maximize the protein concentration across the surface. GFP-solutions with and without 10% glycerol were compared, as polymer[207] or surfactant[208] additives have been reported to suppress the Marangoni effect. Overnight evaporation of 60 μM GFP-DA and GFP-CVIA in 10% glycerol under a stream of nitrogen was shown to yield a homogenous layer of GFP on the surface of paint. However, after being photoconjugated and rinsed in water for a day, most of the GFP was again found to have been washed off regardless of the presence of the diazirine moiety. While there was a hint of immobilized GFP-DA observed, it still displayed a ring shape. Experiments with glycerol-free GFP solutions resulted in a ring-shaped contact area of GFP already in the printing step after the overnight evaporation of the protein-solution, demonstrating a stronger Marangoni effect in the absence of the glycerol additive. The printed GFP also displayed a crispy texture, which presumably indicated protein precipitation due to excessive drying of the solvent. As expected, photoconjugation of the printed GFP and submersion of the protein-coated wells in water resulted in only a small quantity of immobilized GFP-DA in a ring shape.

Overall, surface immobilization was shown to be successful for proteins site-specifically labeled with a diazirine. The negative control GFP-CVIA did not show any adherence to the surface under the conditions that were examined, demonstrating the utility of the photocrosslinking activity of diazirines in surface immobilization. However, the effectiveness of the method was unclear, as immobilization was only observed along the edge of the protein-solution droplet. The degree or efficiency of immobilization was also a deterring factor for scaling up for field applications. Raising the protein concentration was shown to have little effect in increasing the amount of surface immobilization. Glycerol-free printing conditions required careful control of the extent of solvent

evaporation to prevent the proteins from precipitating, and the printed surface displayed ring shapes. Adding glycerol to the protein solution did mitigate the coffee-ring effect and protein-precipitation during the printing step. However, the quantity of immobilized protein was shown to be lower compared with glycerol-free conditions, presumably due to quenching of the diazirines by glycerol that deters its binding to the paint substrate. Regardless of the homogenous layer that was produced immediately after printing, immersion and rinsing in water revealed that the protein retained on the surface in a covalent fashion was confined along the edge of the layer, indicating that the glycerol had minimal effect in alleviating the ring-shape pattern.

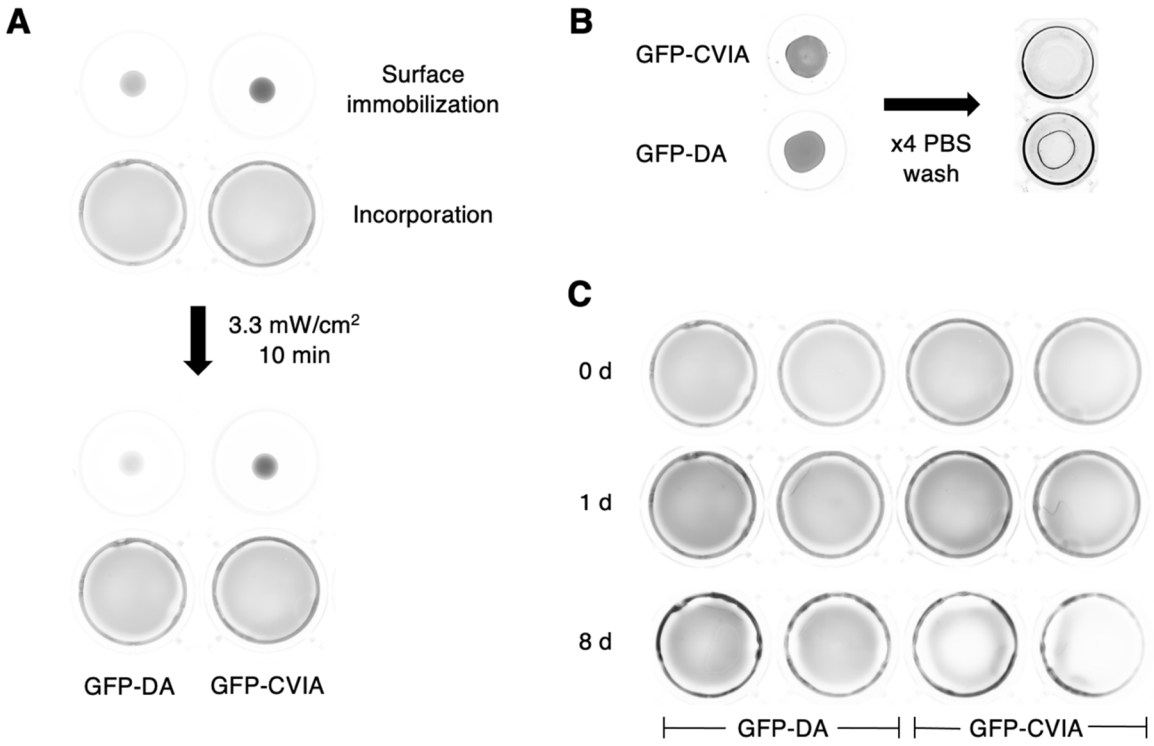

Figure 3.3 Immobilization of GFP-DA characterized by a fluorescent scanner. (A) Photoconjugation conditions results in minimum photoquenching of the GFPs both on the surface and in paint. (B) Photoconjugation of GFP-DA on the paint surface results in a ring-shaped immobilization. GFP-CVIA is not retained on the surface after PBS washing. (C) Photoconjugation of GFP-DA in paint results in higher retention in the substrate than GFP-CVIA. However, failed replications (data not shown) indicate the need for longer time-point studies.

Covalent incorporation of *Sso*Pox in paint

To maximize the degree of protein immobilization, incorporation of the proteins in paint was investigated. To this end, varying amounts of 60 μM GFP-DA and GFP-CVIA were mixed with 500 μL paint and aliquoted into each well of a 12-well plate. Following overnight drying of the paint-protein mixture under a stream of nitrogen, photoconjugation was conducted to the dried paint. Then the protein-paint coated wells were immersed in water to see which ones exhibit higher retention of the GFP in paint. An initial trial of duplicates showed a higher retention for the GFP-DA over GFP-CVIA, suggesting successful diazirine-induced covalent crosslinking (Fig. 3.3C). However, replication of the results was unsuccessful, and both proteins were shown to be retained in paint to an equal degree even after being immersed in water for a month. While it is unclear why the initial trials had shown promising results, we believe it may have been due to an artifact related to the pore sizes of the paint or the fluorescence properties of GFP. It may have been possible that the paint polymerized in a different fashion, leading to larger pore sizes that expedited the elution process of proteins from paint. On the other hand, the effect that was observed may have been an artifact from weakened GFP-fluorescence, and that the difference in signals were representing the stability of the entrapped protein rather than the quantity. Importantly, we believe the reason why the diazirine-labeling was not able to show a distinctive improvement in immobilization efficiencies in subsequent trials is due to the limited time frame of the experiments. In other words, extended observations may be necessary to allow validation of the effect of diazirine crosslinking. Experiments from the Elias group support this hypothesis, where they confirmed minimal leakage of the *Sso*Pox enzymes that do not contain the diazirine moiety in a one month timeframe. The enzyme was also shown to maintain its paraxonase activity while entrapped in paint. Therefore, a more long-term study is currently under progress, where we hope to see the effect of diazirine-mediated covalent immobilization.

3.4 Conclusion

In this work, we demonstrated that PFTase can be utilized to introduce various bioorthogonal moieties to the C-terminus of a biotechnologically relevant *Sso*Pox enzyme. The

introduced functionalities could be exploited for visualization by fluorophore-labeling, physical immobilization by conjugating a polymer to achieve an increase in molecular weight, and covalent immobilization mediated by irradiation with UV light. Site-specific labeling with a TAMRA fluorophore was shown to be successful with high yield and efficiency. These modified *Sso*Pox enzymes will be tested in field studies as antifouling agents on crops once activity measurements are completed. The labeled fluorophore is expected to assist in quantitative analysis of the remaining enzymes applied on plants. While TAMRA was used as the model fluorophore, it would be interesting to expand the types of fluorophores to ones that fluoresce at longer wavelengths as it would allow analysis of the enzymes under more innocuous conditions. Aiming to achieve immobilization of SsoPox in paint substrates, site-specific polymer conjugation was demonstrated by two methods, the grafting-to and grafting-from. Grafting-to conjugation was shown successful with a 10 kDa PEG. Interestingly, presumably due to the large size of the molecule, the conjugation efficiency was shown to be lower than similar reactions with a fluorophore. The yield and efficiency were still adequate for further scale-up studies. Grafting-from conjugation was explored as an alternative method with the anticipation of achieving a higher conjugation yield resulting from less steric hindrance and higher recovery yields due to easier purification. However, the initiation efficiency was shown to be extremely low, therefore further pursuit of that route was deemed unsuitable. The model protein GFP-DA showed promising results that indicate the effectiveness of site-specifically incorporation of a diazirine for immobilization purposes. While preliminary results showed that the protein-diazirine can be covalently bound to paint, longer term studies are required for a more detailed assessment. Therefore, studies with *Sso*Pox-DA are currently ongoing to gauge whether the implemented methods in this study would be applicable to antifouling industry standards that require sustainable effects in time scales of 6 months at a minimum.

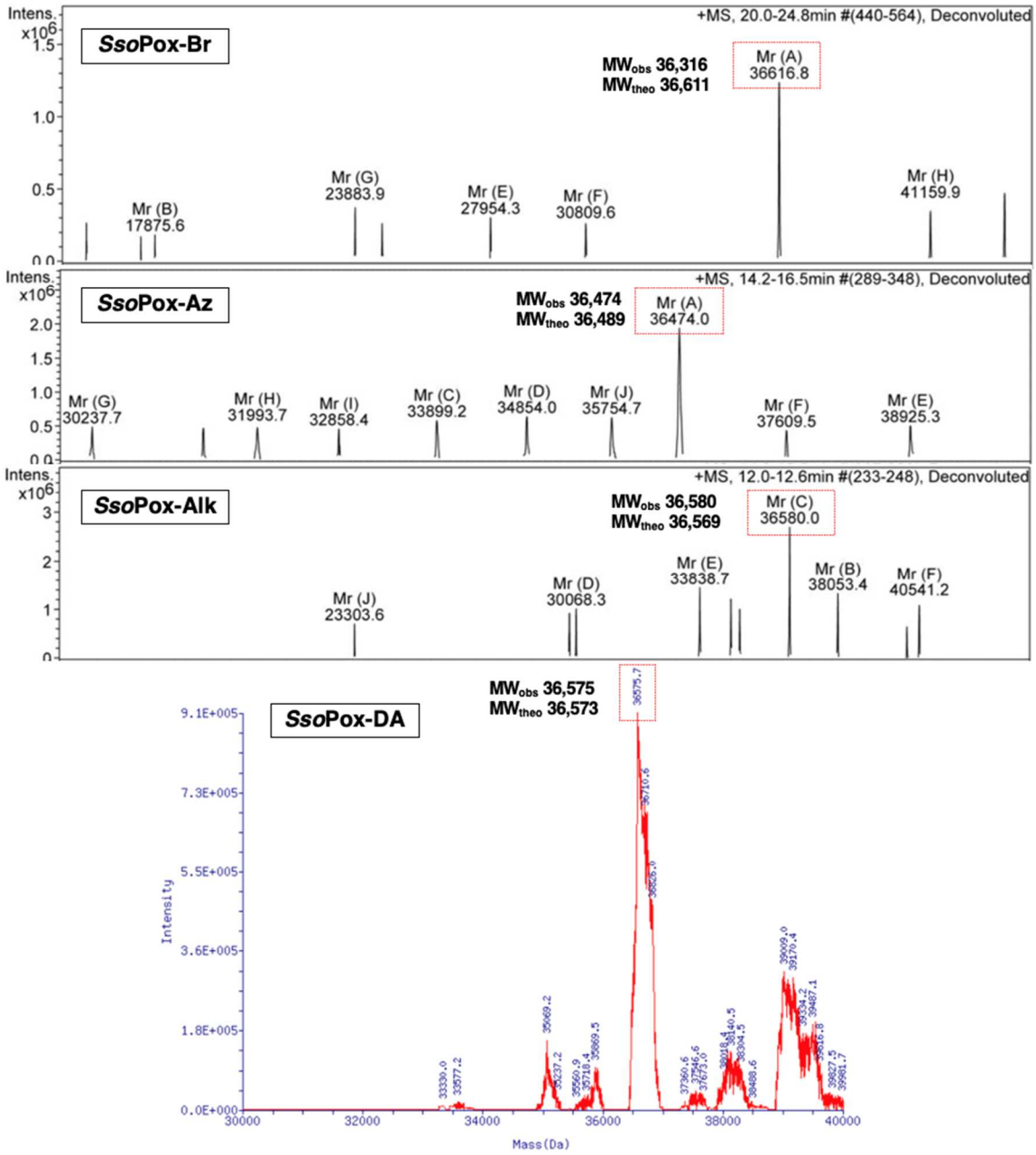

Figure S3.1 Farnesylation of *Sso*Pox-CVIA with OPP-C10-Br, C10-Az, C15-Alk, and C10-DA. Due to the overlap in HPLC elution volume between the *Sso*Pox and yPFTase, deconvoluted mass spectrum showed multiple small residual peaks along with the dominant peak. Absence of the mass of the non-modified *Sso*Pox-CVIA indicated that the prenylation reaction was successful with high efficiency.

Chapter 4. Fabrication of stimuli-responsive hydrogels for mechanistic studies on brain cancer

* Due to the highly collaborative nature of this project and the published manuscript thereof, the inclusion of this work is divided into two parts. The first encompasses the details regarding the part I took in fabricating hydrogels that mimic the brain tissue and the application of that material which led to the discovery of a novel biological phenomenon. The second part demonstrates the full story of this project, which is a reproduced manuscript that contains my work as well as the work accomplished from numerous collaborators which helped to elucidate the mechanism behind my initial discovery. While there is inevitably some overlap between the two sections, especially in the experimental section, including both parts was deemed necessary for the full description of the project.

4.1 Fabrication of photoresponsive hydrogels and its application that led to the discovery of negative durotaxis

Glioblastoma multiforme is the most severe brain cancer with an extremely low recovery rate that results from invasion of glioma cells to the surrounding tissue. Among the various factors that affect cellular migration, one that is specifically affected by the stiffness gradient of the surrounding tissue is a process known as durotaxis. While polyacrylamide hydrogels have been widely used as a substrate for cellular studies, elaborate control on its physical properties remains to be a challenge which is crucial for examining the mechanism behind durotactic behavior. Here we propose a new approach by incorporating novel *o*-nitrobenzyl (*o*-NB) based photocleavable-crosslinkers into polyacrylamide gels which yields stimuli-responsive hydrogels. By controlling the exposure of UV light, we show that we can spatiotemporally control the substrate stiffness in a precise manner. Taking advantage of the high-tunability of the method, a substrate is fabricated to have alternating stiff (15 kPa) and soft (8 kPa) regions connected by steep stiffness gradients, and fibronectins lines are printed across the stiffness gradients. Observation of U-251MG human

glioblastoma cells seeded on the substrates exhibit biased migration toward the softer environments. This negative durotaxis behavior is in contrast with the widely accepted wisdom that durotaxis always occur towards the direction of increasing stiffness gradient. Collaboration with research groups that hold expertise in microbiology and computational modeling leads to elucidation of the mechanism behind cellular sensing of its local environment. Overall, the unique properties of the photoresponsive gels and the methodologies involved in their fabrication are shown effective in mimicking the brain environment, which allows its application as a platform material for cellular studies.

4.1.1 Introduction

While modern technology has been shown effective towards many types of cancers, glioblastoma multiforme (GBM) remains to be a major challenge with poor prognosis with a 1-year survival rate of 37.2% and a 5-year survival rate of 5.1%.[209] One key issue is the highly migratory behavior of gliomas that allow them to invade adjacent tissues and vasculature.[210] While surgical resection of the malignant tumor followed by chemotherapy or radiotherapy remains the standard therapeutic method to treat GBM to this day, even a small remaining tumor left behind can go through rapid proliferation and migration and soon become a full tumor. Therefore, to develop alternative paradigms for brain cancer treatment, there has been an increase in studies focused on understanding the migratory pathologies of gliomas. Cell migration can be triggered by various gradients of external stimuli including light (phototaxis) and dissolved (chemotaxis) or surface-attached small molecules (haptotaxis). Durotaxis is cell migration caused by stiffness gradient of the substrate.[211] While understanding the fundamental mechanism behind different durotactic behavior among cell lines is important, it has been a less explored field compared to other types of migrations due to several methodological limitations. One of the challenges lies in preparing a suitable substrate that fully mimics the brain tissue environment. Some methods that have been developed to mimic the stiffness gradients of the brain in a gel-environment exploit the diffusion of two prepoloymer solutions,[212] tilted-superpositon of two hydrogels,[213] freeze-thaw-induced crosslinking of polyvinyl alcohol,[214] or toehold-mediated strand displacement of DNA[215]. However,

most of these methodologies are incapable of replicating the mechanical properties or stiffness of human brain tissues that are reported to be highly heterogeneous. A large percentage (66%) lie in the range between 3.5 to 25.9 kPa, with a geometric mean of 9.5 kPa, and the slopes of stiffness gradients occur on a micron scale (kPa μm-1).[216] Methods for real-time experiments, that enable simultaneous observation of cell migration while modifying the stiffness, have not been fully developed as well. Light is an external stimulus which allows spatiotemporal control of a from outside of a system, which makes it a suitable candidate for controlling the stiffness properties of substrates. However, while it has been used in some studies, most have been focused on polyethylene glycol (PEG)-based gels aiming for complete degradation of the gel for the fabrication of specific morphologies such as channels.[217] To our knowledge, there has been one report to this date that resulted in photoresponsive polyacrylamide gels, although the methods shown required complicated synthesis and fabrication steps which rendered it difficult to use.[218]

In this study, a simple one-step synthesis of photoresponsive gels is shown by using a novel o-nitrobenzyl bis-acrylate (o-NBbA) crosslinker. 1-D fibronectin patterns are introduced on the surface of the gels and stepwise stiffness gradients are created across the fibronectin lines via controlled exposure of light. Observation of U-251MG cells on the fabricated substrates reveal negative durotaxis, cell movement towards the softer region, which is an unconventional phenomenon that has yet been reported.

4.1.2 Experimental

Synthesis of o-NBbA

2-nitro-4-ethyl aniline (S2)

p-Ethyl aniline (5 g, 41.3 mmol) was added dropwise to a cold solution of concentrated H_2SO_4 (30 mL) and stirred for 5 min. In a separate flask, 5.3 mL of 70% HNO_3 (82.6 mmol) was mixed with an equal volume of H_2SO_4, and added dropwise to the reaction vessel, followed by 15 min stirring at 0 °C. Thin layer chromatography (TLC) analysis (Hex:EtOAc, 2:1, v/v) indicated complete conversion to the product. The reaction was quenched by pouring the mixture into 200 mL ice water. The resulting precipitate was filtered and washed with H_2O to yield compound S2 (6.2 g, 90%).

^{1}H NMR (500 MHz, $CDCl_3$) δ ppm 1.099 (t, *J* = 7.5 Hz, 3H), 2.612 (q, *J* = 7.0 Hz, 2H), 5.558 (s, 2H), 6.804 (dd, *J* = 8.0, 2.5 Hz, 1H), 7.041 (d, *J* = 2.5 Hz, 1H), 7.095 (d, *J* = 8.5 Hz, 1 H)

^{13}C NMR (100 MHz, DMSO-d6) 149.3411, 147.8646, 131.6051, 124.0586, 118.8417, 107.9194, 24.4890, 15.3093

HRMS (m/z): $[M]^+$ calcd for $[C_8H_{10}N_2O_2]^+$ 166.0737, found 166.0737.

4-ethyl-3-nitrophenol (S3)

Compound S2 (6.2 g, 37.3 mmol) was suspended in a mixture of H_2SO_4 and H_2O (1:3, v/v, 25-50 mL) by sonication (if sonification did not yield a homogenous suspension, a few mL of THF was used to dissolve the solid S2, which was then added to the mixture of aqueous H_2SO_4). $NaNO_2$ (3.86 g, 56.0 mmol) dissolved in H_2O (2.5 mL) was added slowly to the reaction flask and stirred at room temperature for 1.5 h. In a separate flask H_2SO_4:H_2O (4:3, v/v, 75 mL) was added and heated to reflux. To the refluxing mixture, the S2 solution was added dropwise and stirred for 30 min. The mixture was quenched with ice water and extracted with EtOAc (3 x 75 mL). After drying the organic layer with Mg_2SO_4, the solvent was removed in vacuo and the crude product was purified by silica gel flash chromatography (Hex:EtOAc, 2:1) to give S3 (3.11 g, 50%) as a yellow oil.

^{1}H NMR (500 MHz, $CDCl_3$) δ ppm 1.249 (t, *J* = 7.5 Hz, 3H), 2.842 (q, *J* = 8.5 Hz, 2H), 7.030 (dd, *J* = 8.5, 2.5 Hz, 1H), 7.230 (d, *J* = 8.5 Hz, 1H), 7.383 (d, *J* = 2.5 Hz, 1H)

^{13}C NMR (100 MHz, $CDCl_3$) 154.2470, 149.5150, 132.3914, 131.3014, 120.7326, 111.4436, 25.6617, 15.1987

HRMS (m/z): $[M - H]^-$ calcd for $[C_8H_8NO_3]^-$ 166.0510, found 166.0524.

tert-butyl 2-(4-ethyl-3-nitrophenoxy)acetate (S4)

Compound S3 (3.11 g, 18.6 mmol) and tert-butyl 2-bromoacetate (4.35 g, 22.3 mmol) were dissolved in DMF (25 mL). Solid K_2CO_3 (5.14 g, 37.2 mmol) was added to the reaction flask and left to stir at +70 °C for 1.5 h until TLC analysis (2:1 Hex:EtOAc, v/v) indicated complete conversion to the product. The solvent was removed in vacuo and redissolved in 100 mL EtOAc. The organic

layer was washed with saturated NH_4Cl (50 mL) and brine, then dried over Na_2SO_4. Solvent removal in vacuo afforded S4 (4.97 g, 95%) as a yellow oil.

1H NMR (500 MHz, $CDCl_3$) δ ppm 1.253 (t, *J* = 7.5 Hz, 3H), 1.5 (s, 9H), 2.857 (q, *J* = 7.5 Hz, 2H), 4.554 (s, 2H), 7.116 (dd, *J* = 8.5, 2.5 Hz, 1H), 7.277 (d, *J* = 8.5 Hz, 1H), 7.391 (d, *J* = 3 Hz, 1H)

^{13}C NMR (100 MHz, $CDCl_3$) 167.3932, 156.3652, 149.4567, 132.3149, 132.2128, 120.6270, 110.0036, 83.0951, 66.0518, 28.1809, 25.7638, 15.1222

HRMS (m/z): $[M + Na]^+$ calcd for $[C_{14}H_{19}NO_5Na]^+$ 304.1155, found 304.1160.

tert-butyl 2-(4-(1-bromoethyl)-3-nitrophenoxy)acetate (S5)

Compound S4 (4.97 g, 17.7 mmol), N-bromosuccinimide (3.8 g, 19.5 mmol) and benzoylperoxide (0.2 g, 1 mmol) were dissolved in CCl_4 (100 mL) and refluxed for 4 h. The reaction mixture was cooled to room temperature and washed with 0.1% $NaHCO_3$ (aq) and brine, then dried over Na_2SO_4. The solvent was removed in vacuo and the crude product was purified by silica gel flash column chromatography (3:1 Hex:EtOAc, v/v) to afford S4 (5.7 g, 90%) as a yellow oil.

^1H NMR (500 MHz, $CDCl_3$) δ ppm 1.498 (s, 9H), 2.054 (d, *J* = 7 Hz, 3H), 4.571 (s, 2H), 5.787 (q, *J* = 7 Hz, 1H), 7.184 (dd, *J* = 8.5, 3 Hz, 1H), 7.299 (d, *J* = 2.5 Hz, 1H), 7.784 (d, *J* = 9 Hz, 1H)

^{13}C NMR (100 MHz, $CDCl_3$) 167.0028, 157.7588, 148.0010, 131.1486, 130.8123, 120.7031, 109.7326, 83.3722, 66.0153, 42.0634, 28.1845, 27.3715

HRMS (m/z): $[M - Br]^+$ calcd for $[C_{14}H_{18}NO_5]^+$ 280.1179, found 280.1163.

2-(4-(1-bromoethyl)-3-nitrophenoxy)ethan-1-ol (S6)

Compound S5 (5.7 g, 15.9 mmol) was dissolved in 100 mL THF and cooled down to -78 °C. DIBAL-H (39.8 mmol) was added to the reaction flask and stirred at -78 °C for 20 min, and then left to stir for an additional 2 h at 0 °C. TLC analysis (3:1 Hex:EtOAc, v/v) indicated essentially complete conversion to the product. The reaction was quenched by slowly adding 30 mL H_2O to the mixture, followed by the addition of 5% HCl (aq) solution until the aqueous solution became acidic (pH = ~4, as judged by pH paper). After vigorously mixing the biphasic mixture in a separatory funnel, the separated organic layer was washed with brine, then dried over Na_2SO_4. The solvent was removed

in vacuo and the crude product was purified by silica gel flash column chromatography to yield S6 (3.23 g, 60%) as a yellow oil.

^{1}H NMR (500 MHz, $CDCl_3$) δ ppm 2.056 (d, J = 5 Hz, 3H), 4.006 (dd, J = 4.5, 4.5 Hz, 2H), 4.142 (dd, J = 4, 4 Hz, 2H), 5.785 (q, J = 7 Hz, 1H), 7.201 (dd, J = 8.5, 2.5 Hz, 1H), 7.356 (d, J = 2.5 Hz, 1H), 7.783 (d, J = 8.5 Hz, 1H)

^{13}C NMR (100 MHz, $CDCl_3$) 158.5634, 148.1515, 131.0462, 130.2806, 120.5139, 109.6535, 70.1749, 61.2504, 42.1290, 27.3423

HRMS (m/z): $[M - Br]^+$ calcd for $[C_{14}H_{18}NO_5]^+$ 210.0761, found 210.0761.

1-(4-(2-hydroxyethoxy)-2-nitrophenyl)ethan-1-ol (S7)

S6 (3.23 g, 11.1 mmol) was dissolved in 250 mL H_2O and refluxed for 1 h. TLC analysis (1:1 Hex:EtOAc, v/v) indicated essentially complete conversion to the product. The product was extracted with EtOAc (3 x 50 mL). The organic layer was washed with brine and then dried over Na_2SO_4. The solvent was evaporated in vacuo and S7 (2.0 g, 80%) was used for the next step without further purification.

^{1}H NMR (500 MHz, $CDCl_3$) δ ppm 1.540 (d, J = 6.4 Hz, 3H), 3.997 (dd, J = 4.6, 4.6 Hz, 2H), 4.120 (dd, J = 7.1, 7.1 Hz, 2H), 5.341 (q, J = 6.2 Hz, 1H), 7.201 (dd, J = 8.8, 2.8 Hz, 1H), 7.410 (d, J = 2.7 Hz, 1H), 7.734 (d, J = 8.8 Hz, 1H)

1-(4-(2-(acryloyloxy)ethoxy)-2-nitrophenyl)ethyl acrylate (o-NBMA, S8)

To a solution of S7 (2.0 g, 8.88 mmol) and acryloyl chloride (26.6 mmol) in CH_2Cl_2 (75 mL), TEA (3.5 eq) was added and the mixture was stirred at room temperature for 24 h. The mixture was washed with H_2O and brine and then dried over Na_2SO_4. The solvent was evaporated in vacuo and the crude material was purified by silica gel flash column chromatography (2.5:1 Hex:EtOAc, v/v) to yield S8 (1.79 g, 60%) as a yellow oil.

^{1}H NMR (500 MHz, $CDCl_3$) δ ppm 1.653 (d, J = 6.5 Hz, 3H), 4.253-4.272 (m, 2H), 4.517-4.536 (m, 2H), 5.849 (dd, J = 16.5, 1.5 Hz, 1H), 5.87 (dd, J = 16.5, 1.5 Hz, 1H), 6.135 (dd, J = 33, 10.5 Hz, 1H), 6.135 (dd, J = 10.5, 1.5 Hz, 1H), 6.333 (dd, J = 6.5, 6.5 Hz, 1H), 6.425 (dd, J = 38.5, 1.5 Hz,

1H), 6.425 (dd, *J* = 4, 1 Hz, 1H), 7.181 (dd, *J* = 8.5, 2.5 Hz, 1H), 7.471 (d, *J* = 2.5 Hz, 1H), 7.547 (d, *J* = 8.5 Hz, 1H)

^{13}C NMR (100 MHz, DMSO-d6) 165.3601, 164.6091, 157.8246, 148.5720, 132.2687, 132.0463, 128.7689, 128.2840, 127.9741, 127.9522, 120.6063, 109.4215, 67.2670, 66.6545, 62.5167, 21.2189

HRMS (m/z): $[M + Na]^+$ calcd for $[C_{16}H_{17}NO_7Na]^+$ 358.0897, found 358.0888.

Fabrication of photoresponsive polyacrylamide hydrogels

Photoresponsive polyacrylamide gel substrates were prepared based on a previously reported method (44). Briefly, Grid-500 high glass-bottom dishes (Fischer, 50-305-810) were activated for gel attachment by sequential treatment with 0.1 M NaOH, 97% (3-aminoproyl)trimethoxysilane (Sigma Aldrich, 281778) and 0.5% glutaraldehyde (Polysciences, 01909). A prepolymer mixture of 40% (w/v) acrylamide solution (25% by volume, Fisher, BP1402), 2% (w/v) bis-acrylamide solution (2.5% by volume, Fisher, BP1404), 50 mM o-nitrobenzyl bis-acrylate (in DMSO, 3.25% by volume), 1M HEPES (pH 7.0, 1% by volume, Sigma Aldrich, H6147) solution, 71.7 mM acrylic acid N-hydroxysuccinimide ester (in DMSO, 4% by volume, Sigma Aldrich, A8060), and H2O (63.25% by volume) was prepared. After degassing for 30 min, polymerization was initiated by adding 10% (w/v) APS (0.6% by volume, Bio-Rad, 161-0700) solution and TEMED (0.4% by volume, Fisher, BP150). Immediately after initiation, 200 µL of gel solution was pipetted onto the activated glass culture dish and covered with a fibronectin-patterned glass coverslip face down (fabricated as described below). After 30 min of polymerization, PBS was added on the dish and the coverslip was removed. Finally, the gel was washed with PBS.

Preparation of 1D fibronectin micropatterns

1D lines of fibronectin were created on the photoresponsive hydrogels following a microcontact printing method widely applied in the field of surface protein fabrication (45). Briefly, PDMS stamps fabricated by photolithography and containing topographical patterns (21 µm width, 40 µm spacing) were obtained from the M. Piel laboratory (Inst. Curie) and used as received (46). The patterned side of the stamp was inked with 100 µg/mL fibronectin (Sigma Aldrich, F1141) for 1 h. After drying

the stamp using a stream of air, the fibronectin-coated stamp was stamped onto a 12 mm no. 1.5 circular coverslip (Fisher, 12-545-80), rinsed with ethanol and treated with plasma (Harrick Plasma) for 60 sec, and a 20 g weight was placed on top of the stamp. The fibronectin pattern was finally transferred to the gel surface by placing the coverslip face down on the prepolymer solution as described above, immediately upon the initiation of polymerization.

Fabrication of stepwise stiffness gradients by controlled UV exposure

Stiffness patterns were fabricated on photoresponsive hydrogels using a Nikon Eclipse Ti-E epifluorescence microscope and Plan Fluor 10x/0.30NA objective (Nikon), controlled by NIS-Elements software (Nikon). The fibronectin-patterned photoresponsive gel was placed on the stage and, using phase-contrast imaging, two regions were selected such that they were 'A' mm (A > 2) apart. A hypothetical line connecting the two regions ran across the fibronectin patterns perpendicularly (Fig. S4.3). The field diaphragm lever was then adjusted so that the diameter of the illuminated area on the substrate was 500 μm. Fluorescence imaging using a 395/25 nm LED (315 mW) and DAPI filter set with LED fluorescence illumination from a SpectraX light Engine (Lumencor) was initiated, and a time lapse movie of the two regions was captured at 0 s intervals for '15 x A' min, leaving the active shutter open during stage movement. This led to a 500 μm x 'A' mm region being photoirradiated to the extent that all the photolabile crosslinkers in the exposed region were cleaved. The process was repeated in regions parallel to and 500 μm apart from the first irradiated area, resulting in a gel that had alternating, 500 μm wide stiff (~15 kPa) and soft (~8 kPa) regions.

Stiffness characterization by bead indentation

The irradiation time-dependent change in the Young's modulus of the photoresponsive polyacrylamide gel was measured using a bead indentation method (17) based on Hertzian indentation theory. A thick (>1 mm) hydrogel was created by pipetting 300 μL of prepolymer solution onto an activated glass culture dish and covering it with a 25 mm no. 1.5 circular coverslip (Fisher, 12-545-102). After polymerization, the coverslip was removed in PBS and the gel was washed with

additional PBS. A silica bead (Polysciences, 1 mm diameter) was placed on the gel after 200 nm crimson fluorospheres were first gravity-settled on the gel surface to function as markers for measuring bead contact area with epifluorescence microscopy. At each irradiation time point, the bead indentation depth (δ) was calculated from the bead radius (R) and the contact radius (r) according to equation (1):

$$\delta = R - \sqrt{R^2 - r^2} \quad (1)$$

From this indentation depth, the Young's modulus (*E*) was calculated using the Poisson ratio of the hydrogel (*v*) and buoyancy corrected bead force (*f*) according to the Hertz solution:

$$E = \frac{3(1 - v^2)f}{4R^{1/2}\delta^{3/2}} \quad (2)$$

For polyacrylamide gels, v = 0.3–0.5 (here, v = 0.3 was used). The glass bead density was measured to be ~2600 kg/m^3.

Characterization of fibronectin density

To demonstrate the sustained uniformity of the fabricated fibronectin patterns after UV irradiation, immunostaining was performed using primary and secondary antibodies. Briefly, fibronectin-coated photoresponsive gels were rinsed five times with PBS after fabrication. After introducing stiffness patterns based on the method described above, gels were incubated with rabbit anti-fibronectin antibody (1:500, Sigma Aldrich F3648) for 60 min at 37 °C. After rinsing five times with PBS, gels were incubated with goat anti-rabbit IgG-rhodamine (1:1000, Invitrogen 31686) for 45 min at rt. Gels were rinsed with PBS five times prior to imaging.

Cell culture

U-251MG human glioblastoma cells were obtained from Dr. G. Yancey Gillespie (U. Alabama-Birmingham), authenticated using a short tandem repeat assay (University of Arizona Genetics Core) and cultured in Dulbecco's modified Eagle's medium (DMEM)/F-12 (Gibco, 11320-074) supplemented with 8% fetal bovine serum (Sigma, F7524). U-251MG cells were cultured in T25

flasks (Becton Dickinson, 353108) placed in a 37 °C 5% CO_2 incubator for 2-3 days with media comprising 45.5% F12 GlutaMAX supplement (Gibco 31765-035), 45.5% high glucose Dulbecco's modified Eagle's medium (Gibco 10566-024), 8% heat-inactivated fetal bovine serum (Gibco 10438-026), and 1% penicillin/streptomycin solution (Cellgro 30-001-CI). Cells were removed from flask by 5 min incubation in 0.25% trypsin with EDTA in Hanks' balanced salt solution (Gibco 25-052-CI) and transferred to the fibronectin-coated photoresponsive gels at a concentration of 10,000 cells per dish. Cell transferred gels were incubated for 30 min prior to imaging.

Brightfield microscopy and analysis of cell migration

Live phase contrast imaging of U-251MG cells on photoresponsive hydrogels was done using a Nikon Eclipse Ti-E microscope and an Andor Zyla 5.5 sCMOS camera (Andor Technology). The objective was a Plan Fluor 10x/0.30NA objective (Nikon) and samples were maintained in a Bold Line stage top humidified incubator (Okolab) at +37 °C/5% CO_2. Time-lapse movies were acquired at 20 or 30 min intervals for 45 to 60 hours. The number of cells in the soft and stiff regions of the gel, in the beginning and end of the experiment, was quantified. Additionally, the movies were analyzed for cells directly on top of a stiffness gradient. Such cells were tracked over time to investigate their bias for migrating toward either stiffness. Mitotic, dying or crowded cells were excluded from the analysis.

4.1.3 Results and Discussion

Synthesis of o-NBbA

Efficient photolysis and facile incorporation into hydrogels were the two main focuses in developing a novel photocleavable crosslinker. Therefore, photocleavage efficiency of various photolabile functionalities was first considered, which led to the selection of o-nitrobenzyl (o-NB). Due to its high one-photon photolysis efficiency and high deprotection yields,[219] o-NB based compounds have been widely used in many applications relevant to biological systems, including hydrogel-based studies focused on achieving controlled release or immobilization of payloads, photodegradation of gels, or modulation of gel stiffness.[220–222] Therefore, it was deemed suitable

for use in fabricating novel photoresponsive gels. Our second focus to enable facile incorporation of the photocleavable crosslinker and hence easy fabrication of the photoresponsive gels. While there was one report to date that utilized a o-NB based crosslinker for the fabrication of photoresponsive polyacrylamide hydrogels, the reported methodology required a multistep functionalization process to incorporate the crosslinker into the gel network.[218] For a more simpler one-step incorporation of the o-NB crosslinker during the gelation step, two acrylate moieties that are para-position to one another were conjugated to the o-Nb core. The size of the final compound was designed to be similar to bis-acrylamide to minimize the physical perturbation of the gel network once it is incorporated. On that note, o-NBbA was synthesized in seven steps from p-ethyl aniline (Fig. S4.2A). Due to its design, the o-NBbA crosslinker copolymerized with acrylamide and bis-acrylamide to produce a photoresponsive polyacrylamide hydrogel in a single step, and photolysis of o-NBbA did not release any byproducts to the gel environment (Fig. S4.2B). It should be noted that after the publication of our work, a paper that utilized an o-NB-based crosslinker very similar to our molecule was published.[223] While the molecule allowed a one-step incorporation of the o-NB molecule into the gel similar to our work, the molecule experienced a high degree of hydrophobicity due to the excessive carbons in the molecule, which eventually led to certain limitations. Their gels also required additional steps to functionalize the gel surface with reactive moieties to anchor ECM-proteins. The facile ECM-coating method that was used in our photoresponsive gels is covered in later sections.

Preparation, characterization, and optimization of the o-NBbA incorporated photoresponsive hydrogels

The o-NBbA incorporated gel was prepared based on a previously reported method.[224] Briefly, a prepolymer mixture based on a 20 kPa polyacrylamide gel was prepared by replacing half (50 mol%) of the bis-acrylamide content with o-NBbA, aiming to create a gel that exhibits an initial stiffness of 20 kPa that is reduced to 10 kPa, or half of the initial stiffness, once completely photolyzed. Polyacrylamide was chosen over other types of other gels such as collagen, hyaluronic acid, or polyethylene glycol-based gels, as it is known to be inert to interactions with cell surface

receptors, which is a particularly important factor to consider in durotaxis studies. The gels were prepared on glass-bottom dishes were activated by silanized to promote covalent adhesion of the gel to the glass surface.

Once prepared, the stiffness or Young's modulus of the gel was characterized using bead indentation (Fig. S4.3b-d).[225] Softening of the gel was conducted via photolysis while measuring the stiffness, which resulted in a stiffness versus time plot that displayed an exponential decay (Fig. S4.3d). However, the initial (15 kPa) and final (8 kPa) stiffness values were shown lower than expected (20 and 10 kPa, respectively). The discrepancy was larger for gels that had replaced a larger portion of the bis-acrylamide (80 mol%) with o-NBbA. Instead of resulting in 20 kPa gels that become 4 kPa after complete photocleavage of the o-NBbA, the gels exhibited an initial stiffness of 4 kPa that reduces to 1 kPa. In addition, substantial amounts of creases were observed on the surface of the gels, which intensified even further after photoirradiation. Interestingly, while both gels displayed lower stiffness values than expected, the percent reduction was in accordance with the aimed values. In other words, gels that replaced 50% or 80% of the bis-acrylamide with o-NBbA resulted in gels that exhibit a 50% or 80% reduction in stiffness, respectively, after photoirradiation.

Previous studies have indicated that gels soften with increasing bis-acrylamide content, which is due to the clustering and phase separation of the crosslinking molecules, which in turn results in the reduction of the elastically effective crosslinkers.[226] As o-NBbA is even less water-soluble than bis-acrylamide, we hypothesized that the reduction of absolute stiffness values occurs due to similar reasons. Visual observation revealed that the turbidity of the prepolymer solution increases with increasing o-NBbA content, demonstrating that phase separation was occurring due to the hydrophobic crosslinker. We believe this indicates that indeed the crosslinker concentration is decreasing with increasing o-NBbA content which is therefore causing the issues with creasing.

The 10% (v/v) methanol that was added to the prepolymer mixture, originally intended to facilitate the solubilization of the hydrophobic o-NBbA with the rest of the prepolymer components, was another factor that was suspected to aggravate the issue of crease formation and low stiffness values. Among various organic solvents, methanol was chosen due to its high solubility parameter (δ) which would allow it to form a homogenous solution with water. However, once the polymerized

gels were washed and immersed in PBS solution, the gels were anticipated to swell due to the osmotic pressure difference with the surrounding medium, which in turn could cause creasing and reduction in stiffness. Experiments confirmed this was indeed the case. It was shown that when the gel is immersed in high concentration PBS (x10), the extent of creases reduces, which eventually disappears once the buffer solution is exchanged to 10% (v/v) methanol in PBS (Fig. S4.11). These results indicated that different solvent compositions of the gel and surrounding medium could result in structural instability of the gel.

Since durotaxis studies require an even surface where stiffness gradients are the only factor that affects cell migration, obtaining a crease-free gel was particularly important. It was also beneficial to obtain a gel that can exhibit a wide range of stiffness values to diversify the durotactic environment. Therefore, optimization of the gel preparation condition was required before moving onto cell-based studies. First, the components of the prepolymer mixture were adjusted. Increasing the acrylamide content while decreasing the crosslinker content, which was aimed to retain a certain level of stiffness while reducing the amount hydrophobic molecules and hence reduce the tendency of the gels to crease, did not yield improvements.[226] However, removing the methanol from the prepolymer mixture was found to produce gels that are more stable against creases without affecting the stiffness. Therefore, the recipe was modified to exclude methanol from this point forward.

Next, the effect of the cover-glass bottom of the culture dishes on gel-creasing was investigated. Prior to casting the gels on cover dishes, the glass bottoms of the dishes were activated according to a procedure known as silanization.[227] The purpose of the process was to promote covalent anchoring of the gel to the glass substrate. However, previous reports showed that a thin layer of gel fixed to a rigid substrate could experience anisotropic swelling. This change in gel volume was shown to introduce equibiaxial compressive strain on the gel surface and hence result in surface creases.[228] Based on this study, gels were prepared on non-silanized culture dishes to confirm whether relieving the stress applied to the gel surface could help preventing creases. The adjustment was found ineffective, and the surface tension between the gel and the glass itself, even without covalent interactions, seemed sufficient to produce enough strain to

promote the buckling of the gel surface. The thickness of the gel was found to be one of the most important factors in preventing creases. Maintaining a minimal thickness (> 600 μm) of the gel led to crease-free gels, which was in accordance with previous reports that demonstrated the inverse correlation between the thickness of the gel and the onset point of creasing.[228,229]

Despite optimizations that led to improvements, we note that the main source of the issue, which is the hydrophobicity of o-NBbA, was not resolved in this study. We believe functionalizing o-NBbA with water-soluble moieties such as charged carboxylic acids or PEG would be most effective in masking the hydrophobicity of the crosslinker, which would allow a wider applicability of o-NBbA in durotaxis studies. However, as the focus this study was to mimic the brain environment that mostly exhibits stiffness values within 25 kPa, this task was held off for future studies. Therefore, the final product that was obtained was a crease-free gel with an initial stiffness value of 15 kPa which reduces to 8 kPa upon full-photolysis. It is also important to note that despite not having more water-soluble pendant groups, the reported o-NBbA was able to maintain enough hydrophilicity that allowed its dissolution in the prepolymer mixture which was due to its molecular design. The o-NBbA molecule contained only a minimum number of carbons required for its photoactivity and crosslinking capabilities. This was later found to be extremely important, as a similar molecule that was reported following our publication which had only a few more carbons compared to our o-NBbA was shown to require surfactants and a series of heating and vortexing procedures for the solubilization of the molecule. Those interested in a more detailed analysis of the correlation between the gel composition that includes this o-NB based photocleavable crosslinker and the mechanical properties or photodegradation kinetics of the resulting gel are directed to this report.[223] It is important to note that our gel product still holds concerns of creasing, especially when the whole gel is exposed to light that leads to a higher degree of swelling. However, as our studies did not require photolysis of the whole gel but rather irradiation of specific regions, for instance, spot- or line-irradiation for the fabrication of stiffness patterns, the swelling of the photo-exposed regions could be buffered by the surrounding non-irradiated regions of the gel, which could minimize the degree of swelling and hence crease formation.

Fabrication of fibronectin and stiffness patterns onto photoresponsive hydrogels

To promote the adhesion of cells on the gel surface, a coated layer of extracellular matrix (ECM) protein was required. The most commonly used ECM-coating method involves the use of sulfo-SANPAH which is a heterobifunctional photoactivatable crosslinker. One end of the crosslinker contains a phenyl azide that binds to the gel upon UV irradiation, and the other end which consists of an activated N-hydroxysuccinimide (NHS) ester binds to the primary amines of the protein, forming a linkage between the two components. However, this method was not applicable for our studies due to the light-sensitive nature of our gel. Therefore, a microcontact printing method was utilized to transfer 1-D patterned ECM to the gel surface (Fig. S4.3a). Briefly, a PDMS stamp containing topographical patterns created by photolithography was used in creating ECM patterns on a coverslip, which was then placed on top of the prepolymer solution facedown during its gelation. The NHS-ester acrylic acid that was included in the prepolymer solution as a tethering agent allowed the covalent-transfer of the ECM from the coverslip to the surface of the gel without additional activation steps. The remaining activated-esters after ECM-printing was passivated with BSA solution. The ECM protein of choice was fibronectin which was printed as line patterns to restrict the cellular movement to 1-dimension as it would allow easier quantification. Theses line patterns later also allowed easier reproduction of the cellular environment in computational simulation studies.

The next step was to introduce stiffness patterns to the gels. Conventional methods that utilize photomasks require additional steps to design masks via photolithography and suffer from low-resolution and low spatiotemporal control due to irradiation that is restricted to predesignated locations according to the design of the photomask. Therefore, we aimed to create stiffness patterns differently by using an LED from a SpectraX light engine instrument installed on the Nikon TiE microscope, which was originally purposed for epifluorescence imaging. The wavelength of the light was set at 395 nm using the DAPI filter. Using a light source attached to the microscope resulted in multiple advantages. Precise spatial control of the area of irradiation could be achieved due to the ease of switching between phase-contrast imaging and LED irradiation. This advantage also allowed temporal control, which could be exploited for photoirradiation at various time points

during live cell culture. While temporally controlled photolysis was not heavily focused in this study, we expect this capability could be exploited in future studies, for instance, in observing cellular responses that result immediately after introducing a stiffness gradient. The dimensions of light could be easily and precisely controlled by adjusting the field diaphragm and objective of the microscope. The diameter of the LED-irradiated region could be set as low as 59 μm using a 40x objective, which could potentially go lower with a higher objective. High resolution stiffness patterns could be created using the microscope software to create dots, lines, or even planes of light-exposed regions. Taking advantage of these features, alternating 8 and 15 kPa regions were created orthogonal to the fibronectin lines (Fig. S4.3a). Although atomic force microscopy (AFM) measurements were omitted, the stiffness gradients created by this method is presumed to be very steep since the only factor that can cause gradients would be the diffraction that occurs at the air-gel interface.

In durotactic studies, it is preferred that the only factor stimulating cellular migration is the stiffness gradient. Therefore, to confirm that photoirradiation solely alters the stiffness, control experiments were performed. The sustained uniformity of the fabricated fibronectin patterns after UV irradiation was demonstrated by immunofluorescence imaging, in which the irradiated and non-irradiated regions of the gel were shown to display no difference in fibronectin density (Fig. S4.12). The topography was investigated by comparing the z-dimension or thickness of the irradiated and non-irradiated regions of the gel. It was shown that the thickness at the 8 kPa region is only 3% or 20 μm higher than the 15 kPa regions, which is well below the cellular dimensions of U-251MG cells. These results demonstrated that the methodology used in creating stiffness patterns would result in minimal side effects that affect the cellular behavior in any other way.

Observation of U-251MG cells on the fabricated gels

Once transferred to the gel, U-251MG cells were found to attach selectively to the fibronectin printed regions and to migrate along the printed lines. Time-lapse movies were taken for 45-60 hours, and the directional bias for cells migrating at the interface between soft and stiff region were tracked. The expectation was that cells would migrate towards the stiffer 15 kPa

regions, since durotaxis has been widely accepted as a biased movement towards the stiffer parts of the substrate for decades since its initial discovery.[211] However, contrary results were observed. U-251MG cells were shown to preferentially congregate towards the softer 8 kPa regions over the 15 kPa regions (Fig. 4.1e). As supported by experiments in previous sections, this contradicting behavior of U-251MG cells was not an artifact since fibronectin density, topography, and gel composition were shown consistent regardless of substrate stiffness. 5 days after transferring the cells to the gel surface, U-251MG cell were shown to have proliferated overtime and therefore was fully occupying the fibronectin printed regions of the gel. Interestingly, the preference towards the softened regions was so great that the cells had started to realign its orientation to maximize the packing density in these softened regions. In other words, instead of fully adhering along a single line of fibronectin, some cells were found latching onto two lines, perpendicular to the direction of the fibronectin lines, to maximize the amount of cellular localization in the 8 kPa region (Fig. S4.12). These observations were sufficient to confirm the discovery of negative durotaxis, a biased migration of cells towards the softened regions of a substrate, which developed into a highly collaborative project across three continents. Research groups that each possess expertise in computational modeling and microbiology were added to the mix to gain a deeper understanding of the mechanism behind this peculiar behavior of U-251MG cells.

4.1.4 Conclusion

In summary, a novel photocleavable crosslinker was developed and employed in fabricating a photoresponsive hydrogel. The gel required an optimization process to form a flat and even surface, a requirement for it to be utilized as a suitable platform for durotaxis studies. Followed by introduction of stiffness patterns, gels were used as a platform to observe the migration behavior of U-251MG cells. Contrary to our expectations, directional bias towards softer regions of the gel was observed. The discovery of negative durotaxis stimulated a collaboration with multiple institutions to define the mechanism behind the capability of the cell to sense and adjust their movement upon its local environment. While the details of the studies are displayed in Chapter 4.2, the following ending paragraph describes the key points without figure assignments.

There was a previous study that reported that the relationship between traction force and substrate stiffness is biphasic, and that cells generate maximal traction force at the intermediate stiffness range.[230] This 'optimal stiffness' could be predicted in this study by using a mathematical model called the motor-clutch model, where two given molecular components dictate cell migration, ATP-dependent myosin 2 (motor), and mechanical adhesions (clutches) typically caused by integrins. Based on this study, it was hypothesized that cells including U-251MG can potentially exhibit negative durotaxis if their optimal stiffness lies more closely towards the softer region over the stiffer region, and hence if more traction is generated at the softer region over the stiffer region. For validation at the molecular level, protein expression levels of U-251MG cells at various Young's moduli was investigated, which was also compared to that of MDA-MB-231 breast cancer cells which are known to exhibit positive durotaxis. Unlike MDA-MB-231 cells, U-251MG cells did not show any correlation between the substrate stiffness and the key mediators of mechanotransduction such as myosin 2 light chain and focal adhesion kinase. Correlation with mechanosensitive adhesion proteins such as talin or vinculin was not observed as well. However, high activity of integrin was observed, which is a component that is involved in the cell's interaction with the fibronectin-coated substrate. Simulation studies were carried out to see whether the in vitro results could be reproduced. Indeed, when the optimal stiffness was set at softer regions, negative durotaxis could be replicated. This directional movement could be reversed to positive durotaxis when the traction force was set to increase with increasing stiffness. Based on these results, knockdown of talin was performed on MDA-MB-231 cells, which is a factor known to be involved in adhesion reinforcement which in turn leads to the monophasic behavior between traction force and substrate stiffness. It was confirmed that talin downregulated MDA-MB-231 cells behave like U-251MG cells, exhibiting negative durotaxis and clustering to the intermediate regions on a 0.5-22 kPa gel, demonstrating the effect of cellular adhesion forces on durotaxis. Overall, the presence of a single mechanism in sensing the local environment which in turn causes durotaxis was observed across two different cell types, which could be explained by the dynamics of traction force based on the motor-clutch model.

4.2 Negative durotaxis: cell movement toward softer environments

Reproduced with permission from Aleksi Isomursu, Keun-Young Park, Jay Hou, Bo Cheng, Ghaidan Shamsan, Benjamin Fuller, Jesse Kasim, M. Mohsen Mahmoodi, Tian Jian Lu, Guy M. Genin, Feng Xu, Min Lin, Mark Distefano, Johanna Ivaska, and David J. Odde. Negative durotaxis: cell movement toward softer environments.

How cells sense tissue stiffness to guide cell migration is a fundamental question in development, fibrosis and cancer. Although durotaxis – traditionally defined as cell migration toward increasing stiffness – is well established, it remains unknown whether individual cells can migrate toward softer environments. Using microfabricated stiffness gradients, we observed directed glioma cell migration toward lower stiffness. This 'negative durotaxis' did not coincide with changes in canonical mechanosensitive signaling or actomyosin contractility. Instead, motor-clutch-based modeling predicted migration toward cell-intrinsic 'optimal stiffness', where cells generate maximal traction. As predicted by the model, positive durotaxis was switched to negative experimentally by lowering the optimal stiffness via downregulation of a key clutch component, talin. Our results identify the molecular mechanism driving context-dependent positive or negative durotaxis, determined by a cell's contractile and adhesive machinery.

The capacity of living cells to undergo controlled migration is critical for tissue homeostasis and development, and underlies pathological conditions like cancer metastasis[231,232]. Cells migrate in response to chemical and physical cues including the elasticity, or stiffness, of the surrounding extracellular matrix (ECM). The well-known tendency for many cells to migrate toward stiffer substrates, known as durotaxis[211,212,233–236], has implications for both developmental morphogenesis[237,238] and cancer cell invasion[236,239].

Despite progress in empirically identifying environmental conditions and molecular components that enable or promote durotaxis[212,233,240–242], our understanding of its fundamental

mechanisms in different cell types is lacking. A long-standing mathematical model for cell migration is based on the motor-clutch mechanism[225,243–245], in which F-actin filaments polymerize against the plasma membrane to push the cell edge forward, while being simultaneously pulled away from the cell edge by ATP-dependent myosin II ('molecular motors') and pushed by force from the ATP-dependent polymerization itself. Retrograde F-actin flow can be mitigated by mechanical connections or 'clutches', typically integrin-mediated adhesions, between the F-actin and ECM to generate traction and bias cell movement toward more adhesive environments[246,247]. Similarly, fibroblasts on stiffness gradients exhibit asymmetric traction, which has been postulated to contribute to their polarization and durotaxis[234,248]. Interactions between actomyosin machinery and integrin-mediated adhesions have also been implicated in neuronal growth and pathfinding; however, the unifying principles underlying these behaviors across cell types have not been established[249–251].

Recently, cellular traction forces were shown to be maximal on substrates of an 'optimal stiffness' that can be predicted by the motor-clutch model[225,230,245,252–255]. However, the biological relevance of this on cell behavior remains to be fully elucidated. Due to the key role of traction in driving mesenchymal cell migration, we predicted that any cell whose adhesion dynamics are governed by the motor-clutch model could potentially migrate toward *softer* environments, if such environments were closer to the cell's optimal stiffness for maximal traction generation. We call this behavior 'negative durotaxis'.

To test our hypothesis, we seeded U-251MG human glioblastoma cells, previously shown to exhibit maximal traction at an optimal stiffness of 5–10 kPa (Fig. 4.1a)[230], on fibronectin-functionalized polyacrylamide hydrogels having a continuous stiffness gradient of approximately 0.5–22 kPa (Fig. 4.1b)[256] – a range representative of healthy and malignant brain tissue[257]. We observed a strong tendency for these cells to undergo negative durotaxis, migrating from the stiffest regions to regions of intermediate stiffness over time (Fig. 4.1b–c). Fewer cells were observed in the softest regions, implying that cells below the optimal stiffness underwent conventional positive durotaxis. To exclude cell proliferation as a cause of these differences, we quantified the rate of EdU incorporation in cells cultured on homogeneous 0.5, 9.6 and 60 kPa substrates. Proliferation

was equal on 9.6 kPa and 60 kPa hydrogels and only slightly lower on 0.5 kPa substrates (Fig. S4.1a–b), suggesting that the absence of cells in the stiffer regions of the gradient was indeed due to biased migration.

To verify this, we cultured cells on photoresponsive hydrogels with alternating 8 and 15 kPa regions, connected by steep stiffness gradients (hereafter 'stepwise gradients') (Figs. S4.2, S4.3; Supplementary Text 1). 20 μm wide fibronectin lines were printed across the gradients to facilitate cell motility. Live imaging revealed that cells migrated along the fibronectin lines and clustered preferentially in the softer 8 kPa regions (Figs. 4.1d–e, g; S4.1c–d; Movie S1). Moreover, tracking of individual U-251MGs confirmed that any cells making contact with a stiffness gradient migrated preferentially to the 8 kPa side (Fig. 4.1f, h; Movie S2). Taken together, these data demonstrate that U-251MGs are capable of negative durotaxis from stiff to soft environments, consistent with their stiffness optimum for maximal traction.

To gain insight into the molecular basis of negative durotaxis, we investigated key mediators of mechanotransduction, whereby biomechanical cues are translated into changes in cell signaling and behavior[258]. We speculated that a biphasic response in any of these could, in part, modulate the negative durotaxis of U-251MGs. However, no changes were observed in myosin II light chain (MLC2), focal adhesion kinase (FAK) or extracellular signal-regulated kinase (ERK) phosphorylation in U-251MGs cultured on substrates with moduli of 0.5, 8 or 50 kPa (Fig. 4.2a–b). These results were surprising because, in most adherent cell types, increasing substrate stiffness supports integrin clustering and focal adhesion (FA) growth, promoting the activation of mechanosensitive downstream signaling pathways[245,259,260].

This prompted us to compare focal adhesions in U-251MGs, capable of negative durotaxis, and MDA-MB-231 breast adenocarcinoma cells, which reportedly undergo positive durotaxis[236]. As expected, MDA-MB-231s displayed stiffness-induced growth of paxillin-positive FAs (Fig. S4.4a) whereas U-251MGs displayed very few FAs even on 60 kPa substrates, as confirmed by immunostaining of paxillin (Fig. 4.2c) and additional FA markers, vinculin and phosphorylated FAK (Fig. S4.4b). This was not due to low expression of mechanosensitive adhesion proteins talin-1, talin-2 or vinculin, or due to low myosin II activity (p-MLC2), as these were expressed at comparable

levels in U-251MG, MDA-MB-231, and human osteosarcoma U-2 OS, another FA-forming[261] cell line (Fig. S4.4c–d). Nevertheless, U-251MGs displayed high β1-integrin activity and their spreading on fibronectin was sensitive to β1-integrin inhibition with a function-blocking antibody (Mab13) (Fig. S4.4e–g), suggesting that they interact with their substrate primarily through integrins.

Hippo-family proteins yes-associated protein 1 (YAP) and transcriptional co-activator with PDZ-binding motif (TAZ) are transcriptional co-regulators that integrate cues from different mechanical and biochemical sources to direct cell behavior. Nuclear localization and activation of YAP/TAZ on stiff substrates are linked to increased F-actin assembly and FA formation; conversely, YAP/TAZ can promote adhesion turnover and cell migration[262] and baseline YAP activity may even be necessary for conventional durotaxis[241]. We stained endogenous YAP from MDA-MB-231s and observed robust stiffness-induced nuclear translocation (Fig. 4.2d–e). In contrast, U-251MGs displayed much lower nuclear YAP on both soft and stiff substrates, with a slight increase but no visible peak between 0.5 and 60 kPa (Fig. 4.2d–e). Thus, mechanosensitive signaling responses of U-251MGs are minimal and not specific to the 5–10 kPa range, and cannot explain negative durotaxis.

The optimal stiffness for U-251MG traction and the increasing overall motility of these cells (random motility coefficient, RMC) with stiffness up to 100 kPa can be explained by motor-clutch dynamics[230]. Without talin unfolding and vinculin-mediated 'clutch reinforcement' and FA growth, the motor-clutch model naturally predicts a biphasic dependence of traction forces on substrate stiffness[245]. After confirming that U-251MGs migrated preferentially toward their known traction optimum in all of our experimental conditions (Fig. 4.1a–h), we investigated whether stochastic computational simulation of cell-level motor-clutch dynamics would be sufficient to reproduce negative durotaxis (Fig. 4.3a, Supplementary Text 2). We simulated the migration of individual U-251MGs on mechanically homogeneous substrates for one hour to allow the system to reach a dynamic steady state, then placed each cell on a continuous substrate consisting of alternating 60 μm wide regions of low and high stiffness, joined together by smooth 30 μm wide stiffness gradients (Figs. 4.3b, S4.5a–b).

On 10–100 pN nm^{-1} gradients, corresponding to ~10–100 kPa for typical adhesion sizes[263],

and where the cells' optimal stiffness overlaps with the softer regions (Fig. 4.3c–d), we found that the majority of cells translocated away from stiffer areas in the first 12 hours of the simulation (Fig. 4.3e–f). This occurred despite the cells being less motile (i.e. having lower RMC) on the softer substrate (Fig. 4.3d). On stiffness gradients, cellular protrusions (modules) displayed higher average traction on soft than on stiff regions (Fig. 4.3g–i). The cells also migrated preferentially toward the softer side, recapitulating the behavior observed in U-251MGs *in vitro* (Fig. 4.3j). By altering the range of the gradient, such that the side associated with higher predicted traction was the stiffer one, durotaxis could be reversed and cells clustered primarily in the stiff regions (Fig. S4.6a–d).

We verified the generality of these principles by applying them to model axonal pathfinding in neuronal development and regeneration (Figs. S4.7, S4.8; Supplementary Text 3). Indeed, the tendency for *Xenopus* retinal ganglion cells to grow toward softer tissue is closely analogous to negative durotaxis[250]. Neurite elongation and pathfinding via the actin-rich neuronal growth cone (GC) at the distal end of the axon involves contractile filopodia of variable length and orientation (Fig. S4.7a). Applying our model to individual filopodia (Fig. S4.7b) and to GCs with multiple filopodia (Fig. S4.8a), we found that the protrusions elongated faster and generated more traction on soft substrates (0.01–0.1 pN nm^{-1}) (Fig. S4.7c–h). This was consistent both with earlier predictions of relatively low optimal stiffness for neurons[225,264,265], and with our hypothesis that positive and negative durotaxis are governed by motor-clutch dynamics in concert with optimal stiffness. The results also suggested that gradient strength may further increase propensity for negative durotaxis: GCs steered to more compliant regions on substrates with stronger gradients (reaching a maximum at ~10 pN nm^{-1}/20 μm), but did not change direction on mild gradients (~0.1 pN nm^{-1}/20 μm) or on substrates that were overall stiff compared to the optimum (>1 pN nm^{-1}) (Fig. S4.8c–e).

While U-251MGs and neurons exhibit biphasic traction forces in the physiological stiffness range, many adherent cell types do not[239,245,266,267]. Rather, their traction increases as a function of substrate stiffness unless talin- and vinculin-mediated FA formation is disrupted, e.g. by depletion of both talin isoforms[245] (Fig. 4.4a). Therefore, we hypothesized that targeting adhesion

reinforcement can generate an intermediate optimal stiffness and enable negative durotaxis in cell types that normally undergo only positive durotaxis. To test this, we used siRNAs to reduce talin-1 and talin-2 expression in MDA-MB-231 cells that exert increasing traction with increasing substrate stiffness[267] and undergo positive durotaxis in the 2–18 kPa range[236]. Talin knockdown (Fig. 4.4b) resulted in significantly fewer and smaller FAs (Fig. 4.4c–e) and reduced traction on ~20 kPa substrates, where adhesion reinforcement is expected to counteract clutch dissociation by rapidly accumulating forces (Figs. 4.4f–h, S9a). EdU incorporation increased from 0.5 to 9.6 kPa and plateaued thereafter, with and without talin silencing (Fig. S4.9b–c). While control MDA-MB-231s seeded on 0.5–22 kPa stiffness gradients migrated toward the stiffest regions available, talin-low MDA-MB-231s phenocopied the negative durotaxis seen in U-251MGs and clustered predominantly in regions of intermediate stiffness (Fig. 4.4i–j). Thus, the familiar positive durotactic behavior can be converted to negative durotaxis by manipulating the adhesive and contractile machinery of a cell to change its optimal stiffness.

The concept of cells moving toward environments where they can exert more traction is intuitive, but has been previously understood in the context of denser, stiffer ECM providing cells with more stable anchorage[235]. Our results demonstrate the additional capacity of individual cells to migrate toward softer environments, i.e. negative durotaxis, which can be explained by a motor-clutch-based model. Cells that lack robust adhesion reinforcement, such as U-251MG glioma cells or talin-low MDA-MB-231 breast cancer cells, tend to exert maximal traction on substrates of intermediate stiffness, and migrate along gradients to reach this optimum by positive or negative durotaxis (Fig. S4.10). The same mechanism is likely to contribute to the recently described neurite growth toward soft matrix[250].

Besides directly reinforcing connections to stiff matrix, mechanosensitive FA formation may promote positive durotaxis by additional mechanisms. Preferential trafficking of adhesion components toward existing FAs[268], local activation of mechanically gated ion channels[269] or other biochemical signaling pathways initiated at the FAs[260] may all contribute to further polarization of cell-matrix adhesion and, consequently, of cellular traction forces. How these factors influence stiffness optima on different substrates, and in different biological conditions, will be an interesting

topic for future research. Taken together, our results point to a single, conserved mechanism for stiffness sensing and durotaxis across a broad range of cell types, with motor-clutch dynamics driving traction generation and choices between positive and negative durotaxis.

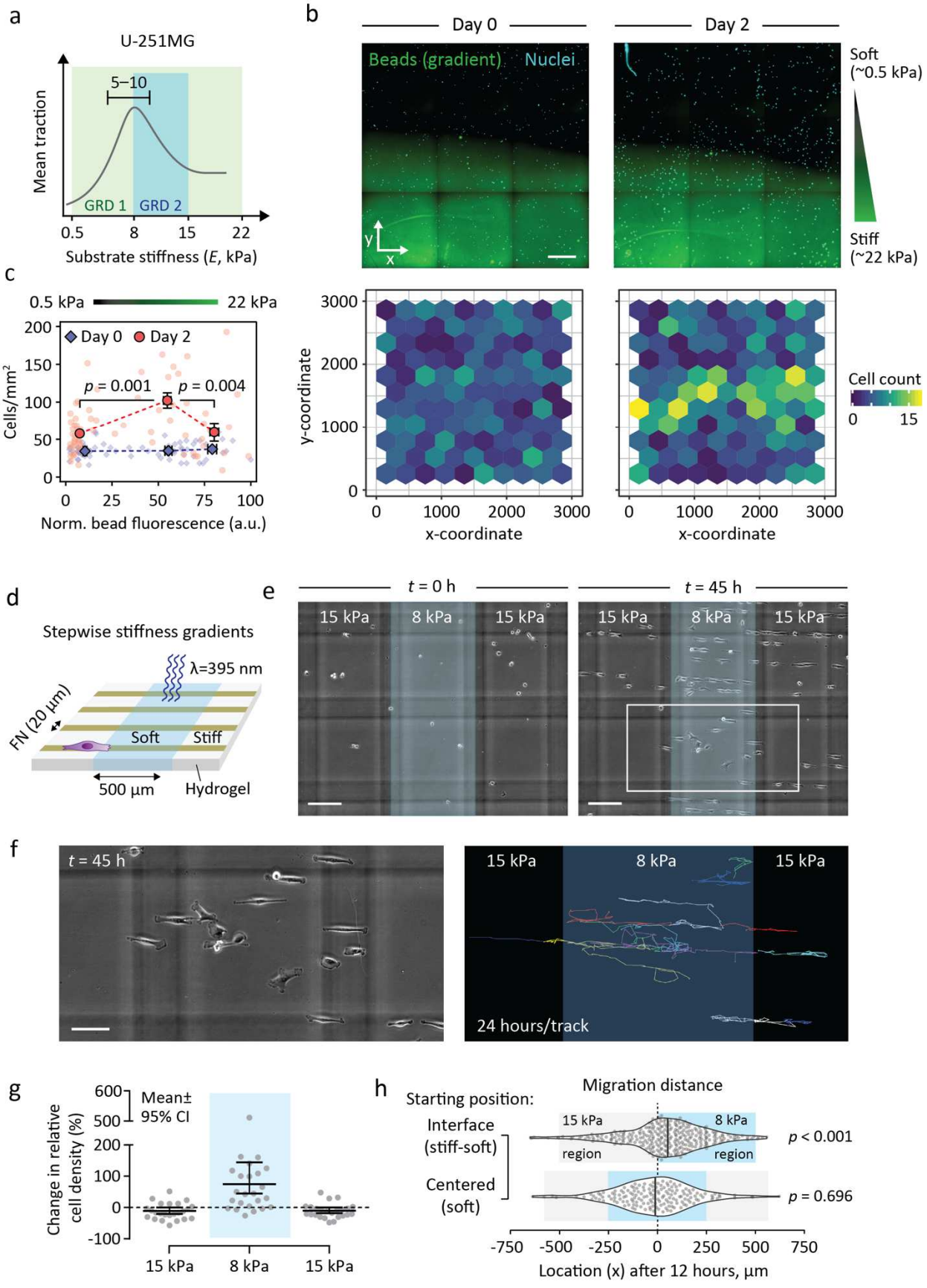
a
U-251MG
5–10
Mean traction
GRD 1
GRD 2
0.5
8
15
22
Substrate stiffness (E, kPa)
b
Day 0
Day 2
Beads (gradient)
Nuclei
Soft
(~0.5 kPa)
Stiff
(~22 kPa)
y
x
c
0.5 kPa
22 kPa
Day 0
Day 2
p = 0.001
p = 0.004
Cells/mm²
Norm. bead fluorescence (a.u.)
y-coordinate
x-coordinate
Cell count
0
15
d
Stepwise stiffness gradients
λ=395 nm
FN (20 µm)
Soft
Stiff
500 µm
Hydrogel
e
t = 0 h
t = 45 h
15 kPa
8 kPa
15 kPa
f
t = 45 h
24 hours/track
g
Mean±
95% CI
Change in relative
cell density (%)
15 kPa
8 kPa
15 kPa
h
Migration distance
Starting position:
Interface
(stiff-soft)
Centered
(soft)
region
p < 0.001
p = 0.696
Location (x) after 12 hours, µm

Figure 4.1 U-251MG glioblastoma cells undergo negative durotaxis. (a) Schematic representation of U-251MG traction, maximal on 5–10 kPa substrates[230], and how it relates to the two stiffness gradients employed here. (b) (Top) Representative region of a diffusion-based polyacrylamide stiffness gradient (Young's modulus ~0.5–22 kPa), at the outset of the experiment and 48 hours later. U-251MG cells are indicated by nuclear staining. Scale bar, 500 μm. (Bottom) Quantification of cells across the gradient. (c) Cell density in different parts of the stiffness gradient. Bins denote pooled regions of interest in the bottom, middle and top third of the gradient, respectively. Mean ± SEM of n = 14–42 ROIs, analyzed by Kruskal-Wallis one-way ANOVA and Dunn's *post hoc* test. (d) Schematic representation of photoresponsive hydrogels with stepwise stiffness gradients. (e–h) U-251MG migration on stepwise gradient hydrogels. A representative example (e) and quantification (g) of the change in cell density across the gradients over time. Blue overlay denotes softer, UV-exposed regions. Vertical and horizontal gray lines in (e) are out-of-focus markings in the underlying glass, used as a reference. Scale bar, 200 μm. Mean ± 95% CI from n = 24 fields of view, from two independent experiments. (f) End points (left) and 24-hour tracks (right) depicting the migration of individual cells in the region denoted by a white rectangle in (e). Scale bar, 100 μm. (h) Violin plots of accumulated distance migrated by individual cells along the x-axis over 12 hours, starting from a gradient (top) or from the middle of a compliant region (bottom). Vertical lines denote medians, n = 164–296 cells from two independent experiments. Analyzed by sign test.

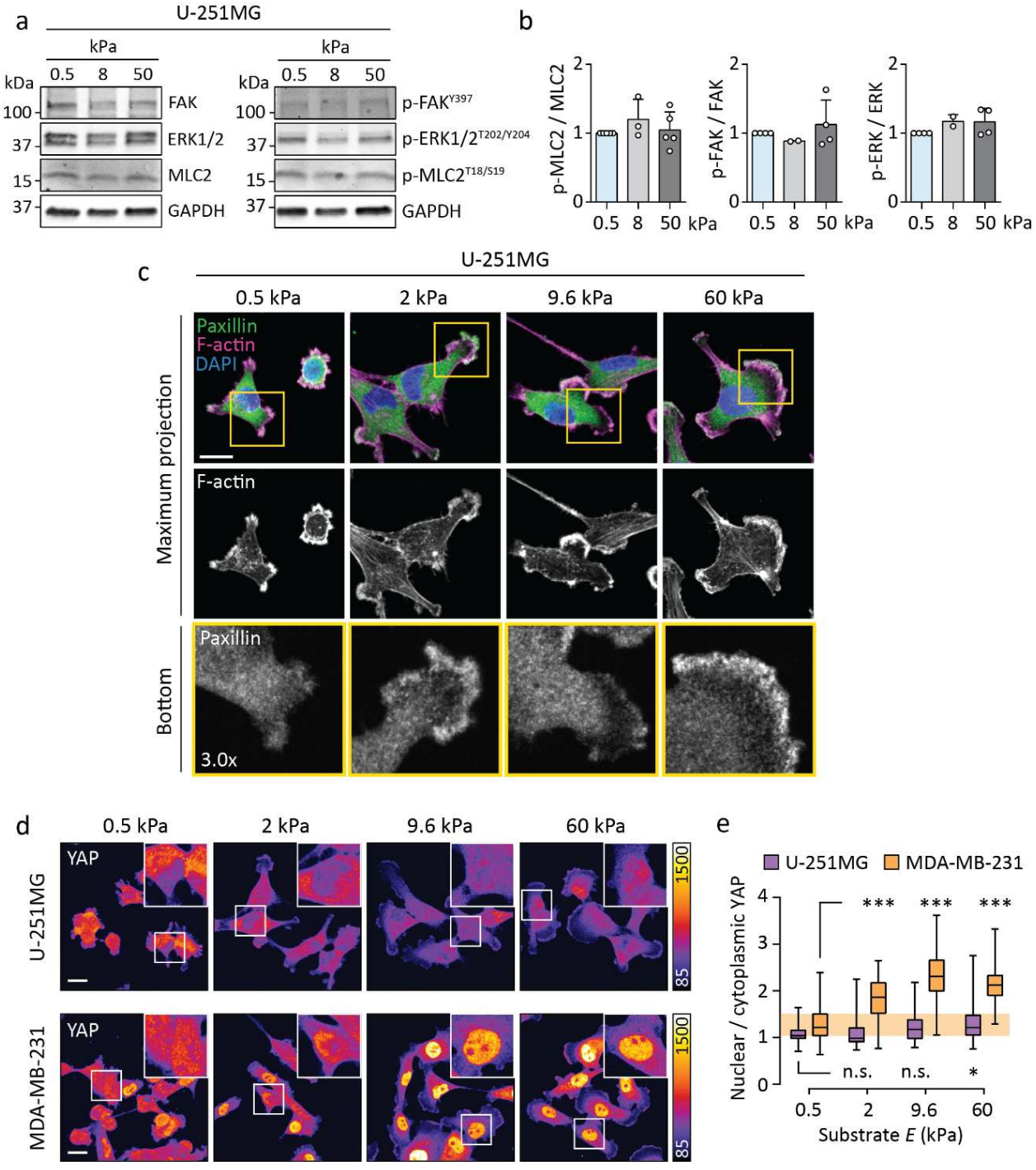
a
U-251MG
kPa
0.5 8 50
kDa
100
37
15
37
FAK
ERK1/2
MLC2
GAPDH
p-FAK Y397
p-ERK1/2 T202/Y204
p-MLC2 T18/S19
b
p-MLC2 / MLC2
p-FAK / FAK
p-ERK / ERK
0.5 8 50 kPa
c
U-251MG
0.5 kPa
2 kPa
9.6 kPa
60 kPa
Maximum projection
Paxillin
F-actin
DAPI
Bottom
3.0x
d
YAP
U-251MG
MDA-MB-231
1500
85
e
U-251MG
MDA-MB-231
Nuclear / cytoplasmic YAP
***
n.s.
*
Substrate E (kPa)

Figure 4.2 U-251MG cells display limited mechanosensitive signaling and adhesion maturation. (a–b) Representative western blot (a) and quantification (b) depicting protein phosphorylation in U-251MGs on 0.5–50 kPa substrates. Mean ± SD of 2–5 independent experiments. (c) Immunofluorescence images of paxillin and F-actin in U-251MGs on 0.5–60 kPa substrates. The bottom panels show individual focal planes from confocal stacks, corresponding to the basal side of each cell. Scale bar, 20 μm. (d–e) Immunofluorescence images (d) and quantification (e) showing the intracellular localization of YAP as a function of substrate stiffness in U-251MG and MDA-MB-231 cells. Insets depict representative nuclei. Scale bar, 20 μm. Each box displays upper and lower quartiles and a median, the whiskers denote minimum and maximum values. n = 57–135 cells, ***$p < 0.001$, *$p = 0.018$, n.s. = not significant, analyzed by Kruskal-Wallis one-way ANOVA and Dunn's *post hoc* test.

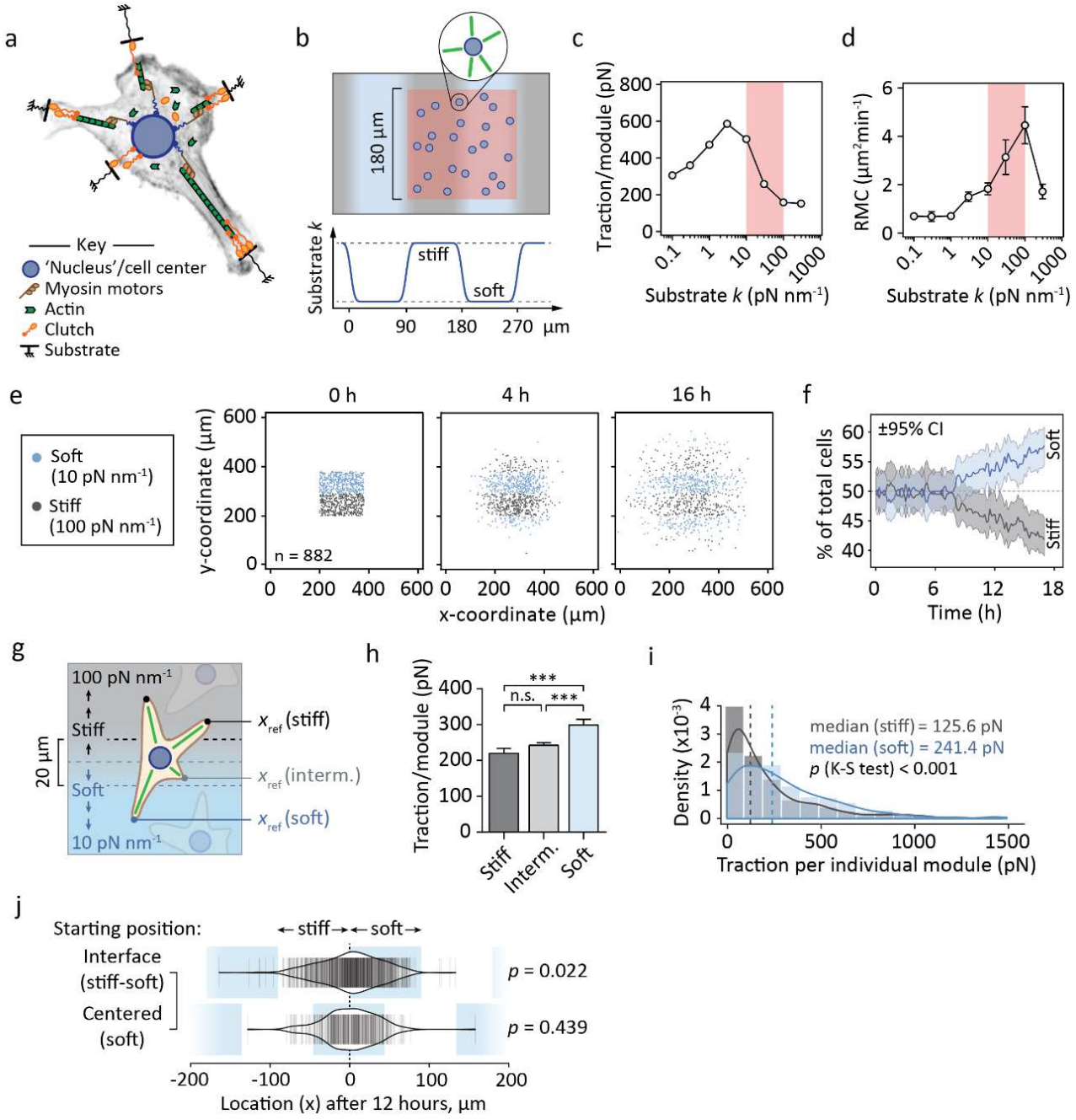
a
Key
'Nucleus'/cell center
Myosin motors
Actin
Clutch
Substrate
b
180 µm
Substrate k
stiff
soft
0
90
180
270 µm
c
Traction/module (pN)
Substrate k (pN nm-1)
d
RMC (µm2min-1)
Substrate k (pN nm-1)
e
Soft
(10 pN nm-1)
Stiff
(100 pN nm-1)
0 h
4 h
16 h
y-coordinate (µm)
n = 882
x-coordinate (µm)
f
±95% CI
% of total cells
Soft
Stiff
Time (h)
g
100 pN nm-1
Stiff
Soft
10 pN nm-1
20 µm
xref (stiff)
xref (interm.)
xref (soft)
h
Traction/module (pN)
n.s.
***
***
Stiff
Interm.
Soft
i
Density (x10-3)
median (stiff) = 125.6 pN
median (soft) = 241.4 pN
p (K-S test) < 0.001
Traction per individual module (pN)
j
Starting position:
stiff
soft
Interface
(stiff-soft)
Centered
(soft)
p = 0.022
p = 0.439
Location (x) after 12 hours, µm

Figure 4.3 Motor-clutch simulations recapitulate negative durotaxis. (a) Schematic representation of the cell migration simulator . Individual modules and a central cell body are attached to the elastic substrate by sets of clutch molecules (Supplementary Text 2). (b) Experimental setup used here and in (Fig. S4.6). Simulated cells in a dynamic steady state were placed on a substrate with repeating stiff and soft regions and tracked over time. An equal number of cells were placed on both stiffnesses (red area). (c–d) Module-wise traction forces (c) and RMC (d) of the simulated cells as a function of substrate stiffness. Red overlay highlights the range of the 10–100 pN nm^{-1} gradient in (e–j). Mean ± SEM of n = 10 cells. (e–f) Evolution of cell density on mechanically heterogeneous substrates over time. (e) Coordinates of individual cells 0, 4 and 16 hours into the simulation. Stiff (≥55 pN nm^{-1}) and compliant (<55 pN nm^{-1}) regions are indicated by gray and blue, respectively. (f) Fraction of cells residing in the stiff and soft regions over the course of the simulation. ±95% CI, n = 882 cells. (g) When individual cells were on top of a stiffness gradient, their traction forces were recorded. (h–i) Forces exerted by clutch modules on stiff, intermediate and soft substrate, while the cell is on top of a stiffness gradient. (h) Bar graphs depicting mean ± SEM of n = 292–1380 modules. ***$p < 0.001$, n.s. = not significant, Kruskal-Wallis one-way ANOVA and Dunn's *post hoc* test. (i) Histograms overlaid with probability density functions, dashed lines indicate medians. n = 292–365 modules, analyzed by Kolmogorov-Smirnov test. (j) Violin plots of accumulated distance migrated by individual cells along the orientation of the gradient and over 12 hours, starting from a gradient (top) or from the middle of a compliant region (bottom). n = 326–759 cells, analyzed by sign test.

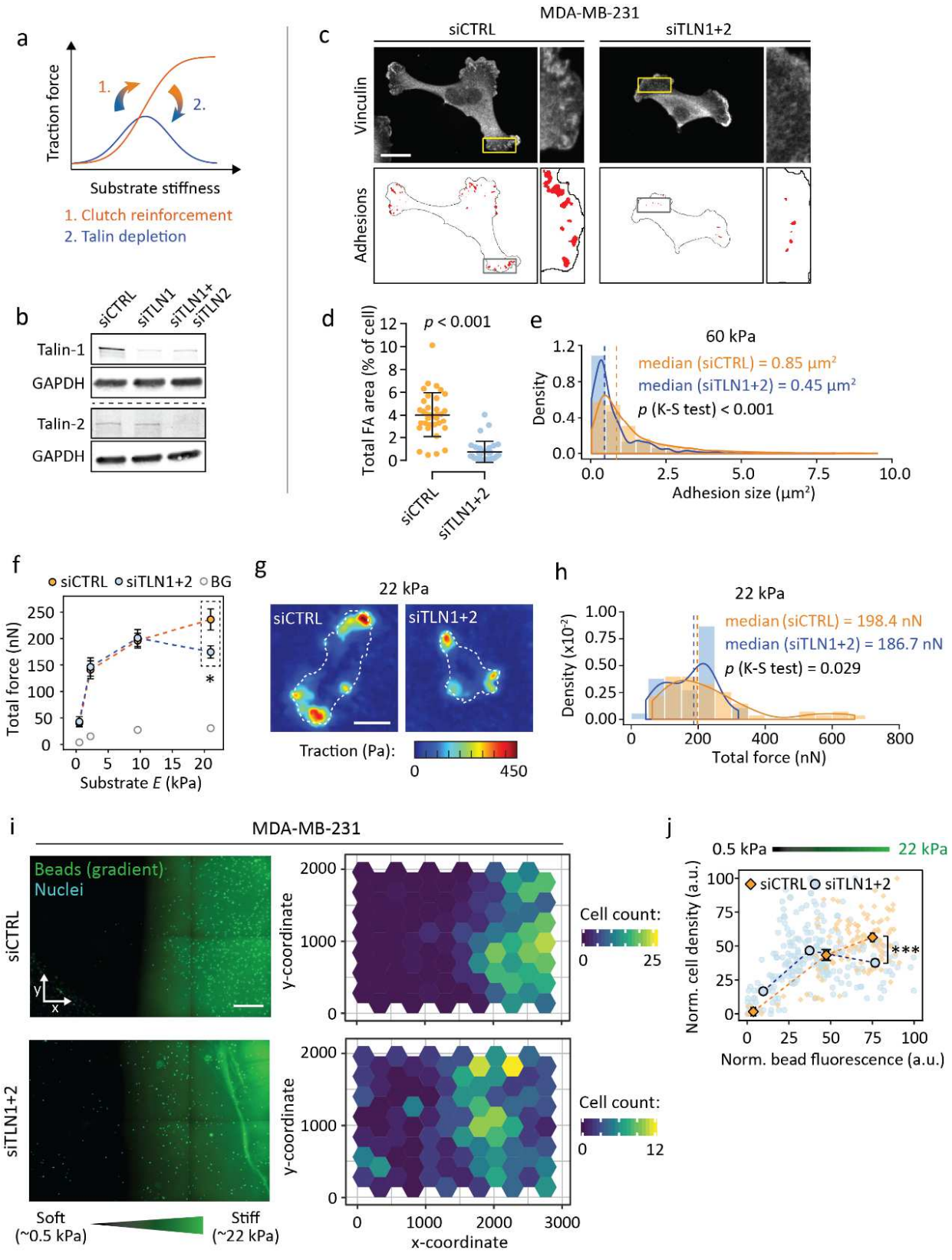
a
Traction force
1.
2.
Substrate stiffness
1. Clutch reinforcement
2. Talin depletion
b
siCTRL
siTLN1
siTLN1+ siTLN2
Talin-1
GAPDH
Talin-2
GAPDH
c
MDA-MB-231
siCTRL
siTLN1+2
Vinculin
Adhesions
d
p < 0.001
Total FA area (% of cell)
siCTRL
siTLN1+2
e
60 kPa
median (siCTRL) = 0.85 µm²
median (siTLN1+2) = 0.45 µm²
p (K-S test) < 0.001
Density
Adhesion size (µm²)
f
siCTRL siTLN1+2 BG
Total force (nN)
Substrate E (kPa)
g
22 kPa
siCTRL
siTLN1+2
Traction (Pa):
0
450
h
22 kPa
median (siCTRL) = 198.4 nN
median (siTLN1+2) = 186.7 nN
p (K-S test) = 0.029
Density (x10⁻²)
Total force (nN)
i
MDA-MB-231
Beads (gradient)
Nuclei
siCTRL
siTLN1+2
y-coordinate
x-coordinate
Cell count:
Soft (~0.5 kPa)
Stiff (~22 kPa)
j
0.5 kPa
22 kPa
siCTRL siTLN1+2
***
Norm. cell density (a.u.)
Norm. bead fluorescence (a.u.)

Figure 4.4 Lowering traction optimum by blocking adhesion reinforcement shifts cells from positive to negative durotaxis. (a) Schematic representation of the relationship between traction forces, substrate stiffness and talin/vinculin-mediated 'clutch reinforcement'. Depletion of these clutch components forces some cell types back into a biphasic traction regime[245]. (b) Representative western blot depicting talin-1 and talin-2 double knockdown in MDA-MB-231 cells. (c–d) Immunofluorescence images (c) and quantification (d) of focal adhesions in MDA-MB-231s on 60 kPa substrate, without and after talin knockdown. Scale bar, 20 μm. Mean ± SD of n = 32–35 cells, analyzed by Mann-Whitney test. (e) Distribution of focal adhesion sizes in control and talin-low cells. Histograms overlaid with probability density functions, dashed lines indicate medians. n = 524–1844 adhesions from 32–35 cells, analyzed by Kolmogorov-Smirnov test. Representative of two independent experiments. (f–h) Traction force analysis of control and talin-low MDA-MB-231s. (f) Total force exerted by the cells as a function of substrate stiffness. Background, BG. Mean ± SEM of n = 18–55 cells from three independent experiments, *p = 0.029. (g) Representative traction maps from cells on 22 kPa substrate. Cell outlines are indicated by white dashed lines. Scale bar, 20 μm. (h) Histograms of the 22 kPa data overlaid with probability density functions, dashed lines indicate medians. n = 37–55 cells from three independent experiments, analyzed by Kolmogorov-Smirnov test. (i) (Left) Representative regions of two 0.5–22 kPa polyacrylamide stiffness gradients, 72 hours after being seeded with MDA-MB-231 cells (indicated by nuclear staining). Scale bar, 500 μm. (Right) Quantification of cells across the gradients. (j) Relative cell densities in different parts of the gradients, overlaid with binned data. Mean ± SEM of n = 13–141 ROIs per bin, from one (siCTRL) or two (siTLN1+2) gradient gels, representative of three independent experiments. Analyzed by Mann-Whitney test.

Materials and Methods

Cell culture and transfections

U-251MG human glioblastoma cells were obtained from Dr. G. Yancey Gillespie (U. Alabama-Birmingham), authenticated using a short tandem repeat assay (University of Arizona Genetics Core) and cultured in Dulbecco's modified Eagle's medium (DMEM)/F-12 (Gibco, 11320-074) supplemented with 8% fetal bovine serum (Sigma, F7524). MDA-MB-231 human breast adenocarcinoma cells were purchased from American Type Culture Collection and authenticated using a short tandem repeat assay (Leibniz Institute DSMZ – German Collection of Microorganisms and Cell Cultures, Braunschweig, Germany). U-2 OS human osteosarcoma cells were acquired from DSMZ. Both MDA-MB-231 and U-2 OS were cultured in high-glucose DMEM (Sigma, D5796-500ML) supplemented with 10% fetal bovine serum (Sigma, F7524), 2 mM L-glutamine (Sigma, G7513-100ML) and 1x non-essential amino acids (Sigma, M7145-100ML). The cells were tested for mycoplasma contamination and cultured at +37 °C, 5% CO_2 in a humidified incubator.

For transient downregulation of target proteins, the cells were transfected with corresponding siRNAs at a 50 nM concentration per oligo. The transfections were conducted using Opti-MEM Reduced Serum Medium (Thermo Fisher Scientific, 31985-047) and Lipofectamine RNAiMAX reagent (Thermo Fisher Scientific, 56532) according to the manufacturer's instructions. The siRNAs used were Hs_TLN1_3 FlexiTube siRNA (Qiagen, SI00086975), Hs_TLN2_3 FlexiTube siRNA (Qiagen, SI00109277) and AllStars Negative Control siRNA (Qiagen, 1027281). Silenced cells were grown for 24 (beginning of migration experiments) to 72 hours before they were used for experiments.

Antibodies

The following antibodies were used at the indicated dilutions: ms anti-paxillin (BD Biosciences, 612405, 1:200 for IF), rbt anti-paxillin (Santa Cruz Biotechnology, sc-5574, 1:200 for IF), ms anti-vinculin (Sigma, V9131, 1:200 for IF, 1:1000 for WB), ms anti-talin-1 (Novus, NBP2-50320, 1:1000 for WB), ms anti-talin-2 (Novus, NBP2-50322, 1:1000 for WB), ms anti-FAK (BD Biosciences, 610088, 1:1000 for WB), rbt anti-p-FAK (Y397) (Cell Signaling Technology, 8556, 1:100 for IF,

1:1000 for WB), rbt anti-MLC2 (Cell Signaling Technology, 3672, 1:1000 for WB), rbt anti-p-MLC2 (T18/S19) (Cell Signaling Technology, 3674, 1:1000 for WB), rbt anti-ERK1/2 (Cell Signaling Technology, 9102, 1:1000 for WB), rbt anti-p-ERK1/2 (T202/Y204) (Cell Signaling Technology, 4370, 1:1000 for WB), ms anti-YAP (Santa Cruz Biotechnology, sc-101199, 1:200 for IF), rbt anti-vimentin (Cell Signaling Technology, 5741, 1:1000 for WB), ms anti-GAPDH (HyTest, MAb 6C5, 1:5000 for WB), ms anti-active β1-integrin (clone 12G10, in-house production, 5 µg/ml for IF), rat anti-inactive β1-integrin (clone Mab13, in-house production, 10 µg/ml for cell culture), and normal rat IgG2a kappa isotype control (eBioscience, 14-4321-85, 10 µg/ml for cell culture).

Additionally, the following secondary antibodies were used for immunofluorescence and immunoblots at the indicated dilutions: Alexa Fluor 488/568-conjugated secondary antibodies raised against mouse (Invitrogen, A21202 and A10037, 1:400 for IF) and rabbit (Invitrogen, A21206 and A10042, 1:400 for IF), IRDye 800CW Donkey anti-Mouse IgG (LI-COR Biosciences, 926-32212, 1:5000 for WB), IRDye 800CW Donkey anti-Rabbit IgG (LI-COR Biosciences, 926-32213, 1:5000 for WB), and IRDye 680LT Donkey anti-Mouse IgG (LI-COR Biosciences, 926-68022, 1:5000 for WB).

EdU incorporation assay

To measure the rate of EdU (5-ethynyl-2′-deoxyuridine) incorporation into DNA, cells were grown on hydrogels for 24 hours, after which they were prepared into fluorescence microscopy samples using an EdU Proliferation Assay Kit (Abcam, ab222421), according to the manufacturer's instructions. Briefly, the cells were supplemented with 20 µM EdU for 2 hours, fixed, permeabilized, and the EdU was stained with iFluor 647 azide via a copper-catalyzed click reaction. Nuclei were counterstained before imaging (see below).

Blocking β1-integrin function with antibodies

U-251MG cells were grown on 0.5 kPa and 60 kPa hydrogels for 24 hours, after which they were treated with 10 µg/ml of anti-inactive β1-integrin (i.e. function-blocking) clone Mab13 or normal rat isotype control for 2 hours (see the list of antibodies for details). The cells were fixed and processed

for immunofluorescence imaging.

Cell migration on stiffness gradient substrates

For analysis of cell migration on continuous 2D stiffness gradients, 15,000 (MDA-MB-231)–20,000 (U-251MG) cells were seeded on a fibronectin-functionalized stiffness gradient hydrogel. Even distribution of cells in the beginning of the experiment was confirmed visually (via brightfield microscopy) and by recording the positions of individual nuclei along the gradient using SiR-DNA. The plate was returned to the incubator for 48 (U-251MG) or 72 hours (MDA-MB-231), after which the cells were fixed and nuclei were re-visualized with DAPI.

For live imaging of U-251MG migration on stepwise gradient hydrogels, 10,000 cells were seeded per dish and allowed to settle in the incubator for 30 min prior to imaging. Time-lapse movies were acquired at 20 or 30 min intervals for 45 to 60 hours. The number of cells in the soft and stiff regions of the gel, in the beginning and end of the experiment, was quantified. Additionally, the movies were analyzed for cells directly on top of a stiffness gradient. Such cells were tracked over time to investigate their bias for migrating toward either stiffness. Mitotic, dying or crowded cells were excluded from the analysis.

Western blotting

Cells on hydrogels were placed on ice, rinsed twice with ice-cold PBS and scraped into lysis buffer [50 mM Tris-HCl pH 7.5, 150 mM NaCl, 1% SDS, 0.5% Triton X-100, 5% glycerol, supplemented with protease (Roche, 05056489001) and phosphatase (Roche, 04906837001) inhibitors]. The lysates were vortexed, placed on a heat block (+90 °C) for 10 min and sonicated before separation by SDS-PAGE (4-20% Mini-PROTEAN TGX Gels, Bio-Rad, 456-1096). Next, the proteins were transferred to nitrocellulose membranes and visualized using 1% Ponceau S staining solution. The membranes were blocked with 5% skimmed milk in TBST and incubated with the indicated primary antibodies overnight at +4°C, followed by fluorophore-conjugated secondary antibodies for 1 to 2 hours at room temperature. All the antibodies were diluted in StartingBlock blocking buffer (Thermo Fisher Scientific, 37538). Finally, the membranes were scanned using an Odyssey infrared imaging

system (LI-COR Biosciences).

Conventional polyacrylamide hydrogels

Glass-bottom dishes (Cellvis, D35-14-1-N) were treated for 20 min at room temperature with 100 µl of Bind-Silane solution – a mixture of 3-(trimethoxysilyl)propylmethacrylate (7.15% by volume, Sigma-Aldrich, M6514) and acetic acid (7.15% by volume) in absolute ethanol – to promote gel attachment to the glass surface. After the Bind-Silane was aspirated, the glass was washed twice with ethanol and left to dry completely. For homogeneous (constant Young's modulus) hydrogels, pre-defined ratios of 40% (w/v) acrylamide (Sigma-Aldrich, A4058) and 2% (w/v) N,N-methyl-bis-acrylamide (Sigma-Aldrich, M1533) were mixed in PBS on ice and vortexed carefully. The final concentrations were adjusted to yield a desired Young's modulus (Table S1). Gels that were indicated for traction force microscopy were supplemented with additional 0.2 µm yellow-green fluorescent (505/515) microspheres (~1.5 x 10^{10}/ml final concentration, Invitrogen, F8811), which were sonicated for 3 min prior to use. Polymerization was initiated by addition of 10% ammonium persulfate (APS, final 0.1% by volume, Bio-Rad) and N,N,N′,N′-tetramethylethylenediamine (TEMED, final 0.2% by volume, Sigma-Aldrich, T-9281) to the solution. Immediately afterwards, 13 µl of the solution was pipetted onto the glass- bottom dish and a 13 mm circular coverslip was placed on top of the droplet. After polymerization for ~1 hour at room temperature, the gel was immersed in PBS for 5 min, the top coverslip was gently removed, and the gel was washed twice with PBS to remove any excess acrylamide. Hydrogels with continuous 2D stiffness gradients were fabricated as described previously[256]. Briefly, 0.5 kPa and 22 kPa acrylamide prepolymer solutions were prepared and 0.1 µm fluorescent (505/515) microspheres (~1.2 x 10^{11}/ml final concentration, Invitrogen, F8803) were added to the 22 kPa solution. After polymerization was initiated, the two solutions were allowed to diffuse together on a glass-bottom dish, under a glass coverslip, to yield a gradient wherein microsphere density correlates linearly with the Young's modulus of the substrate.

Prior to use, the hydrogels were activated by a combination of 0.2 mg/ml Sulfo-SANPAH (Thermo Fisher Scientific, 22589) and 2 mg/ml N-(3-dimethylaminopropyl)-N′-

ethylcarbodiimidehydrochloride (EDC, Sigma-Aldrich, 03450) in 50 mM 4-(2-hydroxyethyl)piperazine-1-ethanesulfonic acid (HEPES). 500 µl of the solution was added on top of the hydrogel and incubated for 30 min at room temperature, protected from light and subjected to gentle agitation. The gel and solution were then UV-irradiated for 10 min (28-32 mW/cm^2) to activate the Sulfo-SANPAH, and the plate was washed with PBS three times to remove any residual compounds. Finally, each hydrogel was functionalized by incubation in 10 µg/ml fibronectin solution overnight at +4°C.

Cells that were collected for protein lysates were cultured on commercial hydrogel-coated 6-well plates (Matrigen, SW6-EC-0.5/SW6-EC-8/SW6-EC-50). These gels were similarly coated with 10 µg/ml of fibronectin before use.

Synthesis of o-NBbA

2-nitro-4-ethyl aniline (S2)

p-Ethyl aniline (5 g, 41.3 mmol) was added dropwise to a cold solution of concentrated H_2SO_4 (30 ml) and stirred for 5 min. In a separate flask, 5.3 ml of 70% HNO_3 (82.6 mmol) was mixed with an equal volume of H_2SO_4, and added dropwise to the reaction vessel, followed by 15 min stirring at 0 °C. Thin layer chromatography (TLC) analysis (Hex:EtOAc, 2:1, v/v) indicated complete conversion to the product. The reaction was quenched by pouring the mixture into 200 ml ice water. The resulting precipitate was filtered and washed with H_2O to yield compound **S2** (6.2 g, 90%).

^{1}H NMR (500 MHz, $CDCl_3$) δ ppm 1.099 (t, J = 7.5 Hz, 3H), 2.612 (q, J = 7.0 Hz, 2H), 5.558 (s, 2H), 6.804 (dd, J = 8.0, 2.5 Hz, 1H), 7.041 (d, J = 2.5 Hz, 1H), 7.095 (d, J = 8.5 Hz, 1 H)

^{13}C NMR (400 MHz, DMSO-d6) 149.3411, 147.8646, 131.6051, 124.0586, 118.8417, 107.9194, 24.4890, 15.3093

HRMS *(m/z):* $[M]^+$ calcd for $[C_8H_{10}N_2O_2]^+$ 166.0737, found 166.0737.

4-ethyl-3-nitrophenol (S3)

Compound **S2** (6.2 g, 37.3 mmol) was suspended in a mixture of H_2SO_4 and H_2O (1:3, v/v, 25-50 ml) by sonication (if sonification did not yield a homogenous suspension, a few ml of THF was used

to dissolve the solid **S2**, which was then added to the mixture of aqueous H_2SO_4). $NaNO_2$ (3.86 g, 56.0 mmol) dissolved in H_2O (2.5 ml) was added slowly to the reaction flask and stirred at room temperature for 1.5 h. In a separate flask H_2SO_4:H_2O (4:3, v/v, 75 ml) was added and heated to reflux. To the refluxing mixture, the **S2** solution was added dropwise and stirred for 30 min. The mixture was quenched with ice water and extracted with EtOAc (3 x 75 ml). After drying the organic layer with Mg_2SO_4, the solvent was removed *in vacuo* and the crude product was purified by silica gel flash chromatography (Hex:EtOAc, 2:1) to give **S3** (3.11 g, 50%) as a yellow oil.

^{1}H NMR (500 MHz, $CDCl_3$) δ ppm 1.249 (t, *J* = 7.5 Hz, 3H), 2.842 (q, *J* = 8.5 Hz, 2H), 7.030 (dd, *J* = 8.5, 2.5 Hz, 1H), 7.230 (d, *J* = 8.5 Hz, 1H), 7.383 (d, *J* = 2.5 Hz, 1H)

^{13}C NMR (400 MHz, $CDCl_3$) 154.2470, 149.5150, 132.3914, 131.3014, 120.7326, 111.4436, 25.6617, 15.1987

HRMS *(m/z):* $[M - H]^-$ calcd for $[C_8H_8NO_3]^-$ 166.0510, found 166.0524.

tert-butyl 2-(4-ethyl-3-nitrophenoxy)acetate (S4)

Compound **S3** (3.11 g, 18.6 mmol) and tert-butyl 2-bromoacetate (4.35 g, 22.3 mmol) were dissolved in DMF (25 ml). Solid K_2CO_3 (5.14 g, 37.2 mmol) was added to the reaction flask and left to stir at +70 °C for 1.5 h until TLC analysis (2:1 Hex:EtOAc, v/v) indicated complete conversion to the product. The solvent was removed *in vacuo* and redissolved in 100 ml EtOAc. The organic layer was washed with saturated NH_4Cl (50 ml) and brine, then dried over Na_2SO_4. Solvent removal *in vacuo* afforded **S4** (4.97 g, 95%) as a yellow oil.

^{1}H NMR (500 MHz, $CDCl_3$) δ ppm 1.253 (t, *J* = 7.5 Hz, 3H), 1.5 (s, 9H), 2.857 (q, *J* = 7.5 Hz, 2H), 4.554 (s, 2H), 7.116 (dd, *J* = 8.5, 2.5 Hz, 1H), 7.277 (d, *J* = 8.5 Hz, 1H), 7.391 (d, *J* = 3 Hz, 1H)

^{13}C NMR (400 MHz, $CDCl_3$) 167.3932, 156.3652, 149.4567, 132.3149, 132.2128, 120.6270, 110.0036, 83.0951, 66.0518, 28.1809, 25.7638, 15.1222

HRMS *(m/z):* $[M + Na]^+$ calcd for $[C_{14}H_{19}NO_5Na]^+$ 304.1155, found 304.1160.

tert-butyl 2-(4-(1-bromoethyl)-3-nitrophenoxy)acetate (S5)

Compound **S4** (4.97 g, 17.7 mmol), N-bromosuccinimide (3.8 g, 19.5 mmol) and benzoylperoxide

(0.2 g, 1 mmol) were dissolved in CCl_4 (100 ml) and refluxed for 4 h. The reaction mixture was cooled to room temperature and washed with 0.1% $NaHCO_3$ (aq) and brine, then dried over Na_2SO_4. The solvent was removed *in vacuo* and the crude product was purified by silica gel flash column chromatography (3:1 Hex:EtOAc, v/v) to afford **S4** (5.7 g, 90%) as a yellow oil.

^{1}H NMR (500 MHz, $CDCl_3$) δ ppm 1.498 (s, 9H), 2.054 (d, *J* = 7 Hz, 3H), 4.571 (s, 2H), 5.787 (q, *J* = 7 Hz, 1H), 7.184 (dd, *J* = 8.5, 3 Hz, 1H), 7.299 (d, *J* = 2.5 Hz, 1H), 7.784 (d, *J* = 9 Hz, 1H)

^{13}C NMR (400 MHz, $CDCl_3$) 167.0028, 157.7588, 148.0010, 131.1486, 130.8123, 120.7031, 109.7326, 83.3722, 66.0153, 42.0634, 28.1845, 27.3715

HRMS *(m/z):* $[M - Br]^+$ calcd for $[C_{14}H_{18}NO_5]^+$ 280.1179, found 280.1163.

2-(4-(1-bromoethyl)-3-nitrophenoxy)ethan-1-ol (S6)

Compound **S5** (5.7 g, 15.9 mmol) was dissolved in 100 ml THF and cooled down to -78 °C. DIBAL-H (39.8 mmol) was added to the reaction flask and stirred at -78 °C for 20 min, and then left to stir for an additional 2 h at 0 °C. TLC analysis (3:1 Hex:EtOAc, v/v) indicated essentially complete conversion to the product. The reaction was quenched by slowly adding 30 ml H_2O to the mixture, followed by the addition of 5% HCl (aq) solution until the aqueous solution became acidic (pH = ~4, as judged by pH paper). After vigorously mixing the biphasic mixture in a separatory funnel, the separated organic layer was washed with brine, then dried over Na_2SO_4. The solvent was removed *in vacuo* and the crude product was purified by silica gel flash column chromatography to yield **S6** (3.23 g, 60%) as a yellow oil.

^{1}H NMR (500 MHz, $CDCl_3$) δ ppm 2.056 (d, *J* = 5 Hz, 3H), 4.006 (dd, *J* = 4.5, 4.5 Hz, 2H), 4.142 (dd, *J* = 4, 4 Hz, 2H), 5.785 (q, *J* = 7 Hz, 1H), 7.201 (dd, *J* = 8.5, 2.5 Hz, 1H), 7.356 (d, *J* = 2.5 Hz, 1H), 7.783 (d, *J* = 8.5 Hz, 1H)

^{13}C NMR (400 MHz, $CDCl_3$) 158.5634, 148.1515, 131.0462, 130.2806, 120.5139, 109.6535, 70.1749, 61.2504, 42.1290, 27.3423

HRMS *(m/z):* $[M - Br]^+$ calcd for $[C_{14}H_{18}NO_5]^+$ 210.0761, found 210.0761.

1-(4-(2-hydroxyethoxy)-2-nitrophenyl)ethan-1-ol (S7)

S6 (3.23 g, 11.1 mmol) was dissolved in 250 ml H_2O and refluxed for 1 h. TLC analysis (1:1 Hex:EtOAc, v/v) indicated essentially complete conversion to the product. The product was extracted with EtOAc (3 x 50 ml). The organic layer was washed with brine and then dried over Na_2SO_4. The solvent was evaporated *in vacuo* and **S7** (2.0 g, 80%) was used for the next step without further purification.

^{1}H NMR (500 MHz, $CDCl_3$) δ ppm 1.540 (d, *J* = 6.4 Hz, 3H), 3.997 (dd, *J* = 4.6, 4.6 Hz, 2H), 4.120 (dd, *J* = 7.1, 7.1 Hz, 2H), 5.341 (q, *J* = 6.2 Hz, 1H), 7.201 (dd, *J* = 8.8, 2.8 Hz, 1H), 7.410 (d, *J* = 2.7 Hz, 1H), 7.734 (d, *J* = 8.8 Hz, 1H)

1-(4-(2-(acryloyloxy)ethoxy)-2-nitrophenyl)ethyl acrylate (o-NBbA, S8)

To a solution of **S7** (2.0 g, 8.88 mmol) and acryloyl chloride (26.6 mmol) in CH_2Cl_2 (75 ml), TEA (3.5 eq) was added and the mixture was stirred at room temperature for 24 h. The mixture was washed with H_2O and brine and then dried over Na_2SO_4. The solvent was evaporated *in vacuo* and the crude material was purified by silica gel flash column chromatography (2.5:1 Hex:EtOAc, v/v) to yield **S8** (1.79 g, 60%) as a yellow oil.

^{1}H NMR (500 MHz, $CDCl_3$) δ ppm 1.653 (d, *J* = 6.5 Hz, 3H), 4.253-4.272 (m, 2H), 4.517-4.536 (m, 2H), 5.849 (dd, *J* = 16.5, 1.5 Hz, 1H), 5.87 (dd, *J* = 16.5, 1.5 Hz, 1H), 6.135 (dd, *J* = 33, 10.5 Hz, 1H), 6.135 (dd, *J* = 10.5, 1.5 Hz, 1H), 6.333 (dd, *J* = 6.5, 6.5 Hz, 1H), 6.425 (dd, *J* = 38.5, 1.5 Hz, 1H), 6.425 (dd, *J* = 4, 1 Hz, 1H), 7.181 (dd, *J* = 8.5, 2.5 Hz, 1H), 7.471 (d, *J* = 2.5 Hz, 1H), 7.547 (d, *J* = 8.5 Hz, 1H)

^{13}C NMR (400 MHz, DMSO-d6) 165.3601, 164.6091, 157.8246, 148.5720, 132.2687, 132.0463, 128.7689, 128.2840, 127.9741, 127.9522, 120.6063, 109.4215, 67.2670, 66.6545, 62.5167, 21.2189

HRMS *(m/z):* $[M + Na]^+$ calcd for $[C_{16}H_{17}NO_7Na]^+$ 358.0897, found 358.0888.

Fabrication of photoresponsive polyacrylamide hydrogels

Photoresponsive polyacrylamide gel substrates were prepared based on a previously reported method[270]. Briefly, Grid-500 high glass-bottom dishes (Fischer, 50-305-810) were activated for gel

attachment by sequential treatment with 0.1 M NaOH, 97% (3-aminoproyl)trimethoxysilane (Sigma Aldrich, 281778) and 0.5% glutaraldehyde (Polysciences, 01909). A prepolymer mixture of 40% (w/v) acrylamide solution (25% by volume, Fisher, BP1402), 2% (w/v) bis-acrylamide solution (2.5% by volume, Fisher, BP1404), 50 mM o-nitrobenzyl bis-acrylate (in DMSO, 3.25% by volume), 1M HEPES (pH 7.0, 1% by volume, Sigma Aldrich, H6147) solution, 71.7 mM acrylic acid N-hydroxysuccinimide ester (in DMSO, 4% by volume, Sigma Aldrich, A8060), and H2O (63.25% by volume) was prepared. After degassing for 30 min, polymerization was initiated by adding 10% (w/v) APS (0.6% by volume, Bio-Rad, 161-0700) solution and TEMED (0.4% by volume, Fisher, BP150). Immediately after initiation, 200 µL of gel solution was pipetted onto the activated glass culture dish and covered with a fibronectin-patterned glass coverslip face down (fabricated as described below). After 30 min of polymerization, PBS was added on the dish and the coverslip was removed. Finally, the gel was washed with PBS.

Preparation of 1D fibronectin micropatterns

1D lines of fibronectin were created on the photoresponsive hydrogels following a microcontact printing method widely applied in the field of surface protein fabrication[271]. Briefly, PDMS stamps fabricated by photolithography and containing topographical patterns (21 µm width, 40 µm spacing) were obtained from the M. Piel laboratory (Inst. Curie) and used as received[272]. The patterned side of the stamp was inked with 100 µg/ml fibronectin (Sigma Aldrich, F1141) for 1 h. After drying the stamp using a stream of air, the fibronectin-coated stamp was stamped onto a 12 mm no. 1.5 circular coverslip (Fisher, 12-545-80), rinsed with ethanol and treated with plasma (Harrick Plasma) for 60 sec, and a 20 g weight was placed on top of the stamp. The fibronectin pattern was finally transferred to the gel surface by placing the coverslip face down on the prepolymer solution as described above, immediately upon the initiation of polymerization.

Fabrication of stepwise stiffness gradients by controlled UV exposure

Stiffness patterns were fabricated on photoresponsive hydrogels using a Nikon Eclipse Ti-E epifluorescence microscope and Plan Fluor 10x/0.30NA objective (Nikon), controlled by NIS-

Elements software (Nikon). The fibronectin-patterned photoresponsive gel was placed on the stage and, using phase-contrast imaging, two regions were selected such that they were 'A' mm (A > 2) apart. A hypothetical line connecting the two regions ran across the fibronectin patterns perpendicularly (Fig. S4.3). The field diaphragm lever was then adjusted so that the diameter of the illuminated area on the substrate was 500 μm. Fluorescence imaging using a 395/25 nm LED (315 mW) and DAPI filter set with LED fluorescence illumination from a SpectraX light Engine (Lumencor) was initiated, and a time lapse movie of the two regions was captured at 0 s intervals for '15 x A' min, leaving the active shutter open during stage movement. This led to a 500 μm x 'A' mm region being photoirradiated to the extent that all the photolabile crosslinkers in the exposed region were cleaved. The process was repeated in regions parallel to and 500 μm apart from the first irradiated area, resulting in a gel that had alternating, 500 μm wide stiff (~15 kPa) and soft (~8 kPa) regions.

Stiffness characterization by bead indentation

The irradiation time-dependent change in the Young's modulus of the photoresponsive polyacrylamide gel was measured using a bead indentation method[225] based on Hertzian indentation theory. A thick (>1 mm) hydrogel was created by pipetting 300 μl of prepolymer solution onto an activated glass culture dish and covering it with a 25 mm no. 1.5 circular coverslip (Fisher, 12-545-102). After polymerization, the coverslip was removed in PBS and the gel was washed with additional PBS. A silica bead (Polysciences, 1 mm diameter) was placed on the gel after 200 nm crimson fluorospheres were first gravity-settled on the gel surface to function as markers for measuring bead contact area with epifluorescence microscopy. At each irradiation time point, the bead indentation depth (δ) was calculated from the bead radius (R) and the contact radius (r) according to equation (1):

$$\delta = R - \sqrt{R^2 - r^2} \quad (1)$$

From this indentation depth, the Young's modulus (E) was calculated using the Poisson ratio of the hydrogel (v) and buoyancy corrected bead force (f) according to the Hertz solution:

$$E = \frac{3(1-v^2)f}{4R^{1/2}\delta^{3/2}} \quad (2)$$

For polyacrylamide gels, v = 0.3–0.5 (here, v = 0.3 was used). The glass bead density was measured to be ~2600 kg/m^3.

Immunofluorescence staining

Samples were fixed for 10 min with warm 4% PFA, followed by permeabilization and blocking for 20 min with 0.3% Triton X-100 in 10% horse serum (Gibco, 16050-122). Primary antibodies were diluted in 10% horse serum and samples were incubated with the antibody overnight at +4 °C. Secondary antibodies were diluted in PBS and samples were incubated with the antibody for one to two hours at room temperature. Where indicated, the nuclei were counterstained using 5 µg/ml DAPI (4',6-diamidino-2-phenylindole) or 500 nM SiR-DNA (Spirochrome, SC007; for live cells) and filamentous actin using 200 nM SiR-actin (Spirochrome, SC001).

Fluorescence and brightfield microscopy

Most fluorescent specimens were imaged using a Marianas spinning disk confocal microscope with a Yokogawa CSU-W1 scanning unit, controlled by SlideBook 6 software (Intelligent Imaging Innovations). The objectives used were a 20x/0.8 Plan-Apochromat (Zeiss) and 40x/1.1 W LD C-Apochromat (Zeiss), and images were acquired using an Orca Flash4 sCMOS camera (Hamamatsu Photonics). The 2D gradient hydrogels with cells were imaged using Nikon Eclipse Ti2-E widefield microscope, controlled by NIS-Elements AR 5.11 software (Nikon). The objective used was a 10x/0.3 CFI Plan-Fluor objective (Nikon), and images were acquired using an Orca Flash4 sCMOS camera (Hamamatsu Photonics) and 2x2 binning.

Live phase contrast imaging of U-251MG cells on photoresponsive hydrogels was done using a Nikon Eclipse Ti-E microscope and an Andor Zyla 5.5 sCMOS camera (Andor Technology). The objective was a Plan Fluor 10x/0.30NA objective (Nikon) and samples were maintained in a Bold Line stage top humidified incubator (Okolab) at +37 °C/5% CO_2.

Traction force microscopy

To measure the tractions exerted by MDA-MB-231 cells on their substrate, polyacrylamide hydrogels of varying stiffness (fibronectin-functionalized and supplemented with fluorescent microbeads) were manufactured on glass-bottom dishes as described above. Cells were seeded on the gels (5,000 cells/plate) approximately 24 hours after transfection with the indicated siRNAs, and grown for another 48 hours before the experiment was conducted. For imaging the cells and beads, a Marianas spinning disk confocal microscope with a stage top incubator unit (+37 °C/5% CO_2) was used. Brightfield images of single cells and fluorescence z-stacks of the beads embedded in the hydrogel were captured before and after cell detachment by addition of 2% sodium dodecyl sulfate.

The resulting data were analyzed using a previously described implementation of Fourier transform traction cytometry . First, displacement fields were calculated using high-resolution subsampling and assuming no outward deformation of the substrate. Optimal L2-regularization was performed on sets of images acquired from soft and stiff gels to determine the final regularization parameter $\lambda = 5 \times 10^{-6}$, which was then used for calculating all the subsequent traction fields. The background, or noise, of the measurements was estimated by analyzing five empty (i.e. no cells) fields of view per substrate stiffness.

Finite element analysis

To estimate the effective spring constant around the interface of a stepwise stiffness gradient, a finite element model using COMSOL Multiphysics (COMSOL, Inc., Burlington, MA) multibody dynamics module was utilized. Two three-dimensional blocks (120 μm x 60 μm x 20 μm) were created and interfaced at (x = 0). Linear elastic material properties were prescribed to both blocks with Poisson's ratio = 0.4, density = 1000 kg/m^3 and Young's modulus = 1 kPa and 10 kPa. A lateral 0.5 nN force was applied on a circular (1 μm radius) surface contact (Figure S4.5a). Fixed boundary conditions were applied to all surfaces except the top surface. The displacement field due to applied loads was computed on a model created using built-in automatic meshing routines (extra-fine mechanics-based mesh). These data were used to calculate effective spring constant at the contact zone (k_{eff} = applied force/average displacement under the circular contact area). The location of

the circular contact and direction of the force were varied, and effective spring constants were calculated accordingly (Figure S4.5b).

Computational modeling of single-cell migration and growth cone steering on stiffness gradients

A previously described[263] C++ version of the stochastic cell migration simulator (CMS) was modified to account for spatial variations in substrate stiffness. The detailed algorithms and equations governing the base CMS have been described in full in[230]. Briefly, the CMS uses the Gillespie Stochastic Simulation Algorithm[274] to simulate an entire cell by connecting several motor-clutch modules to a central cell body and then balancing forces at the center (Fig. 4.3a). Here, the cells were simulated for 60 min to allow them to reach a dynamic steady state, after which each cell was displaced randomly to a 180 μm x 180 μm region on a substrate with repeating soft and stiff areas and connecting stiffness gradients (Fig. 4.3b). Cell positions and traction forces were recorded every second and used to calculate RMC and mean traction force per module. Custom Matlab code was used to quantify module forces on soft and stiff substrates, and to track the displacement of individual cells, from gradients or soft regions, over time. All the CMS simulations were conducted at the Minnesota Supercomputing Institute (MSI). For additional details on the cellular level model and its implementation, see Supplementary Text 2.

The CMS was further modified to investigate filopodial and GC dynamics on substrate stiffness gradients. The filopodia were represented by individual CMS modules that were arranged around an initially semicircular GC. Each filopodia was allocated a set number of molecular clutches – the corresponding substrate clutches were distributed randomly and their spring constants varied linearly with position along the gradient. The details of the GC model and corresponding simulations are presented in Supplementary Text 3.

Image analysis

Images were analyzed using ImageJ (National Institutes of Health) and CellProfiler v2.2.0 (Broad Institute) software. For analysis of YAP nuclear localization, a custom CellProfiler pipeline was used

to segment the cells into nuclei (corresponding to the nuclear counterstain) and cytoplasm (a region of max. 4 μm around the nucleus, excluding parts outside the cell). The mean gray value in the nucleus was divided by the corresponding value in the cytoplasm. For analysis of vinculin-positive adhesions in MDA-MB-231s, a semi-automatic ImageJ script was used: an individual confocal plane from the basal side of the cell was subjected to background removal (rolling ball) and thresholding to exclude cytoplasmic signal and peripheral ruffles. The number and sizes of the remaining adhesions were recorded.

Statistical analysis

Statistical analyses and plotting were performed using GraphPad Prism v6.05 (GraphPad) and R v3.5.1 (R Core Team). Confidence intervals for means were calculated using bias-corrected and accelerated (BCa) bootstrap intervals from 10,000 resamples. Confidence intervals for binomial data were calculated using Wilson score interval. Whenever data were deemed to follow a non-normal distribution (according to Shapiro-Wilk normality test), analyses were conducted using non-parametric methods. The names and/or numbers of individual statistical tests, samples and data points are indicated in figure legends. Unless otherwise noted, all results are representative of three independent experiments and two-tailed *p*-values have been reported.

Supplementary Information

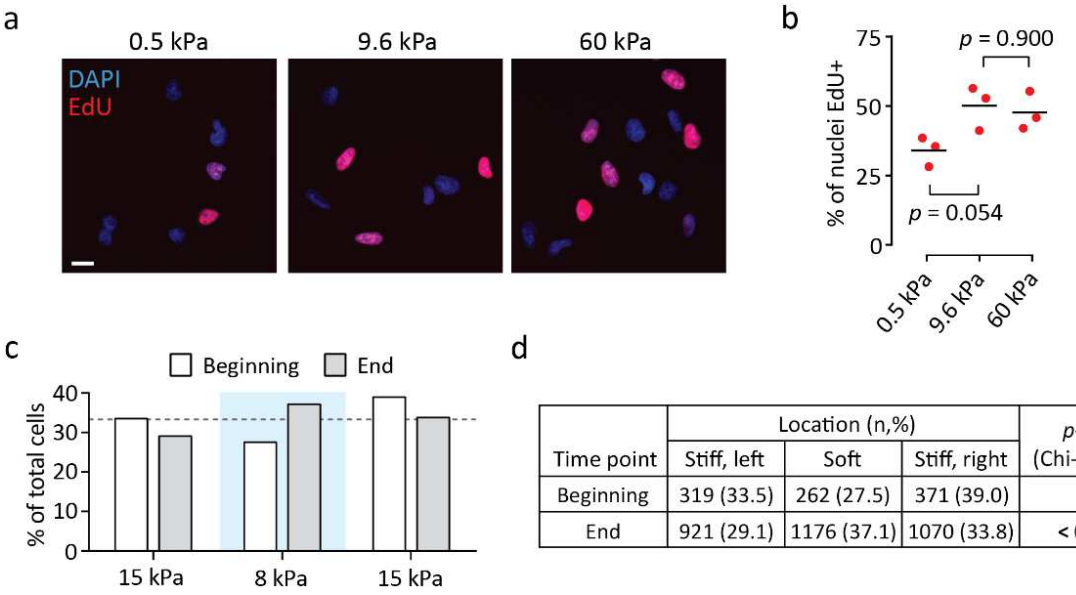

Time point	Location (n,%)			*p*-value (Chi-squared)
	Stiff, left	Soft	Stiff, right	
Beginning	319 (33.5)	262 (27.5)	371 (39.0)	
End	921 (29.1)	1176 (37.1)	1070 (33.8)	**< 0.0001**

Figure S4.1 Mechanosensitivity of U-251MG proliferation and clustering on stepwise stiffness gradients. (a–b) Fluorescence images (a) and quantification (b) depicting EdU incorporation by U-251MG cells on 0.5–60 kPa substrates. Scale bar, 20 µm. Mean values from three independent experiments. Analyzed by one-way ANOVA and Sidak's *post hoc* test. (c–d) Total number of cells in the different gradient regions in (Fig. 4.1e and g). (c) Bar graph, n = 952–3,167 cells per time point. (d) Contingency table summarizing the data, analyzed by chi-squared test.

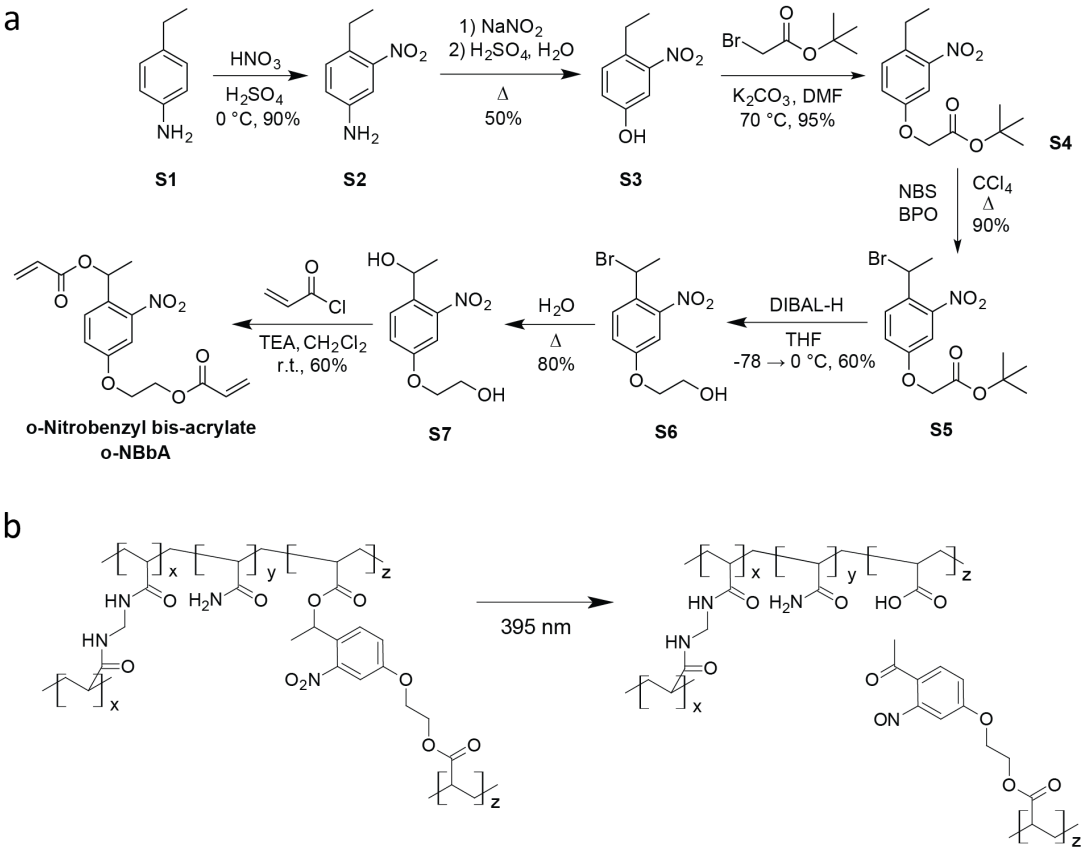

Figure S4.2 Synthesis and photochemistry of o-nitrobenzyl bis-acrylate. (a) Schematic of the synthesis of o-NBbA. (b) Copolymerization of o-NBbA with acrylamide and bis-acrylamide yields hydrogels composed of strands of polyacrylamide crosslinked by either o-NBbA or bis-acrylamide. UV irradiation cleaves the photolabile o-NBbA, resulting in gels with lower crosslinking density and hence lower stiffness. The process does not release any byproducts to the gel environment.

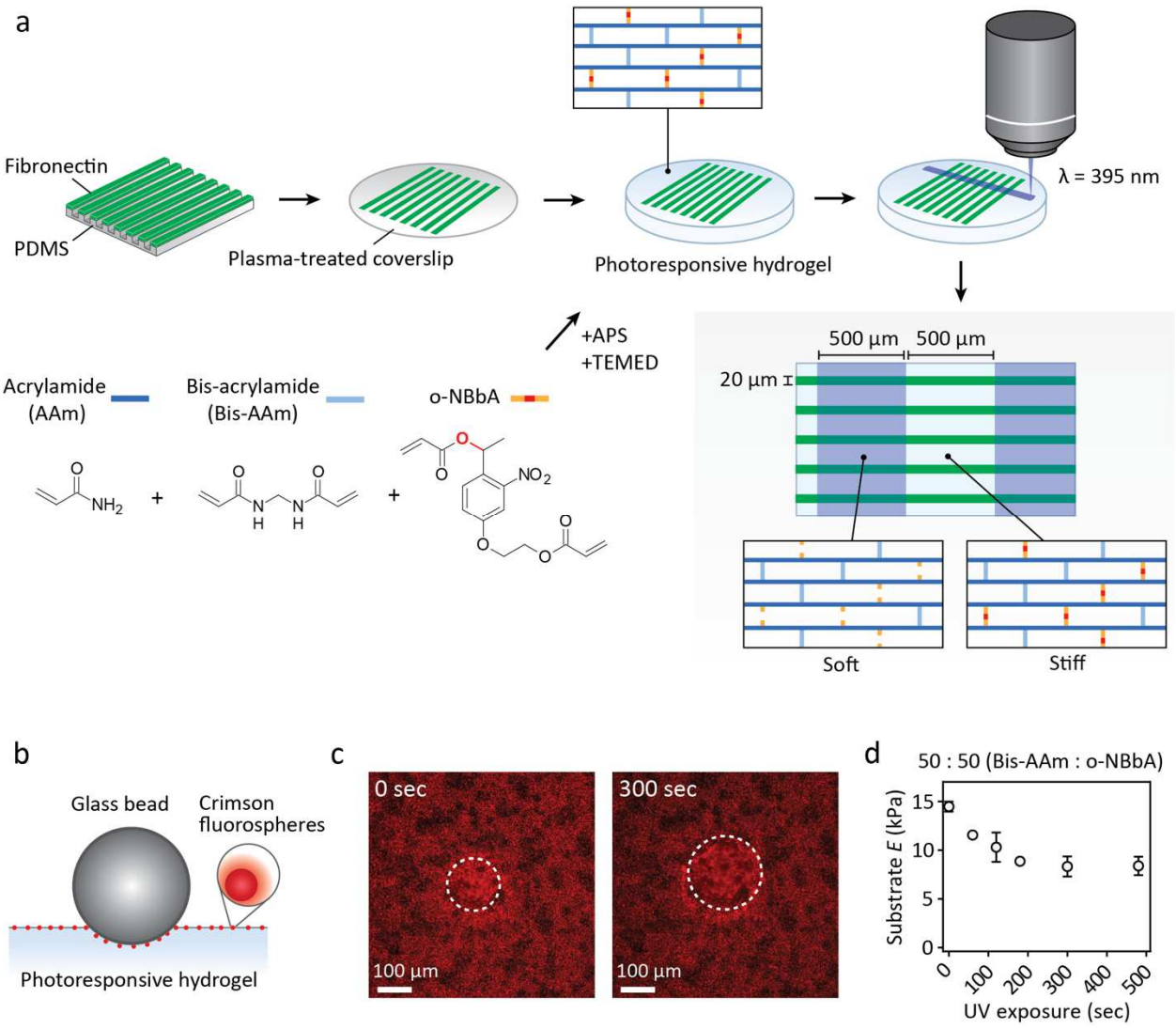

Figure S4.3 Preparation and characterization of photoresponsive hydrogels. (a) Schematic representation of stiffness gradient preparation for migration experiments. The photocleavable carbon-oxygen bond in o-NBbA is indicated by red color. (b–d) Stiffness characterization by bead indentation. A schematic representation of the technique (b), representative fluorescence images (c) and quantified results (d) from the experiment, depicting hydrogel elasticity as a function of UV exposure. Dashed lines indicate indented, out-of-focus areas in the gel. Mean ± SD of n = 3 measurements.

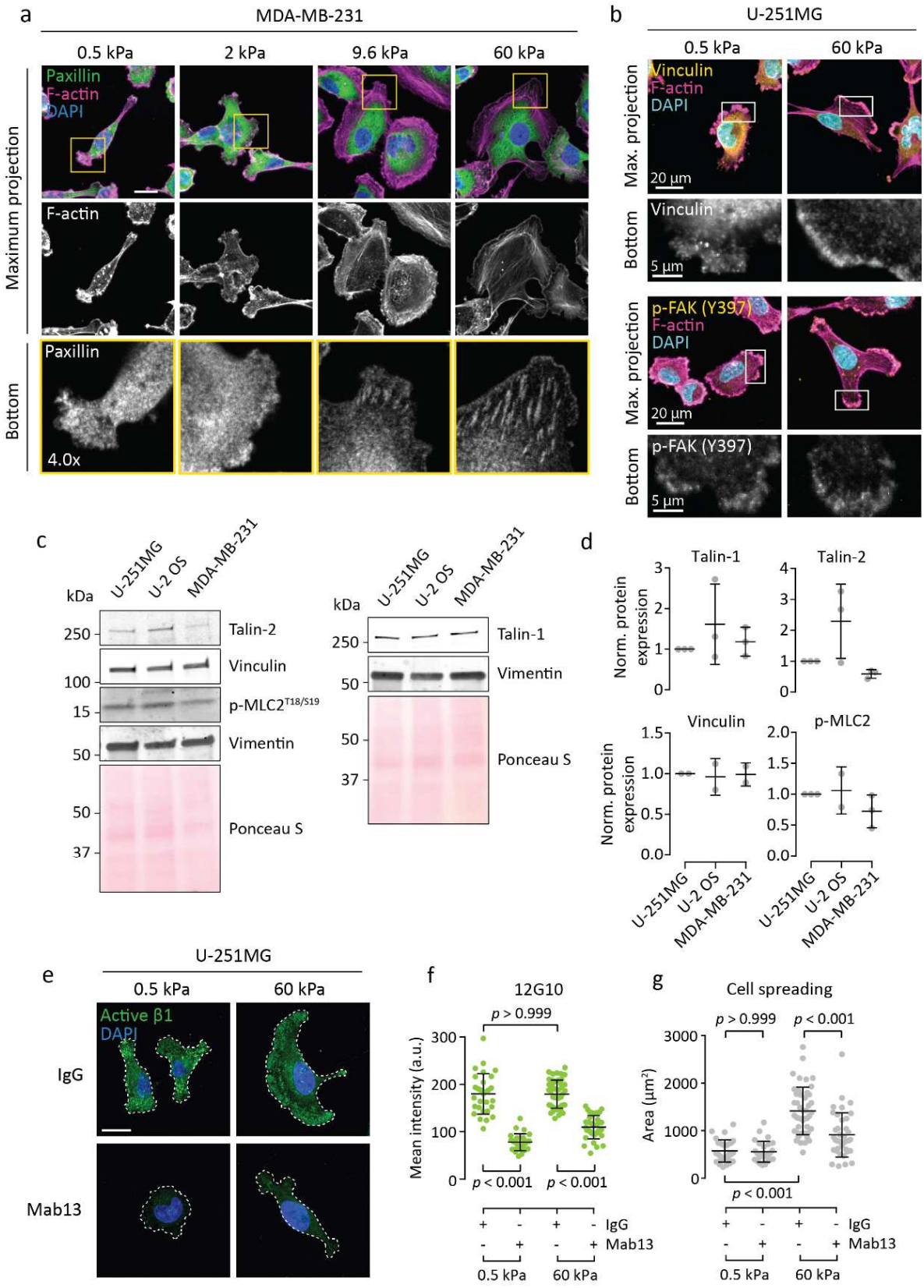

Figure S4.4 Focal adhesion maturation and adhesion components in U-251MG and other cancer

cells. (a) Immunofluorescence images of paxillin and F-actin in MDA-MB-231 cells on 0.5–60 kPa substrates. The bottom panels show individual focal planes from confocal stacks, corresponding to the basal side of each cell. Scale bar, 20 μm. (b) Immunofluorescence images of vinculin (top), p-FAK (bottom) and F-actin in U-251MG cells on 0.5 and 60 kPa substrates. The bottom panels show individual focal planes from confocal stacks, corresponding to the basal side of each cell. (c–d) Representative western blots (c) and quantification (d) depicting talin-1/2, vinculin and p-MLC2 levels across three different cell lines. Densitometric measurements were normalized to vimentin, mean ± SD of 2–3 independent experiments. (e–f) Immunofluorescence images (e) and quantification (f) showing active β1-integrin (clone 12G10) in U-251MGs on 0.5 and 60 kPa substrates. The cells were treated with a control antibody (normal rat IgG) or β1 function-blocking Mab13 for two hours before fixation. Mean ± SD of n = 27–45 cells, analyzed by Kruskal-Wallis one-way ANOVA and Dunn's *post hoc* test. Representative of two independent experiments. (g) Spreading of U-251MGs on 0.5 and 60 kPa substrates, without or after β1-integrin blocking by Mab13. Mean ± SD of n = 27–45 cells, analyzed by Kruskal-Wallis one-way ANOVA and Dunn's *post hoc* test. Representative of two independent experiments.

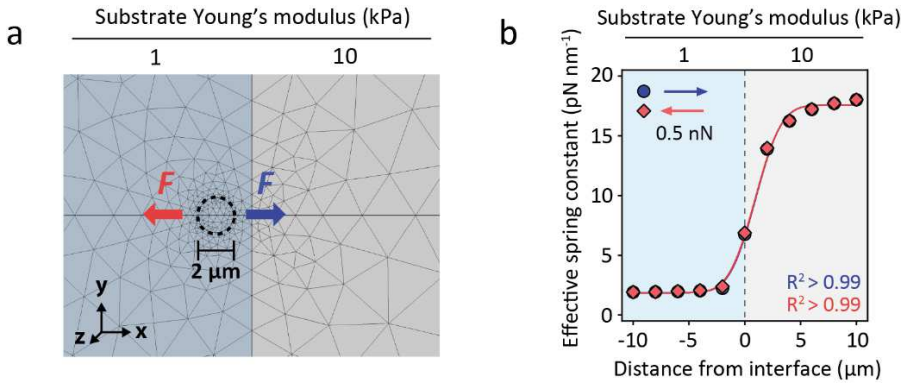

Figure S4.5 Finite element analysis of polyacrylamide displacement next to a stepwise elastic gradient. (a) COMSOL Multiphysics® model setup (b) The effect of steep elastic gradients on the effective spring constant of polyacrylamide. A lateral 0.5 nN force was exerted on the substrate through a circular adhesion zone (r = 1 µm) as shown in (a). The position of the adhesion zone was adjusted repeatedly at 2 µm steps. The direction of the force was varied by 180° but was always parallel to the gradient. In both cases, normal cumulative distribution function was a good fit to the data.

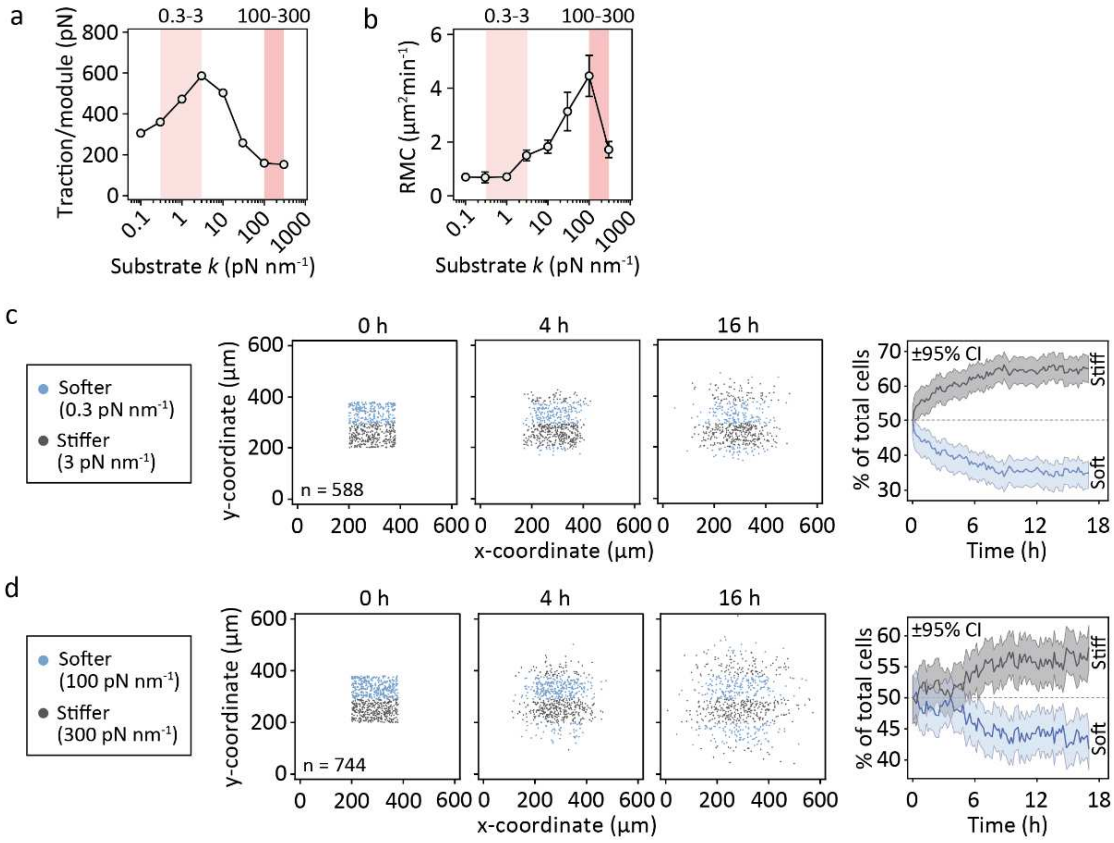

Figure S4.6 Modifying the range of the gradient can reverse durotaxis *in silico*. (a–b) Module traction forces (a) and RMC (b) of the simulated cells as a function of substrate stiffness, as in (Fig. 4.3c-d). Red overlays highlight the ranges of the 0.3–3 pN nm^{-1} and 100–300 pN nm^{-1} gradients in (c–d). Mean ± SEM of n = 10 cells. (c–d) Evolution of cell density on mechanically heterogeneous substrates over time. (c) Coordinates of individual cells on the 0.3–3 pN nm^{-1} gradient 0, 4 and 16 hours into the simulation (left) and the fraction of cells residing in the stiffer and softer areas over the course of the simulation (right). ±95% CI, n = 588 cells. (d) As above, but for the 100–300 pN nm^{-1} gradient. n = 744 cells.

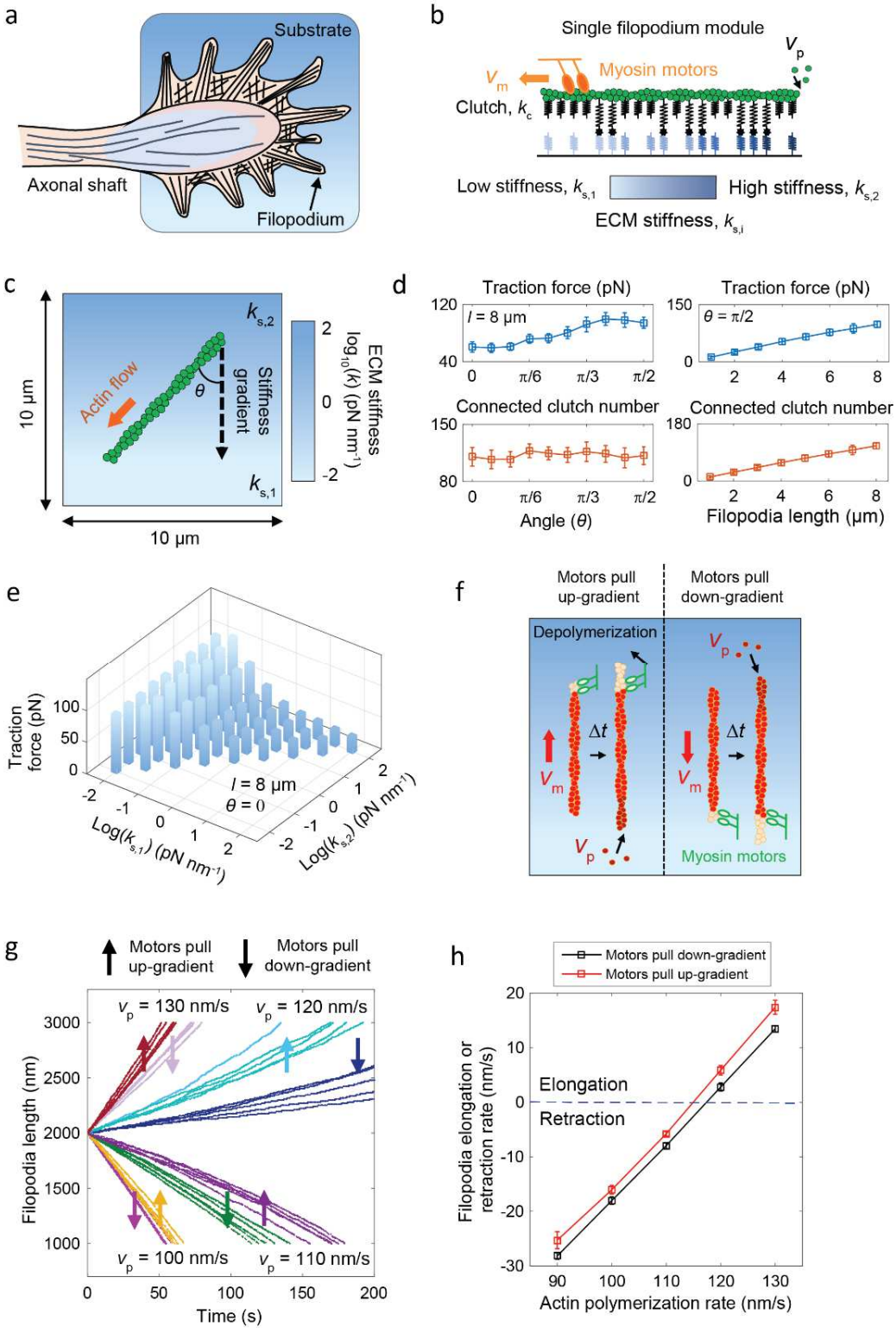
a
Substrate
Axonal shaft
Filopodium
b
Single filopodium module
v_p
v_m
Myosin motors
Clutch, k_c
Low stiffness, $k_{s,1}$
High stiffness, $k_{s,2}$
ECM stiffness, $k_{s,i}$
c
$k_{s,2}$
Actin flow
θ
Stiffness gradient
$k_{s,1}$
10 μm
10 μm
2
0
-2
ECM stiffness $\log_{10}(k)$ (pN nm^{-1})
d
Traction force (pN)
l = 8 μm
Traction force (pN)
θ = π/2
Connected clutch number
Connected clutch number
Angle (θ)
Filopodia length (μm)
e
Traction force (pN)
l = 8 μm
θ = 0
Log($k_{s,1}$) (pN nm^{-1})
Log($k_{s,2}$) (pN nm^{-1})
f
Motors pull up-gradient
Motors pull down-gradient
Depolymerization
v_p
Δt
v_m
Myosin motors
g
Motors pull up-gradient
Motors pull down-gradient
v_p = 130 nm/s
v_p = 120 nm/s
v_p = 100 nm/s
v_p = 110 nm/s
Filopodia length (nm)
Time (s)
h
Motors pull down-gradient
Motors pull up-gradient
Elongation
Retraction
Filopodia elongation or retraction rate (nm/s)
Actin polymerization rate (nm/s)

Figure S4.7 Motor-clutch model of filopodial dynamics. (a) Schematic representation of a neuronal GC. Filopodia, surrounded by a less polarized actin network, reside in the peripheral domain. They are separated from the axon by a thin transitional domain, and a central domain (light blue) that is primarily composed of microtubules. (b) The filopodia in GCs are modeled as individual motor-clutch modules, with adhesion springs (homogeneous stiffness), substrate springs (heterogeneous stiffness) and inward actin flow resulting from active myosin motors. Actin monomers are added into the filaments at a constant rate. (c) Setup used in the single-filopodium simulations. The filopodium interacts with the substrate in a set orientation relative to the linear stiffness gradient. (d) (Left) Traction force exerted by the filopodium increases when the protrusion is pointing down the gradient, toward softer substrate. (Right) Perpendicular to the gradient, traction increases with filopodia length mainly due to more clutches being available to bind with the substrate. Data shown are from *n* = 10 independent simulations. (e) Average traction exerted by a single filopodium on different substrate stiffness gradients. Data represent means of *n* = 10 simulations. (f) Filopodia length is affected by both actin flow, v_m, and the polymerization rate, v_p. Depending on the orientation of the filopodium, the actin may flow toward soft (filopodium pointing up the gradient) or stiff (filopodium pointing down the gradient) substrate. (g) Evolution of filopodia length on stiffness gradients upon different actin polymerization rates. The different combinations of v_p and filopodia orientation are color-coded, while each line represents the temporal variation in the length of a single filopodium. (h) Effect of actin polymerization and orientation relative to a stiffness gradient on the filopodia elongation/retraction rate. Mean ± SEM in (d) and (h).

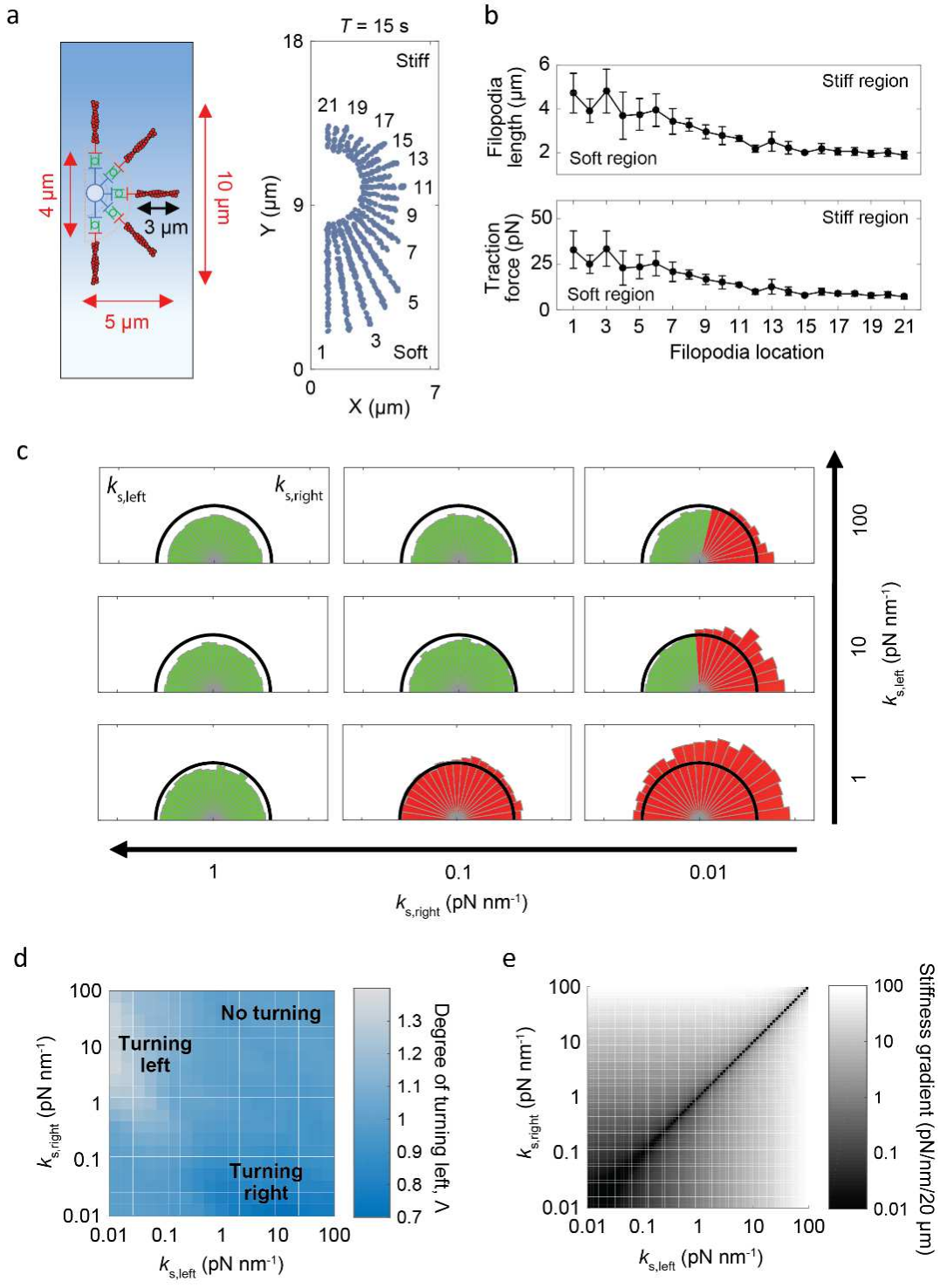
a
4 µm
10 µm
3 µm
5 µm
T = 15 s
Stiff
Soft
Y (µm)
X (µm)
b
Filopodia length (µm)
Stiff region
Soft region
Traction force (pN)
Filopodia location
c
$k_{s,left}$
$k_{s,right}$
$k_{s,left}$ (pN nm^{-1})
$k_{s,right}$ (pN nm^{-1})
d
No turning
Turning left
Turning right
$k_{s,right}$ (pN nm^{-1})
$k_{s,left}$ (pN nm^{-1})
Degree of turning left, Λ
e
$k_{s,right}$ (pN nm^{-1})
$k_{s,left}$ (pN nm^{-1})
Stiffness gradient (pN/nm/20 µm)

Figure S4.8 Motor-clutch model predicts growth cone steering toward soft matrix. (a) Schematic representation of the GC model. (Left) Dimensions of a newly initialized GC. (Right) Each GC consists of multiple filopodia, distributed between –π/2 and π/2 relative to the axon. On stiffness gradients ($k_{s,1}$ = 0.01 pN nm^{-1}, $k_{s,2}$ = 100 pN nm^{-1}), filopodia on the more compliant side of the substrate rapidly outgrow the others, leading to effective turning of the GC. (b) Filopodia length (top) and traction (bottom) based on their orientation around the GC central domain. On stiffness gradients, filopodia pointing toward the softer substrate elongate faster and generate more traction. Data shown are from n = 10 independent simulations. (c) Examples of GC behavior on different stiffness gradients. Green denotes filopodia that are retracting during the course of the simulation, red denotes filopodia that are elongating. Depending on the gradient, individual GCs may retract or enlarge isotropically, or steer toward the softer substrate. Displayed are means of n = 10 simulations. (d) Phase diagram of GC turning to left, Λ, on different mechanically graded substrates. (e) Phase diagram depicting the strength of the stiffness gradient for varying $k_{s,1}$ and $k_{s,2}$. Gradient strength alone cannot explain the magnitude of Λ, if the whole substrate is stiffer than the optimal range for individual filopodia (Fig. S4.7e).

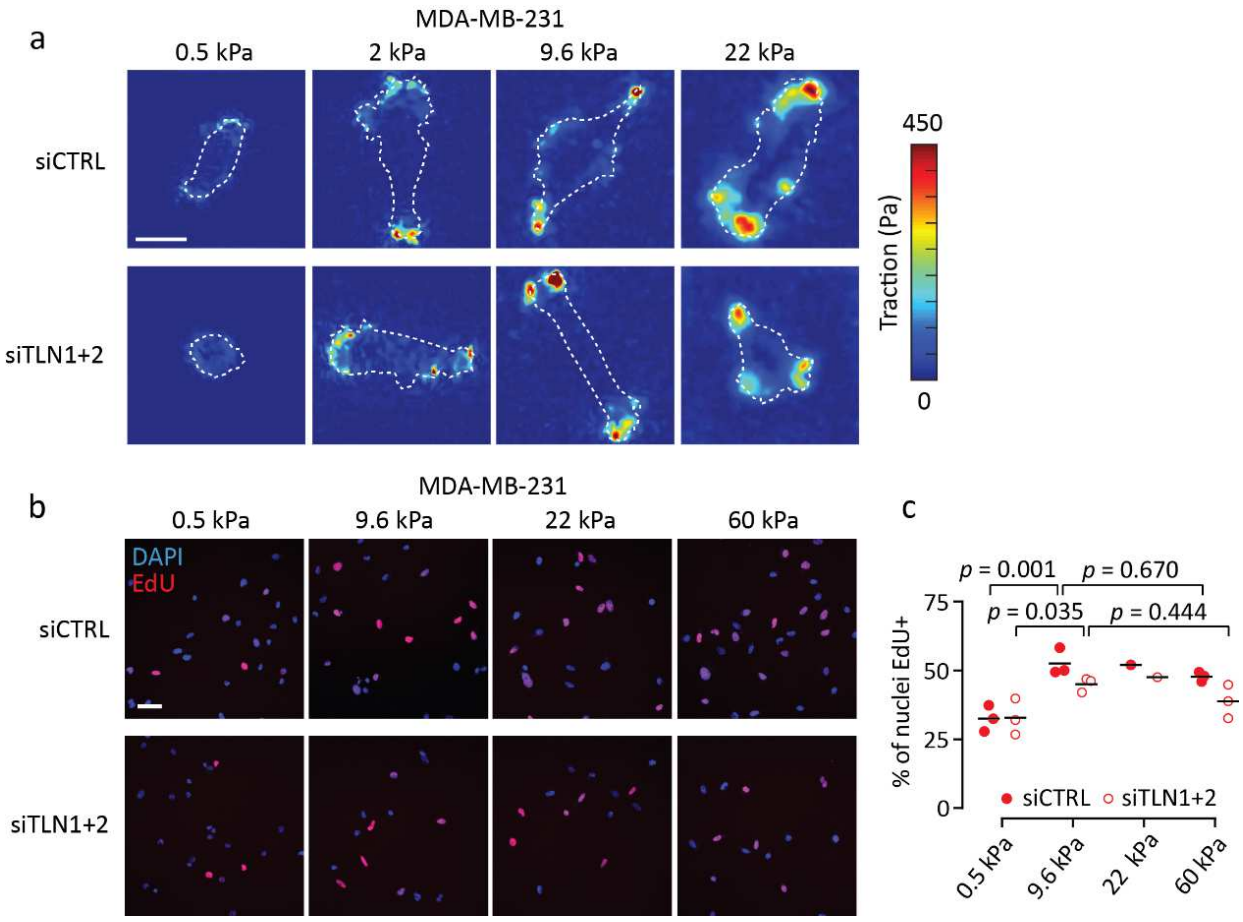

Figure S4.9 Mechanosensitive traction and proliferation of MDA-MB-231 cells. (a) Representative traction maps from MDA-MB-231 cells on 0.5–22 kPa substrates, corresponding to the data in (Fig. 4.4f). Cell outlines are indicated by white dashed lines. Scale bar, 20 μm. (b–c) Fluorescence images (a) and quantification (b) depicting EdU incorporation by control and talin-low MDA-MB-231 cells on 0.5–60 kPa substrates. Scale bar, 50 μm. Mean values from one to three independent experiments. Analyzed by one-way ANOVA and Sidak's *post hoc* test.

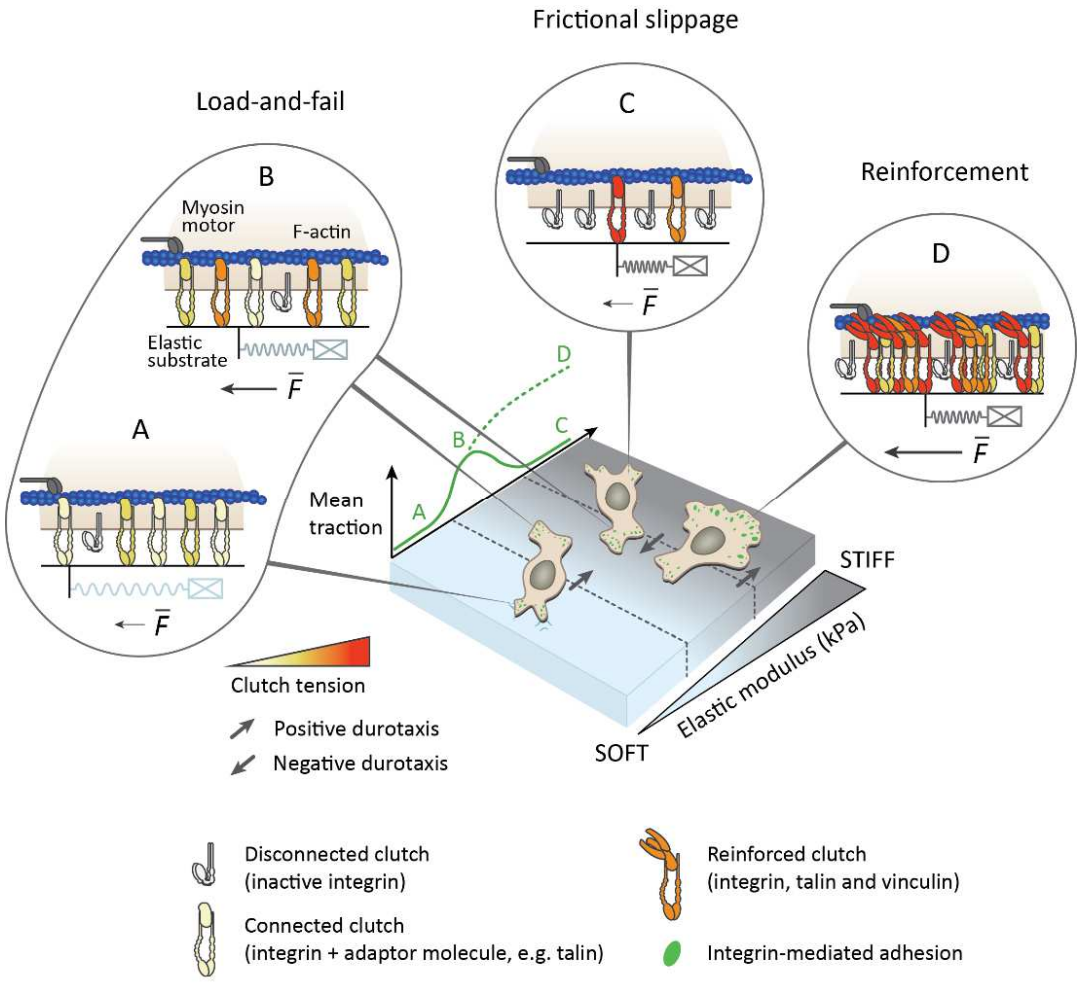

Figure S4.10 Schematic representation of the regulation of positive and negative durotaxis by motor-clutch dynamics. Cell-intrinsic molecular machinery dictates the cell's capacity to exert force on mechanically heterogeneous substrates, driving positive or negative durotaxis. Without clutch reinforcement (mechanosensitive FA formation, D), the motor-clutch model predicts a biphasic relationship between traction force and substrate stiffness (A–C)[17,18,25–29]. This fundamental relationship, and the physical reinforcement of cell-matrix adhesion by FAs, are likely to be further influenced by biochemical signaling pathways and feedback loops that modulate the expression, activity and localization of individual cytoskeletal and clutch components, in a cell type-dependent manner.

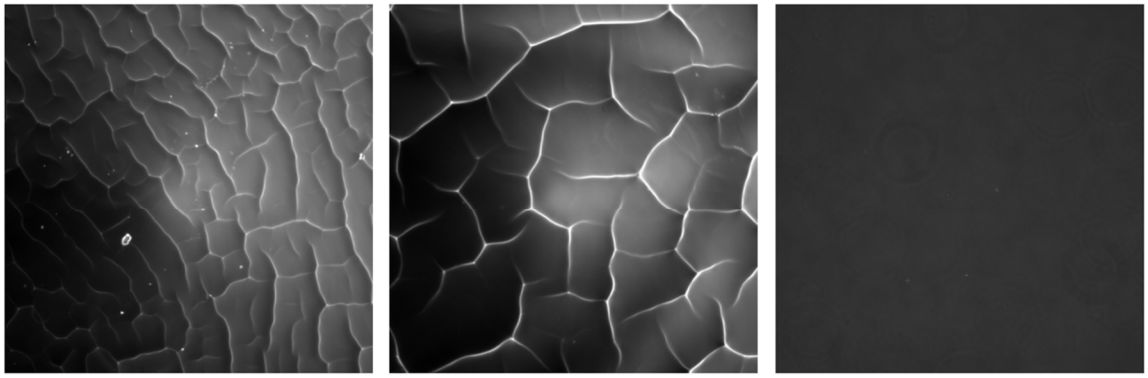

Figure S4.11 Creasing of the photoresponsive gel surface in various solvent conditions. The degree of creasing of the gel immersed in 1x PBS reduces when the solvent is exchanged to 10x PBS, which eventually becomes crease-free when immersed in 10% (v/v) MeOH in water.

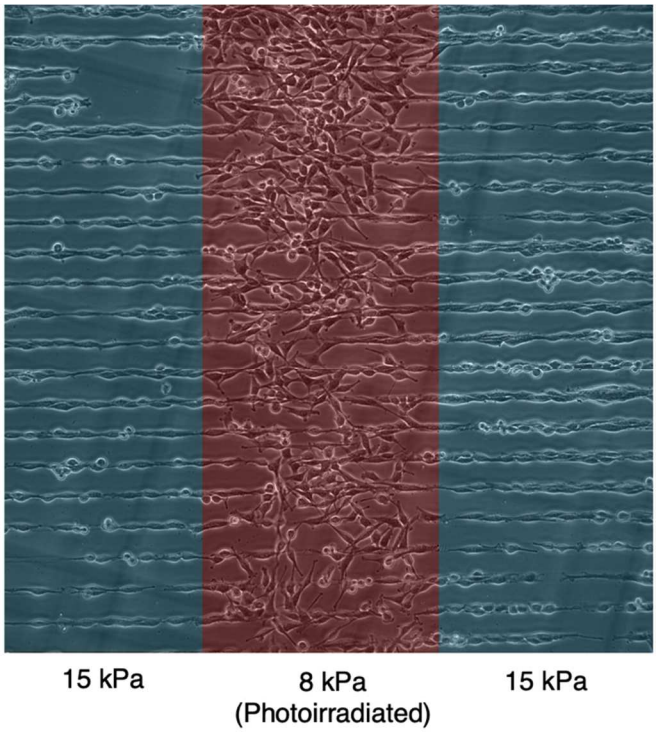

Figure S4.12 U-251MG cells on photopatterned gels 5 days after cell-transfer.

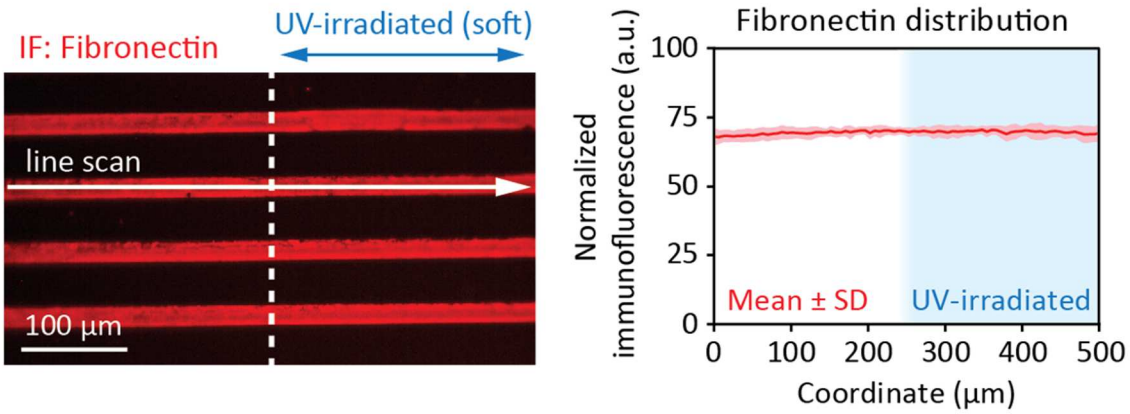

Figure S4.13 Density of the microprinted fibronectin in the UV-irradiated and non-irradiated regions of the photoresponsive gel. Immunofluorescence detection of the fibronectin density by fluorescence microscopy indicated that photocleavage of the gel does not result in changes in fibronectin density.

Supplementary Text 1: Chemistry of o-NBbA and photoresponsive polyacrylamide hydrogels

Polyacrylamide was selected as the base material for the stiffness gradients used in this study, as it is the most widely employed model system for investigating the role of substrate stiffness in directing cell behavior. This is partly due to the ease of obtaining elastic moduli in a wide, physiologically relevant range[49,50]. While other types of gels (e.g. collagen or hyaluronic acid) are known to interact directly with cell surface receptors, including integrins, polyacrylamide gels are inert to such interactions. This allows more control over the types and densities of ligands that will be presented to the cells, making the material ideal for mechanobiological studies. Various methods have been developed to fabricate stiffness gradients in gels to study the durotactic behavior of cells. Some examples exploit the diffusion of two prepolymer solutions[12,30], tilted-superposition of two hydrogels[51], freeze-thaw-induced crosslinking of polyvinyl alcohol[52], or toehold-mediated strand displacement of DNA[53]. Aiming for high-resolution spatiotemporal control over the mechanical properties of the gel, we chose light as the external stimulus[54–58]. Therefore, we aimed to design and synthesize a new, minimalistic and photocleavable crosslinker that contains acrylate moieties. Among various photolabile functionalities that are available, o-nitrobenzyl (o-NB) was chosen due to its high one-photon photolysis efficiency and high deprotection yields[59,60]. o-NB based compounds have been used widely in hydrogel-based studies to achieve controlled release or immobilization of payloads[61–65], photodegradation of gels[66–68], or modulation of gel stiffness[56,69]. However, many of these studies have focused on polyethylene glycol-based gels rather than polyacrylamide, or complete degradation of the gel rather than controlling the Young's modulus. To our knowledge, there has been only one report to date where o-NB-based crosslinkers have been used to fabricate photoresponsive polyacrylamide hydrogels[70]. While the study demonstrates the feasibility of o-NB based crosslinking, the method itself requires multiple steps to crosslink chains of polyacrylamide through the o-NB moiety, which made its application here unwieldy.

In this study, a simple one-step synthesis of photoresponsive polyacrylamide gels was enabled by the functionalization of an o-NB group with two acrylate moieties to yield a crosslinker that would cleave upon photolysis. The photocleavable crosslinker, o-nitrobenzyl bis-acrylate (o-NBbA), was

synthesized in seven steps from p-ethyl aniline (Fig. S4.2a) and designed so that its cleavage would not release any byproducts in the medium (Fig. S4.2b). Based on a previously reported polyacrylamide recipe[44], a photoresponsive gel with an initial stiffness of 20 kPa that can be reduced down to 10 kPa was designed by replacing 50 mol % of bis-acrylamide with o-NBbA. The resulting gel exhibited a Young's modulus of ~15 kPa that was reduced down to ~8 kPa after complete cleavage of the o-NBbA crosslinker by exposure to 395 nm light for 5 min (Fig. S4.3b–d). The slight discrepancy between the expected and measured substrate stiffness could be due to the relatively low water solubility and partial phase separation of o-NBbA in the prepolymer solution, which would result in softening of the hydrogel post-polymerization[71].

The light source used for the photocleavage was an LED from a SpectraX light engine instrument installed in a Nikon TiE microscope, originally intended for epifluorescence imaging. This method had several advantages: spatial control can be achieved easily, as the location of the substrate can be precisely chosen via phase-contrast imaging and the area of irradiation can be controlled with the field diaphragm and objectives. For instance, the diameter of the LED-irradiated area could be adjusted to as low as 59 μm using a 40x objective with a nearly closed field diaphragm, or as high as 978 μm under a 10x objective with a fully opened field diaphragm. Stiffness patterns could also be created using the 'time lapse movie' function of the NIS-Elements software (Nikon). Here, alternating stiffness gradients were created by initiating a time-lapse movie between two regions of the gel, a method that could be modified to yield more complex 1D patterns or even 2D shapes. Although not explored here, temporal control would be equally possible: for example, stiffness gradients could be introduced in gels at various time points during live cell culture, while simultaneously observing cellular behavior and responses.

To conjugate fibronectin to the surface of the gel via covalent interaction, acrylic acid N-hydroxysuccinimide (NHS) ester was used as the tethering agent. While two methods, addition of acrylic acid NHS ester in the pregel solution followed by stamping of fibronectin, or stamping of the pregel solution with fibronectin preincubated with acrylic acid NHS ester, both produced fibronectin-patterned hydrogels, the former was chosen since it yielded more consistent results. Once the gel had been fabricated, any remaining NHS ester moieties in the gel were passivated with bovine

serum albumin (BSA) in PBS to prevent any non-specific interactions between the gel and cells.

Supplementary Text 2: Implementation of the cell migration simulator using mechanically heterogeneous substrates

To establish whether our observations of negative (and positive) durotaxis could be explained through a single set of principles, namely the motor-clutch dynamics of cell-matrix adhesions, we developed a modified version of the cell migration simulator (CMS) that can be used for modeling cell migration on mechanically heterogeneous substrates. The detailed governing equations and algorithms of the original CMS were described previously[28]. Briefly, the CMS comprises multiple motor-clutch models (i.e. modules) that mimic cellular protrusions, and determines cell motion by a force balance between the modules and a central cell body (Fig. 4.3a). In the CMS, new modules are nucleated stochastically, module length increases over time via actin polymerization that is simultaneously counteracted by myosin-induced retraction of actin fibers, and modules are removed when they become too short. In addition, total actin and numbers of clutches and motors are kept constant in accordance with the conservation of mass.

In each motor-clutch system, adhesion clutches bind to elastic substrate springs with a constant rate of k_{on}. Connected clutches form a direct mechanical link from the intracellular cytoskeleton to the extracellular substrate – forces are borne from active myosin motors and transmitted by the resulting inward actin flow. The unbinding rate of a connected clutch i, $k_{off,i}$, varies with force F_i according to the Bell model[72]:

$$k_{off,i} = k_{off}^{*}\, exp(F_i/F_b)$$
$$F_i = k_c x_i \tag{S1}$$

where k_{off}^{*} is the clutch unbinding rate in the absence of loading, F_b is the characteristic clutch rupture force, and x_i is the elongation of the spring representing the i^{th} connected clutch with a spring constant k_c. The actin filaments are pulled by n_m myosin motors, each capable of exerting a force F_m, and balanced by the traction force F_s, resulting in inward actin flow with the effective actin flow rate (v_m) based on

$$v_m = v_m^{*}\left(1 - \frac{F_s}{F_{stall}}\right) \tag{S2}$$

where v_m^{*} is the unloaded rate, $F_{stall} = n_m F_m$ is the stall force of the ensemble of myosin motors,

and the traction force F_s transmitted by all the connected clutches is given by:

$$F_s = \sum_{i=1}^{n_{c,on}} F_i \tag{S3}$$

in which $n_{c,on}$ is the number of connected clutch bonds. Actin monomers are added to the barbed ends of actin filaments in the cellular protrusions (modules) at a polymerization rate v_p, constrained by the total actin length A_{tot} in the cell according to the relation:

$$v_p = v_p^*(A_{free}/A_{tot}) \tag{S4}$$

where A_{free} is the amount of available G-actin and v_p^* is the maximum polymerization rate. Module elongation and retraction both result from this actin polymerization and the actin flow rate (v_m). New modules are nucleated at a nucleation rate k_{mod}, also constrained by actin availability:

$$k_{mod} = k_{mod}^*(A_{free}/A_{tot}) \tag{S5}$$

where k_{mod}^* is the maximum module nucleation rate. Actin filaments are depolymerized into actin monomers when they pass through the position of the myosin motors. Filaments can also be capped and polymerization arrested by actin capping proteins at a capping rate k_{cap}. Actin filaments, and the corresponding modules, are removed from the simulation when their length falls below l_{min}.

Monte Carlo simulations were conducted using a direct Gillespie Stochastic Simulation Algorithm[48], with each time step determined based on total event rates, including k_{on}, $k_{off,i}$, k_{mod}, and k_{cap}, and the event execution determined based on accumulated event rates. The CMS C++ version, described in[37], was modified to account for variations in substrate stiffness (described below), and simulations were conducted in Mesabi computer cluster at the Minnesota Supercomputing Institute (MSI).

After the simulated cells had reached a dynamic steady state (60 min), they were displaced randomly to a 180 μm x 180 μm region (Fig. 4.3b), and the substrate stiffnesses (k_s) experienced by the cell body and each protrusion were determined based on their respective y-coordinates (y). The substrate could be either soft (k_{soft}), stiff (k_{stiff}), or between the two extremes [gradients following a normal cumulative distribution function, described by the following error functions (erf)]:

$$k_s = k_{soft} \qquad 105 < y_{mod180} \leq 165 \qquad \text{(S6)}$$

$$k_s = k_{soft} + \frac{1}{2}\left(1 + \text{erf}(y_{mod180}/7071)\right)(k_{stiff} - k_{soft}) \qquad -15 < y_{mod180} \leq 15 \qquad \text{(S7)}$$

$$k_s = k_{stiff} \qquad 15 < y_{mod180} \leq 75 \qquad \text{(S8)}$$

$$k_s = k_{stiff} + \frac{1}{2}\left(1 + \text{erf}\left((y_{mod180} - 90)/7071\right)\right)(k_{soft} - k_{stiff}) \qquad 75 < y_{mod180} \leq 105 \qquad \text{(S9)}$$

where $y_{mod180} = (y \bmod 180)/y_0$ with $(y \bmod 180)$ representing the remainder of y divided by 180 μm (ranging from -15 to 165) and $y_0 =$ 1 μm. This way, the number of cells in both soft and stiff regions was initially the same. In addition, by repeating the same stiffness pattern *ad infinitum*, the finite amount of cells placed in the finite rectangular region was representative of infinite cells placed on an infinite substrate with the same initial distribution of cells between soft and stiff areas. A normal cumulative distribution function was selected due to a finite element model of polyacrylamide, which demonstrated that the effective spring constant around a stepwise gradient of elastic modulus follows a similar distribution (Fig. S4.5). This was true regardless of the orientation of the applied traction (soft-to-stiff vs. stiff-to-soft).

Here, we adopted the high-motor-clutch parameter values used previously[28] to describe U-251MG migration on mechanically distinct but isotropic substrates (Table S2). Clutch stiffness was further adjusted to 8 pN nm^{-1} to better recapitulate the stiffness-dependence of U-251MG speed *in vitro*[28]. During the CMS simulations, cell positions and traction forces were recorded every second. The data collected during the first 60 min were analyzed to ensure that the simulated cells had indeed reached a dynamic steady state. Random motility coefficients (RMC) were calculated as described previously[28]. Briefly, the mean squared displacement, $\langle r^2 \rangle$, was calculated with overlapping time periods Δt = 10 min, 20 min, ..., and plotted as a function of Δt. The first half of the plotted curve was fitted with a straight line (slope = $\langle r^2 \rangle / \Delta t$), and RMC was given by RMC = $\langle r^2 \rangle / 4\Delta t$. Module forces were recorded every 10 min and averaged throughout the simulation to yield the average traction force per module. Custom Matlab scripts were employed to analyze the change in cell numbers in soft and stiff regions over time, to compare module forces in the soft and stiff parts of the gradients, and to track individual cells over time based on their initial location in soft or graded substrate regions.

On 10–100 pN nm^{-1} gradients, we found that the majority of cells translocated away from stiffer regions and toward soft areas (Fig. 4.3e–f), which were associated with higher traction forces per module and lower overall migration speed, RMC (Fig. 4.3c–d). We also tested whether altering the range of the gradient would affect the durotaxis. On 0.3–3 pN nm^{-1} gradients, the stiffer side was associated with higher traction forces and higher RMC (Fig. S4.6a–b). On these substrates, simulated cells displayed rapid accumulation in the stiffer regions (Fig. S4.6c). Finally, when the gradient was chosen such that there would be no appreciable difference in mean traction forces (100–300 pN nm^{-1}), cells clustered primarily in stiffer regions with lower RMC (Fig. S4.6a–b,d).

Supplementary Text 3: Modeling axonal pathfinding and mechanosensitive steering of growth cones

Axonal growth cones (GCs) (Fig. S4.7a) can turn or contract in response to substrate stiffness gradients[23,73] by controlling the dynamics of adhesions, filopodial remodeling, and active contraction[38]. To establish whether motor-clutch dynamics could explain the mechanosensitive turning of neuronal GCs[23], akin to the negative durotaxis exhibited by the U-251MG glioblastoma cells, we modified the CMS to model an individual GC on a functionally graded substrate. A group of i filopodia, each modeled as a single molecular clutch module (Fig. 4.7b), were attached to a GC central domain. Each module was allocated n_i molecular clutches (linear springs of stiffness k_c) and n_i corresponding substrate clutches (linear springs of stiffness $k_{s,i}$). Substrate clutches were distributed randomly, and had values $k_{s,1} \leq k_{s,i} \leq k_{s,2}$ that varied linearly with position along the gradient.

Monte Carlo simulations were conducted to evaluate filopodial and GC dynamics over time. We modeled a GC as having 21 potential growth sites for filopodia, chosen from a uniform orientation distribution between –π/2 and π/2, relative to the direction of the 'axon'. New protrusions with an initial length l_{in} and width l_{wid}, dictating the effective clutch-ligand binding area, were added into the simulation at a rate k_{mod} and assigned n_m myosin motors; note that we used an actin filament in the schematic diagram (Fig. S4.8a) to represent the filament bundle in the filopodium. The adhesion and substrate clutches under each filament then evolved according to the clutch binding and unbinding dynamics described above. Unlike the cellular level CMS, our modified model assumes a relatively stable pool of actin monomer in the GC. Thus, the actin polymerization rate v_p remained constant during each simulation. See Table S3 for parameter details.

First, we investigated whether the dozens of filopodia within a GC might enable mechanically directed growth by evaluating the response of an individual 8 μm filopodium to a linear stiffness gradient of 0.01 to 100 pN nm^{-1} (Fig. S4.7b). The filopodium was placed on a 10 μm x 10 μm square substrate and oriented at an angle $0 \leq \theta \leq \pi/2$ relative to the gradient (Fig. S4.7c). When the filopodium length was fixed, simply increasing the orientation between the filopodium and the gradient was sufficient to significantly increase traction force generation (Fig. S4.7d). Conversely,

when the orientation was fixed at π/2, i.e. perpendicular to the gradient, we found that both traction force and the number of engaged clutches increased linearly with filopodium length (Fig. S4.7d). Next, we investigated the impact of different stiffness gradients for traction force generation using a fixed filopodium length (8 μm) and orientation (0). Maximal traction forces resulted from the filopodium sensing a soft region, in the range of 0.01 to 0.1 pN nm^{-1}. The higher end of the stiffness gradient proved significantly less important for the overall traction (Fig. S4.7e). This result demonstrates that a filopodium can generate comparatively high forces even if only a part of it is located on softer substrate. Thus, high traction force generation by individual filopodia is favored at a low optimal stiffness and forces drastically drop on stiffer matrices.

Higher traction forces are often accompanied by a decrease in actin retrograde flow, as myosin-borne forces are transmitted to the ECM instead of freely displacing actin. Regardless of filopodia orientation, actin in GCs flows toward the structure's center, and much like traction forces, actin flow rates can also differ for different types of neurons[39]. We therefore investigated how both the speed and direction of actin flow relative to the stiffness gradient affect the dynamics of single filopodia. By studying filopodia oriented at their growing end with either the stiffer or more compliant end of a stiffness gradient (Fig. S4.7f), we found that orientation toward the compliant end of the substrate (and hence actin retrograde flow toward the stiff end of the substrate) led to increased extension rates and decreased retraction rates (Fig. S4.7g). In all cases, the overall growth rate of filopodia was a trade-off between growth at the constant actin polymerization rate v_p, and shortening at the actin flow rate v_m, which varied almost linearly with substrate stiffness (Fig. S4.7h). For an intermediate polymerization rate of v_p = 120 nm s^{-1}, orientation affected filopodia growth rate by a factor of two (Fig. S4.7h). Together, these results provide a mechanism by which individual filopodia can exert more traction and elongate faster on softer substrates.

We then investigated whether these changes in filopodial dynamics could contribute to GC steering on stiffness gradients. First, we evaluated the degree of GC turning on one type of stiffness gradient ($k_{s,1}$ = 0.01 pN nm^{-1} and $k_{s,2}$ = 100 pN nm^{-1}) by studying an initially semicircular GC with 21 uniformly distributed filopodia (Fig. S4.8a). Within 15 seconds of simulation, the filopodia pointing toward the compliant end of the substrate outgrew the rest, resulting in an effective turning of the

GC (Fig. S4.8a). As expected from the previous results, filopodia in the softer regions of the gradient were longer and generated higher traction forces (Fig. S4.8b).

To investigate the effect of different stiffness gradients on GC turning in detail, we repeated our simulations over a broad range of possible substrate stiffnesses, with $k_{s,left}$ and $k_{s,right}$ varying from 0.01 to 100 pN nm^{-1}. To quantify the degree of turning, we defined a parameter $\Lambda = \bar{l}_{left}/\bar{l}_{right}$, which represents the degree to which the GC has turned left. Here, $\bar{l}_{left}$ and $\bar{l}_{right}$ are the average lengths of filopodia in the left-hand and right-hand sides of the GC after 100 seconds of simulation, respectively. In addition to developing polarity through turning, the GC could enlarge, with all filopodia elongating as compared to their initial length, or retract (Fig. S4.8c). Enlarged GCs appeared on very compliant substrates (red section, $k_{s,left}$ and $k_{s,right}$ on the order of 0.01 to 0.1 pN nm^{-1}) with a negligible stiffness gradient, and retractile GCs appeared on higher stiffnesses, independent of the actual strength of the gradient (green section, $k_{s,left}$ and $k_{s,right}$ on the order of 1 to 100 pN nm^{-1}). Finally, polarized GCs appeared on compliant substrates with a moderate or high stiffness gradient ($k_{s,left}$ on the order of 0.01 to 0.1 pN nm^{-1}, >1 pN/nm/20 μm). A phase diagram for GC turning illustrates how the structure can either remain straight or turn to the more compliant side (Fig. S4.8d), and reveals that a stronger gradient may also promote GC turning, unless the range of the gradient as a whole is significantly stiffer than the optimal stiffness range for individual filopodia (Fig. S4.8e). Thus, the motor-clutch model can recapitulate mechanosensitive GC steering toward softer matrix *in silico*.

Table S4.1 Relative acrylamide and bis-acrylamide concentrations and corresponding Young's moduli for homogeneous (constant modulus) hydrogels

Final acrylamide %	Final bis-acrylamide %	Volume of (40%) AA stock, µl	Volume of (2%) bis-AA stock, µl	PBS, µl	~Young's modulus, kPa*
5.4	0.04	63	10	397	0.5
5.7	0.08	63	17.5	365	2
7.5	0.2	94	50	356	9.6
12	0.2	150	50	300	22
18	0.4	225	100	175	60

*Values obtained using atomic force microscopy, see reference[30].

Table S4.2 Parameters for the cellular level CMS

Parameter	**Symbol**	**Value**	**Ref.**
Total number of myosin motors	N_m	10,000	28
Total number of clutches	N_c	7,500	28
Maximum total actin length	A_{tot}	100 µm	28
Maximum actin polymerization rate	v_p^*	200 nm/s	28
Maximum module nucleation rate	k_{mod}^*	1 s^{-1}	28
Module capping rate	k_{cap}	0.001 s^{-1}	28
Initial module length	l_{in}	5 µm	28
Minimum module length	l_{min}	0.1 µm	28
Cell spring constant	k_{cell}	10,000 pN/nm	28
Number of cell body clutches	$n_{c,cell}$	10	28
Substrate spring constant	k_s	0.3–300 pN/nm	Adjusted
Maximum number of module motors	n_m^*	1,000	28
Myosin motor stall force	F_m	2 pN	28

Unloaded actin flow rate	v_m^*	120 nm/s	28
Maximum number of module clutches	n_c^*	750	28
Clutch on-rate	k_{on}	1 s^{-1}	28
Unloaded clutch off-rate	k_{off}^*	0.1 s^{-1}	28
Clutch spring constant	k_c	8 pN/nm	Adjusted
Characteristic clutch rupture force	F_b	2 pN	28

Table S4.3 Parameters for the filopodia/GC model

Parameter	**Symbol**	**Value**	**Ref.**
Actin polymerization rate	v_p	90–130 nm/s	74, adjusted
Module nucleation rate	k_{mod}	1 s^{-1}	28
Initial filopodium length	l_{in}	3 μm	Adapted from 28
Minimum filopodium length	l_{min}	0.1 μm	Adapted from 28
Filopodium width for ligand binding	l_{wid}	0.2 μm	75
Substrate spring constant (soft region)	$k_{s,1}$	10^{-2}–10^2 pN/nm	Adjusted
Substrate spring constant (stiff region)	$k_{s,2}$	10^{-2}–10^2 pN/nm	Adjusted
Initial number of module motors	n_m	50	26
Myosin motor stall force	F_m	2 pN	26
Unloaded actin flow rate	v_m^*	120 nm/s	26
Initial number of module clutches	n_c	50	26
Clutch on-rate	k_{on}	0.3 s^{-1}	26
Unloaded clutch off-rate	k_{off}^*	0.1 s^{-1}	26
Clutch spring constant	k_c	1 pN/nm	26
Characteristic clutch rupture force	F_b	2 pN	26

Captions for Movies S1–S2

Movie S1. Evolution of U-251MG glioblastoma cell distribution on stiffness gradient hydrogels over time. Blue overlay in the middle denotes a softer, UV-irradiated region. Vertical and horizontal lines are out-of-focus markings in the underlying glass. Scale bar, 200 μm.

Movie S2. Migration of individual U-251MG cells on stiffness gradient hydrogels. (Top) Phase-contrast data showing migrating cells over the span of 24 hours. Scale bar, 100 μm. (Bottom) Tracks corresponding to the cells in the top panel. Softer, UV-irradiated hydrogel is marked with gray color.

Reference

(1) Hentschel, A.; Zahedi, R. P.; Ahrends, R. Protein Lipid Modifications—More than Just a Greasy Ballast. *PROTEOMICS* **2016**, *16* (5), 759–782. https://doi.org/10.1002/pmic.201500353.

(2) Wang, M.; Casey, P. J. Protein Prenylation: Unique Fats Make Their Mark on Biology. *Nat. Rev. Mol. Cell Biol.* **2016**, *17* (2), 110–122. https://doi.org/10.1038/nrm.2015.11.

(3) Jiang, H.; Zhang, X.; Chen, X.; Aramsangtienchai, P.; Tong, Z.; Lin, H. Protein Lipidation: Occurrence, Mechanisms, Biological Functions, and Enabling Technologies. *Chem. Rev.* **2018**, *118* (3), 919–988. https://doi.org/10.1021/acs.chemrev.6b00750.

(4) Resh, M. D. Fatty Acylation of Proteins: The Long and the Short of It. *Prog. Lipid Res.* **2016**, *63*, 120–131. https://doi.org/10.1016/j.plipres.2016.05.002.

(5) Ciepla, P.; Magee, A. I.; Tate, E. W. Cholesterylation: A Tail of Hedgehog. *Biochem. Soc. Trans.* **2015**, *43* (2), 262–267. https://doi.org/10.1042/BST20150032.

(6) Running, M. The Role of Lipid Post–Translational Modification in Plant Developmental Processes. *Front. Plant Sci.* **2014**, *5*, 50. https://doi.org/10.3389/fpls.2014.00050.

(7) Resh, M. D. Covalent Lipid Modifications of Proteins. *Curr. Biol. CB* **2013**, *23* (10), R431–R435. https://doi.org/10.1016/j.cub.2013.04.024.

(8) Chen, B.; Sun, Y.; Niu, J.; Jarugumilli, G. K.; Wu, X. Protein Lipidation in Cell Signaling and Diseases: Function, Regulation, and Therapeutic Opportunities. *Cell Chem. Biol.* **2018**, *25* (7), 817–831. https://doi.org/10.1016/j.chembiol.2018.05.003.

(9) Ganesan, L.; Levental, I. Pharmacological Inhibition of Protein Lipidation. *J. Membr. Biol.* **2015**, *248* (6), 929–941. https://doi.org/10.1007/s00232-015-9835-4.

(10) Fraser, N. J.; Howie, J.; Wypijewski, K. J.; Fuller, W. Therapeutic Targeting of Protein S-Acylation for the Treatment of Disease. *Biochem. Soc. Trans.* **2019**, *48* (1), 281–290. https://doi.org/10.1042/BST20190707.

(11) Palsuledesai, C. C.; Distefano, M. D. Protein Prenylation: Enzymes, Therapeutics, and Biotechnology Applications. *ACS Chem. Biol.* **2015**, *10* (1), 51–62. https://doi.org/10.1021/cb500791f.

(12) Rashidian, M.; Dozier, J. K.; Distefano, M. D. Enzymatic Labeling of Proteins: Techniques and Approaches. *Bioconjug. Chem.* **2013**, *24* (8), 1277–1294. https://doi.org/10.1021/bc400102w.

(13) Zhang, Y.; Park, K.-Y.; Suazo, K. F.; Distefano, M. D. Recent Progress in Enzymatic Protein Labelling Techniques and Their Applications. *Chem. Soc. Rev.* **2018**, *47* (24), 9106–9136. https://doi.org/10.1039/C8CS00537K.

(14) Tate, E. W.; Kalesh, K. A.; Lanyon-Hogg, T.; Storck, E. M.; Thinon, E. Global Profiling of Protein Lipidation Using Chemical Proteomic Technologies. *Curr. Opin. Chem. Biol.* **2015**, *24*, 48–57.

(15) Gao, X.; Hannoush, R. N. A Decade of Click Chemistry in Protein Palmitoylation: Impact on Discovery and New Biology. *Cell Chem. Biol.* **2018**, *25* (3), 236–246. https://doi.org/10.1016/j.chembiol.2017.12.002.

(16) Wang, Y.-C.; Distefano, M. D. Synthetic Isoprenoid Analogues for the Study of Prenylated Proteins: Fluorescent Imaging and Proteomic Applications. *Bioorganic Chem.* **2016**, *64* (Supplement C), 59–65. https://doi.org/10.1016/j.bioorg.2015.12.003.

(17) Peng, T.; Thinon, E.; Hang, H. C. Proteomic Analysis of Fatty-Acylated Proteins. *Curr. Opin. Chem. Biol.* **2016**, *30*, 77–86. https://doi.org/10.1016/j.cbpa.2015.11.008.

(18) Suazo, K. F.; Schey, G.; Schaber, C.; Odom John, A. R.; Distefano, M. D. Proteomic Analysis of Protein–Lipid Modifications: Significance and Application. *Mass Spectrometry‐Based Chemical Proteomics*. August 13, 2019, pp 317–347.

(19) Kolb, H. C.; Finn, M. G.; Sharpless, K. B. Click Chemistry: Diverse Chemical Function from a Few Good Reactions. *Angew. Chem. Int. Ed.* **2001**, *40* (11), 2004–2021. https://doi.org/10.1002/1521-3773(20010601)40:11<2004::AID-ANIE2004>3.0.CO;2-5.

(20) Sletten, E. M.; Bertozzi, C. R. Bioorthogonal Chemistry: Fishing for Selectivity in a Sea of Functionality. *Angew. Chem. Int. Ed.* **2009**, *48* (38), 6974–6998. https://doi.org/doi:10.1002/anie.200900942.
(21) Sletten, E. M.; Bertozzi, C. R. From Mechanism to Mouse: A Tale of Two Bioorthogonal Reactions. *Acc. Chem. Res.* **2011**, *44* (9), 666–676. https://doi.org/10.1021/ar200148z.
(22) McKay, C. S.; Finn, M. G. Click Chemistry in Complex Mixtures: Bioorthogonal Bioconjugation. *Chem. Biol.* **2014**, *21* (9), 1075–1101. https://doi.org/10.1016/j.chembiol.2014.09.002.
(23) Oliveira, B. L.; Guo, Z.; Bernardes, G. J. L. Inverse Electron Demand Diels–Alder Reactions in Chemical Biology. *Chem. Soc. Rev.* **2017**, *46* (16), 4895–4950. https://doi.org/10.1039/C7CS00184C.
(24) Kölmel, D. K.; Kool, E. T. Oximes and Hydrazones in Bioconjugation: Mechanism and Catalysis. *Chem. Rev.* **2017**, *117* (15), 10358–10376. https://doi.org/10.1021/acs.chemrev.7b00090.
(25) Kim, E.; Koo, H. Biomedical Applications of Copper-Free Click Chemistry: In Vitro, in Vivo, and Ex Vivo. *Chem. Sci.* **2019**, *10* (34), 7835–7851. https://doi.org/10.1039/C9SC03368H.
(26) Saxon, E.; Bertozzi, C. R. Cell Surface Engineering by a Modified Staudinger Reaction. *Science* **2000**, *287* (5460), 2007–2010. https://doi.org/10.1126/science.287.5460.2007.
(27) Bednarek, C.; Wehl, I.; Jung, N.; Schepers, U.; Bräse, S. The Staudinger Ligation. *Chem. Rev.* **2020**, *120* (10), 4301–4354. https://doi.org/10.1021/acs.chemrev.9b00665.
(28) Lin, F. L.; Hoyt, H. M.; van Halbeek, H.; Bergman, R. G.; Bertozzi, C. R. Mechanistic Investigation of the Staudinger Ligation. *J. Am. Chem. Soc.* **2005**, *127* (8), 2686–2695. https://doi.org/10.1021/ja044461m.
(29) Tornøe, C. W.; Christensen, C.; Meldal, M. Peptidotriazoles on Solid Phase: [1,2,3]-Triazoles by Regiospecific Copper(I)-Catalyzed 1,3-Dipolar Cycloadditions of Terminal Alkynes to Azides. *J. Org. Chem.* **2002**, *67* (9), 3057–3064. https://doi.org/10.1021/jo011148j.
(30) Rostovtsev, V. V; Green, L. G.; Fokin, V. V; Sharpless, K. B. A Stepwise Huisgen Cycloaddition Process: Copper(I)-Catalyzed Regioselective "Ligation" of Azides and Terminal Alkynes. *Angew. Chem. Int. Ed.* **2002**, *41* (14), 2596–2599. https://doi.org/10.1002/1521-3773(20020715)41:14<2596::AID-ANIE2596>3.0.CO;2-4.
(31) Meldal, M.; Tornøe, C. W. Cu-Catalyzed Azide−Alkyne Cycloaddition. *Chem. Rev.* **2008**, *108* (8), 2952–3015. https://doi.org/10.1021/cr0783479.
(32) Neumann, S.; Biewend, M.; Rana, S.; Binder, W. H. The CuAAC: Principles, Homogeneous and Heterogeneous Catalysts, and Novel Developments and Applications. *Macromol. Rapid Commun.* **2020**, *41* (1), 1900359. https://doi.org/10.1002/marc.201900359.
(33) Chan, T. R.; Hilgraf, R.; Sharpless, K. B.; Fokin, V. V. Polytriazoles as Copper(I)-Stabilizing Ligands in Catalysis. *Org. Lett.* **2004**, *6* (17), 2853–2855. https://doi.org/10.1021/ol0493094.
(34) Hong, V.; Presolski, S. I.; Ma, C.; Finn, M. G. Analysis and Optimization of Copper-Catalyzed Azide–Alkyne Cycloaddition for Bioconjugation. *Angew. Chem. Int. Ed.* **2009**, *48* (52), 9879–9883. https://doi.org/10.1002/anie.200905087.
(35) Presolski, S. I.; Hong, V.; Cho, S.-H.; Finn, M. G. Tailored Ligand Acceleration of the Cu-Catalyzed Azide−Alkyne Cycloaddition Reaction: Practical and Mechanistic Implications. *J. Am. Chem. Soc.* **2010**, *132* (41), 14570–14576. https://doi.org/10.1021/ja105743g.
(36) Soriano del Amo, D.; Wang, W.; Jiang, H.; Besanceney, C.; Yan, A. C.; Levy, M.; Liu, Y.; Marlow, F. L.; Wu, P. Biocompatible Copper(I) Catalysts for in Vivo Imaging of Glycans. *J. Am. Chem. Soc.* **2010**, *132* (47), 16893–16899. https://doi.org/10.1021/ja106553e.
(37) Das, D.; Tnimov, Z.; Nguyen, U. T. T.; Thimmaiah, G.; Lo, H.; Abankwa, D.; Wu, Y.; Goody, R. S.; Waldmann, H.; Kirill, A. Flexible and General Synthesis of Functionalized Phosphoisoprenoids for the Study of Prenylation in Vivo and in Vitro. *ChemBioChem* **2012**, *13* (5), 674–683. https://doi.org/10.1002/cbic.201100733.
(38) Uttamapinant, C.; Tangpeerachaikul, A.; Grecian, S.; Clarke, S.; Singh, U.; Slade, P.; Gee, K. R.; Ting, A. Y. Fast, Cell-Compatible Click Chemistry with Copper-Chelating Azides for

Biomolecular Labeling. *Angew. Chem. Int. Ed.* **2012**, *51* (24), 5852–5856. https://doi.org/10.1002/anie.201108181.
(39) Jiang, H.; Zheng, T.; Lopez-Aguilar, A.; Feng, L.; Kopp, F.; Marlow, F. L.; Wu, P. Monitoring Dynamic Glycosylation in Vivo Using Supersensitive Click Chemistry. *Bioconjug. Chem.* **2014**, *25* (4), 698–706. https://doi.org/10.1021/bc400502d.
(40) Bevilacqua, V.; King, M.; Chaumontet, M.; Nothisen, M.; Gabillet, S.; Buisson, D.; Puente, C.; Wagner, A.; Taran, F. Copper-Chelating Azides for Efficient Click Conjugation Reactions in Complex Media. *Angew. Chem. Int. Ed.* **2014**, *53* (23), 5872–5876. https://doi.org/10.1002/anie.201310671.
(41) Kennedy, D. C.; McKay, C. S.; Legault, M. C. B.; Danielson, D. C.; Blake, J. A.; Pegoraro, A. F.; Stolow, A.; Mester, Z.; Pezacki, J. P. Cellular Consequences of Copper Complexes Used To Catalyze Bioorthogonal Click Reactions. *J. Am. Chem. Soc.* **2011**, *133* (44), 17993–18001. https://doi.org/10.1021/ja2083027.
(42) Agard, N. J.; Prescher, J. A.; Bertozzi, C. R. A Strain-Promoted [3 + 2] Azide−Alkyne Cycloaddition for Covalent Modification of Biomolecules in Living Systems. *J. Am. Chem. Soc.* **2004**, *126* (46), 15046–15047. https://doi.org/10.1021/ja044996f.
(43) Dommerholt, J.; Rutjes, F. P. J. T.; van Delft, F. L. Strain-Promoted 1,3-Dipolar Cycloaddition of Cycloalkynes and Organic Azides. *Top. Curr. Chem.* **2016**, *374* (2), 16. https://doi.org/10.1007/s41061-016-0016-4.
(44) Agard, N. J.; Baskin, J. M.; Prescher, J. A.; Lo, A.; Bertozzi, C. R. A Comparative Study of Bioorthogonal Reactions with Azides. *ACS Chem. Biol.* **2006**, *1* (10), 644–648. https://doi.org/10.1021/cb6003228.
(45) Mbua, N. E.; Guo, J.; Wolfert, M. A.; Steet, R.; Boons, G.-J. Strain-Promoted Alkyne–Azide Cycloadditions (SPAAC) Reveal New Features of Glycoconjugate Biosynthesis. *ChemBioChem* **2011**, *12* (12), 1912–1921. https://doi.org/10.1002/cbic.201100117.
(46) Sletten, E. M.; Bertozzi, C. R. A Hydrophilic Azacyclooctyne for Cu-Free Click Chemistry. *Org. Lett.* **2008**, *10* (14), 3097–3099. https://doi.org/10.1021/ol801141k.
(47) Ning, X.; Guo, J.; Wolfert, M. A.; Boons, G.-J. Visualizing Metabolically Labeled Glycoconjugates of Living Cells by Copper-Free and Fast Huisgen Cycloadditions. *Angew. Chem. Int. Ed.* **2008**, *47* (12), 2253–2255. https://doi.org/10.1002/anie.200705456.
(48) Chang, P. V; Prescher, J. A.; Sletten, E. M.; Baskin, J. M.; Miller, I. A.; Agard, N. J.; Lo, A.; Bertozzi, C. R. Copper-Free Click Chemistry in Living Animals. *Proc. Natl. Acad. Sci.* **2010**, *107* (5), 1821 LP – 1826. https://doi.org/10.1073/pnas.0911116107.
(49) van Geel, R.; Pruijn, G. J. M.; van Delft, F. L.; Boelens, W. C. Preventing Thiol-Yne Addition Improves the Specificity of Strain-Promoted Azide–Alkyne Cycloaddition. *Bioconjug. Chem.* **2012**, *23* (3), 392–398. https://doi.org/10.1021/bc200365k.
(50) Karver, M. R.; Weissleder, R.; Hilderbrand, S. A. Bioorthogonal Reaction Pairs Enable Simultaneous, Selective, Multi-Target Imaging. *Angew. Chem. Int. Ed.* **2012**, *51* (4), 920–922. https://doi.org/10.1002/anie.201104389.
(51) Nikić, I.; Plass, T.; Schraidt, O.; Szymański, J.; Briggs, J. A. G.; Schultz, C.; Lemke, E. A. Minimal Tags for Rapid Dual-Color Live-Cell Labeling and Super-Resolution Microscopy. *Angew. Chem. Int. Ed.* **2014**, *53* (8), 2245–2249. https://doi.org/10.1002/anie.201309847.
(52) Rashidian, M.; Keliher, E. J.; Bilate, A. M.; Duarte, J. N.; Wojtkiewicz, G. R.; Jacobsen, J. T.; Cragnolini, J.; Swee, L. K.; Victora, G. D.; Weissleder, R.; Ploegh, H. L. Noninvasive Imaging of Immune Responses. *Proc. Natl. Acad. Sci.* **2015**, *112* (19), 6146–6151.
(53) Yang, J.; Šečkutė, J.; Cole, C. M.; Devaraj, N. K. Live-Cell Imaging of Cyclopropene Tags with Fluorogenic Tetrazine Cycloadditions. *Angew. Chem. Int. Ed.* **2012**, *51* (30), 7476–7479. https://doi.org/10.1002/anie.201202122.
(54) Yang, J.; Liang, Y.; Šečkutė, J.; Houk, K. N.; Devaraj, N. K. Synthesis and Reactivity Comparisons of 1-Methyl-3-Substituted Cyclopropene Mini-Tags for Tetrazine Bioorthogonal Reactions. *Chem. – Eur. J.* **2014**, *20* (12), 3365–3375. https://doi.org/10.1002/chem.201304225.
(55) Engelsma, S. B.; Willems, L. I.; van Paaschen, C. E.; van Kasteren, S. I.; van der Marel, G. A.; Overkleeft, H. S.; Filippov, D. V. Acylazetine as a Dienophile in Bioorthogonal Inverse

Electron-Demand Diels–Alder Ligation. *Org. Lett.* **2014**, *16* (10), 2744–2747. https://doi.org/10.1021/ol501049c.
(56) Cohen, J. D.; Zou, P.; Ting, A. Y. Site-Specific Protein Modification Using Lipoic Acid Ligase and Bis-Aryl Hydrazone Formation. *Chembiochem Eur. J. Chem. Biol.* **2012**, *13* (6), 888–894. https://doi.org/10.1002/cbic.201100764.
(57) Dirksen, A.; Dirksen, S.; Hackeng, T. M.; Dawson, P. E. Nucleophilic Catalysis of Hydrazone Formation and Transimination: Implications for Dynamic Covalent Chemistry. *J. Am. Chem. Soc.* **2006**, *128* (49), 15602–15603. https://doi.org/10.1021/ja067189k.
(58) Dirksen, A.; Hackeng, T. M.; Dawson, P. E. Nucleophilic Catalysis of Oxime Ligation. *Angew. Chem. Int. Ed.* **2006**, *45* (45), 7581–7584. https://doi.org/10.1002/anie.200602877.
(59) Dirksen, A.; Dawson, P. E. Rapid Oxime and Hydrazone Ligations with Aromatic Aldehydes for Biomolecular Labeling. *Bioconjug. Chem.* **2008**, *19* (12), 2543–2548. https://doi.org/10.1021/bc800310p.
(60) Rashidian, M.; Mahmoodi, M. M.; Shah, R.; Dozier, J. K.; Wagner, C. R.; Distefano, M. D. A Highly Efficient Catalyst for Oxime Ligation and Hydrazone–Oxime Exchange Suitable for Bioconjugation. *Bioconjug. Chem.* **2013**, *24* (3), 333–342. https://doi.org/10.1021/bc3004167.
(61) Kalia, J.; Raines, R. T. Hydrolytic Stability of Hydrazones and Oximes. *Angew. Chem. Int. Ed Engl.* **2008**, *47* (39), 7523–7526. https://doi.org/10.1002/anie.200802651.
(62) Rashidian, M.; Song, J. M.; Pricer, R. E.; Distefano, M. D. Chemoenzymatic Reversible Immobilization and Labeling of Proteins without Prior Purification. *J. Am. Chem. Soc.* **2012**, *134* (20), 8455–8467. https://doi.org/10.1021/ja211308s.
(63) Bandyopadhyay, A.; Gao, J. Iminoboronate Formation Leads to Fast and Reversible Conjugation Chemistry of α-Nucleophiles at Neutral PH. *Chem. – Eur. J.* **2015**, *21* (42), 14748–14752. https://doi.org/10.1002/chem.201502077.
(64) Nisal, R.; P. Jose, G.; Shanbhag, C.; Kalia, J. Rapid and Reversible Hydrazone Bioconjugation in Cells without the Use of Extraneous Catalysts. *Org. Biomol. Chem.* **2018**, *16* (23), 4304–4310. https://doi.org/10.1039/C8OB00946E.
(65) Agarwal, P.; van der Weijden, J.; Sletten, E. M.; Rabuka, D.; Bertozzi, C. R. A Pictet-Spengler Ligation for Protein Chemical Modification. *Proc. Natl. Acad. Sci.* **2013**, *110* (1), 46 LP – 51. https://doi.org/10.1073/pnas.1213186110.
(66) Drake, P. M.; Albers, A. E.; Baker, J.; Banas, S.; Barfield, R. M.; Bhat, A. S.; de Hart, G. W.; Garofalo, A. W.; Holder, P.; Jones, L. C.; Kudirka, R.; McFarland, J.; Zmolek, W.; Rabuka, D. Aldehyde Tag Coupled with HIPS Chemistry Enables the Production of ADCs Conjugated Site-Specifically to Different Antibody Regions with Distinct in Vivo Efficacy and PK Outcomes. *Bioconjug. Chem.* **2014**, *25* (7), 1331–1341. https://doi.org/10.1021/bc500189z.
(67) Kudirka, R.; Barfield, R. M.; McFarland, J.; Albers, A. E.; de Hart, G. W.; Drake, P. M.; Holder, P. G.; Banas, S.; Jones, L. C.; Garofalo, A. W.; Rabuka, D. Generating Site-Specifically Modified Proteins via a Versatile and Stable Nucleophilic Carbon Ligation. *Chem. Biol.* **2015**, *22* (2), 293–298. https://doi.org/10.1016/j.chembiol.2014.11.019.
(68) Zeng, Y.; Ramya, T. N. C.; Dirksen, A.; Dawson, P. E.; Paulson, J. C. High-Efficiency Labeling of Sialylated Glycoproteins on Living Cells. *Nat. Methods* **2009**, *6* (3), 207–209. https://doi.org/10.1038/nmeth.1305.
(69) Spears, R. J.; Fascione, M. A. Site-Selective Incorporation and Ligation of Protein Aldehydes. *Org. Biomol. Chem.* **2016**, *14* (32), 7622–7638. https://doi.org/10.1039/C6OB00778C.
(70) Hoyle, C. E.; Bowman, C. N. Thiol–Ene Click Chemistry. *Angew. Chem. Int. Ed.* **2010**, *49* (9), 1540–1573. https://doi.org/10.1002/anie.200903924.
(71) Lowe, A. B. Thiol–Ene "Click" Reactions and Recent Applications in Polymer and Materials Synthesis: A First Update. *Polym. Chem.* **2014**, *5* (17), 4820–4870. https://doi.org/10.1039/C4PY00339J.
(72) Koo, S. P. S.; Stamenović, M. M.; Prasath, R. A.; Inglis, A. J.; Du Prez, F. E.; Barner-Kowollik, C.; Van Camp, W.; Junkers, T. Limitations of Radical Thiol-Ene Reactions for

Polymer–Polymer Conjugation. *J. Polym. Sci. Part Polym. Chem.* **2010**, *48* (8), 1699–1713. https://doi.org/10.1002/pola.23933.
(73) Derboven, P.; D'hooge, D. R.; Stamenovic, M. M.; Espeel, P.; Marin, G. B.; Du Prez, F. E.; Reyniers, M.-F. Kinetic Modeling of Radical Thiol–Ene Chemistry for Macromolecular Design: Importance of Side Reactions and Diffusional Limitations. *Macromolecules* **2013**, *46* (5), 1732–1742. https://doi.org/10.1021/ma302619k.
(74) Teders, M.; Henkel, C.; Anhäuser, L.; Strieth-Kalthoff, F.; Gómez-Suárez, A.; Kleinmans, R.; Kahnt, A.; Rentmeister, A.; Guldi, D.; Glorius, F. The Energy-Transfer-Enabled Biocompatible Disulfide–Ene Reaction. *Nat. Chem.* **2018**, *10* (9), 981–988. https://doi.org/10.1038/s41557-018-0102-z.
(75) Nolan, M. D.; Scanlan, E. M. Applications of Thiol-Ene Chemistry for Peptide Science . *Frontiers in Chemistry* . 2020, p 1060.
(76) Grim, J. C.; Marozas, I. A.; Anseth, K. S. Thiol-Ene and Photo-Cleavage Chemistry for Controlled Presentation of Biomolecules in Hydrogels. *J. Control. Release Off. J. Control. Release Soc.* **2015**, *219*, 95–106. https://doi.org/10.1016/j.jconrel.2015.08.040.
(77) Spicer, C. D.; Davis, B. G. Selective Chemical Protein Modification. *Nat. Commun.* **2014**, *5*, 4740.
(78) Roque, A. C. A.; Lowe, C. R.; Taipa, M. Â. Antibodies and Genetically Engineered Related Molecules: Production and Purification. *Biotechnol. Prog.* **2004**, *20* (3), 639–654. https://doi.org/10.1021/bp030070k.
(79) Young, T. S.; Schultz, P. G. Beyond the Canonical 20 Amino Acids: Expanding the Genetic Lexicon. *J. Biol. Chem.* **2010**, *285* (15), 11039–11044. https://doi.org/10.1074/jbc.R109.091306.
(80) Mann, R. K.; Beachy, P. A. Novel Lipid Modifications of Secreted Protein Signals. *Annu. Rev. Biochem.* **2004**, *73* (1), 891–923. https://doi.org/10.1146/annurev.biochem.73.011303.073933.
(81) Subramanian, T.; Pais, J. E.; Liu, S.; Troutman, J. M.; Suzuki, Y.; Leela Subramanian, K.; Fierke, C. A.; Andres, D. A.; Spielmann, H. P. Farnesyl Diphosphate Analogues with Aryl Moieties Are Efficient Alternate Substrates for Protein Farnesyltransferase. *Biochemistry* **2012**, *51* (41), 8307–8319. https://doi.org/10.1021/bi3011362.
(82) Nguyen, U. T. T.; Guo, Z.; Delon, C.; Wu, Y.; Deraeve, C.; Fränzel, B.; Bon, R. S.; Blankenfeldt, W.; Goody, R. S.; Waldmann, H.; Wolters, D.; Alexandrov, K. Analysis of the Eukaryotic Prenylome by Isoprenoid Affinity Tagging. *Nat. Chem. Biol.* **2009**, *5* (4), 227–235. https://doi.org/10.1038/nchembio.149.
(83) Dozier, J. K.; Khatwani, S. L.; Wollack, J. W.; Wang, Y.-C.; Schmidt-Dannert, C.; Distefano, M. D. Engineering Protein Farnesyltransferase for Enzymatic Protein Labeling Applications. *Bioconjug. Chem.* **2014**, *25* (7), 1203–1212.
(84) Zahn, T. J.; Whitney, J.; Weinbaum, C.; Gibbs, R. A. Synthesis and Evaluation of GGPP Geometric Isomers: Divergent Substrate Specificities of FTase and GGTase I. *Bioorg. Med. Chem. Lett.* **2001**, *11* (12), 1605–1608. https://doi.org/10.1016/S0960-894X(01)00292-X.
(85) Rose, M. W.; Xu, J.; Kale, T. A.; O'Doherty, G.; Barany, G.; Distefano, M. D. Enzymatic Incorporation of Orthogonally Reactive Prenylazide Groups into Peptides Using Geranylazide Diphosphate via Protein Farnesyltransferase: Implications for Selective Protein Labeling. *Pept. Sci.* **2005**, *80* (2–3), 164–171. https://doi.org/10.1002/bip.20239.
(86) Restituyo, J. A.; Comstock, L. R.; Petersen, S. G.; Stringfellow, T.; Rajski, S. R. Conversion of Aryl Azides to O-Alkyl Imidates via Modified Staudinger Ligation. *Org. Lett.* **2003**, *5* (23), 4357–4360. https://doi.org/10.1021/ol035635s.
(87) Rose, M. W.; Rose, N. D.; Boggs, J.; Lenevich, S.; Xu, J.; Barany, G.; Distefano, M. D. Evaluation of Geranylazide and Farnesylazide Diphosphate for Incorporation of Prenylazides into a CAAX Box-Containing Peptide Using Protein Farnesyltransferase. *J. Pept. Res.* **2005**, *65* (6), 529–537. https://doi.org/10.1111/j.1399-3011.2005.00261.x.
(88) Xu, J.; DeGraw, A. J.; Duckworth, B. P.; Lenevich, S.; Tann, C.-M.; Jenson, E. C.; Gruber, S. J.; Barany, G.; Distefano, M. D. Synthesis and Reactivity of 6,7-Dihydrogeranylazides: Reagents for Primary Azide Incorporation into Peptides and Subsequent Staudinger

Ligation. *Chem. Biol. Drug Des.* **2006**, *68* (2), 85–96. https://doi.org/10.1111/j.1747-0285.2006.00420.x.
(89) Duckworth, B. P.; Xu, J.; Taton, T. A.; Guo, A.; Distefano, M. D. Site-Specific, Covalent Attachment of Proteins to a Solid Surface. *Bioconjug. Chem.* **2006**, *17* (4), 967–974. https://doi.org/10.1021/bc060125e.
(90) Speers, A. E.; Cravatt, B. F. Profiling Enzyme Activities In Vivo Using Click Chemistry Methods. *Chem. Biol.* **2004**, *11* (4), 535–546. https://doi.org/10.1016/j.chembiol.2004.03.012.
(91) Gauchet, C.; Labadie, G. R.; Poulter, C. D. Regio- and Chemoselective Covalent Immobilization of Proteins through Unnatural Amino Acids. *J. Am. Chem. Soc.* **2006**, *128* (29), 9274–9275. https://doi.org/10.1021/ja061131o.
(92) Labadie, G. R.; Viswanathan, R.; Poulter, C. D. Farnesyl Diphosphate Analogues with ω-Bioorthogonal Azide and Alkyne Functional Groups for Protein Farnesyl Transferase-Catalyzed Ligation Reactions. *J. Org. Chem.* **2007**, *72* (24), 9291–9297. https://doi.org/10.1021/jo7017747.
(93) Duckworth, B. P.; Zhang, Z.; Hosokawa, A.; Distefano, M. D. Selective Labeling of Proteins by Using Protein Farnesyltransferase. *ChemBioChem* **2007**, *8* (1), 98–105. https://doi.org/10.1002/cbic.200600340.
(94) Duckworth, B. P.; Chen, Y.; Wollack, J. W.; Sham, Y.; Mueller, J. D.; Taton, T. A.; Distefano, M. D. A Universal Method for the Preparation of Covalent Protein–DNA Conjugates for Use in Creating Protein Nanostructures. *Angew. Chem. Int. Ed.* **2007**, *46* (46), 8819–8822. https://doi.org/10.1002/anie.200701942.
(95) Nguyen, U. T. T.; Cramer, J.; Gomis, J.; Reents, R.; Gutierrez‐Rodriguez, M.; Goody, R. S.; Alexandrov, K.; Waldmann, H. Exploiting the Substrate Tolerance of Farnesyltransferase for Site‐Selective Protein Derivatization. *ChemBioChem* **2007**, *8* (4), 408–423. https://doi.org/doi:10.1002/cbic.200600440.
(96) Wollack, J. W.; Silverman, J. M.; Petzold, C. J.; Mougous, J. D.; Distefano, M. D. A Minimalist Substrate for Enzymatic Peptide and Protein Conjugation. *Chembiochem Eur. J. Chem. Biol.* **2009**, *10* (18), 2934–2943. https://doi.org/10.1002/cbic.200900566.
(97) Rashidian, M.; Dozier, J. K.; Lenevich, S.; Distefano, M. D. Selective Labeling of Polypeptides Using Protein Farnesyltransferase via Rapid Oxime Ligation. *Chem. Commun.* **2010**, *46* (47), 8998–9000. https://doi.org/10.1039/C0CC03305G.
(98) Berry, A. F. H.; Heal, W. P.; Tarafder, A. K.; Tolmachova, T.; Baron, R. A.; Seabra, M. C.; Tate, E. W. Rapid Multilabel Detection of Geranylgeranylated Proteins by Using Bioorthogonal Ligation Chemistry. *ChemBioChem* **2010**, *11* (6), 771–773. https://doi.org/10.1002/cbic.201000087.
(99) Weinrich, D.; Lin, P.; Jonkheijm, P.; Nguyen, U. T. T.; Schröder, H.; Niemeyer, C. M.; Alexandrov, K.; Goody, R.; Waldmann, H. Oriented Immobilization of Farnesylated Proteins by the Thiol‐Ene Reaction. *Angew. Chem. Int. Ed.* **2010**, *49* (7), 1252–1257. https://doi.org/doi:10.1002/anie.200906190.
(100) Wang, Y.; Kilic, O.; Csizmar, C. M.; Ashok, S.; Hougland, J. L.; Distefano, M. D.; Wagner, C. R. Engineering Reversible Cell–Cell Interactions Using Enzymatically Lipidated Chemically Self-Assembled Nanorings. *Chem. Sci.* **2021**, *12* (1), 331–340. https://doi.org/10.1039/D0SC03194A.
(101) Khatwani, S. L.; Kang, J. S.; Mullen, D. G.; Hast, M. A.; Beese, L. S.; Distefano, M. D.; Taton, T. A. Covalent Protein-Oligonucleotide Conjugates by Copper-Free Click Reaction. *Bioorg. Med. Chem.* **2012**, *20* (14), 4532–4539. https://doi.org/10.1016/j.bmc.2012.05.017.
(102) Rashidian, M.; Kumarapperuma, S. C.; Gabrielse, K.; Fegan, A.; Wagner, C. R.; Distefano, M. D. Simultaneous Dual Protein Labeling Using a Triorthogonal Reagent. *J. Am. Chem. Soc.* **2013**, *135* (44), 16388–16396. https://doi.org/10.1021/ja403813b.
(103) Mahmoodi, M. M.; Rashidian, M.; Zhang, Y.; Distefano, M. D. Application of Meta- and Para-Phenylenediamine as Enhanced Oxime Ligation Catalysts for Protein Labeling, PEGylation, Immobilization, and Release. *Curr. Protoc. Protein Sci.* **2015**, *79* (1), 15.4.1-15.4.28. https://doi.org/10.1002/0471140864.ps1504s79.

(104) Tolstyka, Z. P.; Richardson, W.; Bat, E.; Stevens, C. J.; Parra, D. P.; Dozier, J. K.; Distefano, M. D.; Dunn, B.; Maynard, H. D. Chemoselective Immobilization of Proteins by Microcontact Printing and Bioorthogonal Click Reactions. *Chembiochem* **2013**, *14* (18), 2464–2471. https://doi.org/10.1002/cbic.201300478.
(105) Seo, J.; Lee, S.; Poulter, C. D. Regioselective Covalent Immobilization of Recombinant Antibody-Binding Proteins A, G, and L for Construction of Antibody Arrays. *J. Am. Chem. Soc.* **2013**, *135* (24), 8973–8980. https://doi.org/10.1021/ja402447g.
(106) Seo, J.; Poulter, C. D. Sandwich Antibody Arrays Using Recombinant Antibody-Binding Protein L. *Langmuir* **2014**, *30* (22), 6629–6635. https://doi.org/10.1021/la500822w.
(107) Choi, S.; Seo, J.; Bohaty, R. F. H.; Poulter, C. D. Regio- and Chemoselective Immobilization of Proteins on Gold Surfaces. *Bioconjug. Chem.* **2014**, *25* (2), 269–275. https://doi.org/10.1021/bc400413d.
(108) Wollack, J. W.; Monson, B. J.; Dozier, J. K.; Dalluge, J. J.; Poss, K.; Hilderbrand, S. A.; Distefano, M. D. Site-Specific Labeling of Proteins and Peptides with Trans-Cyclooctene Containing Handles Capable of Tetrazine Ligation. *Chem. Biol. Drug Des.* **2014**, *84* (2), 140–147. https://doi.org/10.1111/cbdd.12303.
(109) Zhang, Y.; Blanden, M. J.; Sudheer, Ch.; Gangopadhyay, S. A.; Rashidian, M.; Hougland, J. L.; Distefano, M. D. Simultaneous Site-Specific Dual Protein Labeling Using Protein Prenyltransferases. *Bioconjug. Chem.* **2015**, *26* (12), 2542–2553. https://doi.org/10.1021/acs.bioconjchem.5b00553.
(110) Yeo, J. E.; Wickramaratne, S.; Khatwani, S.; Wang, Y.-C.; Vervacke, J.; Distefano, M. D.; Tretyakova, N. Y. Synthesis of Site-Specific DNA–Protein Conjugates and Their Effects on DNA Replication. *ACS Chem. Biol.* **2014**, *9* (8), 1860–1868. https://doi.org/10.1021/cb5001795.
(111) Lee, J.; Choi, H.; Yun, M.; Kang, Y.; Jung, J.; Ryu, Y.; Kim, T. Y.; Cha, Y.; Cho, H.; Min, J.; Chung, C.; Kim, H. Enzymatic Prenylation and Oxime Ligation for the Synthesis of Stable and Homogeneous Protein–Drug Conjugates for Targeted Therapy. *Angew. Chem. Int. Ed.* **2015**, *54* (41), 12020–12024. https://doi.org/doi:10.1002/anie.201505964.
(112) Lee, B. I.; Park, M.-H.; Byeon, J.-J.; Shin, S.-H.; Choi, J.; Park, Y.; Park, Y.-H.; Chae, J.; Shin, Y. G. Quantification of an Antibody-Conjugated Drug in Fat Plasma by an Affinity Capture LC-MS/MS Method for a Novel Prenyl Transferase-Mediated Site-Specific Antibody-Drug Conjugate. *Mol. Basel Switz.* **2020**, *25* (7), 1515. https://doi.org/10.3390/molecules25071515.
(113) Zhang, Y.; Auger, S.; Schaefer, J. V; Plückthun, A.; Distefano, M. D. Site-Selective Enzymatic Labeling of Designed Ankyrin Repeat Proteins Using Protein Farnesyltransferase BT - Bioconjugation: Methods and Protocols; Massa, S., Devoogdt, N., Eds.; Springer New York: New York, NY, 2019; pp 207–219. https://doi.org/10.1007/978-1-4939-9654-4_14.
(114) Ho, S. H.; Tirrell, D. A. Chemoenzymatic Labeling of Proteins for Imaging in Bacterial Cells. *J. Am. Chem. Soc.* **2016**, *138* (46), 15098–15101. https://doi.org/10.1021/jacs.6b07067.
(115) Ho, S. H.; Tirrell, D. A. N-Myristoyl Transferase (NMT)-Catalyzed Labeling of Bacterial Proteins for Imaging in Fixed and Live Cells BT - Enzyme-Mediated Ligation Methods; Nuijens, T., Schmidt, M., Eds.; Springer New York: New York, NY, 2019; pp 315–326. https://doi.org/10.1007/978-1-4939-9546-2_16.
(116) Kulkarni, C.; Lo, M.; Fraseur, J. G.; Tirrell, D. A.; Kinzer-Ursem, T. L. Bioorthogonal Chemoenzymatic Functionalization of Calmodulin for Bioconjugation Applications. *Bioconjug. Chem.* **2015**, *26* (10), 2153–2160. https://doi.org/10.1021/acs.bioconjchem.5b00449.
(117) Fraseur, J. G.; Kinzer-Ursem, T. L. Next Generation Calmodulin Affinity Purification: Clickable Calmodulin Facilitates Improved Protein Purification. *PloS One* **2018**, *13* (6), e0197120–e0197120. https://doi.org/10.1371/journal.pone.0197120.
(118) Heal, W. P.; Wickramasinghe, S. R.; Bowyer, P. W.; Holder, A. A.; Smith, D. F.; Leatherbarrow, R. J.; Tate, E. W. Site-Specific N-Terminal Labelling of Proteinsin Vitro and in Vivo Using N-Myristoyl Transferase and Bioorthogonal Ligation Chemistry. *Chem. Commun.* **2008**, No. 4, 480–482. https://doi.org/10.1039/B716115H.

(119) Heal, W. P.; Wickramasinghe, S. R.; Leatherbarrow, R. J.; Tate, E. W. N-Myristoyl Transferase-Mediated Protein Labelling in Vivo. *Org. Biomol. Chem.* **2008**, *6* (13), 2308–2315. https://doi.org/10.1039/B803258K.
(120) Heal, W. P.; Wright, M. H.; Thinon, E.; Tate, E. W. Multifunctional Protein Labeling via Enzymatic N-Terminal Tagging and Elaboration by Click Chemistry. *Nat Protoc.* **2012**, *7* (1), 105–117.
(121) Kulkarni, C.; Kinzer‐Ursem, T. L.; Tirrell, D. A. Selective Functionalization of the Protein N Terminus with N‐Myristoyl Transferase for Bioconjugation in Cell Lysate. *ChemBioChem* **2013**, *14* (15), 1958–1962. https://doi.org/10.1002/cbic.201300453.
(122) Gao, H.; Sun, W.; Song, Z.; Yu, Y.; Wang, L.; Chen, X.; Zhang, Q. A Method to Generate and Analyze Modified Myristoylated Proteins. *Chembiochem Eur. J. Chem. Biol.* **2017**, *18* (3), 324–330. https://doi.org/10.1002/cbic.201600608.
(123) Ejendal, K. F. K.; Fraseur, J. G.; Kinzer-Ursem, T. L. Protein Labeling and Bioconjugation Using N-Myristoyltransferase BT - Bioconjugation: Methods and Protocols; Massa, S., Devoogdt, N., Eds.; Springer New York: New York, NY, 2019; pp 149–165. https://doi.org/10.1007/978-1-4939-9654-4_11.
(124) Ho, S. H.; Tirrell, D. A. Enzymatic Labeling of Bacterial Proteins for Super-Resolution Imaging in Live Cells. *ACS Cent. Sci.* **2019**, *5* (12), 1911–1919. https://doi.org/10.1021/acscentsci.9b00617.
(125) Kudirka, R. A.; Barfield, R. M.; McFarland, J. M.; Drake, P. M.; Carlson, A.; Bañas, S.; Zmolek, W.; Garofalo, A. W.; Rabuka, D. Site-Specific Tandem Knoevenagel Condensation–Michael Addition To Generate Antibody–Drug Conjugates. *ACS Med. Chem. Lett.* **2016**, *7* (11), 994–998. https://doi.org/10.1021/acsmedchemlett.6b00253.
(126) Urquhart, L. Top Companies and Drugs by Sales in 2019. *Nat. Rev. Drug Discov.* **2020**, *19* (4), 228.
(127) Vogel, C.; Cobleigh, M. A.; Tripathy, D.; Gutheil, J. C.; Harris, L. N.; Fehrenbacher, L.; Slamon, D. J.; Murphy, M.; Novotny, W. F.; Burchmore, M.; Shak, S.; Stewart, S. J. First-Line, Single-Agent Herceptin® (Trastuzumab) in Metastatic Breast Cancer: A Preliminary Report. *Eur. J. Cancer* **2001**, *37*, 25–29. https://doi.org/10.1016/S0959-8049(00)00405-6.
(128) Swierczewska, M.; Lee, K. C.; Lee, S. What Is the Future of PEGylated Therapies? *Expert Opin. Emerg. Drugs* **2015**, *20* (4), 531–536. https://doi.org/10.1517/14728214.2015.1113254.
(129) Qi, Y.; Chilkoti, A. Growing Polymers from Peptides and Proteins: A Biomedical Perspective. *Polym. Chem.* **2014**, *5* (2), 266–276. https://doi.org/10.1039/C3PY01089A.
(130) Lewis, A.; Tang, Y.; Brocchini, S.; Choi, J.; Godwin, A. Poly(2-Methacryloyloxyethyl Phosphorylcholine) for Protein Conjugation. *Bioconjug. Chem.* **2008**, *19* (11), 2144–2155. https://doi.org/10.1021/bc800242t.
(131) Nauka, P. C.; Lee, J.; Maynard, H. D. Enhancing the Conjugation Yield of Brush Polymer–Protein Conjugates by Increasing the Linker Length at the Polymer End-Group. *Polym. Chem.* **2016**, *7* (13), 2352–2357. https://doi.org/10.1039/C6PY00080K.
(132) Bontempo, D.; Maynard, H. D. Streptavidin as a Macroinitiator for Polymerization: In Situ Protein−Polymer Conjugate Formation. *J. Am. Chem. Soc.* **2005**, *127* (18), 6508–6509. https://doi.org/10.1021/ja042230+.
(133) Lele, B. S.; Murata, H.; Matyjaszewski, K.; Russell, A. J. Synthesis of Uniform Protein−Polymer Conjugates. *Biomacromolecules* **2005**, *6* (6), 3380–3387. https://doi.org/10.1021/bm050428w.
(134) Gao, W.; Liu, W.; Mackay, J. A.; Zalutsky, M. R.; Toone, E. J.; Chilkoti, A. In Situ Growth of a Stoichiometric PEG-like Conjugate at a Protein's N-Terminus with Significantly Improved Pharmacokinetics. *Proc. Natl. Acad. Sci.* **2009**, *106* (36), 15231. https://doi.org/10.1073/pnas.0904378106.
(135) Mansfield, K. M.; Maynard, H. D. Site-Specific Insulin-Trehalose Glycopolymer Conjugate by Grafting from Strategy Improves Bioactivity. *ACS Macro Lett.* **2018**, *7* (3), 324–329. https://doi.org/10.1021/acsmacrolett.7b00974.
(136) Hu, J.; Wang, G.; Zhao, W.; Liu, X.; Zhang, L.; Gao, W. Site-Specific in Situ Growth of an Interferon-Polymer Conjugate That Outperforms PEGASYS in Cancer Therapy. *Biomaterials* **2016**, *96*, 84–92. https://doi.org/10.1016/j.biomaterials.2016.04.035.

(137) Roberts, M. J.; Bentley, M. D.; Harris, J. M. Chemistry for Peptide and Protein PEGylation. *MOST CITED Pap. Hist. Adv. DRUG Deliv. Rev. TRIBUTE 25TH Anniv. J.* **2012**, *64*, 116–127. https://doi.org/10.1016/j.addr.2012.09.025.
(138) Johnson, J. A.; Lu, Y. Y.; Van Deventer, J. A.; Tirrell, D. A. Residue-Specific Incorporation of Non-Canonical Amino Acids into Proteins: Recent Developments and Applications. *Model Syst. Synth. Modif.* **2010**, *14* (6), 774–780. https://doi.org/10.1016/j.cbpa.2010.09.013.
(139) Suazo, K. F.; Park, K.-Y.; Distefano, M. D. A Not-So-Ancient Grease History: Click Chemistry and Protein Lipid Modifications. *Chem. Rev.* **2021**. https://doi.org/10.1021/acs.chemrev.0c01108.
(140) Liu, X.; Sun, M.; Sun, J.; Hu, J.; Wang, Z.; Guo, J.; Gao, W. Polymerization Induced Self-Assembly of a Site-Specific Interferon α-Block Copolymer Conjugate into Micelles with Remarkably Enhanced Pharmacology. *J. Am. Chem. Soc.* **2018**, *140* (33), 10435–10438. https://doi.org/10.1021/jacs.8b06013.
(141) Gao, W.; Liu, W.; Christensen, T.; Zalutsky, M. R.; Chilkoti, A. In Situ Growth of a PEG-like Polymer from the C Terminus of an Intein Fusion Protein Improves Pharmacokinetics and Tumor Accumulation. *Proc. Natl. Acad. Sci.* **2010**, *107* (38), 16432. https://doi.org/10.1073/pnas.1006044107.
(142) Shilova O.N.; Deyev S.M. DARPins: Promising Scaffolds for Theranostics. *Acta Naturae* **2019**, *11* (4), 42–53. https://doi.org/10.32607/20758251-2019-11-4-42-53.
(143) Maetzel, D.; Denzel, S.; Mack, B.; Canis, M.; Went, P.; Benk, M.; Kieu, C.; Papior, P.; Baeuerle, P. A.; Munz, M.; Gires, O. Nuclear Signalling by Tumour-Associated Antigen EpCAM. *Nat. Cell Biol.* **2009**, *11* (2), 162–171. https://doi.org/10.1038/ncb1824.
(144) Simon, M.; Stefan, N.; Borsig, L.; Plückthun, A.; Zangemeister-Wittke, U. Increasing the Antitumor Effect of an EpCAM-Targeting Fusion Toxin by Facile Click PEGylation. *Mol. Cancer Ther.* **2014**, *13* (2), 375. https://doi.org/10.1158/1535-7163.MCT-13-0523.
(145) Martin-Killias, P.; Stefan, N.; Rothschild, S.; Plückthun, A.; Zangemeister-Wittke, U. A Novel Fusion Toxin Derived from an EpCAM-Specific Designed Ankyrin Repeat Protein Has Potent Antitumor Activity. *Clin Cancer Res* **2011**, *17* (1), 100–110. https://doi.org/10.1158/1078-0432.ccr-10-1303.
(146) Stefan, N.; Martin-Killias, P.; Wyss-Stoeckle, S.; Honegger, A.; Zangemeister-Wittke, U.; Plückthun, A. DARPins Recognizing the Tumor-Associated Antigen EpCAM Selected by Phage and Ribosome Display and Engineered for Multivalency. *J Mol Biol* **2011**, *413* (4), 826–843. https://doi.org/10.1016/j.jmb.2011.09.016.
(147) Zhang, L.; Zhao, W.; Liu, X.; Wang, G.; Wang, Y.; Li, D.; Xie, L.; Gao, Y.; Deng, H.; Gao, W. Site-Selective in Situ Growth of Fluorescent Polymer-Antibody Conjugates with Enhanced Antigen Detection by Signal Amplification. *Biomaterials* **2015**, *64*, 2–9. https://doi.org/10.1016/j.biomaterials.2015.06.020.
(148) Johnson, R. N.; Kopečková, P.; Kopeček, J. Biological Activity of Anti-CD20 Multivalent HPMA Copolymer-Fab' Conjugates. *Biomacromolecules* **2012**, *13* (3), 727–735. https://doi.org/10.1021/bm201656k.
(149) Yurkovetskiy, A. V.; Yin, M.; Bodyak, N.; Stevenson, C. A.; Thomas, J. D.; Hammond, C. E.; Qin, L.; Zhu, B.; Gumerov, D. R.; Ter-Ovanesyan, E.; Uttard, A.; Lowinger, T. B. A Polymer-Based Antibody–Vinca Drug Conjugate Platform: Characterization and Preclinical Efficacy. *Cancer Res.* **2015**, *75* (16), 3365. https://doi.org/10.1158/0008-5472.CAN-15-0129.
(150) Kovář, M.; Strohalm, J.; Etrych, T.; Ulbrich, K.; Říhová, B. Star Structure of Antibody-Targeted HPMA Copolymer-Bound Doxorubicin: A Novel Type of Polymeric Conjugate for Targeted Drug Delivery with Potent Antitumor Effect. *Bioconjug. Chem.* **2002**, *13* (2), 206–215. https://doi.org/10.1021/bc010063m.
(151) Etrych, T.; Chytil, P.; Kovář, L.; Říhová, B.; Ulbrich, K. Micellar and Antibody-Targeted Polymer Therapeutics. *Macromol. Symp.* **2010**, *295* (1), 1–12. https://doi.org/10.1002/masy.200900066.
(152) Tappertzhofen, K.; Metz, V. V.; Hubo, M.; Barz, M.; Postina, R.; Jonuleit, H.; Zentel, R. Synthesis of Maleimide-Functionalyzed HPMA-Copolymers and in Vitro Characterization

of the ARAGE- and Human Immunoglobulin (HuIgG)–Polymer Conjugates. *Macromol. Biosci.* **2013**, *13* (2), 203–214. https://doi.org/10.1002/mabi.201200344.
(153) Pauli, J.; Licha, K.; Berkemeyer, J.; Grabolle, M.; Spieles, M.; Wegner, N.; Welker, P.; Resch-Genger, U. New Fluorescent Labels with Tunable Hydrophilicity for the Rational Design of Bright Optical Probes for Molecular Imaging. *Bioconjug. Chem.* **2013**, *24* (7), 1174–1185. https://doi.org/10.1021/bc4000349.
(154) Pauli, J.; Grabolle, M.; Brehm, R.; Spieles, M.; Hamann, F. M.; Wenzel, M.; Hilger, I.; Resch-Genger, U. Suitable Labels for Molecular Imaging – Influence of Dye Structure and Hydrophilicity on the Spectroscopic Properties of IgG Conjugates. *Bioconjug. Chem.* **2011**, *22* (7), 1298–1308. https://doi.org/10.1021/bc1004763.
(155) Hamblett, K. J.; Senter, P. D.; Chace, D. F.; Sun, M. M. C.; Lenox, J.; Cerveny, C. G.; Kissler, K. M.; Bernhardt, S. X.; Kopcha, A. K.; Zabinski, R. F.; Meyer, D. L.; Francisco, J. A. Effects of Drug Loading on the Antitumor Activity of a Monoclonal Antibody Drug Conjugate. *Clin. Cancer Res.* **2004**, *10* (20), 7063. https://doi.org/10.1158/1078-0432.CCR-04-0789.
(156) Nagy, A.; Plonowski, A.; Schally, A. V. Stability of Cytotoxic Luteinizing Hormone-Releasing Hormone Conjugate (AN-152) Containing Doxorubicin 14-O</Em>-Hemiglutarate in Mouse and Human Serum in Vitro:</Em> Implications for the Design of Preclinical Studies. *Proc. Natl. Acad. Sci.* **2000**, *97* (2), 829. https://doi.org/10.1073/pnas.97.2.829.
(157) Zhang, Y. APPLICATIONS OF ENZYMATIC PROTEIN LABELING BY FARNESYLTRANSFERASE TOWARDS DUAL-PROTEIN MODIFICATION AND CONSTRUCTION OF TARGETED DELIVERY SYSTEMS. *Univ. Minn. PhD Diss.*
(158) Kubetzko, S.; Sarkar, C. A.; Plückthun, A. Protein PEGylation Decreases Observed Target Association Rates via a Dual Blocking Mechanism. *Mol. Pharmacol.* **2005**, *68* (5), 1439. https://doi.org/10.1124/mol.105.014910.
(159) Simon, M.; Zangemeister-Wittke, U.; Plückthun, A. Facile Double-Functionalization of Designed Ankyrin Repeat Proteins Using Click and Thiol Chemistries. *Bioconjug. Chem.* **2012**, *23* (2), 279–286. https://doi.org/10.1021/bc200591x.
(160) Veronese, F. M. Peptide and Protein PEGylation: A Review of Problems and Solutions. *Biomaterials* **2001**, *22* (5), 405–417. https://doi.org/10.1016/S0142-9612(00)00193-9.
(161) Wang, Y.-S.; Youngster, S.; Grace, M.; Bausch, J.; Bordens, R.; Wyss, D. F. Structural and Biological Characterization of Pegylated Recombinant Interferon Alpha-2b and Its Therapeutic Implications. *Pept. Protein Pegylation* **2002**, *54* (4), 547–570. https://doi.org/10.1016/S0169-409X(02)00027-3.
(162) Veronese, F. M.; Caliceti, P.; Schiavon, O. Branched and Linear Poly(Ethylene Glycol): Influence of the Polymer Structure on Enzymological, Pharmacokinetic, and Immunological Properties of Protein Conjugates. *J. Bioact. Compat. Polym.* **1997**, *12* (3), 196–207. https://doi.org/10.1177/088391159701200303.
(163) Winkler, J.; Martin-Killias, P.; Plückthun, A.; Zangemeister-Wittke, U. EpCAM-Targeted Delivery of Nanocomplexed SiRNA to Tumor Cells with Designed Ankyrin Repeat Proteins. *Mol. Cancer Ther.* **2009**, *8* (9), 2674. https://doi.org/10.1158/1535-7163.MCT-09-0402.
(164) Petersburg, J. R.; Shen, J.; Csizmar, C. M.; Murphy, K. A.; Spanier, J.; Gabrielse, K.; Griffith, T. S.; Fife, B.; Wagner, C. R. Eradication of Established Tumors by Chemically Self-Assembled Nanoring Labeled T Cells. *ACS Nano* **2018**, *12* (7), 6563–6576. https://doi.org/10.1021/acsnano.8b01308.
(165) Doronina, S. O.; Toki, B. E.; Torgov, M. Y.; Mendelsohn, B. A.; Cerveny, C. G.; Chace, D. F.; DeBlanc, R. L.; Gearing, R. P.; Bovee, T. D.; Siegall, C. B.; Francisco, J. A.; Wahl, A. F.; Meyer, D. L.; Senter, P. D. Development of Potent Monoclonal Antibody Auristatin Conjugates for Cancer Therapy. *Nat. Biotechnol.* **2003**, *21* (7), 778–784. https://doi.org/10.1038/nbt832.
(166) Lyon, R. P.; Bovee, T. D.; Doronina, S. O.; Burke, P. J.; Hunter, J. H.; Neff-LaFord, H. D.; Jonas, M.; Anderson, M. E.; Setter, J. R.; Senter, P. D. Reducing Hydrophobicity of Homogeneous Antibody-Drug Conjugates Improves Pharmacokinetics and Therapeutic Index. *Nat. Biotechnol.* **2015**, *33* (7), 733–735. https://doi.org/10.1038/nbt.3212.

(167) Simon, M.; Frey, R.; Zangemeister-Wittke, U.; Plückthun, A. Orthogonal Assembly of a Designed Ankyrin Repeat Protein–Cytotoxin Conjugate with a Clickable Serum Albumin Module for Half-Life Extension. *Bioconjug. Chem.* **2013**, *24* (11), 1955–1966. https://doi.org/10.1021/bc4004102.
(168) Mohamed, M. M.; Sloane, B. F. Cysteine Cathepsins: Multifunctional Enzymes in Cancer. *Nat Rev Cancer* **2006**, *6* (10), 764–775. https://doi.org/10.1038/nrc1949.
(169) Dorywalska, M.; Dushin, R.; Moine, L.; Farias, S. E.; Zhou, D.; Navaratnam, T.; Lui, V.; Hasa-Moreno, A.; Casas, M. G.; Tran, T.-T.; Delaria, K.; Liu, S.-H.; Foletti, D.; O'Donnell, C. J.; Pons, J.; Shelton, D. L.; Rajpal, A.; Strop, P. Molecular Basis of Valine-Citrulline-PABC Linker Instability in Site-Specific ADCs and Its Mitigation by Linker Design. *Mol Cancer Ther* **2016**, *15* (5), 958–970. https://doi.org/10.1158/1535-7163.mct-15-1004.
(170) Caculitan, N. G.; dela Cruz Chuh, J.; Ma, Y.; Zhang, D.; Kozak, K. R.; Liu, Y.; Pillow, T. H.; Sadowsky, J.; Cheung, T. K.; Phung, Q.; Haley, B.; Lee, B.-C.; Akita, R. W.; Sliwkowski, M. X.; Polson, A. G. Cathepsin B Is Dispensable for Cellular Processing of Cathepsin B-Cleavable Antibody–Drug Conjugates. *Cancer Res.* **2017**, *77* (24), 7027. https://doi.org/10.1158/0008-5472.CAN-17-2391.
(171) Lam, M.-H.; Lucas, J.; Maderna, A.; Wald, H.; Wojciechowicz, M.; Dushin, R.; Peano, B.; Wang, F.; Myers, J.; Tan, X.; Musto, S.; Charati, M.; Gerber, H.-P.; Loganzo, F. Abstract 4837: Extracellular Proteolytic Cleavage of Peptide-Linked Antibody-Drug Conjugates Promotes Bystander Killing of Cancer Cells. *Cancer Res.* **2014**, *74* (19 Supplement), 4837. https://doi.org/10.1158/1538-7445.AM2014-4837.
(172) Dal Corso, A.; Cazzamalli, S.; Gébleux, R.; Mattarella, M.; Neri, D. Protease-Cleavable Linkers Modulate the Anticancer Activity of Noninternalizing Antibody–Drug Conjugates. *Bioconjug. Chem.* **2017**, *28* (7), 1826–1833. https://doi.org/10.1021/acs.bioconjchem.7b00304.
(173) Joubert, N.; Beck, A.; Dumontet, C.; Denevault-Sabourin, C. Antibody–Drug Conjugates: The Last Decade. *Pharmaceuticals* **2020**, *13* (9). https://doi.org/10.3390/ph13090245.
(174) Rashidian, M.; Ingram, J. R.; Dougan, M.; Dongre, A.; Whang, K. A.; LeGall, C.; Cragnolini, J. J.; Bierie, B.; Gostissa, M.; Gorman, J.; Grotenbreg, G. M.; Bhan, A.; Weinberg, R. A.; Ploegh, H. L. Predicting the Response to CTLA-4 Blockade by Longitudinal Noninvasive Monitoring of CD8 T Cells. *J. Exp. Med.* **2017**, *214* (8), 2243–2255. https://doi.org/10.1084/jem.20161950.
(175) Rabin, N.; Zheng, Y.; Opoku-Temeng, C.; Du, Y.; Bonsu, E.; Sintim, H. O. Biofilm Formation Mechanisms and Targets for Developing Antibiofilm Agents. *Future Med. Chem.* **2015**, *7* (4), 493–512. https://doi.org/10.4155/fmc.15.6.
(176) Khatoon, Z.; McTiernan, C. D.; Suuronen, E. J.; Mah, T.-F.; Alarcon, E. I. Bacterial Biofilm Formation on Implantable Devices and Approaches to Its Treatment and Prevention. *Heliyon* **2018**, *4* (12), e01067. https://doi.org/10.1016/j.heliyon.2018.e01067.
(177) Percival, S. L.; Suleman, L.; Vuotto, C.; Donelli, G. Healthcare-Associated Infections, Medical Devices and Biofilms: Risk, Tolerance and Control. *Journal of Medical Microbiology*, **2015**, *64*, 323–334. https://doi.org/10.1099/jmm.0.000032.
(178) Flemming, H.-C. Biofouling in Water Systems – Cases, Causes and Countermeasures. *Appl. Microbiol. Biotechnol.* **2002**, *59* (6), 629–640. https://doi.org/10.1007/s00253-002-1066-9.
(179) Wang, H.; Christiansen, D. E.; Mehraeen, S.; Cheng, G. Winning the Fight against Biofilms: The First Six-Month Study Showing No Biofilm Formation on Zwitterionic Polyurethanes. *Chem. Sci.* **2020**, *11* (18), 4709–4721. https://doi.org/10.1039/C9SC06155J.
(180) Huang, S.; Bergonzi, C.; Schwab, M.; Elias, M.; Hicks, R. E. Evaluation of Biological and Enzymatic Quorum Quencher Coating Additives to Reduce Biocorrosion of Steel. *PLOS ONE* **2019**, *14* (5), e0217059. https://doi.org/10.1371/journal.pone.0217059.
(181) Lejars, M.; Margaillan, A.; Bressy, C. Fouling Release Coatings: A Nontoxic Alternative to Biocidal Antifouling Coatings. *Chem. Rev.* **2012**, *112* (8), 4347–4390. https://doi.org/10.1021/cr200350v.

(182) Bridier, A.; Briandet, R.; Thomas, V.; Dubois-Brissonnet, F. Resistance of Bacterial Biofilms to Disinfectants: A Review. *Biofouling* **2011**, *27* (9), 1017–1032. https://doi.org/10.1080/08927014.2011.626899.
(183) Mah, T.-F. C.; O'Toole, G. A. Mechanisms of Biofilm Resistance to Antimicrobial Agents. *Trends Microbiol.* **2001**, *9* (1), 34–39. https://doi.org/10.1016/S0966-842X(00)01913-2.
(184) Guardiola, F. A.; Cuesta, A.; Meseguer, J.; Esteban, M. A. Risks of Using Antifouling Biocides in Aquaculture. *Int. J. Mol. Sci.* **2012**, *13* (2). https://doi.org/10.3390/ijms13021541.
(185) Chen, M.; Yu, Q.; Sun, H. Novel Strategies for the Prevention and Treatment of Biofilm Related Infections. *Int. J. Mol. Sci.* **2013**, *14* (9). https://doi.org/10.3390/ijms140918488.
(186) Lowe, S.; O'Brien-Simpson, N. M.; Connal, L. A. Antibiofouling Polymer Interfaces: Poly(Ethylene Glycol) and Other Promising Candidates. *Polym. Chem.* **2015**, *6* (2), 198–212. https://doi.org/10.1039/C4PY01356E.
(187) Callow, J. A.; Callow, M. E. Trends in the Development of Environmentally Friendly Fouling-Resistant Marine Coatings. *Nat. Commun.* **2011**, *2* (1), 244. https://doi.org/10.1038/ncomms1251.
(188) Lyon, G. J.; Muir, T. W. Chemical Signaling among Bacteria and Its Inhibition. *Chem. Biol.* **2003**, *10* (11), 1007–1021. https://doi.org/10.1016/j.chembiol.2003.11.003.
(189) Ng Filomena S. W.; Wright Daniel M.; Seah Stephen Y. K. Characterization of a Phosphotriesterase-Like Lactonase from Sulfolobus Solfataricus and Its Immobilization for Disruption of Quorum Sensing. *Appl. Environ. Microbiol.* **2011**, *77* (4), 1181–1186. https://doi.org/10.1128/AEM.01642-10.
(190) Kim, J.-H.; Choi, D.-C.; Yeon, K.-M.; Kim, S.-R.; Lee, C.-H. Enzyme-Immobilized Nanofiltration Membrane To Mitigate Biofouling Based on Quorum Quenching. *Environ. Sci. Technol.* **2011**, *45* (4), 1601–1607. https://doi.org/10.1021/es103483j.
(191) Jiang, W.; Xia, S.; Liang, J.; Zhang, Z.; Hermanowicz, S. W. Effect of Quorum Quenching on the Reactor Performance, Biofouling and Biomass Characteristics in Membrane Bioreactors. *Water Res.* **2013**, *47* (1), 187–196. https://doi.org/10.1016/j.watres.2012.09.050.
(192) Lee, B.; Yeon, K.-M.; Shim, J.; Kim, S.-R.; Lee, C.-H.; Lee, J.; Kim, J. Effective Antifouling Using Quorum-Quenching Acylase Stabilized in Magnetically-Separable Mesoporous Silica. *Biomacromolecules* **2014**, *15* (4), 1153–1159. https://doi.org/10.1021/bm401595q.
(193) Rémy, B.; Plener, L.; Poirier, L.; Elias, M.; Daudé, D.; Chabrière, E. Harnessing Hyperthermostable Lactonase from Sulfolobus Solfataricus for Biotechnological Applications. *Sci. Rep.* **2016**, *6* (1), 37780. https://doi.org/10.1038/srep37780.
(194) Bzdrenga, J.; Daudé, D.; Rémy, B.; Jacquet, P.; Plener, L.; Elias, M.; Chabrière, E. Biotechnological Applications of Quorum Quenching Enzymes. *First Int. Conf. CBRN Res. Innov.* **2017**, *267*, 104–115. https://doi.org/10.1016/j.cbi.2016.05.028.
(195) Hiblot, J.; Gotthard, G.; Elias, M.; Chabriere, E. Differential Active Site Loop Conformations Mediate Promiscuous Activities in the Lactonase SsoPox. *PLOS ONE* **2013**, *8* (9), e75272. https://doi.org/10.1371/journal.pone.0075272.
(196) Vervacke, J. S.; Funk, A. L.; Wang, Y.-C.; Strom, M.; Hrycyna, C. A.; Distefano, M. D. Diazirine-Containing Photoactivatable Isoprenoid: Synthesis and Application in Studies with Isoprenylcysteine Carboxyl Methyltransferase. *J. Org. Chem.* **2014**, *79* (5), 1971–1978.
(197) Bryant, K. L.; Mancias, J. D.; Kimmelman, A. C.; Der, C. J. KRAS: Feeding Pancreatic Cancer Proliferation. *Trends Biochem. Sci.* **2014**, *39* (2), 91–100. https://doi.org/10.1016/j.tibs.2013.12.004.
(198) DeGraw, A. J.; Palsuledesai, C.; Ochocki, J. D.; Dozier, J. K.; Lenevich, S.; Rashidian, M.; Distefano, M. D. Evaluation of Alkyne-Modified Isoprenoids as Chemical Reporters of Protein Prenylation. *Chem. Biol. Drug Des.* **2010**, *76* (6), 460–471. https://doi.org/10.1111/j.1747-0285.2010.01037.x.
(199) Del Vecchio, P.; Elias, M.; Merone, L.; Graziano, G.; Dupuy, J.; Mandrich, L.; Carullo, P.; Fournier, B.; Rochu, D.; Rossi, M.; Masson, P.; Chabriere, E.; Manco, G. Structural Determinants of the High Thermal Stability of SsoPox from the Hyperthermophilic

Archaeon Sulfolobus Solfataricus. *Extremophiles* **2009**, *13* (3), 461–470. https://doi.org/10.1007/s00792-009-0231-9.
(200) Luo, Q.; Joubert, M. K.; Stevenson, R.; Ketchem, R. R.; Narhi, L. O.; Wypych, J. Chemical Modifications in Therapeutic Protein Aggregates Generated under Different Stress Conditions. *J. Biol. Chem.* **2011**, *286* (28), 25134–25144. https://doi.org/10.1074/jbc.M110.160440.
(201) Tanase, M.; Urbanska, A. M.; Zolla, V.; Clement, C. C.; Huang, L.; Morozova, K.; Follo, C.; Goldberg, M.; Roda, B.; Reschiglian, P.; Santambrogio, L. Role of Carbonyl Modifications on Aging-Associated Protein Aggregation. *Sci. Rep.* **2016**, *6* (1), 19311. https://doi.org/10.1038/srep19311.
(202) Dubinsky, L.; Krom, B. P.; Meijler, M. M. Diazirine Based Photoaffinity Labeling. *Chem. Proteomics* **2012**, *20* (2), 554–570. https://doi.org/10.1016/j.bmc.2011.06.066.
(203) Kim, W.-J.; Kim, A.; Huh, C.; Park, C. W.; Ah, C. S.; Kim, B. K.; Yang, J.-H.; Chung, K. H.; Choi, Y. H.; Hong, J.; Sung, G. Y. Photo Selective Protein Immobilization Using Bovine Serum Albumin. *Appl. Surf. Sci.* **2012**, *261*, 880–889. https://doi.org/10.1016/j.apsusc.2012.08.111.
(204) McCormick, A. M.; Wijekoon, A.; Leipzig, N. D. Specific Immobilization of Biotinylated Fusion Proteins NGF and Sema3A Utilizing a Photo-Cross-Linkable Diazirine Compound for Controlling Neurite Extension. *Bioconjug. Chem.* **2013**, *24* (9), 1515–1526. https://doi.org/10.1021/bc400058n.
(205) Isomursu, A.; Park, K.-Y.; Hou, J.; Cheng, B.; Shamsan, G.; Fuller, B.; Kasim, J.; Mahmoodi, M. M.; Lu, T. J.; Genin, G. M.; Xu, F.; Lin, M.; Distefano, M.; Ivaska, J.; Odde, D. J. Negative Durotaxis: Cell Movement toward Softer Environments. *bioRxiv* **2020**, 2020.10.27.357178. https://doi.org/10.1101/2020.10.27.357178.
(206) Deegan, R. D.; Bakajin, O.; Dupont, T. F.; Huber, G.; Nagel, S. R.; Witten, T. A. Capillary Flow as the Cause of Ring Stains from Dried Liquid Drops. *Nature* **1997**, *389* (6653), 827–829. https://doi.org/10.1038/39827.
(207) Cui, L.; Zhang, J.; Zhang, X.; Huang, L.; Wang, Z.; Li, Y.; Gao, H.; Zhu, S.; Wang, T.; Yang, B. Suppression of the Coffee Ring Effect by Hydrosoluble Polymer Additives. *ACS Appl. Mater. Interfaces* **2012**, *4* (5), 2775–2780. https://doi.org/10.1021/am300423p.
(208) Still, T.; Yunker, P. J.; Yodh, A. G. Surfactant-Induced Marangoni Eddies Alter the Coffee-Rings of Evaporating Colloidal Drops. *Langmuir* **2012**, *28* (11), 4984–4988. https://doi.org/10.1021/la204928m.
(209) Ostrom, Q. T.; Gittleman, H.; Fulop, J.; Liu, M.; Blanda, R.; Kromer, C.; Wolinsky, Y.; Kruchko, C.; Barnholtz-Sloan, J. S. CBTRUS Statistical Report: Primary Brain and Central Nervous System Tumors Diagnosed in the United States in 2008-2012. *Neuro-Oncol.* **2015**, *17* (suppl_4), iv1–iv62. https://doi.org/10.1093/neuonc/nov189.
(210) Giese, A.; Bjerkvig, R.; Berens, M. E.; Westphal, M. Cost of Migration: Invasion of Malignant Gliomas and Implications for Treatment. *J. Clin. Oncol.* **2003**, *21* (8), 1624–1636. https://doi.org/10.1200/JCO.2003.05.063.
(211) Lo, C. M.; Wang, H. B.; Dembo, M.; Wang, Y. L. Cell Movement Is Guided by the Rigidity of the Substrate. *Biophys. J.* **2000**, *79* (1), 144–152.
(212) Isenberg, B. C.; DiMilla, P. A.; Walker, M.; Kim, S.; Wong, J. Y. Vascular Smooth Muscle Cell Durotaxis Depends on Substrate Stiffness Gradient Strength. *Biophys. J.* **2009**, *97* (5), 1313–1322. https://doi.org/10.1016/j.bpj.2009.06.021.
(213) Hadden, W. J.; Young, J. L.; Holle, A. W.; McFetridge, M. L.; Kim, D. Y.; Wijesinghe, P.; Taylor-Weiner, H.; Wen, J. H.; Lee, A. R.; Bieback, K.; Vo, B.-N.; Sampson, D. D.; Kennedy, B. F.; Spatz, J. P.; Engler, A. J.; Choi, Y. S. Stem Cell Migration and Mechanotransduction on Linear Stiffness Gradient Hydrogels. *Proc. Natl. Acad. Sci.* **2017**, *114* (22), 5647–5652. https://doi.org/10.1073/pnas.1618239114.
(214) Kim, T. H.; An, D. B.; Oh, S. H.; Kang, M. K.; Song, H. H.; Lee, J. H. Creating Stiffness Gradient Polyvinyl Alcohol Hydrogel Using a Simple Gradual Freezing-Thawing Method to Investigate Stem Cell Differentiation Behaviors. *Biomaterials* **2015**, *40*, 51–60. https://doi.org/10.1016/j.biomaterials.2014.11.017.

(215) Jiang, F. X.; Yurke, B.; Schloss, R. S.; Firestein, B. L.; Langrana, N. A. Effect of Dynamic Stiffness of the Substrates on Neurite Outgrowth by Using a DNA-Crosslinked Hydrogel. *Tissue Eng. Part A* **2010**, *16* (6), 1873–1889. https://doi.org/10.1089/ten.TEA.2009.0574.
(216) Bouchonville, N.; Meyer, M.; Gaude, C.; Gay, E.; Ratel, D.; Nicolas, A. AFM Mapping of the Elastic Properties of Brain Tissue Reveals KPa Mm−1 Gradients of Rigidity. *Soft Matter* **2016**, *12* (29), 6232–6239. https://doi.org/10.1039/C6SM00582A.
(217) Kloxin, A. M.; Tibbitt, M. W.; Kasko, A. M.; Fairbairn, J. A.; Anseth, K. S. Tunable Hydrogels for External Manipulation of Cellular Microenvironments through Controlled Photodegradation. *Adv. Mater.* **2010**, *22* (1), 61–66. https://doi.org/10.1002/adma.200900917.
(218) Frey, M. T.; Wang, Y.-L. A Photo-Modulatable Material for Probing Cellular Responses to Substrate Rigidity. *Soft Matter* **2009**, *5*, 1918–1924. https://doi.org/10.1039/b818104g.
(219) Wieboldt, R.; Gee, K. R.; Niu, L.; Ramesh, D.; Carpenter, B. K.; Hess, G. P. Photolabile Precursors of Glutamate: Synthesis, Photochemical Properties, and Activation of Glutamate Receptors on a Microsecond Time Scale. *Proc. Natl. Acad. Sci. U. S. A.* **1994**, *91* (19), 8752–8756.
(220) Kloxin, A. M.; Kasko, A. M.; Salinas, C. N.; Anseth, K. S. Photodegradable Hydrogels for Dynamic Tuning of Physical and Chemical Properties. *Science* **2009**, *324* (5923), 59–63. https://doi.org/10.1126/science.1169494.
(221) Rosales, A. M.; Vega, S. L.; DelRio, F. W.; Burdick, J. A.; Anseth, K. S. Hydrogels with Reversible Mechanics to Probe Dynamic Cell Microenvironments. *Angew. Chem. Int. Ed Engl.* **2017**, *56* (40), 12132–12136. https://doi.org/10.1002/anie.201705684.
(222) Luo, Y.; Shoichet, M. S. A Photolabile Hydrogel for Guided Three-Dimensional Cell Growth and Migration. *Nat. Mater.* **2004**, *3* (4), 249–253. https://doi.org/10.1038/nmat1092.
(223) Norris, S. C. P.; Soto, J.; Kasko, A. M.; Li, S. Photodegradable Polyacrylamide Gels for Dynamic Control of Cell Functions. *ACS Appl. Mater. Interfaces* **2021**. https://doi.org/10.1021/acsami.0c19627.
(224) Wang, Y. L.; Pelham, R. J. Preparation of a Flexible, Porous Polyacrylamide Substrate for Mechanical Studies of Cultured Cells. *Methods Enzymol.* **1998**, *298*, 489–496. https://doi.org/10.1016/s0076-6879(98)98041-7.
(225) Chan, C. E.; Odde, D. J. Traction Dynamics of Filopodia on Compliant Substrates. *Science* **2008**, *322* (5908), 1687–1691. https://doi.org/10.1126/science.1163595.
(226) Denisin, A. K.; Pruitt, B. L. Tuning the Range of Polyacrylamide Gel Stiffness for Mechanobiology Applications. *ACS Appl. Mater. Interfaces* **2016**, *8* (34), 21893–21902. https://doi.org/10.1021/acsami.5b09344.
(227) Radola, B. J. ULTRATHIN-LAYER ISOELECTRIC FOCUSING IN 50-100 Pm POLYACRYLAMIDE GELS ON SILANIZED GLASS PLATES OR POLYESTER FILMS; Radola, B. J., International Conference on Electrophoresis <2, 1979, München>, Eds.; De Gruyter, 2019; pp 79–94. https://doi.org/10.1515/9783111713625-007.
(228) Yoon, J.; Kim, J.; Hayward, R. C. Nucleation, Growth, and Hysteresis of Surface Creases on Swelled Polymer Gels. *Soft Matter* **2010**, *6* (22), 5807–5816. https://doi.org/10.1039/C0SM00372G.
(229) Trujillo, V.; Kim, J.; Hayward, R. C. Creasing Instability of Surface-Attached Hydrogels. *Soft Matter* **2008**, *4* (3), 564–569. https://doi.org/10.1039/B713263H.
(230) Bangasser, B. L.; Shamsan, G. A.; Chan, C. E.; Opoku, K. N.; Tüzel, E.; Schlichtmann, B. W.; Kasim, J. A.; Fuller, B. J.; McCullough, B. R.; Rosenfeld, S. S.; Odde, D. J. Shifting the Optimal Stiffness for Cell Migration. *Nat. Commun.* **2017**, *8* (1), 1–10. https://doi.org/10.1038/ncomms15313.
(231) Ladoux, B.; Mège, R.-M.; Trepat, X. Front-Rear Polarization by Mechanical Cues: From Single Cells to Tissues. *Trends Cell Biol.* **2016**, *26* (6), 420–433. https://doi.org/10.1016/j.tcb.2016.02.002.
(232) Hamidi, H.; Ivaska, J. Every Step of the Way: Integrins in Cancer Progression and Metastasis. *Nat. Rev. Cancer* **2018**, *18* (9), 533–548. https://doi.org/10.1038/s41568-018-0038-z.

(233) Plotnikov, S. V.; Pasapera, A. M.; Sabass, B.; Waterman, C. M. Force Fluctuations within Focal Adhesions Mediate ECM-Rigidity Sensing to Guide Directed Cell Migration. *Cell* **2012**, *151* (7), 1513–1527. https://doi.org/10.1016/j.cell.2012.11.034.
(234) Breckenridge, M. T.; Desai, R. A.; Yang, M. T.; Fu, J.; Chen, C. S. Substrates with Engineered Step Changes in Rigidity Induce Traction Force Polarity and Durotaxis. *Cell. Mol. Bioeng.* **2014**, *7* (1), 26–34. https://doi.org/10.1007/s12195-013-0307-6.
(235) Sunyer, R.; Conte, V.; Escribano, J.; Elosegui-Artola, A.; Labernadie, A.; Valon, L.; Navajas, D.; Garcia-Aznar, J. M.; Munoz, J. J.; Roca-Cusachs, P.; Trepat, X. Collective Cell Durotaxis Emerges from Long-Range Intercellular Force Transmission. *Science* **2016**, *353* (6304), 1157–1161. https://doi.org/10.1126/science.aaf7119.
(236) DuChez, B. J.; Doyle, A. D.; Dimitriadis, E. K.; Yamada, K. M. Durotaxis by Human Cancer Cells. *Biophys. J.* **2019**, *116* (4), 670–683. https://doi.org/10.1016/j.bpj.2019.01.009.
(237) Barriga, E. H.; Franze, K.; Charras, G.; Mayor, R. Tissue Stiffening Coordinates Morphogenesis by Triggering Collective Cell Migration in Vivo. *Nature* **2018**, *554* (7693), 523–527. https://doi.org/10.1038/nature25742.
(238) Zhu, M.; Tao, H.; Samani, M.; Luo, M.; Wang, X.; Hopyan, S.; Sun, Y. Spatial Mapping of Tissue Properties in Vivo Reveals a 3D Stiffness Gradient in the Mouse Limb Bud. *Proc. Natl. Acad. Sci.* **2020**, *117* (9), 4781–4791. https://doi.org/10.1073/pnas.1912656117.
(239) McKenzie, A. J.; Hicks, S. R.; Svec, K. V.; Naughton, H.; Edmunds, Z. L.; Howe, A. K. The Mechanical Microenvironment Regulates Ovarian Cancer Cell Morphology, Migration, and Spheroid Disaggregation. *Sci. Rep.* **2018**, *8* (1), 1–20. https://doi.org/10.1038/s41598-018-25589-0.
(240) Hartman, C. D.; Isenberg, B. C.; Chua, S. G.; Wong, J. Y. Vascular Smooth Muscle Cell Durotaxis Depends on Extracellular Matrix Composition. *Proc. Natl. Acad. Sci.* **2016**, *113* (40), 11190–11195. https://doi.org/10.1073/pnas.1611324113.
(241) Lachowski, D.; Cortes, E.; Robinson, B.; Rice, A.; Rombouts, K.; Del Río Hernández, A. E. FAK Controls the Mechanical Activation of YAP, a Transcriptional Regulator Required for Durotaxis. *FASEB J. Off. Publ. Fed. Am. Soc. Exp. Biol.* **2018**, *32* (2), 1099–1107. https://doi.org/10.1096/fj.201700721R.
(242) Puleo, J. I.; Parker, S. S.; Roman, M. R.; Watson, A. W.; Eliato, K. R.; Peng, L.; Saboda, K.; Roe, D. J.; Ros, R.; Gertler, F. B.; Mouneimne, G. Mechanosensing during Directed Cell Migration Requires Dynamic Actin Polymerization at Focal Adhesions. *J. Cell Biol.* **2019**, *218* (12), 4215–4235. https://doi.org/10.1083/jcb.201902101.
(243) Abercrombie, M. The Croonian Lecture, 1978 - The Crawling Movement of Metazoan Cells. *Proc. R. Soc. Lond. B Biol. Sci.* **1980**, *207* (1167), 129–147. https://doi.org/10.1098/rspb.1980.0017.
(244) Mitchison, T.; Kirschner, M. Cytoskeletal Dynamics and Nerve Growth. *Neuron* **1988**, *1* (9), 761–772. https://doi.org/10.1016/0896-6273(88)90124-9.
(245) Elosegui-Artola, A.; Oria, R.; Chen, Y.; Kosmalska, A.; Pérez-González, C.; Castro, N.; Zhu, C.; Trepat, X.; Roca-Cusachs, P. Mechanical Regulation of a Molecular Clutch Defines Force Transmission and Transduction in Response to Matrix Rigidity. *Nat. Cell Biol.* **2016**, *18* (5), 540–548. https://doi.org/10.1038/ncb3336.
(246) DiMilla, P. A.; Barbee, K.; Lauffenburger, D. A. Mathematical Model for the Effects of Adhesion and Mechanics on Cell Migration Speed. *Biophys. J.* **1991**, *60* (1), 15–37. https://doi.org/10.1016/S0006-3495(91)82027-6.
(247) Klank, R. L.; Decker Grunke, S. A.; Bangasser, B. L.; Forster, C. L.; Price, M. A.; Odde, T. J.; SantaCruz, K. S.; Rosenfeld, S. S.; Canoll, P.; Turley, E. A.; McCarthy, J. B.; Ohlfest, J. R.; Odde, D. J. Biphasic Dependence of Glioma Survival and Cell Migration on CD44 Expression Level. *Cell Rep.* **2017**, *18* (1), 23–31. https://doi.org/10.1016/j.celrep.2016.12.024.
(248) Rens, E. G.; Merks, R. M. H. Cell Shape and Durotaxis Explained from Cell-Extracellular Matrix Forces and Focal Adhesion Dynamics. *iScience* **2020**, *23* (9), 101488. https://doi.org/10.1016/j.isci.2020.101488.

(249) Schmidt, C. E.; Dai, J.; Lauffenburger, D. A.; Sheetz, M. P.; Horwitz, A. F. Integrin-Cytoskeletal Interactions in Neuronal Growth Cones. *J. Neurosci. Off. J. Soc. Neurosci.* **1995**, *15* (5 Pt 1), 3400–3407.
(250) Koser, D. E.; Thompson, A. J.; Foster, S. K.; Dwivedy, A.; Pillai, E. K.; Sheridan, G. K.; Svoboda, H.; Viana, M.; Costa, L. da F.; Guck, J.; Holt, C. E.; Franze, K. Mechanosensing Is Critical for Axon Growth in the Developing Brain. *Nat. Neurosci.* **2016**, *19* (12), 1592–1598. https://doi.org/10.1038/nn.4394.
(251) Franze, K. Integrating Chemistry and Mechanics: The Forces Driving Axon Growth. *Annu. Rev. Cell Dev. Biol.* **2020**, *36* (1), 61–83. https://doi.org/10.1146/annurev-cellbio-100818-125157.
(252) Bangasser, B. L.; Odde, D. J. Master Equation-Based Analysis of a Motor-Clutch Model for Cell Traction Force. *Cell. Mol. Bioeng.* **2013**, *6* (4), 449–459. https://doi.org/10.1007/s12195-013-0296-5.
(253) Bangasser, B. L.; Rosenfeld, S. S.; Odde, D. J. Determinants of Maximal Force Transmission in a Motor-Clutch Model of Cell Traction in a Compliant Microenvironment. *Biophys. J.* **2013**, *105* (3), 581–592. https://doi.org/10.1016/j.bpj.2013.06.027.
(254) Cheng, B.; Lin, M.; Li, Y.; Huang, G.; Yang, H.; Genin, G. M.; Deshpande, V. S.; Lu, T. J.; Xu, F. An Integrated Stochastic Model of Matrix-Stiffness-Dependent Filopodial Dynamics. *Biophys. J.* **2016**, *111* (9), 2051–2061. https://doi.org/10.1016/j.bpj.2016.09.026.
(255) Lerche, M.; Elosegui-Artola, A.; Kechagia, J. Z.; Guzmán, C.; Georgiadou, M.; Andreu, I.; Gullberg, D.; Roca-Cusachs, P.; Peuhu, E.; Ivaska, J. Integrin Binding Dynamics Modulate Ligand-Specific Mechanosensing in Mammary Gland Fibroblasts. *iScience* **2020**, *23* (3), 100907. https://doi.org/10.1016/j.isci.2020.100907.
(256) Barber-Pérez, N.; Georgiadou, M.; Guzmán, C.; Isomursu, A.; Hamidi, H.; Ivaska, J. Mechano-Responsiveness of Fibrillar Adhesions on Stiffness-Gradient Gels. *J. Cell Sci.* **2020**, *133* (12). https://doi.org/10.1242/jcs.242909.
(257) Miroshnikova, Y. A.; Mouw, J. K.; Barnes, J. M.; Pickup, M. W.; Lakins, J. N.; Kim, Y.; Lobo, K.; Persson, A. I.; Reis, G. F.; McKnight, T. R.; Holland, E. C.; Phillips, J. J.; Weaver, V. M. Tissue Mechanics Promote IDH1-Dependent HIF1α-Tenascin C Feedback to Regulate Glioblastoma Aggression. *Nat. Cell Biol.* **2016**, *18* (12), 1336–1345. https://doi.org/10.1038/ncb3429.
(258) Kechagia, J. Z.; Ivaska, J.; Roca-Cusachs, P. Integrins as Biomechanical Sensors of the Microenvironment. *Nat. Rev. Mol. Cell Biol.* **2019**, *20* (8), 457–473. https://doi.org/10.1038/s41580-019-0134-2.
(259) Atherton, P.; Stutchbury, B.; Wang, D.-Y.; Jethwa, D.; Tsang, R.; Meiler-Rodriguez, E.; Wang, P.; Bate, N.; Zent, R.; Barsukov, I. L.; Goult, B. T.; Critchley, D. R.; Ballestrem, C. Vinculin Controls Talin Engagement with the Actomyosin Machinery. *Nat. Commun.* **2015**, *6* (1), 1–12. https://doi.org/10.1038/ncomms10038.
(260) Cheng, B.; Wan, W.; Huang, G.; Li, Y.; Genin, G. M.; Mofrad, M. R. K.; Lu, T. J.; Xu, F.; Lin, M. Nanoscale Integrin Cluster Dynamics Controls Cellular Mechanosensing via FAKY397 Phosphorylation. *Sci. Adv.* **2020**, *6* (10), eaax1909. https://doi.org/10.1126/sciadv.aax1909.
(261) Kanchanawong, P.; Shtengel, G.; Pasapera, A. M.; Ramko, E. B.; Davidson, M. W.; Hess, H. F.; Waterman, C. M. Nanoscale Architecture of Integrin-Based Cell Adhesions. *Nature* **2010**, *468* (7323), 580–584. https://doi.org/10.1038/nature09621.
(262) Mason, D. E.; Collins, J. M.; Dawahare, J. H.; Nguyen, T. D.; Lin, Y.; Voytik-Harbin, S. L.; Zorlutuna, P.; Yoder, M. C.; Boerckel, J. D. YAP and TAZ Limit Cytoskeletal and Focal Adhesion Maturation to Enable Persistent Cell Motility. *J. Cell Biol.* **2019**, *218* (4), 1369–1389. https://doi.org/10.1083/jcb.201806065.
(263) Hou, J. C.; Shamsan, G. A.; Anderson, S. M.; McMahon, M. M.; Tyler, L. P.; Castle, B. T.; Heussner, R. K.; Provenzano, P. P.; Keefe, D. F.; Barocas, V. H.; Odde, D. J. Modeling Distributed Forces within Cell Adhesions of Varying Size on Continuous Substrates. *Cytoskeleton* **2019**, *76* (11–12), 571–585. https://doi.org/10.1002/cm.21561.

(264) Betz, T.; Koch, D.; Lu, Y.-B.; Franze, K.; Käs, J. A. Growth Cones as Soft and Weak Force Generators. *Proc. Natl. Acad. Sci.* **2011**, *108* (33), 13420–13425. https://doi.org/10.1073/pnas.1106145108.
(265) Koch, D.; Rosoff, W. J.; Jiang, J.; Geller, H. M.; Urbach, J. S. Strength in the Periphery: Growth Cone Biomechanics and Substrate Rigidity Response in Peripheral and Central Nervous System Neurons. *Biophys. J.* **2012**, *102* (3), 452–460. https://doi.org/10.1016/j.bpj.2011.12.025.
(266) Ghibaudo, M.; Saez, A.; Trichet, L.; Xayaphoummine, A.; Browaeys, J.; Silberzan, P.; Buguin, A.; Ladoux, B. Traction Forces and Rigidity Sensing Regulate Cell Functions. *Soft Matter* **2008**, *4* (9), 1836–1843. https://doi.org/10.1039/B804103B.
(267) Kuipers, A. J.; Middelbeek, J.; Vrenken, K.; Pérez-González, C.; Poelmans, G.; Klarenbeek, J.; Jalink, K.; Trepat, X.; van Leeuwen, F. N. TRPM7 Controls Mesenchymal Features of Breast Cancer Cells by Tensional Regulation of SOX4. *Biochim. Biophys. Acta Mol. Basis Dis.* **2018**, *1864* (7), 2409–2419. https://doi.org/10.1016/j.bbadis.2018.04.017.
(268) Fourriere, L.; Kasri, A.; Gareil, N.; Bardin, S.; Bousquet, H.; Pereira, D.; Perez, F.; Goud, B.; Boncompain, G.; Miserey-Lenkei, S. RAB6 and Microtubules Restrict Protein Secretion to Focal AdhesionsRAB6 and MTs Restrict Secretion to Focal Adhesions. *J. Cell Biol.* **2019**, *218* (7), 2215–2231. https://doi.org/10.1083/jcb.201805002.
(269) Kobayashi, T.; Sokabe, M. Sensing Substrate Rigidity by Mechanosensitive Ion Channels with Stress Fibers and Focal Adhesions. *Curr. Opin. Cell Biol.* **2010**, *22* (5), 669–676. https://doi.org/10.1016/j.ceb.2010.08.023.
(270) Wang, Y. L.; Pelham, R. J. Preparation of a Flexible, Porous Polyacrylamide Substrate for Mechanical Studies of Cultured Cells. *Methods Enzymol.* **1998**, *298*, 489–496. https://doi.org/10.1016/s0076-6879(98)98041-7.
(271) Polio, S. R.; Smith, M. L. Patterned Hydrogels for Simplified Measurement of Cell Traction Forces. *Methods Cell Biol.* **2014**, *121*, 17–31. https://doi.org/10.1016/B978-0-12-800281-0.00002-6.
(272) Théry, M.; Piel, M. Adhesive Micropatterns for Cells: A Microcontact Printing Protocol. *Cold Spring Harb. Protoc.* **2009**. https://doi.org/10.1101/pdb.prot5255.
(273) Han, S. J.; Oak, Y.; Groisman, A.; Danuser, G. Traction Microscopy to Identify Force Modulation in Sub-Resolution Adhesions. *Nat. Methods* **2015**, *12* (7), 653–656. https://doi.org/10.1038/nmeth.3430.
(274) Gillespie, D. T. Exact Stochastic Simulation of Coupled Chemical Reactions. *J. Phys. Chem.* **1977**, *81* (25), 2340–2361. https://doi.org/10.1021/j100540a008.